Engineering Strategies to Improve All-Solid-State Battery Performance under Low-Pressure Conditions

Benjamin Hennequart

▶ **To cite this version:**

Benjamin Hennequart. Engineering Strategies to Improve All-Solid-State Battery Performance under Low-Pressure Conditions. Material chemistry. Sorbonne Université, 2023. English. NNT : 2023SORUS638 . tel-04524445

HAL Id: tel-04524445
https://theses.hal.science/tel-04524445

Submitted on 28 Mar 2024

HAL is a multi-disciplinary open access archive for the deposit and dissemination of scientific research documents, whether they are published or not. The documents may come from teaching and research institutions in France or abroad, or from public or private research centers.

L'archive ouverte pluridisciplinaire **HAL**, est destinée au dépôt et à la diffusion de documents scientifiques de niveau recherche, publiés ou non, émanant des établissements d'enseignement et de recherche français ou étrangers, des laboratoires publics ou privés.

Sorbonne Université

École doctorale – ED 397 – Physique et Chimie des Matériaux

Collège de France

Laboratoire – Chaire de Chimie du Solide et Énergie

Engineering Strategies to Improve All-Solid-State Battery Performance under Low-Pressure Conditions

Benjamin Hennequart

Doctoral thesis in Materials Science / Chemistry

Directed by Jean-Marie Tarascon and Christophe Lethien

President of the jury: Dr. Mathieu Morcrette

Presented and defended in public on December 18th 2023 in front of the jury,

Dr. Mathieu Morcrette	Research director, LRCS	Referee
Dr. Valérie Pralong	Research director, CRISMAT	Referee
Dr. Florian Strauss	Group Leader, Karlsruhe Institute of Technology	Examiner
Dr. Damien Dambournet	Associate professor, PHENIX, Sorbonne Université	Examiner
Dr. Fanny Bardé	Founder and CTO, SOLiTHOR	Examiner
Prof. Jean-Marie Tarascon	Professor, CSE, Collège de France	Director
Prof. Christophe Lethien	Professor, IEMN, Université de Lille	Co-director

Except where otherwise noted, this work is licensed under
http://creativecommons.org/licenses/by-nc-nd/3.0/

Sorbonne Université

École doctorale – ED 397 – Physique et Chimie des Matériaux

Collège de France

Laboratoire – Chaire de Chimie du Solide et Énergie

Ingénierie pour Améliorer les Performances des Batteries Tout-Solide sous Faible Pression

Benjamin Hennequart

Thèse de doctorat en Chimie des Matériaux

Dirigée par Jean-Marie Tarascon et Christophe Lethien

Président du jury : Dr. Mathieu Morcrette

Présentée et soutenue publiquement le 18 Décembre 2023 devant un jury composé de,

Dr. Mathieu Morcrette	Directeur de recherche, LRCS	Rapporteur
Dr. Valérie Pralong	Directrice de recherche, CRISMAT	Rapportrice
Dr. Florian Strauss	Group Leader, Karlsruhe Institute of Technology	Examinateur
Dr. Damien Dambournet	Chargé de recherche, PHENIX, Sorbonne Université	Examinateur
Dr. Fanny Bardé	Founder and CTO, SOLiTHOR	Examinatrice
Prof. Jean-Marie Tarascon	Professeur, CSE, Collège de France	Directeur
Prof. Christophe Lethien	Professeur, IEMN, Université de Lille	Co-directeur

Except where otherwise noted, this work is licensed under
http://creativecommons.org/licenses/by-nc-nd/3.0/

Acknowledgements

First and foremost, I would like to express my sincere gratitude to Jean-Marie Tarascon for welcoming me in his lab. You have given me your trust to carry out my work with a degree of freedom beyond what I would have hoped. Your guidance and consistent availability have played a pivotal role in shaping this research journey. Through your passion and hard work, you have cultivated an enthusiastic and vibrant lab environment for scientific exploration that has undoubtedly contributed to my growth as a scientist in every regard.

I would also like to thank Christophe Lethien. Although changes in the project's direction limited your direct involvement in this thesis, you consistently provided me with constructive, and when relevant, positive feedback on my presentations and publications.

In many regards, this thesis has greatly benefited from the contributions of various people whom I would like to express my gratitude to for their time and energy. In particular, special thanks to Michaël Deschamps for his help in carrying out the NMR study, Ronan Chometon and Juan Forero-Saboya for their invaluable time spent in performing SEM imaging, Jacques Louis and Gwenaëlle Rousse for their assistance with crystallography and XRD analysis and Carine Davoisne who helped me acquire SEM imaging of my air-sensitive samples. Thanks to Thomas Marchandier and his team in Saint-Gobain for providing me with electrolytes. I am also grateful to Elisa Quemin for her invaluable help with impedance spectroscopy, and I extend my thanks to Maria Platonova for her assistance with various experiments. Many thanks to Romain Dugas for the time dedicated not only to designing low-pressure cells but also in answering my many scientific questions.

Beyond science, these three years spent in the lab were truly enjoyable. I want to specifically express my heartfelt gratitude to my incredible PhD colleagues and friends from the solid-state team, Elisa, Ronan and Tuncay. The atmosphere in the team and these long hours doing experiment followed by our bar sessions would not have been the same without you. Of course, I also thank my great officemates, Damien and Romain, for the countless terrible jokes and shared laughter. Thanks to Benjamin for joining me in our numerous movie sessions, to Jessica for her invaluable help in dealing with all the administrative nightmares. A special thanks to Elisa Q., Ronan, Tuncay, Benjamin, Damien, Jacques, Thomas, Alexia, Elisa G.,

Clémence and to all the former, current, and new lab members whose contributions to the lab's atmosphere have made being a part of it truly enjoyable.

I would like to thank Dr Mathieu Morcrette and Dr Valérie Pralong for their time spent reviewing this thesis and to Dr Florian Strauss, Dr Fanny Bardé and Dr Damien Dambournet for being part of the jury.

Enfin, bien sûr, je remercie infiniment mes parents, mes frères et ma sœur pour le soutien qu'ils m'ont apporté tout au long des hauts et des bas de cette thèse, mais aussi une mention spéciale à Robin, mon cousin, pour ses rires, ses petits plats, pour m'avoir supporté et soutenu ces trois années, et particulièrement pendant les derniers mois de cette thèse.

Table of contents

Broader context and thesis outline

Broader context

In a world where economic growth is the prime driving force for development, the scale of global energy consumption has witnessed an unprecedented surge driven by rapid industrialization and population growth over the past century and this trend is set to persist as emerging economies develop and mature. Traditional energy sources, predominantly relying on fossil fuel combustion have historically dominated the energy landscape due to their abundance, accessibility, and cost-effectiveness. However, the extensive use of fossil fuel since the industrial revolution in the late 18th century has already led to a worrying increase in anthropogenic greenhouse gas (GHG) emissions that today are unequivocally linked to the ongoing climate change and global rise in temperature[1] (Figure 1b). In light of such climate deregulation crisis, addressing global energy demand requires comprehensive and impactful effort and policies from governments, industries, and societies worldwide to limit GHG emissions (Figure 1a). By 2020, the global surface temperature had already increased by 1.1°C and projections from the most recent Intergovernmental Panel on Climate Change (IPCC) report[1] report that limiting our impact on the environment involves a strong necessity in transitioning to sustainable and low-carbon energy alternatives and in electrifying the transportation sector. Both of which have seen their price plummet, making them more accessible and attractive for widespread adoption (Figure 2).

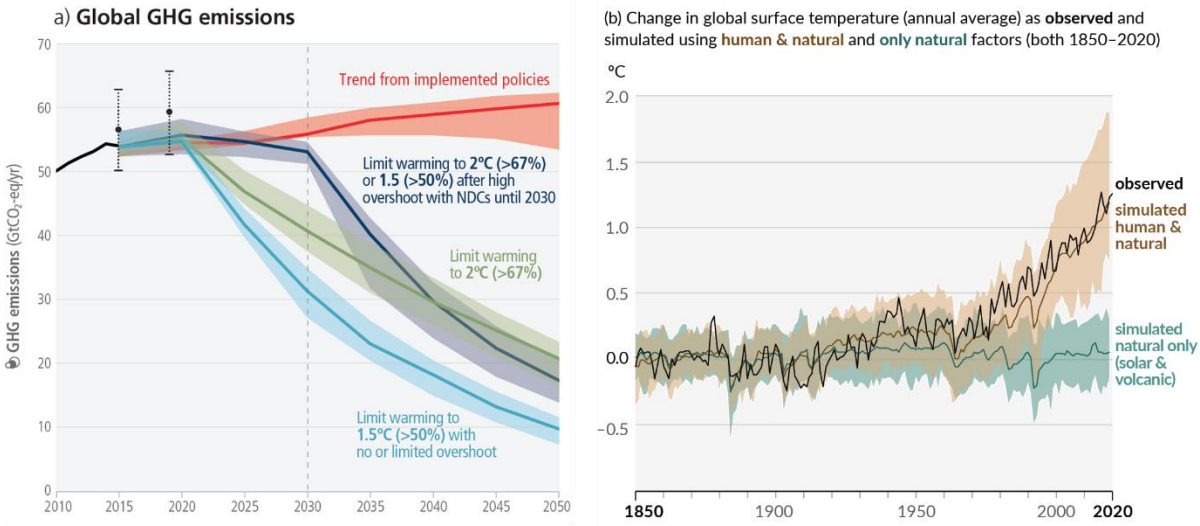

Figure 1. (a) Projected global greenhouse gases emissions depending on followed scenario and trend with the current implemented policies (pre-COP26, red) and (b) change in global surface temperature observed from 1850 to 2020 (black line) and simulated evolution due to natural drivers (green) or human and natural drivers (brown). Adapted from IPCC's AR6 Synthesis report[1].

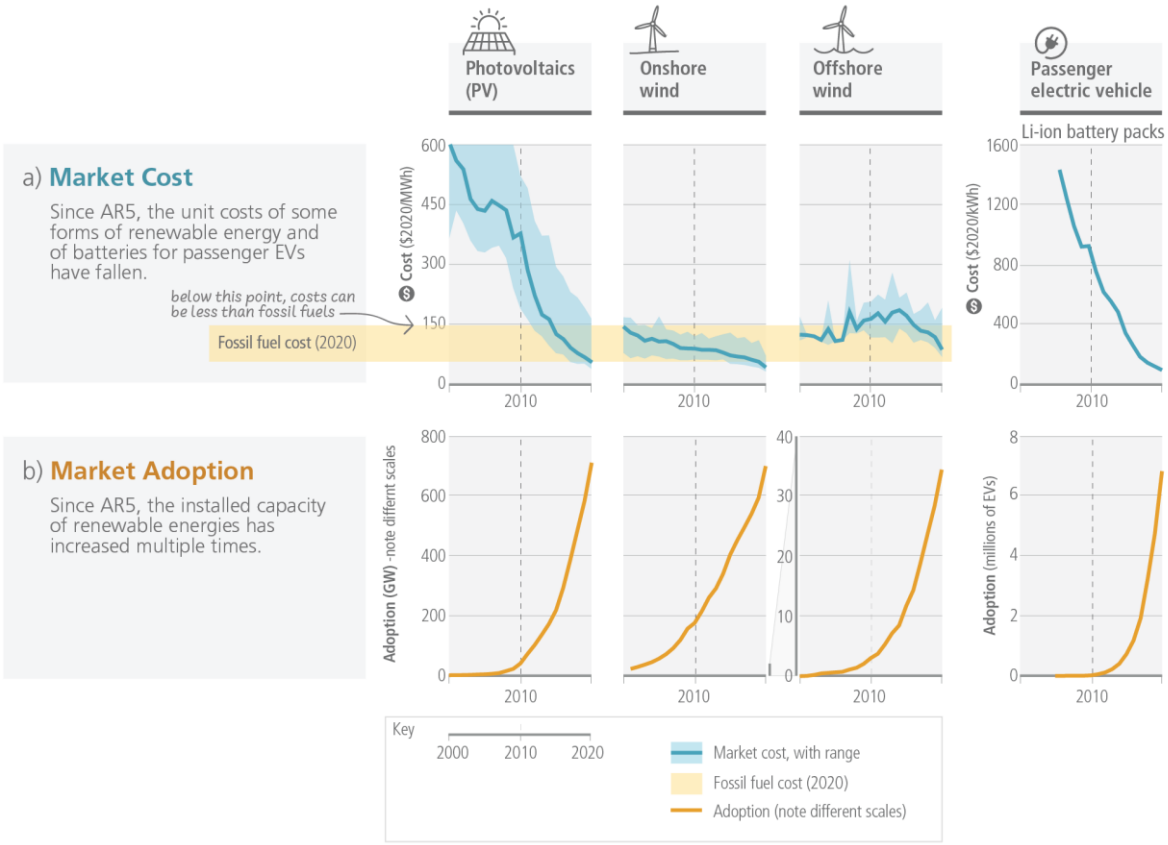

Figure 2. (a) Market cost as compared to fossil fuel cost in 2020 (orange band) and (b) market adoption of photovoltaic (PV), onshore/offshore wind energies and Li-ion battery pack for EVs evolution from 2000 to 2020. Adapted from IPCC's AR6 Synthesis report[1].

Towards this goal, energy storage systems (ESS) are the basis for this transformation. For more than 100 years already, mechanical EES such as dams and pumped-storage hydroelectricity facilities have been used to store excess electricity and balance the load on the electrical grid.[2,3] However, in a world shifting towards renewable but intermittent energy sources and electrified vehicles, energy storage is becoming increasingly important. In recent years, electrochemical energy storage devices, such as batteries, fuels cells or supercapacitors have seen important advancements both in terms of performance and cost. Notably, rechargeable lithium-ion batteries (LIBs) have emerged as the dominant technology in this sector, offering high energy densities[4,5] (up to 350 $Wh.kg^{-1}$) and competitive prices[1] (decreasing from 921 to 137 $2020/kWh between 2010 and 2020, Figure 2a). Already widely adopted in mobile devices, their significance has grown even more in the automotive industry where they play a centre role in the electrification of transportation. Moreover, LIBs are

finding increasing application in large-scale grid storage systems, further highlighting their versatility and impact on shaping the future of energy.

Certainly, the emergence of new applications for lithium-ion batteries, especially in electric vehicles (EVs), brings new requirements. Two key areas that demand improvement are energy density and safety.[6] Increasing the energy density of batteries is essential for enhancing the driving range of EVs while reducing their weight and size. Additionally, safety is of paramount importance, given the potential risks of fires associated with high-power operations of LIBs in EVs.

The aim of this thesis is to contribute to the advancement of practical high-energy all-solid-state battery technology and it will be presented as follow.

Thesis outline

Mainly, this thesis will specifically focus on exploring concepts that enable the reduction of operating pressure of solid-state batteries without affecting their overall performance. This work is divided into five chapters as detailed below:

Chapter 1 introduces the current Li-ion technology and traces the historical development of solid electrolytes from the early 1970s to the present, leading to the resurgence of all-solid-state batteries (ASSBs). The chapter then presents the state-of-the-art ASSBs and discusses their main challenges, emphasizing on the significance of reducing operating pressure for their practical application.

Chapter 2 concentrates on the design of cathode composites that can operate at significantly low pressure by employing a novel family of solid electrolytes known as halide-based SE. The specific chosen solid electrolytes for investigation in this chapter are $Li_3YBr_2Cl_4$ and Li_3InCl_6, selected for their favourable mechanical and electrochemical properties with the former furnished by Saint-Gobain.

Chapter 3 focuses on the use of a possible new concept in all-solid-state battery known as the solid-electrolyte-free cathode composite, which allows important enhancement in the energy density of cathode active material owing to their mixed ionic-electronic conductivity properties.

Chapter 4 is dedicated to the implementation of lithium metal anodes into the systems discussed in the previous chapters. It is followed with a brief discussion on the controversy on the technique used for the study of the lithium/SE interface called Critical Current Density (CCD) determination, which appears to have limitations and could potentially benefit from improvements to enhance its reliability.

To conclude, the last part provides a comprehensive summary of the findings from this thesis and offers valuable insights and guidance for future research to build upon the work presented in this study.

Chapter 1 – Today's Battery Technologies and the Resurgence of All-Solid-State Batteries

1.1 – Overview of Energy Storage and Batteries Technologies

In the history of battery technologies, significant breakthroughs led to the development of modern batteries. Luigi Galvani's first observations of muscular contractions induced by electrical currents in a frog's leg in 1780 marked an important milestone. He noticed that when two different metal came simultaneously into contact with a dead frog's leg, an electrical current flowed between them, causing the frog's leg to twitch; he called this phenomenon "animal electricity". Building on Galvani's discovery, a few years later, in 1800, Alessandro Volta's invention of the Voltaic pile revolutionized the field by introducing the first chemical battery (Figure 1.1). The Voltaic pile is a stack of alternated bilayer of zinc and copper disks, separated by brine-soaked paper disks that demonstrated the production of a steady current.

Figure 1.1. Voltaic pile on display at the Tempio Voltiano museum in Como, Italy. Picture by I, GuidoB, reproduced from reference[7].

With the combination of Galvani's observations and Volta's invention, the understanding of electricity and battery principles began to take shape, and the development of batteries progressed rapidly over the subsequent century. Notably, we can mention the work of Georges Leclanché and Carl Gassner on "dry cell" design between 1868 and 1888, which is the foundation of today's primary alkaline cells, or the development of the lead-acid batteries in 1859 by Gaston Planté, which revolutionized battery technology as the first

rechargeable battery. These innovations paved the way for modern batteries and electrochemical devices we rely on today.

○ General scientific background: the working principle of batteries

Electrochemical storage devices consist in several essential components: a positive and a negative electrode (typically called cathode and anode respectively for batteries), where chemical energy is stored. They are insulated by an ion-conducting electrolyte that facilitates ion movement and connected via an external circuit, enabling the flow of electrons outside of the cell and the harnessing of electrical energy (Figure 1.2).

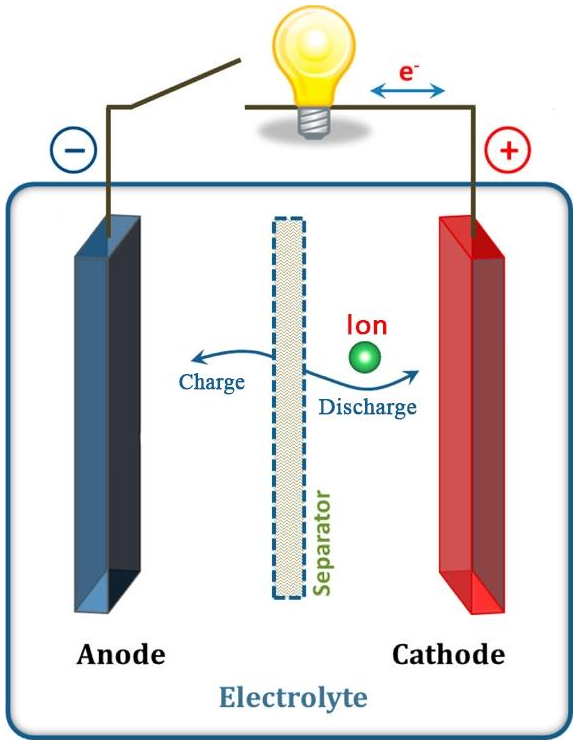

Figure 1.2. Schematic of a battery. Adapted from reference[8].

Among these devices, we can differentiate two classes: the primary and secondary battery systems. In brief, primary cells, characterised by non-reversible chemical reactions, are incapable of being recharged after depletion. In contrast, secondary batteries, featuring reversible reactions, are rechargeable. In secondary systems, the electrochemical reactions taking place at the electrodes are responsible for energy storage or release (charge or discharge) depending on the direction of the flow of electron. Battery performance is determined by various metrics, such as energy density, power density, calendar life, safety, cost or environmental impact, to name a few. Among these, improvement in energy density

and specific energy has been the primary driving force behind technological progress in the field. Also known as volumetric and gravimetric energy respectively, they refers to the amount of energy stored in a battery and are defined as the product of the cell voltage (U) by the capacity (Q) of a particular system (Equation 1.1), expressed per unit of volume ($Wh.L^{-1}$) or mass ($Wh.kg^{-1}$).

$$E(Wh.kg^{-1}) = Q(mAh.g^{-1}) \cdot U(V) \qquad \text{Equation 1.1}$$

The average cell voltage (U) is determined by the averaged difference in potential of the two electrodes of the cell while the capacity (Q) is the total amount of charges transported, typically expressed as amps per unit of mass of electrochemically active material (mAh/g) and calculated with the following Equation 1.2.

$$Q(mAh.g^{-1}) = \frac{nF}{3.6 \cdot M} \qquad \text{Equation 1.2}$$

where *n* is the number of electron involved in the reaction, *F* the Faraday constant ($F = eN_A \approx 96485\ \mathrm{C/mol}$) and *M* the molecular mass of electrode material.

○ The journey towards the state-of-the-art Li-ion batteries and their limitations

Early on, in the pursuit of enhancing battery performance, lithium-based systems were deemed highly promising owing to the low electrochemical potential (-3.04 V *vs.* SHE), lightweight nature (6.94 g/mol) and high capacity (3860 mAh/g) of lithium, thereby enhancing cell voltage and specific capacity. From the 1970s, Li-based battery started being developed with the discovery of multiple lithium intercalation compounds. Intercalation chemistry, a term first introduced by Rouxel[9,10] in 1971 and discussed for application in electrochemical cells by Steele and Armand[10,11] in 1972, serves as the fundamental mechanism for most of the current electrode material. It refers to a host/guest solid-state redox reaction involving the reversible insertion and extraction of guest ions (Li^+, Na^+, etc.) into and from the crystal lattice of a host material during the discharge and charge processes of a battery. These insertion and extraction of ions occur without causing significant structural damage (*eg.* bond breaking) to the host material resulting in a high level of reversibility and an extended calendar life. In 1975, Whittimgham laid the foundation of Li-based battery systems with the first use in a battery of a Li^+-intercalation compound, the layered dichalcogenides TiS_2. This material having a reasonably high lithium potential (around 1.8 V *vs.* Li^+/Li) and allowing for reversible insertion

and extraction of Li ions was promising for use as a cathode material in Li-based batteries coupled to a Li-metal anode, following the reactions below.

$$(at\ positive\ electrode)\quad TiS_2 + Li^+ + e^- \rightleftarrows LiTiS_2 \qquad \text{Equation 1.3}$$

$$(at\ negative\ electrode)\quad Li \rightleftarrows Li^+ + e^- \qquad \text{Equation 1.4}$$

Exxon explored the potential commercialisation of this TiS_2/Li metal system while the similar MoS_2/Li metal system was developed and commercialised by Moli Energy in the 1980s. However, both systems faced challenges, particularly related to safety risks associated with the use of a lithium metal anode (LMA). During the charging process, the use of a LMA often leads to uneven plating of lithium on the anode's surface, forming dendrites (Figure 1.3a). These growing dendrites ultimately cause internal short circuits leading to potential fire hazards and safety issues.

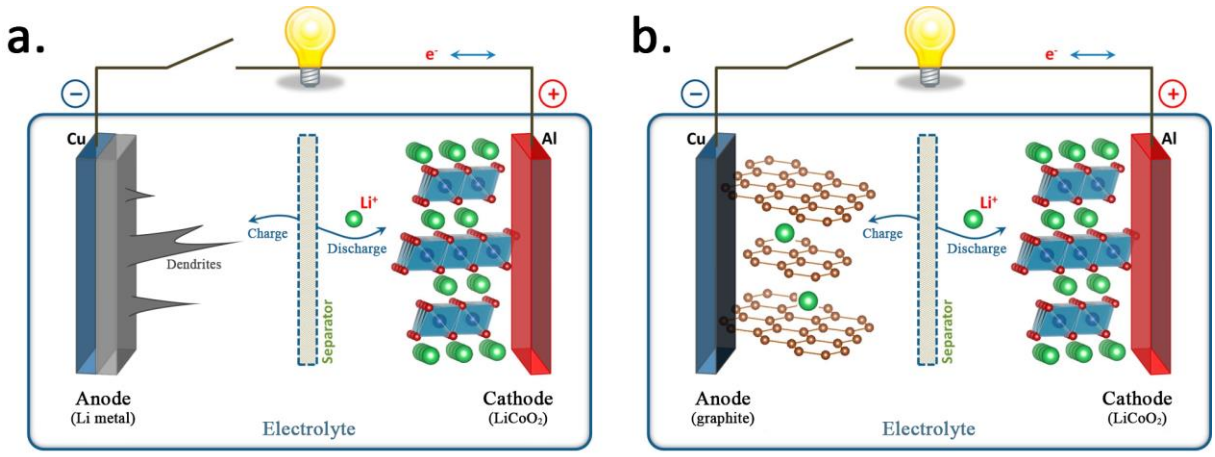

Figure 1.3. Scheme of (a) a lithium metal based cell with dendrite formation and (b) a typical lithium-ion cell with a graphite anode. Adapted from reference[8].

Despite the setbacks faced by early lithium-based systems, research and development efforts persevered. In 1980, John B. Goodenough introduced a new transition metal layered oxide $LiCoO_2$ (LCO), a higher potential oxide cathode compound that held great promise for battery technology. The pursuit of safer and more efficient battery systems continued, and in 1991, Sony achieved a significant milestone by commercialising the first lithium-ion battery (LIB). This revolutionary battery, pioneered by Akira Yoshino, incorporated Goodenough's $LiCoO_2$ cathode and a newly developed carbonaceous anode (Figure 1.3b). The use of carbon-based intercalation materials for the anode mitigated the safety risks associated with lithium metal, allowing for the successful commercialisation and widespread adoption of LIBs in

diverse applications. In recognition of their outstanding contributions on the development of lithium-ion batteries, M. Stanley Whittingham, John B. Goodenough, and Akira Yoshino were awarded the Nobel Prize in Chemistry in 2019.

In the subsequent decades following Sony's battery commercialisation, remarkable progress was achieved in the development of cathode materials, with notable example being the NMC/NCA family ($LiNi_{1-x-y}Mn_xCo_yO_2$ and $LiNi_{1-x-y}Co_xAl_yO_2$). Within this family, the partial substitution of cobalt in $LiCoO_2$ to other transition metal such as nickel or manganese has led to significant improvements in specific capacity, structural and thermal stability. This family, and particularly the NMC622 ($LiNi_{0.6}Mn_{0.2}Co_{0.2}O_2$) and NMC811 ($LiNi_{0.8}Mn_{0.1}Co_{0.1}O_2$) compositions are now widely utilised in the current generation of Li-ion batteries.[12] The next-generation cathode materials include the Li-rich layered oxides compounds ($Li_{1+x}M_{1-x}O_2$ with M a transition metal) that show a 25% increase in energy density but still suffer from non-resolved hurdles such as voltage fade and low energy efficiency.[13] However, it is worth mentioning that, in parallel of the layered oxide, other Co-free compounds have been developed such as the spinel $LiMn_2O_4$ or the polyanionic $LiFePO_4$ (LFP) family phases, thereby enhancing the battery's specific energy and/or environmental friendliness while simultaneously addressing the ethical concerns associated with cobalt extraction. In particular, the latter LFP chemistry have seen an important penetration in today's market (Figure 1.4) and a substantial growth is projected for this technology in the coming decades owing to its use in light electric vehicles.[12]

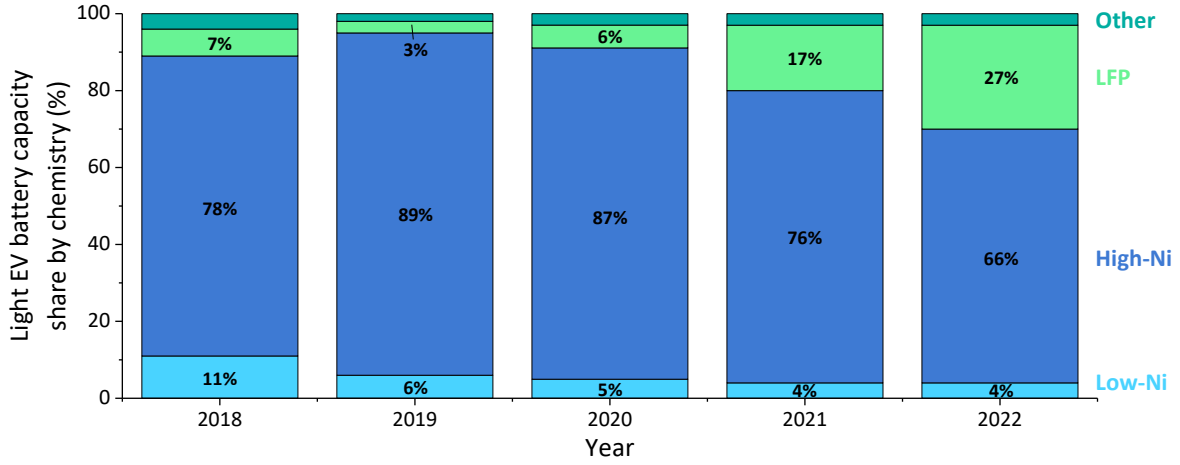

Figure 1.4. Electric light-duty vehicle (EV) battery capacity by chemistry, market share evolution from 2018 to 2022. Low-Ni includes NMC333. High-Ni includes NMC532, NMC622, NMC721, NMC811, NCA and NMCA. Cathode sales share is based on battery capacity. Adapted from reference[12].

Due to their remarkable energy density[14] and decreasing costs[1], current Li-ion batteries have gained widespread adoption in portable electronics and electric vehicles (EVs).[1] However, they are now approaching their theoretical limits, with energy densities reaching approximately 300 to 350 $Wh.kg^{-1}$, and achieving further significant improvements will necessitate substantial paradigm shifts. A key constraint lies in the challenges associated with introducing lithium metal anodes, which have the potential to substantially enhance the energy density. Although several alternative paths to enhance energy density are currently under exploration such as anionic redox compounds, Li-sulphur systems or full silicon anodes, these paths are still in the early stages of research and development. Presently, the most advanced system, utilising an NMC-type cathode and a Li metal anode, reaches energy density of up to 575 $Wh.kg^{-1}$ (Figure 1.5), nearly double that of previous systems but to the expense of a poor cycle life.[15]

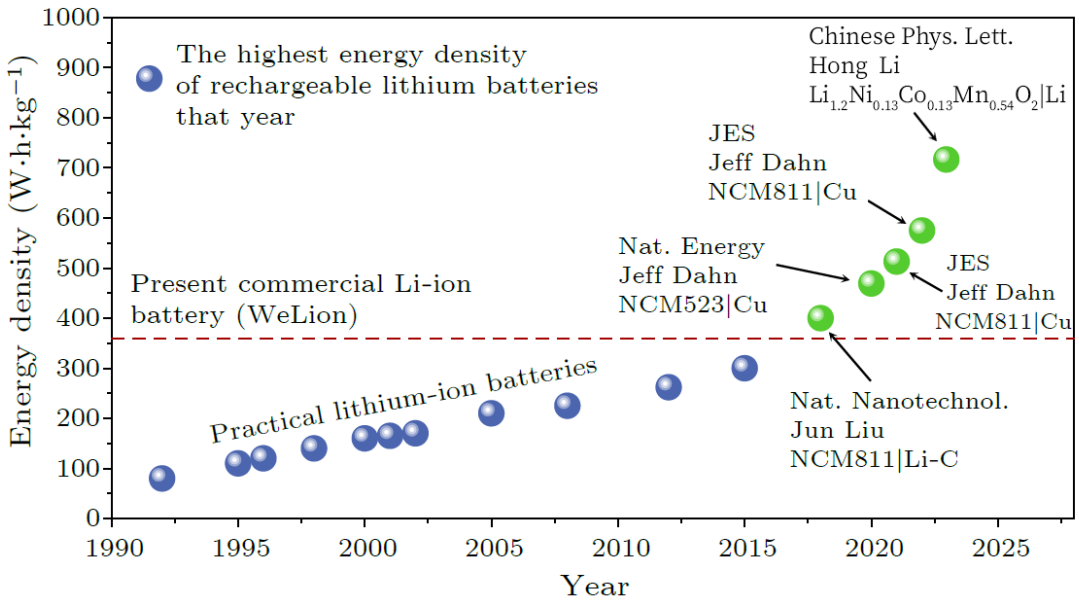

Figure 1.5. Evolution of the energy density of rechargeable intercalation-type cathode pouch cells in the past 30 years. Green dots highlight cells including a lithium metal anode (or anodeless designs, designated by Cu for copper current collector). Adapted from reference[14].

The pursuit of enhanced energy density by integration of the LMA has revealed the need to push towards novel battery systems capable of preventing dendrite growth and ensuring superior safety. Thus, the investigation into all-solid-state battery systems has emerged as a promising avenue to address these challenges.

1.2 – The Resurgence of All-Solid-State Batteries: An Historical Approach on Solid Electrolyte Development

○ The potential benefits of all-solid-state batteries

The success of LIBs in powering a diverse range of applications is undeniable. Nevertheless, with the ever-increasing requirements for increased energy density, improved safety, and prolonged battery life, researchers have turned their attention to all-solid-state batteries (ASSBs) as a promising transformative alternative. Unlike conventional LIB cells that utilise liquid electrolytes as the ionic carriers, ASSBs adopt a solid electrolyte that serves both as a Li-ion conductor and as a separator, presenting a fundamental shift in their design and composition that could offer a range of promising benefits.

Notably, by replacing the flammable organic liquid electrolyte to a ceramic solid electrolyte (SE) (Figure 1.6), ASSBs holds the promise to substantially improve safety by effectively mitigating fire hazards arising from electrolyte leakage. Moreover, owing to their solid nature, SEs are anticipated to allow the use of LMAs by effectively create an impenetrable solid barrier to lithium dendrites, addressing a long-standing challenge in traditional LIBs. As a result, ASSBs incorporating LMAs are projected to exhibit a substantial increase in energy density over LIBs. Theoretical estimates propose a potential enhancement of 70% in volumetric energy density and 40% in gravimetric energy density.[16]

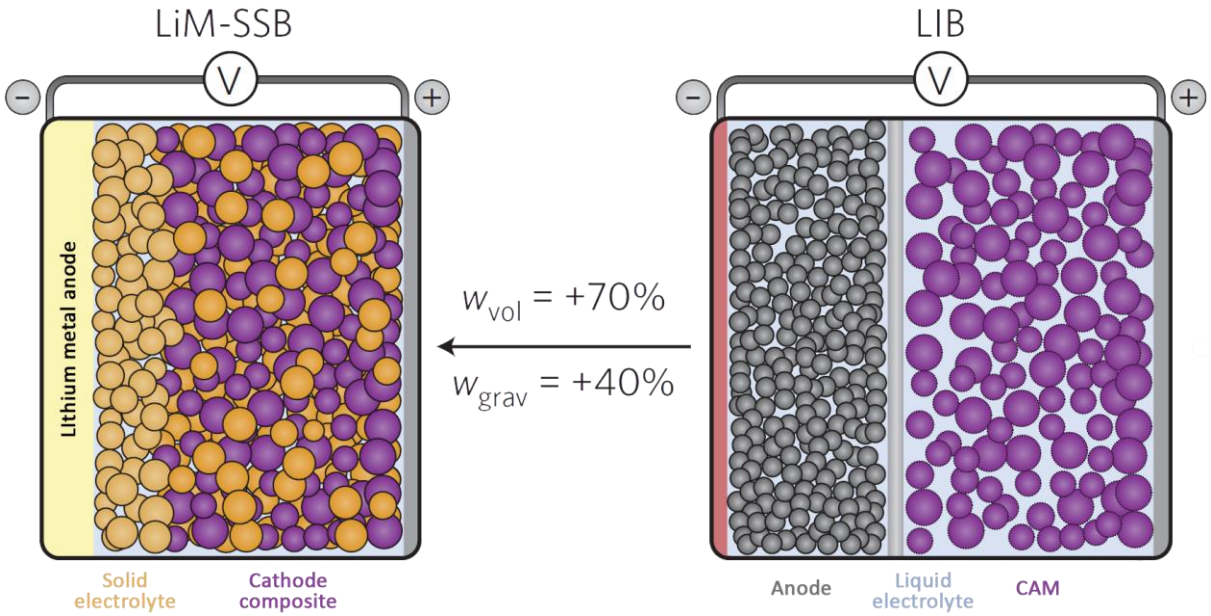

Figure 1.6. Scheme of a typical lithium-ion battery (right) and a lithium metal all-solid-state battery (left) with compared volumetric (w_{vol}) and gravimetric (w_{grav}) energy densities of both systems. CAM stands for cathode active material. Adapted from reference[16].

ASSB offer another significant advantage in terms kinetics primarily attributed to the unity transference number ($t_+ = 1$) of such SEs. This unique feature is expected to allow ASSBs to achieve higher power density compared to their liquid counterparts, which usually have lower transference numbers due to the presence of mobile anions in solution.

In addition to the aforementioned benefits, this technology offers further advantages, notably the ability to leverage the wide range of chemistry possibilities of SEs, enabling the use of higher voltage cathode active material (CAM) and offering a wider temperature range operation, further contributing to increase energy density and safety, respectively. Another notable advantage is the effective suppression of the chemical cross talk issues between electrodes observed in conventional LIBs that arise from the dissolution of species in the liquid electrolyte (LE) often resulting in self-discharge and battery degradation.

Furthermore, looking at the assembly of the ASSB, the concept of a bipolar stacking architecture can be considered (Figure 1.7a). It involves the arrangement of cells connected directly in series within a battery module by placing cathodes and anodes on opposite sides of a single current collector, the bipolar plate (green plates in Figure 1.7a). In theory, this design could offer enhanced power capabilities and energy density, as well as reduced costs.[17] In addition, owing to the homogeneity of the electron flow through the bipolar plates compared to regular current collectors (Figure 1.7b and d), it was calculated that the power capabilities were improved while heat generation upon cycling at high rates reduced.[17] However, in practice, its implementation presents significant challenges and it is not clear if the bipolar architecture would offer significant advantages over the typical parallel stacking that consists in double-coated current collector cells arranged in parallel and that is already readily used in LIBs (Figure 1.7c). An in-depth study on the actual benefits of such architecture over the parallel one is still needed. The main issue of a bipolar system lies in the lack control of individual cell potential within the stack. As a result, all cells present in the bipolar stack must be precisely identical in terms of manufacturing and behaviour over cycling. This uniformity is essential to ensure the proper operation of the entire stack and avoid imbalances that could potentially compromise the overall efficiency and stability of the system. Additionally, adapting the manufacturing process of such system remains crucial to prevent any internal short circuit due to misalignment of the different layers.

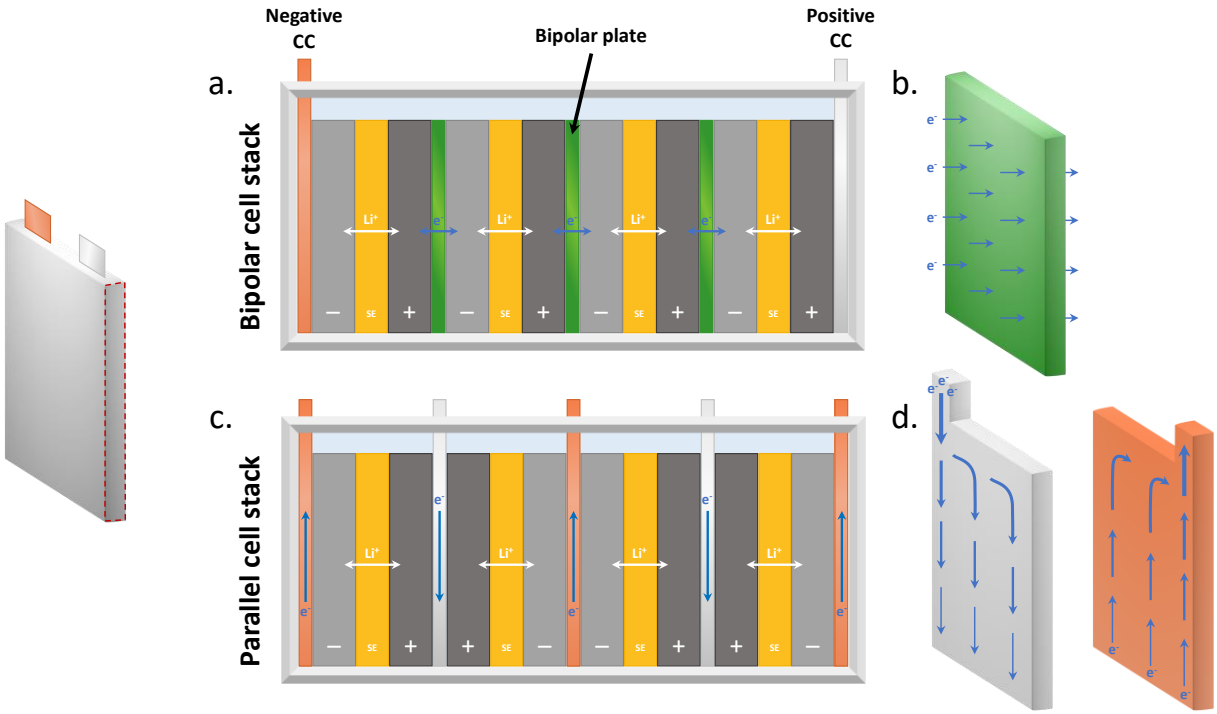

Figure 1.7. Differences between bipolar and regular parallel cell stacking architecture. Schematics of (a) a bipolar and (b) a regular parallel monopolar cell architecture with four cells in a pouch cell of identical energy, and the electron flow difference in the monopolar and bipolar plates. CC stands for current collector.

Given the many advantages mentioned above, ASSBs have received significant attention in recent years. To understand the development and progress of SEs, it is essential to explore their historical evolution, which highlights the evolution of the materials and technologies used in this field.

○ From the early inorganic solid conductor discoveries to the first solid lithium-ion conductors

The field of solid-state ionics and the study of ionic conductors can be traced back to the early 19th century when scientific knowledge was far from what it is today. The laws of thermodynamics had not yet been formulated, and the periodic structure of crystals was still unknown. Concepts such as point disorder and entropy were not yet developed, and the very existence of atoms and ions was still disputed. It is in that historical context that in just a few years, between 1831 and 1834, Michael Faraday discovered the motion of mobile ions in both liquid and solid thus laying the foundation of electrochemistry and solid-state ionics. In 1834, Faraday's observation of remarkable conduction properties in heated solid Ag_2S and PbF_2 marks the earliest recorded instance of a transition from poorly conducting to conducting state in an ionically conducting material, which are now recognised as solid electrolytes.[10]

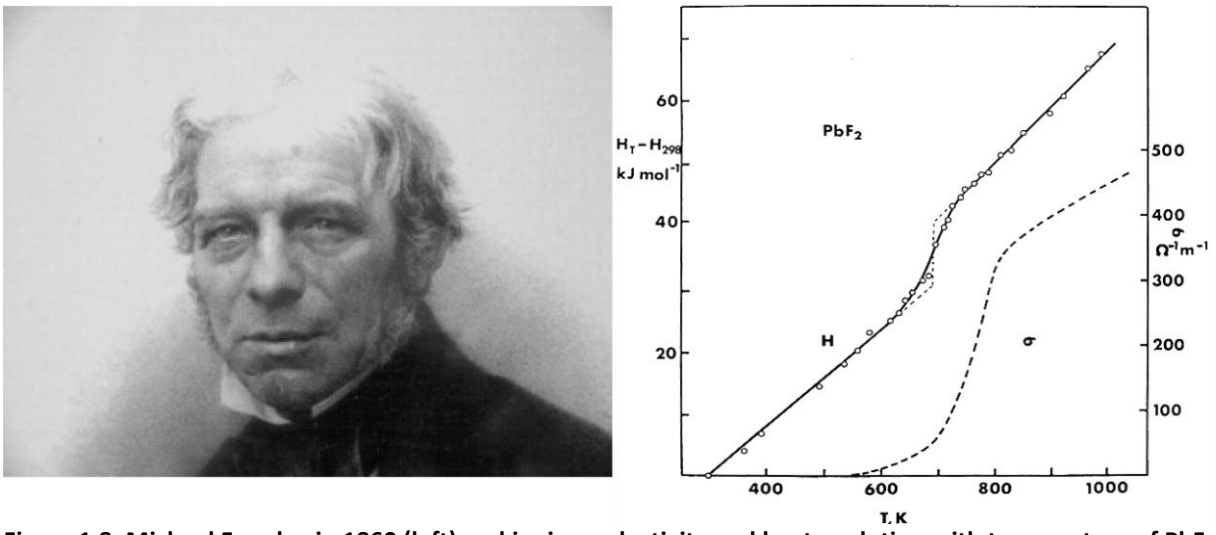

Figure 1.8. Michael Faraday in 1860 (left) and ionic conductivity and heat evolution with temperature of PbF_2 (right). Reproduced from references[10,18,19].

Over the following century, progress in the study of ionic conductors was relatively slow, marked by a few notable discoveries. One of these was made by Nernst in 1900, who described the high conductivity observed in yttria-stabilized zirconia[10,20], which was later confirmed to be an oxygen-ion conductor[10,21] During this period, other highly conductive silver ion conductors were also studied, with notably the silver halides.[22] However, it was not until the late 1960s that a significant turning point was observed in the field of solid-state ionics when two remarkable fast-ion conductors, rubidium silver iodide ($RbAg_4I_5$) and β-alumina were discovered. The introduction of $RbAg_4I_5$[23] brought promising prospects with its high silver ion conductivity at room temperature (RT), while β-alumina $M_{1+\delta}Al_{11}O_{17}$, unveiled by Yao and Kummer in 1967, was the first ambient temperature fast ionic conductor, other than silver, to be discovered. Notably, β-alumina stands out amongst solid conductors, demonstrating high conductivity for various ionic species such as monovalent Li^+, Na^+, K^+, H_3O^+ or divalent Mg^{2+}, Ca^{2+} cations.[24] Upon these discoveries, batteries incorporating such electrolytes into full solid-state cells were developed; however, they encountered challenges stemming from the low energy density (about 5 $Wh.kg^{-1}$) in $RbAg_4I_5$ cells and the high brittleness of β-alumina. These obstacles resulted in the gradual discontinuation of their utilisation without attaining the threshold of commercial viability.

Simultaneously, other lower conducting SE were studied, in particular Li^+ conductors such as lithium nitride[25] (Li_3N) with its relatively good ionic conductivity (10^{-4} S/cm) or lithium iodide (LiI). First studied in the 1930s[26] and although exhibiting a low Li^+ ion conductivity of

only about 10^{-7} S/cm, the latter is of particular importance since it got successfully employed in a primary non-rechargeable cell for cardiac pacemaker in 1972 in Italy, when the first lithium-battery-powered (Li|LiI|I_2) device was implanted into a human being.[27,28] To this day, several millions of people have benefited from implantable devices powered by diverse iterations of the Li/I_2 battery design.

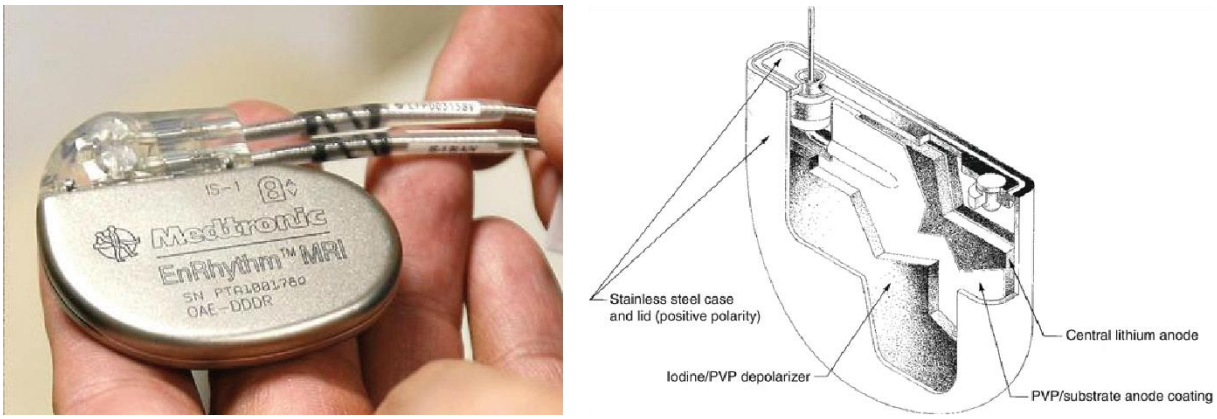

Figure 1.9. Image of a modern implantable cardiac pacemaker powered by a Li/LiI/I_2 primary cell (left) and cross view of the device with the battery (right). Reproduced from references[29,30].

In the following decades, the exploration of solid conductors for Na^+ and Li^+ ions led to significant breakthroughs. Particularly noteworthy was Goodenough's discovery[31] of the fast sodium ion conduction in NASICON (Sodium SuperIonic CONductor)-type compounds ($Na_{1+x}Zr_2Si_xP_{3-x}O_{12}$, $0 \leq x \leq 3$) in 1976. Drawing inspiration from this, in 1986, Subramanian *et al.* explored Li-conduction within several similar NASICON-type structure. This pursuit led them to the identification of the conduction in $LiTi_2(PO_4)_3$ ($2 \cdot 10^{-6}$ S/cm at RT) which could further be improved by partial substitution of Ti by Al to give rise to the compound $Li_{1.3}Al_{0.3}Ti_{1.7}(PO_4)_3$ (LATP) exhibiting a conductivity of $7 \cdot 10^{-4}$ S/cm at RT. Concurrently during this period, other types of SE were under examination and it is within this timeframe that a separation into different families characterised by diverse compositions, ionic and electronic conductivities, and mechanical properties, became apparent. Today, we separate these ceramic SE into mainly three different families: oxide, sulphide and halide SEs. It is worth highlighting that polymer-based and hybrid polymer/ceramic SE have also been subjects of investigation since the 1970s;[32] however, they do not fall within the scope of this thesis and will not be addressed hereafter.

Altogether, the amalgam of these historical discoveries opens the way for high performance SEs, a journey explored in the next section.

○ The race towards high performing inorganic solid electrolytes: The rise of different families

After these initial advances the research on ionic conductors has continued but at a slower pace due to the rapid development of liquid Li-ion batteries that took the forefront and mobilised most of the research efforts.

In the quest for better SE, several key requirements must be met to realise a functional battery. Among others, a robust solid electrolyte must have a high ionic conductivity (> 10^{-3} S/cm at RT), possess a broad electrochemical stability window (preferably ranging from 0 to 5 V vs. Li^+/Li), demonstrate sufficient chemical stability with moisture, cathode material and lithium metal, while also being easy to process. In the decades following the early discoveries, the main driving force behind SE developments has been the enhancement of ionic conductivity. In that purpose, several new types of solid electrolytes were then developed.

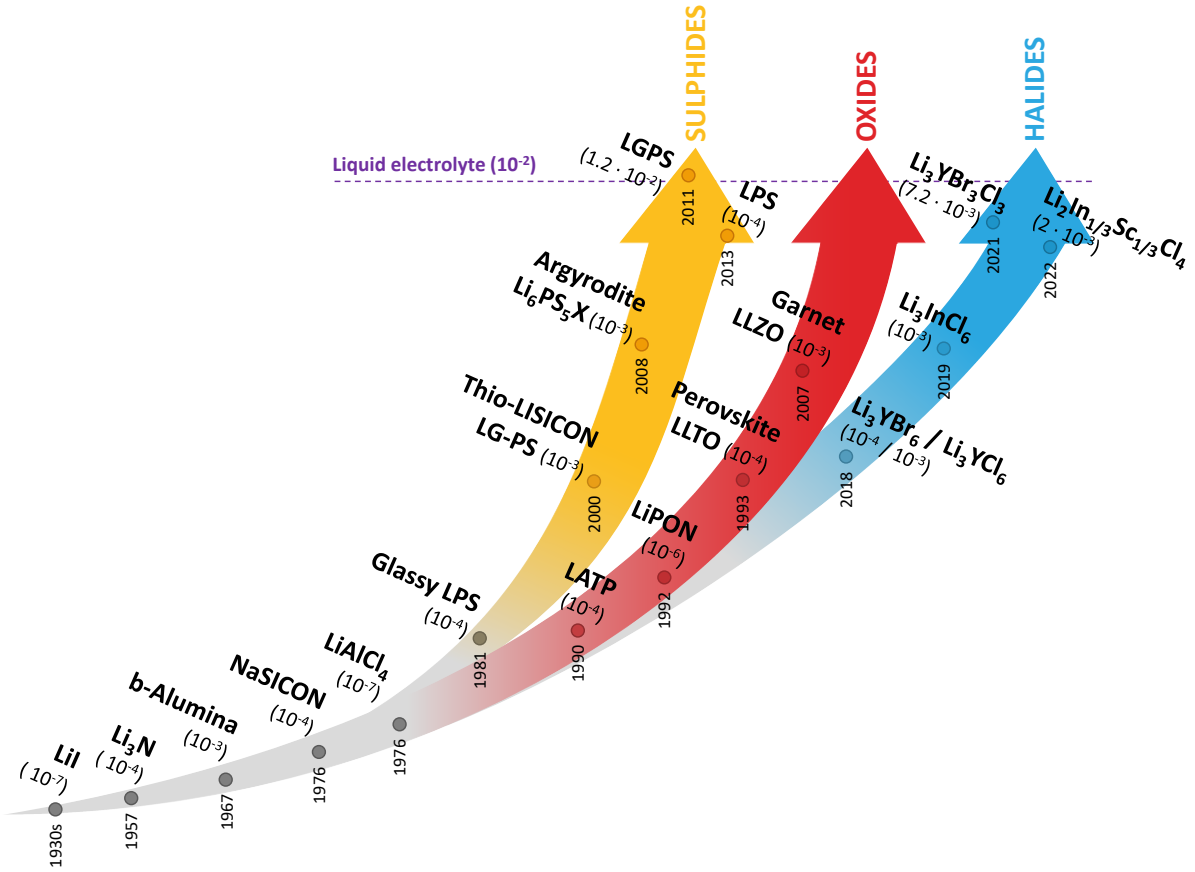

Figure 1.10. Chronological development of the three main families of inorganic solid electrolytes towards superionic Li^+ conductivity. Ionic conductivities, denoted in parentheses, are expressed in S/cm.

The oxide solid electrolyte family was further explored after the NASICON and LATP works from the 70's and 90's. Noteworthy are the perovskite-type $Li_{3x}La_{2/3-x}TiO_3$ (LLTO), discovered in 1993, which exhibits an ionic conductivity of around 10^{-5}-10^{-4} S/cm[33,34] and the garnet-type $Li_7La_3Zr_2O_{12}$ (LLZO), described in 2007 by Weppner's group[35], showing a conductivity of $7 \cdot 10^{-4}$ S/cm (at 25°C) which was further improved[36] in 2013 to > 10^{-3} S/cm (at RT) by partial substitution of Zr by Al, Ga, Ta, etc. These oxide SEs often demonstrate good stability with moisture, exhibit high thermal stability and have wide electrochemical potential stability window, making them ideal for coupling with high potential CAM. However, although presenting some advantages, due to their high mechanical rigidity, these oxides are difficult to process and integration into ASSB cells remains challenging. Moreover, their conductivities are still lacking behind the ones of their liquid counterparts.

Sulphide solid electrolytes (SSEs) have been under investigation since 1981 when research began with the substitution of oxygen with sulphur in the glassy Li_2O-P_2O_5 thus resulting in the formation of the sulphide glass Li_2S-P_2S_5.[37,38] This compound and its derivatives were found to exhibit conductivities in the range of 10^{-4} S/cm at RT. Throughout the following decade, no notable improvements were observed until the year 2000, when Kanno's group introduced a new family of SSEs, the thio-LiSICON (Lithium SuperIonic CONductors) $Li_{4-x}Ge_{1-x}P_xS_4$ ($0 < x < 1$) family[39], which exhibited conductivities of 10^{-3} S/cm, and it is in 2011 that the same research group made another significant contribution. Unveiling the discovery of a new SE $Li_{10}GeP_2S_{12}$ (LGPS)[40], the first capable of reaching high ionic conductivities ($1.2 \cdot 10^{-2}$ S/cm) which are comparable to those of their liquid counterpart (typically around 10^{-2} S/cm). This discovery marked the rebirth of the ASSB field, which had been suffering from limited advancements. From then on, the race towards the best performance SSE's compounds starts. Other families of SSE were developed over the years. In 2016, Kanno's group unveiled another highly conducting SE the $Li_{9.54}Si_{1.74}P_{1.44}S_{11.7}Cl_{0.3}$, with a LGPS-type structure, it displayed an exceptionally high conductivity of 25 mS/cm.[41] In addition from 2008 onwards, the argyrodite-type SSEs (Li_6PS_5X, X = Cl, Br, I) were also developed in parallel.[42] To date, this class of SSEs remains the most widely used and studied, with Nazar's group achieving the highest conductivity with the $Li_{5.5}PS_{4.5}Cl_{1.5}$ argyrodite composition. SSEs show high ionic conductivity and excellent mechanical ductility, allowing for simple processing through

cold-pressing. However, they suffer from poor chemical and electrochemical stability, as well as sensitivity to moisture which results in the release of toxic H_2S gas.[38,43]

The third SE class is the halide-based SE. They have been studied since the 1930s, primarily with the lithium halides (LiX with X = F, Cl, Br, I)[27,44] and later in 1976 by Weppner and Huggins with their work on $LiAlCl_4$, however they were still poorly conductive (10^{-7}-10^{-6} S/cm). It is only recently, in 2018, that they have regain much interest with the discoveries of the Li_3YCl_6 and Li_3YBr_6 by Asano and co-workers, which exhibited excellent RT ionic conductivities of $5.1 \cdot 10^{-4}$ and $1.7 \cdot 10^{-3}$ S/cm, respectively.[45] Since then, the development of new metal-halide SE, now generally characterised by the formula Li_aMX_b (where M represents a metal cation such as In, Zr, Y or Sc, and X a halide), has taken off with the introduction in recent years of a series of high performing halide SEs.[44,46–54] A case in point is the study on the mixed halide $Li_3YBr_3Cl_3$, which exhibited an exceptional conductivity of $7.2 \cdot 10^{-3}$ S/cm after hot-pressing at 170°C[46] as well as of $Li_2In_{1/3}Sc_{1/3}Cl_4$ which revealed an excellent stability with high potential CAM as demonstrated by Nazar *et al.*[54] Compared to oxide or sulphide SEs, halide SEs combine the merits of both of their advantages. Notably, they display a broader electrochemical stability window (up to 6.71 V vs. Li/Li^+)[55] and a better chemical stability toward CAM, traits often associated with oxides, while also offering high ionic conductivity at RT and remarkable deformability, characteristics reminiscent of sulphide-based SE. However, they still lack in stability towards both moisture and low potential anodes such as Li metal.

Overall, when designing an ASSB, the selection of the SE plays an essential role. This choice significantly influences the battery's performance by impacting chemical compositions, compatibility with the CAM and Li, processability, and overall cost. The main distinctions are outlined in Figure 1.11 below.

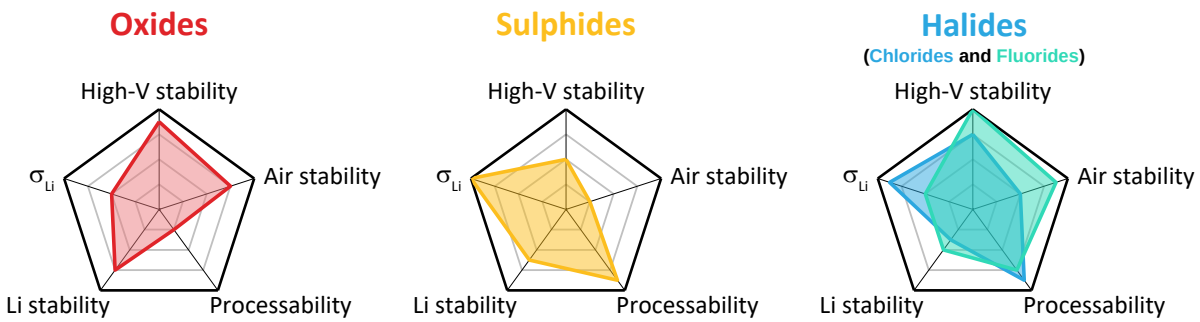

Figure 1.11. Key metrics comparison for the three main solid electrolyte families. Adapted from reference[56].

Expanding upon these three core families, other types have been studied in the past few years. Particularly notable is the emerging lithium-metal-oxyhalide family, which has introduced some promising high-conductivity compounds. Examples include the glassy Li_3OCl phase, reaching an ionic conductivity of 25 mS/cm at 25°C, or the $LiTaOCl_4$ and $LiNbOCl_4$ (12.4 and 10.4 mS/cm, respectively, at 25°C).[57–61] Additionally, nitride-based SE like Li_3N and Li_5NCl_2, despite exhibiting low conductivities, are still under investigation as they hold the promise of a stable interface with Li metal, a property lacking in most high conductivity SEs.[62,63]

1.3 – Persisting Challenges in All-Solid-State Batteries

Given the evolving landscape of SEs and the diversity within the existing families being discussed, it is essential to understand the remaining challenges associated with designing ASSBs. Indeed, although being expected to present some transformative advantages compared to liquid-based electrolytes, the use of SEs have proven difficult on multiple aspects.

○ Chemical and electrochemical interfacial reactivity in ASSBs

Since ASSBs are made entirely of solid materials, most of the issues currently encountered arise from the various Solid-Solid interfaces within the cell. Figure 1.12 illustrates the main challenges pertaining to ASSB design, which are mainly divided between the cathode and anode interfaces.

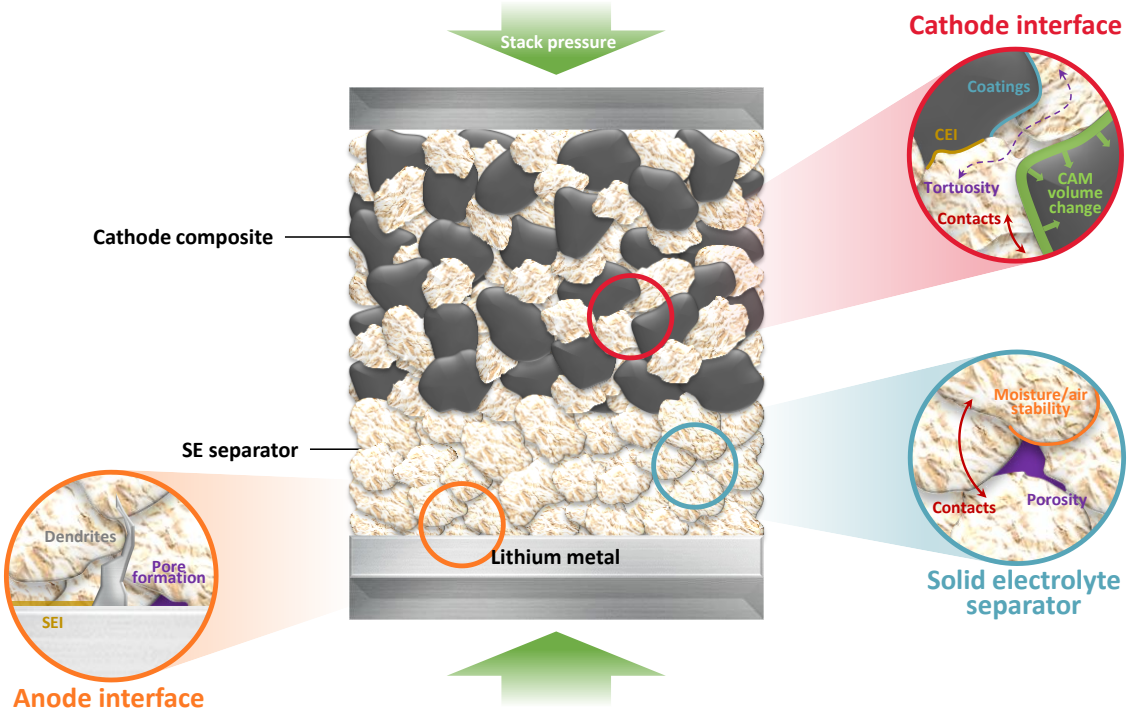

Figure 1.12. ASSB cell illustration and main challenges associated to their development.

Similar to liquid systems, the high potential of advanced CAMs or the strong reduction capability of lithium metal raises stability concerns at electrolyte/electrode interfaces. Three types of interfaces can be formed; they are listed below and illustrated in Figure 1.13:

1. *Thermodynamically Stable Interface*: This type of interface is inherently stable and experiences no chemical reactions between the electrolyte and electrode. Typical examples are the nitride-based SE/Li^0 interfaces.[64]

2. *Non-Passivated Mixed-Conductive Interphase (MCI)*: In this case, the interface is unstable and a mixed ionic/electronic interphase is formed, thus resulting in the continuous growth of the interphase until short-circuit.

3. *Passivated Kinetically Stable Interphase (SEI)*: Formed by chemical reactions at the electrolyte-electrode interface, this interphase is electronically insulative while ideally being ionically conductive. Therefore, it is self-limiting and passivates the surface preventing further decomposition. Typically observed for most sulphide SEs in contact with CAM or Li^0 and recently reported for some F-based halide SEs/Li^0 interface.[48,50,65]

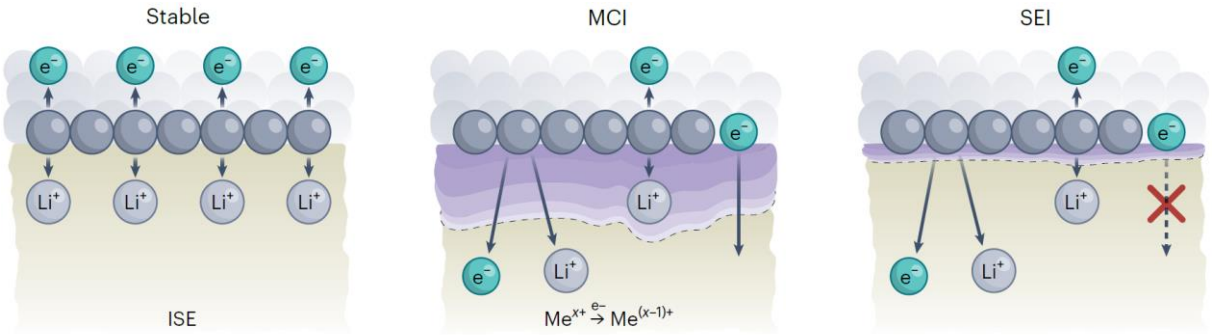

Figure 1.13. Illustration of the three types of interfaces that can be formed at the AM/SE interface. Reproduced from reference[66].

Such interphases are formed at the lithium metal anode (LMA) surface and within electrode composites at interfaces between SE and e^--conductive surfaces such as carbon additives or CAMs. Both the kinetically stable (SEI) and thermodynamically stable interfaces are beneficial for long-term battery performance. The thermodynamic stability is determined by the electrochemical potential stability window of each electrolyte and corresponds to the voltage range within which the SE remains stable. It can be computationally calculated by density functional theory (DFT) or determined experimentally via cyclic voltammetry (CV) measurements (Figure 1.14a). Although taking into account the kinetic dimension of such

reactivity, the latter often leads to overestimation of the stability window. This is primarily due to the challenge of precisely determining the current threshold at which the system is considered unstable. Furthermore, an insufficient electronic surface in contact with the SE can also contribute to overpotential of the reactivity, thereby resulting in an overestimation of the stability window. The electrochemical potential stability windows of typical SEs used in ASSB are given in Figure 1.14b.

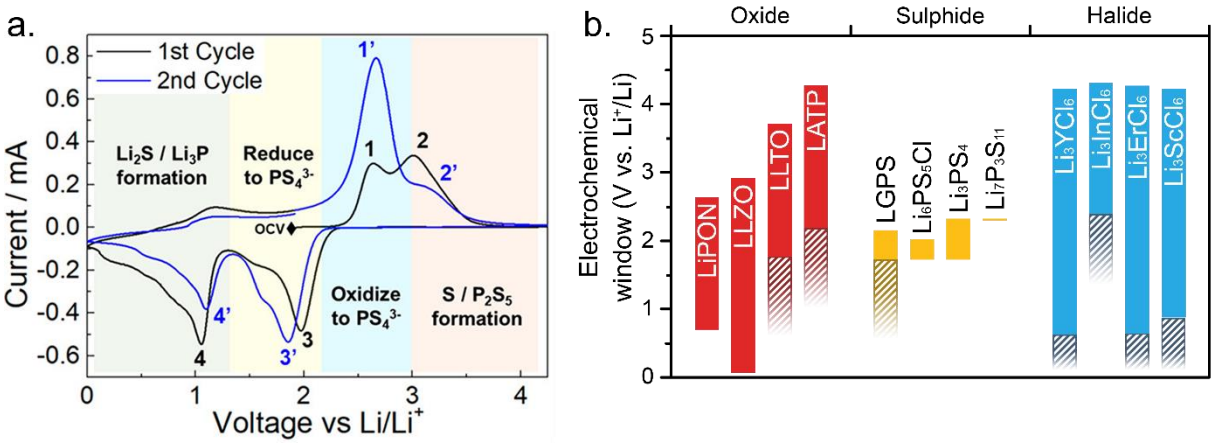

Figure 1.14. Electrochemical stability window of solid electrolytes. (a) Cyclic voltammetry measurement on a LPSCl+C/LPSCl/Li cell in the voltage range 0-4.2 V vs. Li/Li$^+$. Reproduced from reference[67]. (b) Calculated electrochemical potential window of typical solid electrolytes. Hashed regions correspond to SE that are unstable and form a mixed conducting interface (MCI) upon contact with lithium metal. Adapted from reference[68].

Hence, it is critical to consider this intrinsic stability window when pairing SE with electrode materials. Since, if upon cycling the AM potential goes beyond the SE stability window, an interphase will form. For instance, Li_6PS_5Cl, with its narrow thermodynamic stability window, displays instabilities at both high and low potential. This results in the formation of insulative species (left phase equilibrium in Figure 1.15), as per the proposed mechanism[67] below, ultimately giving rise to a self-limiting SEI at both the CAM and Li metal interfaces.

In oxidation: $Li_6PS_5Cl \rightarrow LiCl + \frac{1}{2}P_2S_5 + \frac{5}{2}S + 5Li^+ + 5e^-$

In reduction: $Li_6PS_5Cl + 8Li^+ + 8e^- \rightarrow LiCl + Li_3P + 5Li_2S$

On the other end, halide-based SEs, such as Li_3InCl_6 or Li_3YCl_6, usually exhibiting high oxidation limits and are well suited for high-potential CAM. However, due to their limited reduction stability and the presence of the central metal cation that can be reduced from M^{n+} to the electronically conductive M^0, these SEs decompose at low potential into species that exhibit both ionic and electronic conductivities (as depicted in Figure 1.15). Consequently, this

decomposition gives rise to a mixed-conductive interphase (MCI) which prevents their use in direct contact with low-potential anode materials. Such MCI formation is also observed with other SEs such as LGPS, LLTO or LATP due to their metal cations Ge^{4+} and Ti^{+4} that can easily be reduced.[69–71]

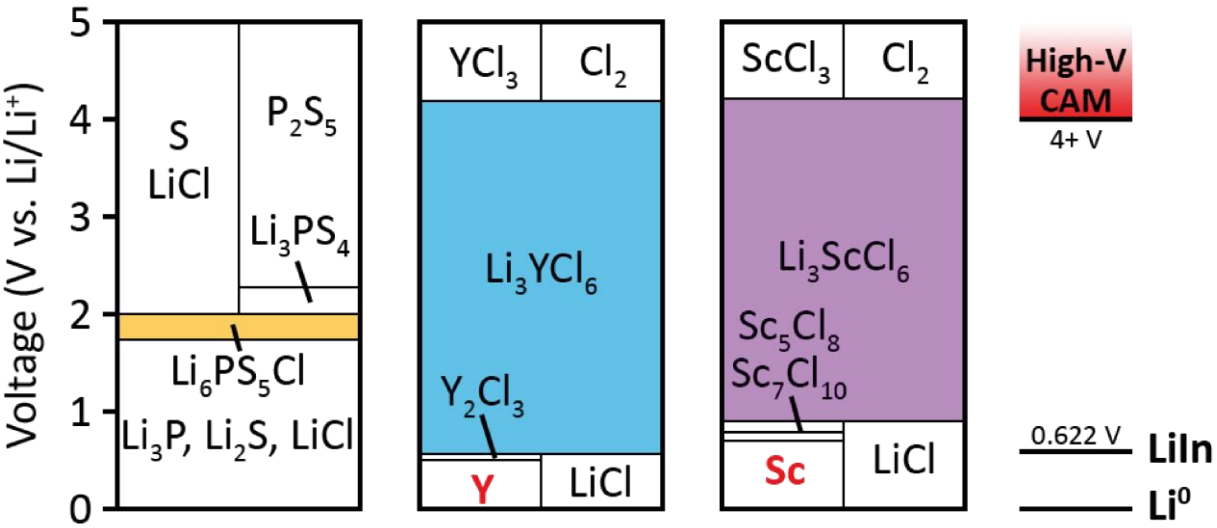

Figure 1.15. Calculated phase equilibria for (left to right) Li_6PS_5Cl, Li_3YCl_6 and Li_3ScCl_6 and potential of Li metal, LiIn alloy and high potential CAMs. Calculations based on first-principle calculations (DFT). Stable potential window of SEs are coloured and electronically conductive species are in red. Adapted from references[48,56,72].

Apart from the intrinsic thermodynamic reactivity of SEs, they also can experience chemical and electrochemical reactivity against the CAMs themselves when combine into the cathode composite. Such reactivity is dependent on many factors such as chemical compositions and their compatibility, state-of-charge (SOC), surface species and so on. Using techniques such as time-of-flight secondary-ion mass spectrometry (ToF-SIMS) and X-ray photoelectron spectroscopy (XPS), Janek *et al.* demonstrated that sulphide-based SEs readily undergo reactions with transition metal oxides at high potentials. In particular, their study unveiled that argyrodite-type Li_6PS_5Cl or β-Li_3PS_4 SEs react with NMC622, resulting in the formation of sulphate (SO_x) and phosphate (PO_x) species at the interface, as illustrated in Figure 1.16 from their work.[43,73] This phenomenon was well correlated with a decrease in battery performance. Thus showing how critical interfaces and their understanding are in ASSBs.

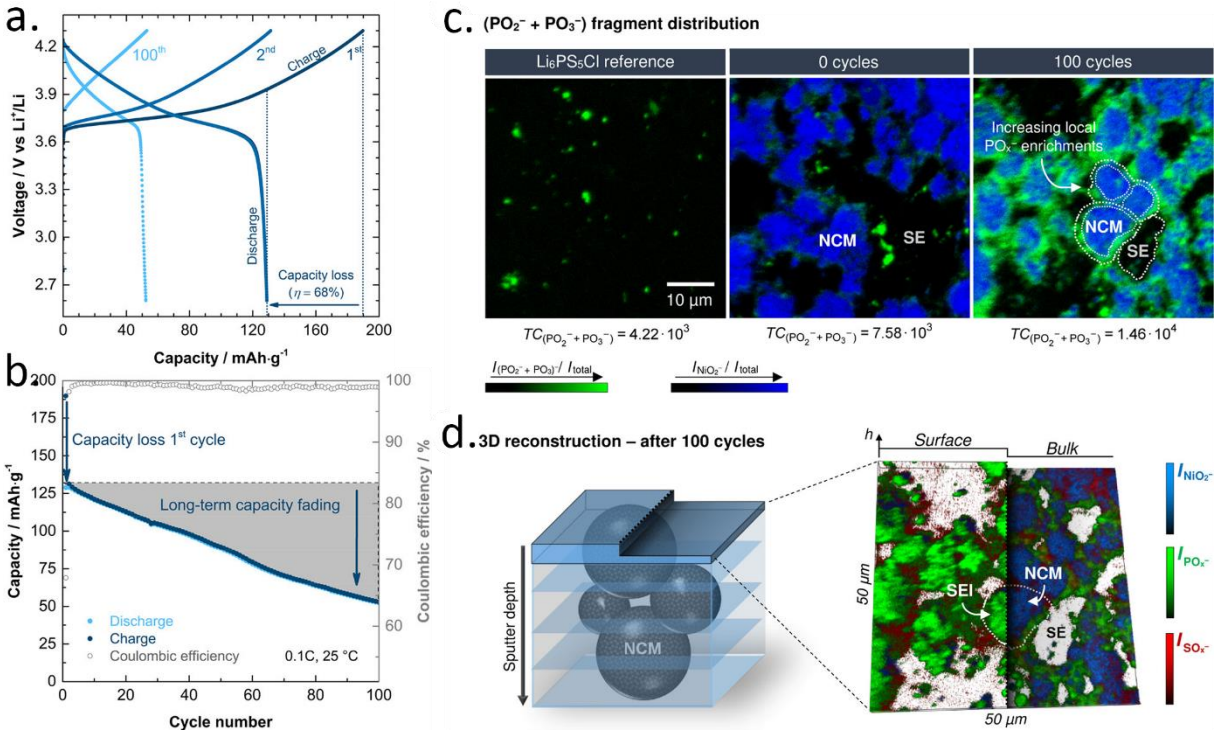

Figure 1.16. Electrochemical reactivity of argyrodite solid electrolyte and NMC materials. (a) Galvanostatic cycling of 1st, 2nd and 100th cycles and (b) capacity retention of a NMC622:LPSCl/LPSCl/LiIn cell. (c) Local fragment distribution of NiO^{2-} (blue) and PO_x^- (green) for the reference SE and the uncycled and cycled composite cathode. (d) Three-dimensional reconstruction of the depth profile of the cycled composite cathode. Reproduced from reference[43].

Lastly, SEs can also exhibit reactivity towards their surroundings, typically in response to air or moisture exposure. Oxide SEs, in particular, tend to demonstrate the highest stability in this aspect. Conversely, sulphide or halide SEs are more reactive with moist air, resulting in a decline in ionic conductivity due to structural deterioration and SE decomposition.[74–76] Moreover, in the case of sulphide SEs, this reactivity results in the release of toxic H_2S gas, which is a major concern for large-scale production of SE or ASSB.

Altogether, it is clear that understanding the formation and evolution of interfaces in ASSBs is of crucial importance as it can lead to severe cell performance degradation. However, while decomposition reactions pose challenges, they can hopefully be mitigated through chemical design strategies of the interface or interphase. Coatings, widely used in typical liquid-based LIBs, have emerged as a promising approach to tackle such decomposition issues in ASSBs. Recent efforts have focused on applying coatings to the CAM to either prevent or at least slow down decomposition reactions. Notably, coatings like $LiNbO_3$ or Li_2ZrO_3 have demonstrated significant success in recent years.[77] In addition, coatings on SE has also been studied mainly as a mean of preventing the environmental reactivity due to air and moisture

that lead to SE decomposition and loss of ionic conductivity.[74,78,79] The straightforward coating of argyrodite LPSCl SE with Li_2CO_3, achieved through a CO_2 gas phase approach was shown to greatly improve the moisture stability of the SE as well as its chemical stability towards NMCs.[74]

○ Formulation, processing and integration

In addition to the aforementioned interfacial reactivity problems, the formulation, processing and integration of the different components into an ASSB pose significant hurdles. Among these components, the cathode composite stands out as particularly challenging.

A cathode composite consists of various materials, including the AM, SE, conductive additives and potentially a polymer binder. This assortment of materials introduces a high degree of complexity due to their distinct chemical, physical and mechanical properties. It is therefore extremely important to know the microstructure of these composite in order to optimise their formulation and processing. An effective composite is characterised by a range of metrics, including achieving high ionic and electronic percolation, maintaining low tortuosity, minimising porosity, achieving high AM loading while minimising the amount of electrochemically inactive components (SE, conductive or polymer additives). Collectively, these factors should result in high power and energy density ASSBs, while maintaining loading levels that are suitable for industrial-scale production, therefore enabling competitive performance compared to conventional lithium-ion batteries (LIBs).

In pursuit of these objectives, the necessity of optimising the individual components within the composite and their intricate interactions becomes evident. While achieving the highest SE ionic conductivity is clearly of paramount importance, optimising the particle size and morphology of the different components in the composite has been shown to also be of critical importance in insuring high AM utilisation as well as good rate performances.[80,81] In particular the AM/SE particle size ratio significantly influences percolation, and various theoretical investigations have explored its implications on the energy density of composites (Figure 1.17).[80,82,83]

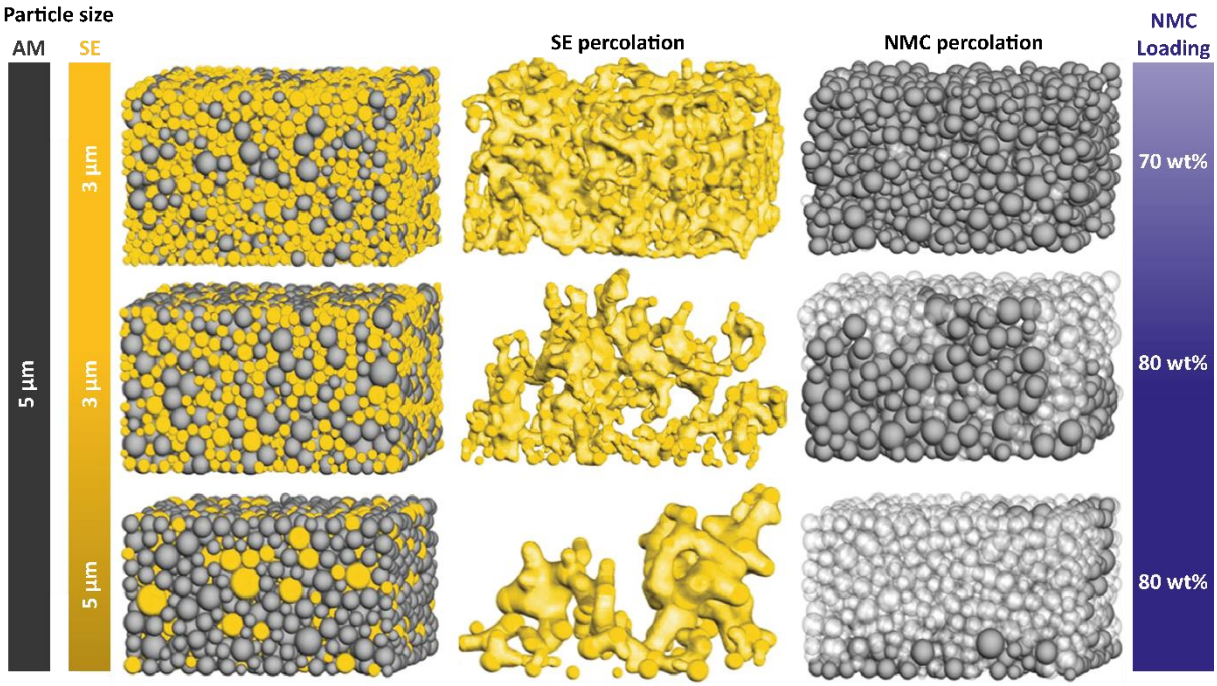

Figure 1.17. Visualisation of modelled NMC/SE composites and percolation through the electrode thickness depending on AM/SE particle size ratio and NMC loading. On the right panels, the solid and transparent grey particles represent the percolated/active NMC particle and inactive NMC respectively. Adapted from reference[80].

In addition to its size, the morphology of the active material (AM) can significantly impact cell performance. The material may be monolithic or polylithic, which involves an assembly of small primary particles with varying orientations. Such morphological variations can alter the mechanical integrity of the particles, leading to crack formation and isolated AM regions within the cell as a consequence of volume changes and stress accumulation during cycling (Figure 1.18).

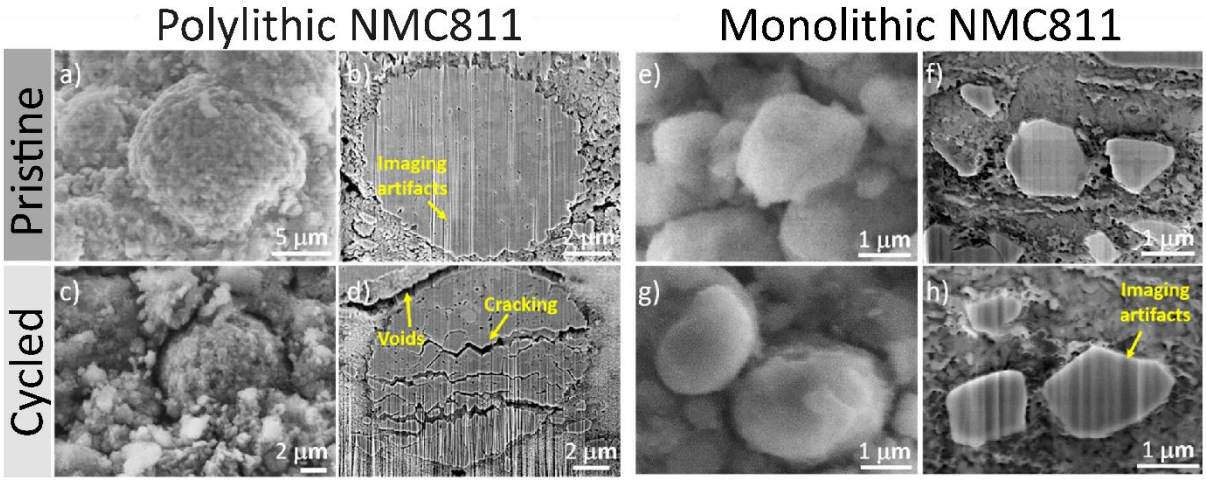

Figure 1.18. SEM images of pristine and cycled NMC as either polylithic or monolithic particles. (a, c, e, g) SEM images and (b, d, f, h) cross-sectional FIB-SEM images collected from as-prepared (a, b, e, f) and cycled (c, d, g, h) NMC811 composite cathodes prepared with (a–d) Polylithic-NMC811 and (e-h) Monolithic-NMC811. Reproduced from reference[84].

Moreover, ensuring close physical contact between AM and SE is crucial to facilitate ion transport and maximise the AM utilisation, especially for high loading composite cathodes. The state of interfacial contact is influenced by the properties of the SEs, with a focus on their mechanical attributes. Specifically, the hardness and elasticity of the SE play a significant role in composite formulation and processing, impacting the overall quality of the resulting interface.[85] A SE with excessively high rigidity, like oxide SEs, requires a high-temperature sintering process to establish effective particle contacts within the composite. Conversely, materials like sulphide or halide SEs exhibit greater ductility[85–87], allowing for efficient contact through straightforward cold pressing. Thus reducing interfacial resistance and simplifying the process of preparing and assembling ASSB. Additionally, it is important to note that in general, ductile SEs tend to outperform brittle ones when it comes to withstanding the strains and stresses generated at the AM/SE interface during cycling due to AM volume change which can be as high as 7% for NMCs (Figure 1.19).[85,88] As a result, micro-cracks or fractures are likely to form, and utilising the ductile property of some SEs can lead to a more closely integrated interfacial contact.[89,90] Maintaining an intimate interface between SEs and electrodes is of paramount importance and is usually addressed by subjecting the cell to a significant external pressure.[91] This point will be discussed in more detail in the next section.

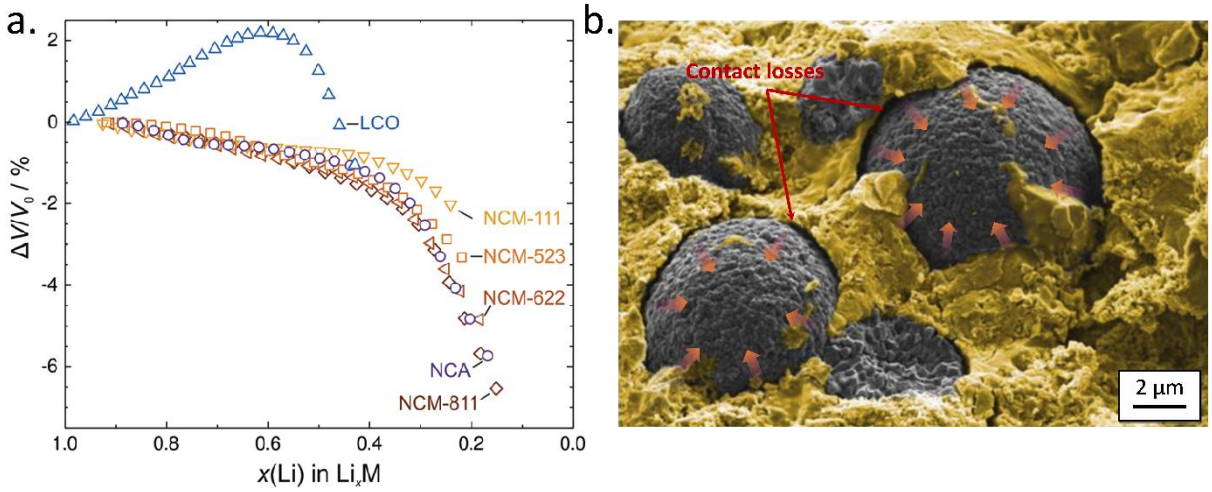

Figure 1.19. Volume change of CAM with state-of-charge. (a) The unit cell volume of various CAMs as a function of the state of lithiation obtained from crystallographic data versus and (b) False colour scanning electron microscopic image showing the contact loss between NCM (grey particles) and a thiophosphate SE (yellow particles). Adapted from references[92,93].

Overall, it is clear that addressing transport limitations in thick electrodes, which stems from the discussed percolation and mechanical problems, need to be addressed in order to achieve performance similar to conventional LIBs. To achieve this, it may be necessary to

develop and adapt advanced manufacturing techniques that allow precise control over the electrode microstructure.

When considering the fabrication of such cathode composite, the primary objective is to achieve a high degree of homogeneity within the composite structure. To realise this, various techniques are employed, they are usually separated into two types: the dry and wet processing. Among the former, the simplest method, often used in laboratory-scale research, is the manual hand grinding approach, utilising a mortar and pestle. However, this method lacks repeatability due to its dependence on the operator's actions, applied force, and grinding duration. Additionally, it is not a scalable solution and as an alternative, ball-milling techniques are commonly adopted. These techniques offer increased homogeneity and repeatability across different batches, with enhanced overall control. Numerous studies have attempted to determine the best conditions for preparing composites using this technique.[94] In recent developments, a mechano-fusion technique was reported as a scalable process for producing composites with high AM loading by improving the contact between the AM and the SE (Figure 1.20).[94]

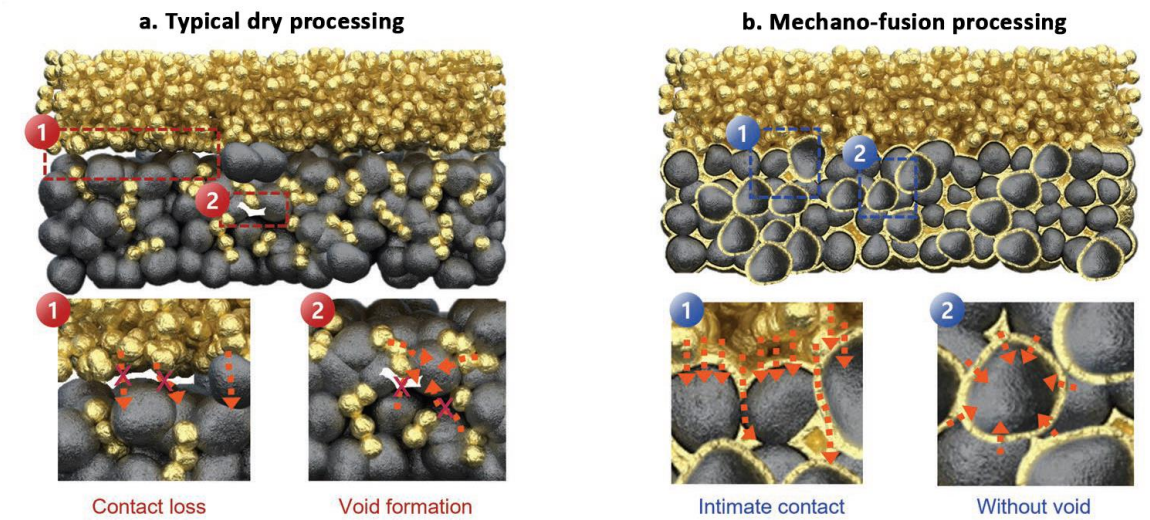

Figure 1.20. Schematic illustration of (a) a typical NCM composite cathode obtained by hand grinding or ball milling and (b) an NCM@LPSCl composite cathode obtained through a mechano-fusion technique. Reproduced from reference[94].

Various other composite fabrication techniques are available, including wet processes that employ slurry-based methods to achieve high component homogeneity. These techniques offer the advantage of using technologies already established in the fabrication of conventional liquid LIBs, rendering them more scalable. However, adopting solvent-based approaches raises concerns about the stability of the different components, especially the SE,

when in contact with such solvents.[95–97] Alternatively, SE dissolved in solution can be infiltrated into porous electrodes prepared by conventional slurry processing, thus filling the pore with ionically conductive material. The obtained composite electrodes are then subjected to subsequent solvent evaporation, heat treatment, and cold pressing.[98–100]

As far as ASSB assembly is concerned, several challenges also emerge at this phase. At the laboratory scale, ASSBs are constructed as pellets by sequentially compacting the SE separator and the electrode materials (Figure 1.21a). However, this procedure, which leads to the creation of thick ASSB pellets with limited energy density, is complex, time-consuming, and therefore costly to implement. A more practical approach for upscaling ASSBs would involve the production of sheet-type electrodes (Figure 1.21b-c) thus also replicating conventional LIB electrodes preparation. To insure the mechanical cohesion of sheet-type electrode, such process often involves the use of a polymer as binder. Its incorporation can take two different routes: the slurry-based, where the polymer is dissolve in solution and mixed with the other components, or the dry route that can involve either extrusion, chemical or physical deposition techniques for example. The solvent route in the electrode fabrication, although introducing more complexity, has already been successfully used in small scale pouch-type cells.[96,101]

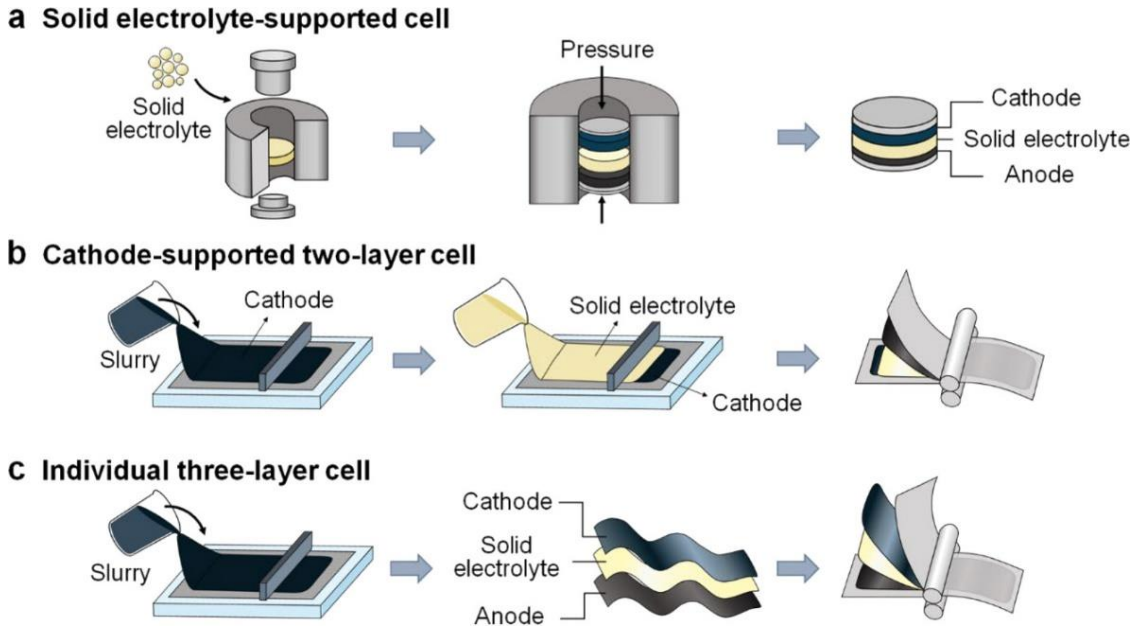

Figure 1.21. Schematic illustration of cell fabrication as: (a) a pellet, (b) a cathode-supported two-layer, and (c) a sheet-type individual three-layer cell. Reproduced from reference[97].

Moreover, when scaling up from lab scale (< 1 cm^2) to pouch cell size cell (tens of cm^2), additional considerations regarding pressure are necessary.

Firstly, upon assembly, a high pressure (> 300 MPa) is often applied to densify the various components and establish contact between particles. For small cells, this can easily be achieved through uniaxial pressure (Figure 1.22a, middle). However, as the cell size increases, utilising the same protocol becomes impractical due to the immense forces required to achieve such pressure. In that context, other densifying techniques need to be considered. Calendaring (Figure 1.22a on the left), readily used in typical electrode preparation for LIBs can be considered; although it can sometimes have limitations in effectively eliminating pores from the SE and the electrode layers. Another more recent technique is the cold/warm isostatic press process (Figure 1.22a right), which consists in the application of a uniform pressure in all directions, effectively reducing voids within the composite to a significant extent. However, the practical implementation of this method on a larger scale is constrained by its cost and processing time.

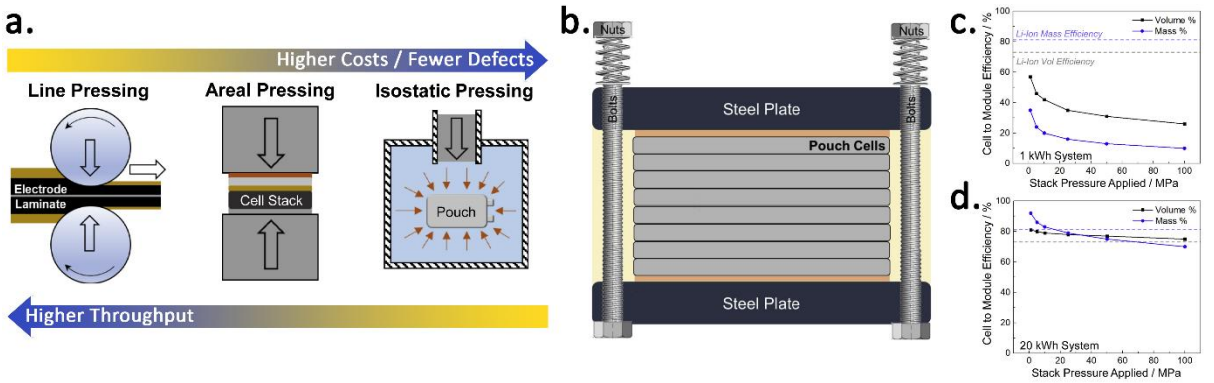

Figure 1.22. (a) Schematic of the three major strategies to achieve densification of pouch-type cells ASSBs. (b) Schematic of an ASSB cell module with hardware to apply stack pressure, and cell to module conversion efficiencies vs. stack pressure based on a system of (c) 1 and (d) 20 kWh. Adapted from reference[102].

Secondly, during operation, the stack pressure and its homogeneity throughout the cell surface are also of paramount importance as applying pressure allows the mitigation of contact loss due to volume changes. In the literature, the electrochemical performances of ASSBs are frequently assessed at high external pressure (often exceeding 50 MPa) to ensure close contact between the electrode particles. However, similar to the assembly procedure discussed above, applying such pressure for operation is not viable, as it would require excessive forces. This would necessitate the use of additional hardware (thick rigid module housing, strong spring, etc. as shown in Figure 1.22b) which would greatly imped the energy

density at the module/pack level (Figure 1.22c-d). Thus the need to introduce better processing to decrease the necessity for such high pressures.

○ The necessity of decreasing the stack pressure for Li metal implementation

The potential benefit of ASSB in increasing the energy density of the cell is possible at the condition of having a high capacity anode, with the lithium metal anode (LMA) standing out as the optimal candidate. In introducing LMA in ASSBs, several thermodynamic, kinetic, and morphological requirements need to be fulfilled.[103]

One of the primary challenges is the low redox potential of lithium metal which poses complexities in handling and selecting compatible materials for assembling battery cells. Lithium metal readily reacts with various components of ambient air (N_2, O_2, H_2O, CO_2) and therefore has a native passivation layers (Figure 1.23) containing compounds such as Li_3N, LiOH, Li_2O, and Li_2CO_3 at its surface[104] that are forming even in trace amounts within a dry, inert atmosphere and get trapped between the LMA and the SE separator upon assembly. This makes it highly complicated to achieve a pristine metallic surface for homogeneous contact with the SE, even under seemingly ideal inert atmosphere such as an argon-filled glovebox. The bulk contamination of lithium metal is also challenging with some reporting non-negligible oxygen solubility or high sodium impurities that can strongly influence the reactivity of the metal.[103,105] Furthermore, the choice of compatible SE is also of paramount importance with only few realising a thermodynamically stable interface while others passivate on contact.

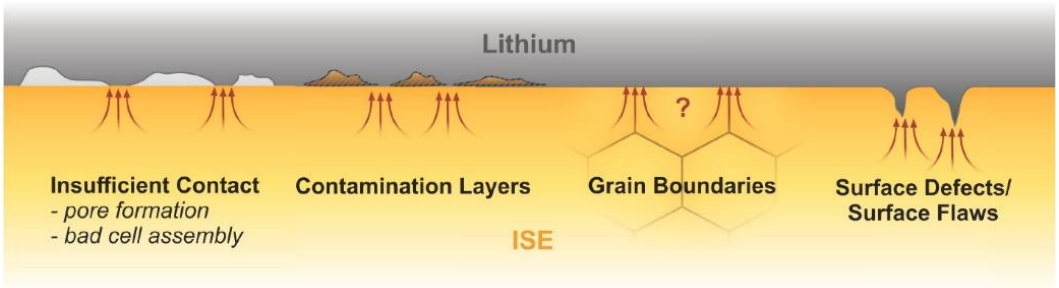

Figure 1.23. Different causes for current constriction at a Li/SE interface due to insufficient contact or pore formation, partial coverage with contaminations or the presence of other charge transfer hindering interlayers, grain boundaries and protrusions at the interface or surface defects. Reproduced from reference[103].

Moreover, lithium is a soft metal with a yield strength of 0.7 ± 0.2 MPa.[103] It undergoes plastic deformation when subjected to pressures exceeding this threshold and, as previously demonstrated by Doux *et al.*, pressures < 5 MPa are required for proper operation of LMAs with an Li_6PS_5Cl SE separator while pressures > 5 MPa leads to the mechanical extrusion of the

lithium through the SE.[91] Therefore, decreasing the pressure is also a prerequisite to LMA integration. However, with a bare LMA, reports have highlighted the importance in maintaining some level of pressure to prevent issues like pore formation and contact losses (Figure 1.23) during stripping, which could potentially result in current constriction and contribute to cell failure.[106] Thus, at this stage finding the right balance in pressure seems to be crucial in ensuring the stable and efficient operation of lithium metal ASSBs.

Significantly decreasing the stack pressure, while necessary for lithium implementation and practical applications, is likely to also have a negative impact on the performance of the positive electrode. As mentioned earlier, to this day, most studies employ extremely high stack pressures, often exceeding 50 MPa, when cycling ASSBs. This is done in order to mitigate the electrochemical fatigue that can lead to contact losses and crack formation (Figure 1.24) within the cathode composite due to the volume changes experienced by the CAM upon lithiation and delithiation.[107] Hence, it becomes crucial to minimise or eliminate sources of strain within the electrodes and to engineer materials capable of offering efficient stress relief mechanisms, thereby mitigating the occurrence of fractures and accommodating the inevitable volume changes of most of the high performance CAMs.

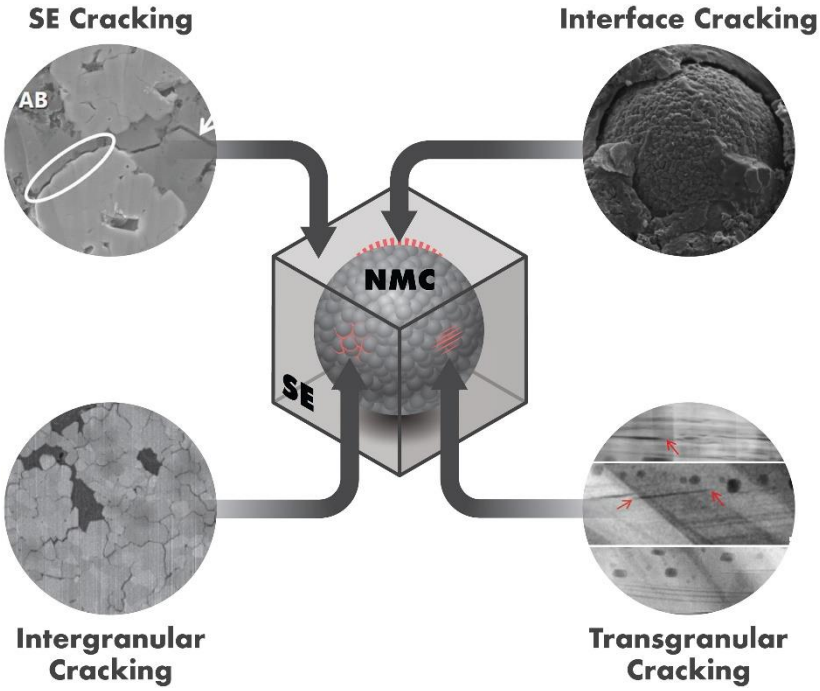

Figure 1.24. Different types of fatigue damage identified in composite cathodes. Reproduced from reference[107].

Overall, decreasing the pressure and integrating LMAs into high-energy density cells still poses several challenges. Most of the current literature, bypass these issues through some

impractical and misleading tricks. Some of these include raising the temperature to enhance plating homogeneity, using low current densities, reducing CAM loading to minimise the current and the amount of plated Li, or increasing the thickness of the separator to prevent dendrites from penetrating through the SE. However, some more practical interlayer, coating and alloying strategies have recently shown promising results in increasing lithium stability with atmosphere and SE as well as in enabling homogeneous plating and stripping even at higher current densities.[101,108–111]

1.4 – Exploring the Cutting-Edge of All-Solid-State Batteries

Having developed a comprehensive understanding of the current challenges associated with ASSB design, it is now important to highlight some innovative strategies that have been implemented to overcome these obstacles in recent years. The forthcoming state-of-the-art analysis will focus on three main areas: SE development, noteworthy ASSB full cell performance and low-pressure strategies.

○ The latest solid electrolyte developments

In recent years, there have been significant advancements in the performance of SEs. Notably, the conductivity and stability of argyrodite SEs have seen remarkable improvements.

The argyrodite-SE, with the most common Li_6PS_5Cl phase, is showing conductivities of about $2 \cdot 10^{-3}$ S/cm. This conductivity was greatly improved in 2019 when Nazar's group reported that halide substitution ($Li_{7-x}PS_{6-x}Cl_x$ with x = 1.0-2.0) could improve the ionic conductivities. They demonstrated an optimal performance for $Li_{5.5}PS_{4.5}Cl_{1.5}$ through a simple solid-state synthesis and obtained a conductivity of up to $9.4 \cdot 10^{-3}$ S/cm.[112] This new composition was then employed recently in 2022, to significantly improve NMC/Li-In cell performance at high rate, low temperature and moderately high loading.[113] Notably, they were able to reach 80 mAh/g at a 5C rate at RT and maintain a capacity of 115 mAh/g at 2C for over 250 cycles afterwards (Figure 1.25a). They also demonstrated exceptional rate capabilities at low temperature of -20°C with stable 50.6 mAh/g at a C/2 rate after 100 cycles as depicted in Figure 1.25b and c. Additionally, extended cycling tests were conducted at 5C and 10C, yielding relatively stable capacities (Figure 1.25d and e). At 5C, they reached around 100 mAh/g for 4500 cycles with a 99.4% capacity retention, and at 10C, about 75 mAh/g for 10000 cycles with an 82.4% capacity retention.

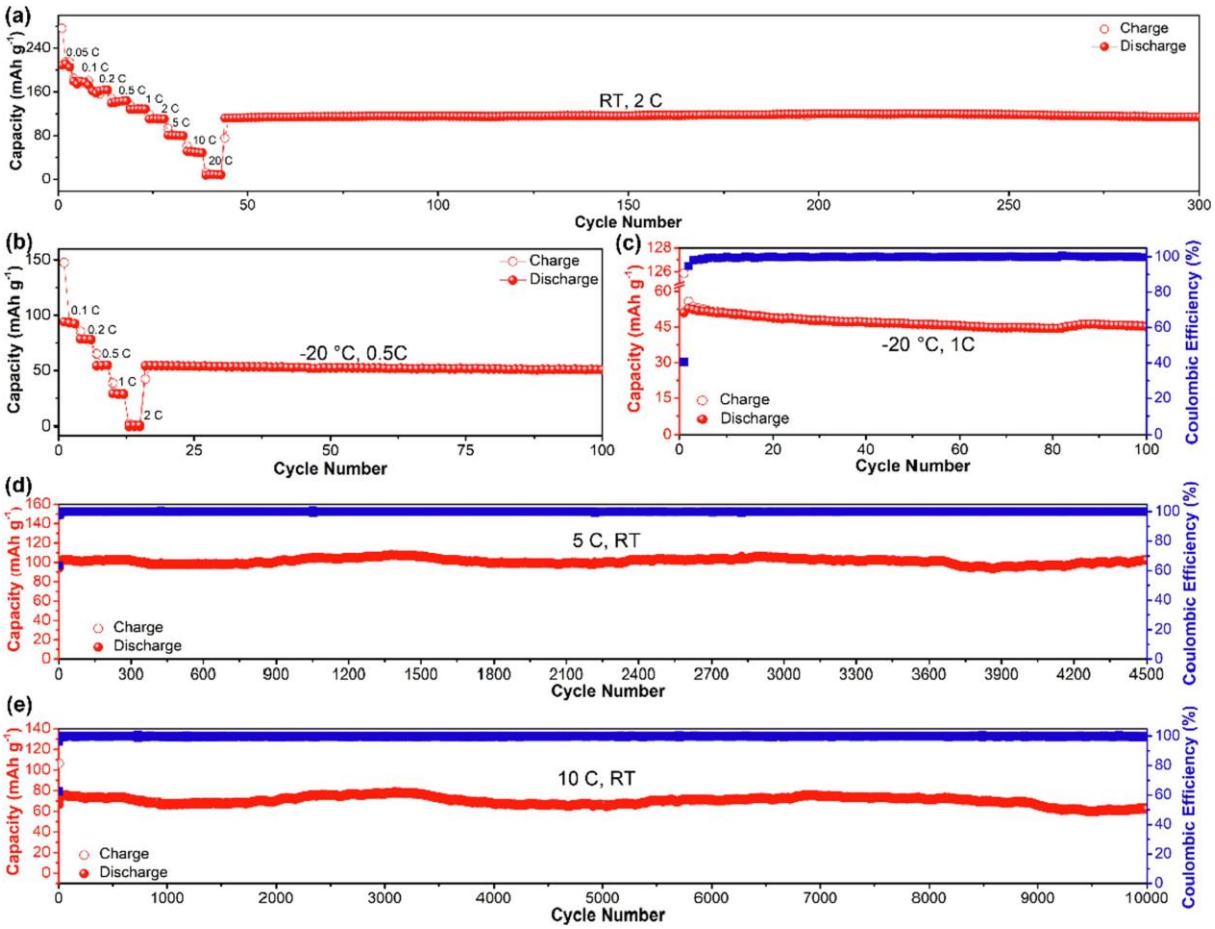

Figure 1.25. Rate capability and cyclability evaluation of the NMC622/$Li_{5.5}PS_{4.5}Cl_{1.5}$/LiIn ASSBs. The rate capability of the fabricated SSBs working at (a) RT and (b) −20 °C. Cycling performance under different temperatures and C-rates: (c) cycled at 1C under −20 °C, (d) 5C and (e) 10C at RT. Reproduced from reference[113].

Significantly increasing the ionic conductivity was not the only improvement that argyrodite received. The SE's stability against environmental factors such as moisture and air, as well as its compatibility with high potential cathode active materials and lithium was the subjects of significant improvements as well.[74,78] One remarkable achievement was the development of a protective coating on argyrodite particles.[74] This protective layer, formed through a facile and scalable spontaneous gas-solid reaction with CO_2 gas (Figure 1.26a), resulted in the deposition of a thin Li_2CO_3 coating on the surface of the argyrodite particles. This protective coating was able to considerably improve the SE ionic conductivity retention after exposure to moist air from a 1.8% to an impressive 80.9% (Figure 1.26b) with just a 1.5 hours long gas-treatment that formed a 70 µm-thick Li_2CO_3 coating. Furthermore, stability towards CAMs was improved, demonstrating an excellent capacity retention of 89.4% after 2100 cycles owing to the 50 µm-thick layer of Li_2CO_3 formed by a 1h CO_2 treatment. This coating, although displaying a low conductivity was thin enough to allow sufficient conduction through the SE (Figure 1.26e).

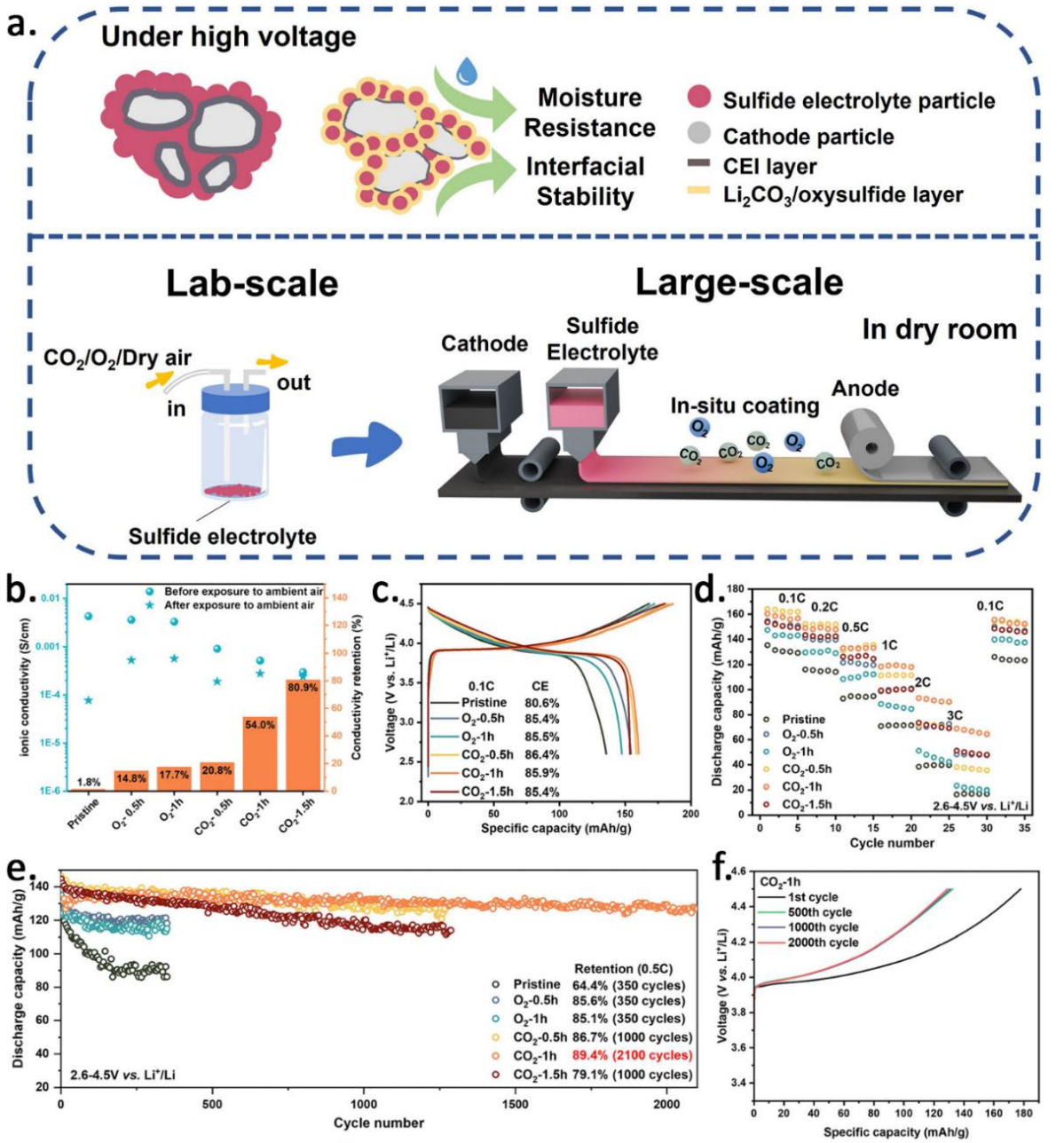

Figure 1.26. (a) Schematic illustration of the solid-gas reaction and its application. (b) Ionic conductivity of treated samples before and after exposure to humid air for 1h and conductivity retentions, (c) initial cycles at 0.1C rate, (d) rate capabilities, (e) long-term cycling and (f) charge profiles with CO2-1h LPSC at different cycles. Reproduced from reference[74].

Since around 2018, the year when halide-based SE resurfaced, their exploration has yielded noteworthy advancements as well. The discovery of new halides such as $Li_2In_xSc_{2/3-x}Cl_4$ (LiInScCl) or $Li_{3-x}Zr_x(Ho/Lu)_{1-x}Cl_6$ by Nazar's group which, although both showing ionic conductivity in the 1-2 mS/cm range, exhibited remarkable cycling stability towards Ni-rich NMC materials.[49,54] Specifically, the former demonstrated a RT ionic conductivity of up to 2.0 mS/cm for the $Li_2In_{1/3}Sc_{1/3}Cl_4$ composition and displayed exceptionally long cycling performance for up to 3000 cycles with over 80% capacity retention at a high upper cut-off

potential of 4.3 V *vs.* Li^+/Li (Figure 1.27a). Furthermore, they showed remarkable stability of this SE at cut-off potential of up to 4.8 V *vs.* Li^+/Li as well as stable capacities for high loading cells of up to 21.6 mg_{AM}/cm^2 and 52.5 mg_{AM}/cm^2 for NMC851005 and LCO respectively (Figure 1.27b-d). With these loadings, they reached aerial capacities of approximatively 3 to 4 mAh/cm^2, which are suitable for industrial-scale applications. Despite their impressive performance, it is worth noting that these halide-based SEs, like many others in the literature, still incorporate expensive and scarce elements such as indium and scandium.

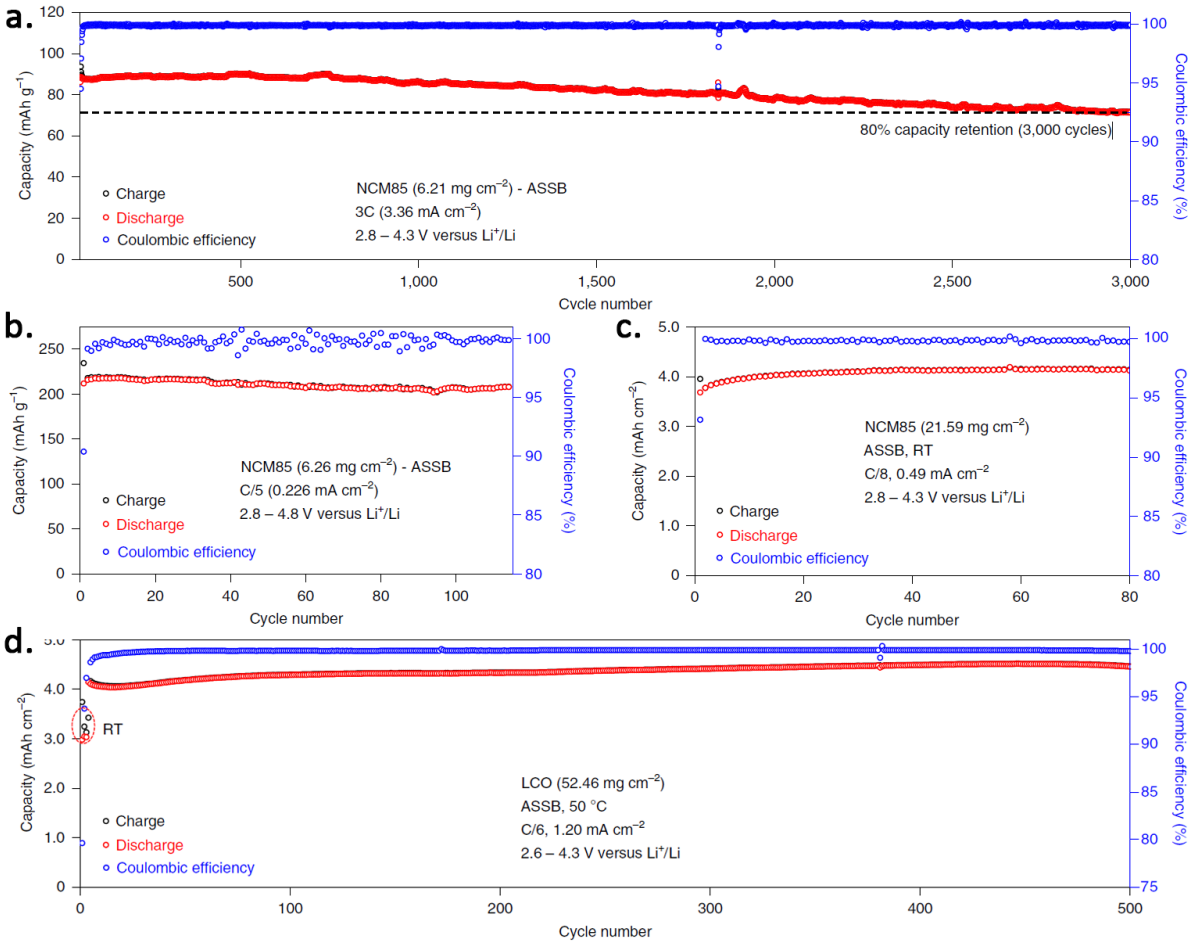

Figure 1.27. Long-term cycling of NMC851005/LiInScCl/LiIn cells (a) at a 3C rate between 2.8 and 4.3 V vs. Li^+/Li, (b) at C/5 between 2.8 and up to 4.8 V vs. Li^+/Li and (c-d) high loading cycling of (c) NMC at RT and (d) LCO at 50°C. Reproduced from reference[54].

Nevertheless, the Li stability remains one of the main challenges, as halide SEs are unstable at low potential. For instance, the calculated thermodynamic reduction stability limits for Li_3YCl_6 and Li_3YBr_6 are 0.62 and 0.59 V vs. Li^+/Li, respectively. To avoid this issue, most studies employ a LiIn alloy anode, which potential is of 0.622 V vs. Li^+/Li or use an additional protective layer of stable SE such as argyrodite. However, these strategies introduce complexity in the cell manufacturing and lower the overall energy density.

Nonetheless, some striking advancements have been made in that regard. One noteworthy example dates back to 2021, when a research group employed a partial fluorination strategy of Li_3YBr_6 to form $Li_3YBr_{5.7}F_{0.3}$.[65] This modified SE demonstrated improved stability at low potentials while retaining most of the ionic conductivity exhibited by the non-fluorinated SE (Figure 1.28a and b). Additionally, the modified SE displayed enhanced contact stability with lithium metal. As depicted in Figure 1.28c and d, stable symmetric cycling was achieved for 1000 hours, in contrast to the unmodified SE that failed after only 300 hours due to the formation and growth of the MCI layer. This improvement was attributed to the in-situ formation of a fluoride-rich interfacial layer, composed of LiF and YF_x compounds, during lithium plating/stripping. This layer passivated the surface and limited the further growth of the interphase, resulting in the observed stability enhancement.[65,114,115]

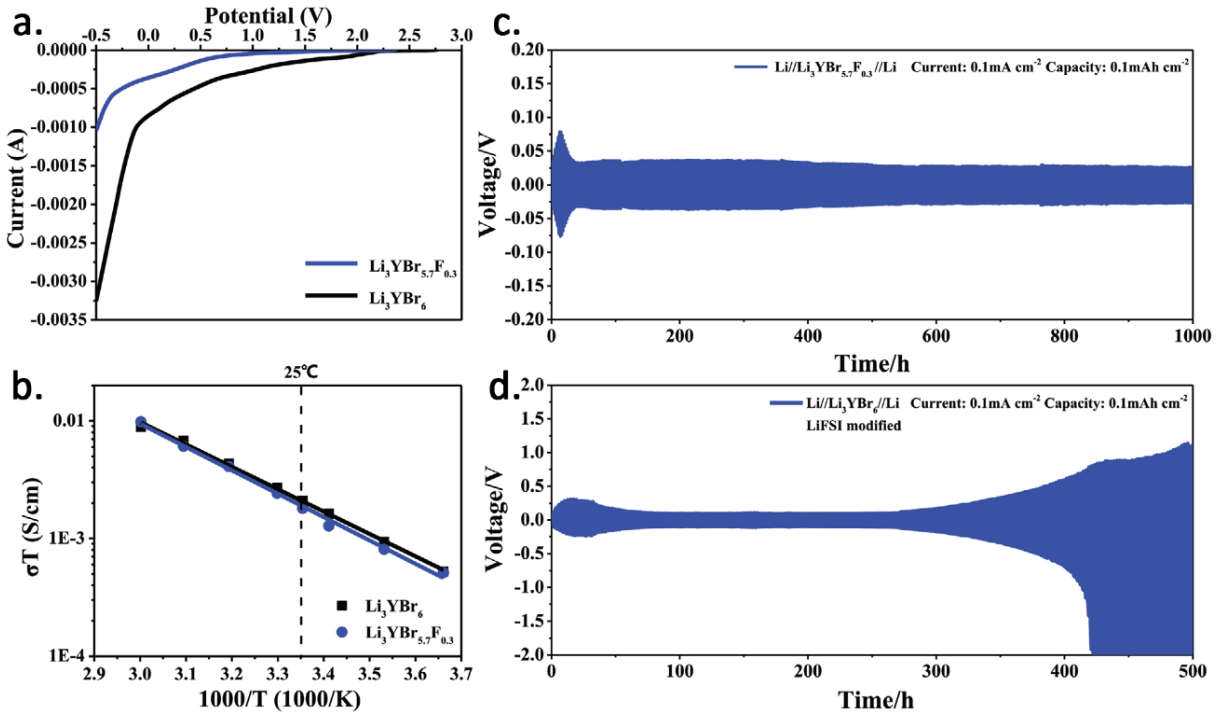

Figure 1.28. (a) Linear sweep voltammetry curve and (b) Arrhenius plots of Li_3YBr_6 and $Li_3YBr_{5.7}F_{0.3}$. (c,d) Li symmetric cell cycling at 0.1 mA/cm² with a capacity of 0.1 mAh/cm² in (c) a Li/$Li_3YBr_{5.7}F_{0.3}$/Li and d) Li/Li_3YBr_6/Li symmetric cell configurations. Reproduced from reference[65].

Similarly, in 2023, a significant breakthrough was achieved with the discovery of a new $LaCl_3$-based halide SE with a UCl_3-type lattice that exhibited exceptional compatibility with lithium metal.[50] Through Ta doping, the resulting optimised $Li_{0.388}Ta_{0.238}La_{0.475}Cl_3$ SE showed a high conductivity of 3.02 mS/cm and, when coupled to Li in a symmetric cell (Figure 1.29c), demonstrated stable operation for more than 5000 hours. Such interface stabilisation was rationalised by the formation of an insulating LiCl-rich buffer layer upon Li contact

(Figure 1.29b). They also demonstrated stable NMC532/Li cell operation for more than 100 cycles with an 81.6% retention (Figure 1.29c-e). Moreover, their investigation extended to various other compositions such as $Li_{0.495}Zr_{0.259}Ca_{0.086}La_{0.432}Cl_3$. Such versatile electrolyte formulation promises enormous potential for the use of more abundant and cheaper elements for the design and fabrication of such SE stable with Li metal.

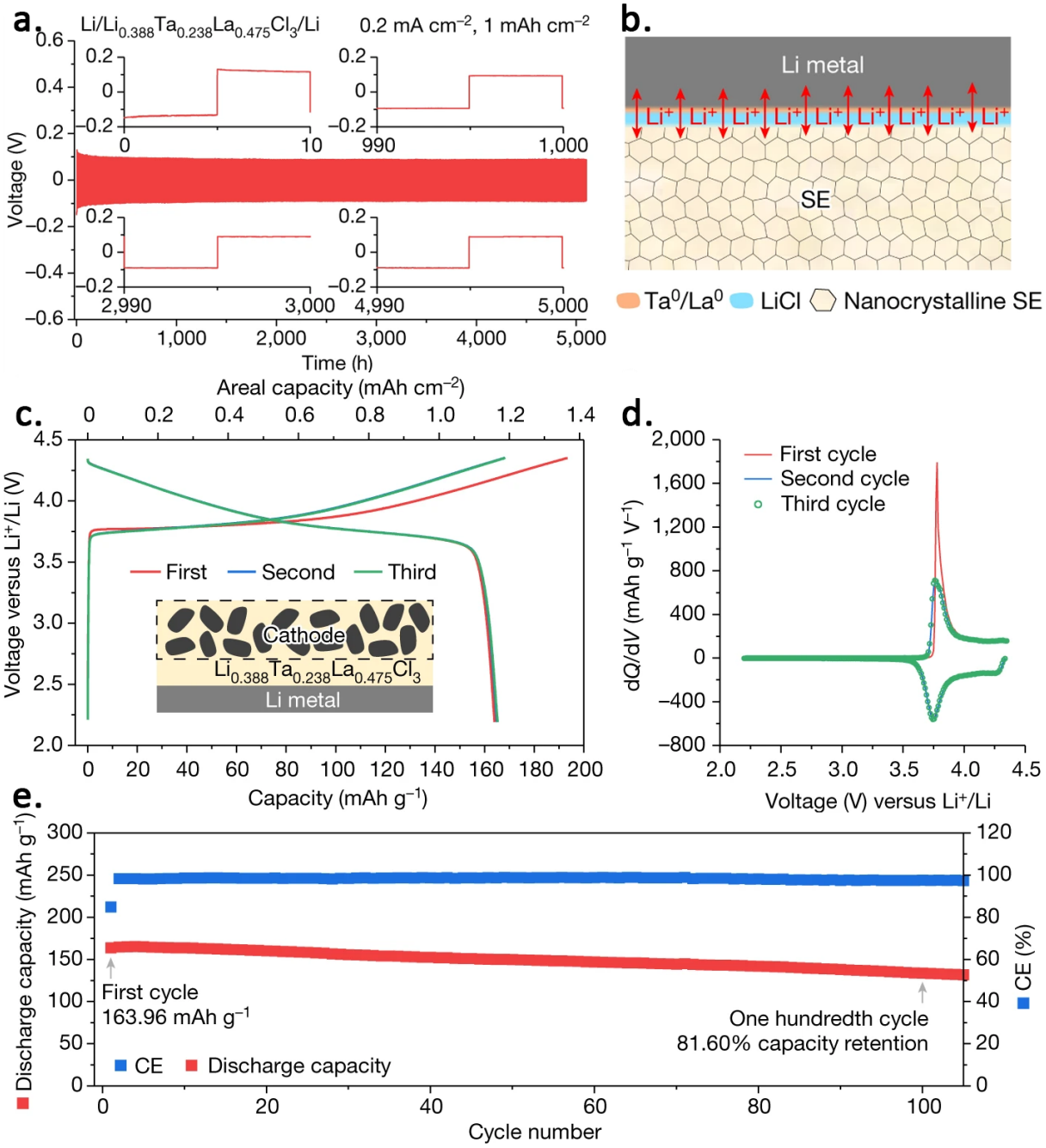

Figure 1.29. (a) Symmetric cell cycling, (b) schematic of interface stabilisation and (c) galvanostatic, (d) dQ/dV and (e) retention of a NMC532/Li^0 cell with the La-based SE. Adapted from reference[50].

Apart from these advancements, a surprising concept comprising a full-halide cell was published by Cheng Ma's group in 2023.[116] It consists in the use of the Ti-based halide Li_3TiCl_6

(LTC) as separator, with its ionic conductivity of 1 mS/cm, as well as cathode and anode materials (LTC+C) playing on the Ti^{3+}/Ti^{4+} and Ti^{2+}/Ti^{3+} redox, respectively (Figure 1.30). Such cell could not reach high capacities nor stability but the concept allows for higher energy density, as the electrodes are free of the electrochemically inactive SE mass.

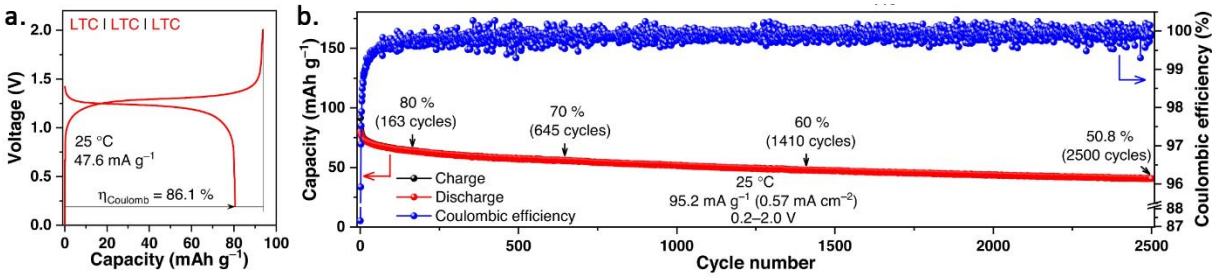

Figure 1.30. (a) 1st cycle and (b) retention of a LTC+C/LTC/LTC+C cell. Adapted from reference[116].

New classes of solid electrolytes are also attracting attention due to their promising characteristics. One notable example is the lithium-metal-oxyhalide family, which has recently shown very promising results. A significant breakthrough comes in 2023 with a publication by Panasonic presenting two new oxyhalide SEs: $LiNbOCl_4$ (LNOC) and $LiTaOCl_4$ (LTOC). These oxyhalides display exceptional ionic conductivities, with LNOC and LTOC achieving 10.7 and 12.4 mS/cm, respectively. Additionally, the study highlighted the high-rate capability of these materials in ASSB full cells, using LNOC as the cathode SE (Figure 1.31b and c).

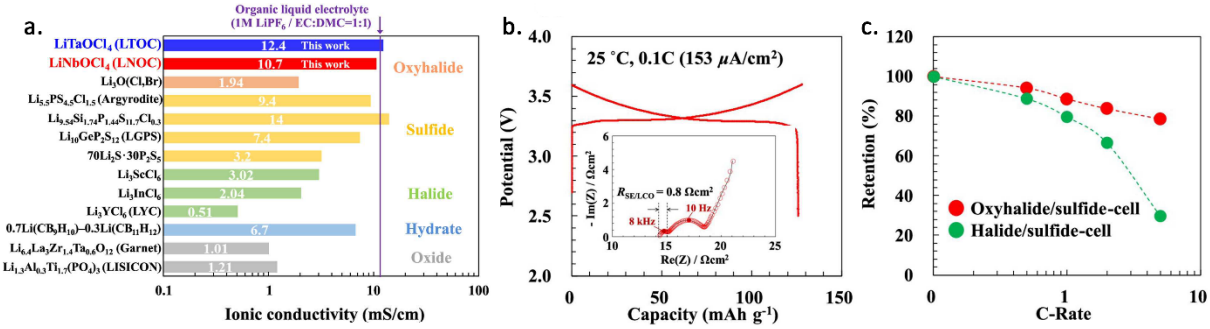

Figure 1.31. (a) Ionic conductivity comparison between LNOC, LTOC and other reported SEs measured at RT. (b) First galvanostatic cycle and (c) rate capabilities of LCO/LNOC/LPSCl/Graphite (in red) and LCO/LYC/LPSCl/Graphite (in green) full cells. Adapted from reference[60].

Collectively, recent years have seen remarkable advances in the development of highly performing SEs. These new SEs have proved capable of operating over a wide range of potentials, with impressive conductivities, reaching those of traditional liquid electrolytes, while simultaneously exhibiting robust cycling stability. This progress holds significant promise for the evolution of solid-state battery technology.

○ Emerging progress in full cell ASSB systems

The integration of various components has indeed posed persistent challenges in the development of ASSBs. However, some significant progresses in the performance of full cell are worth highlighting here.

In 2020, a ground-breaking study by Lee *et al.* presented a significant advancement in the design and integration of ASSBs.[101] The authors reported a new large pouch ASSB cell comprising a NMC/Li_6PS_5Cl/VGCF cathode, a Li_6PS_5Cl separator and an anodeless design (Figure 1.32a). To combat the Li dendrite issue, they implemented a novel interlayer between the current collector and the SE, composed of carbon and silver nanoparticles (Ag-C), that enabled homogeneous Li plating/stripping across a large surface area of a 0.6 Ah prototype pouch cell (Figure 1.32b). Experimentally, they obtained stable cycling for over 1000 cycles, retaining 89% of the initial capacity (Figure 1.32c). Notably, their utilisation of the isostatic pressing procedure (WIP) was one the first to be reported and although disruptive at the time, one should mention that the cycling temperature used was still high (60°C) which considerably aid the use of lithium metal.

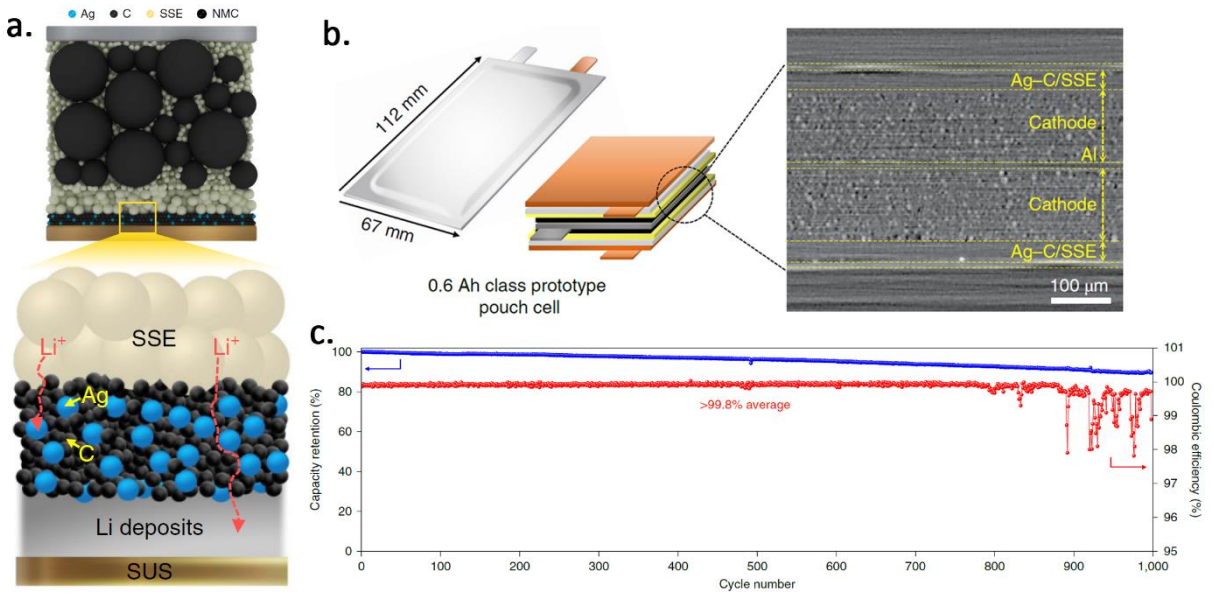

Figure 1.32. (a) Schematic of an ASSB implementing the Ag-C interlayer. (b) Pouch cell illustration and X-ray computed tomography of the cell cross section. (c) Capacity retention of the 0.6 Ah pouch cell prototype cycled at 60°C. Adapted from reference[101]

More recently, in 2023, the same research group further extended their innovative approach when they demonstrated the use of this same interlayer in an oxide-based SE cell, although a liquid electrolyte was still used in the cathode to facilitate Li transport.[108] The

mechanism underlying the homogeneous plating and stripping aided by the Ag-Graphite interlayer was recently studied by Peter Bruce's group.[110] They revealed that upon charge, Li initially electrochemically intercalates into graphite before chemically reacting with silver to form Li-Ag alloys. This process continues until the complete formation of LiC_6 and $Li_{10}Ag_3$; lithium plating then occurs between the Ag-C interlayer and the current collector.

In 2021, another breakthrough shook the ASSB world when Meng's group reported the use of a high energy density silicon anode paired to a Li_6PS_5Cl separator in a full cell design ASSB.[117] They assembled a cell (Figure 1.33a) with an anode composed of 99.9% micro silicon (µSi) anode and a high loading NMC811 cathode (25 mg_{AM}/cm^2) and demonstrated an exceptional cycling performance at 1C for 500 cycles, maintaining an 80% capacity retention (Figure 1.33b). The superior performance achieved in comparison to liquid systems was attributed to the significant volume expansion of µSi. This expansion, counterintuitively, played a beneficial role by leading to a high degree of densification of the anode. However, it is worth noting that despite achieving long cycling, the capacity of the NMC811 was largely underutilised, only reaching approximately 80 mAh/g, while the applied pressure needed to be excessively high as well in the order of 400 and 100 MPa for the formation and subsequent cycles, respectively.

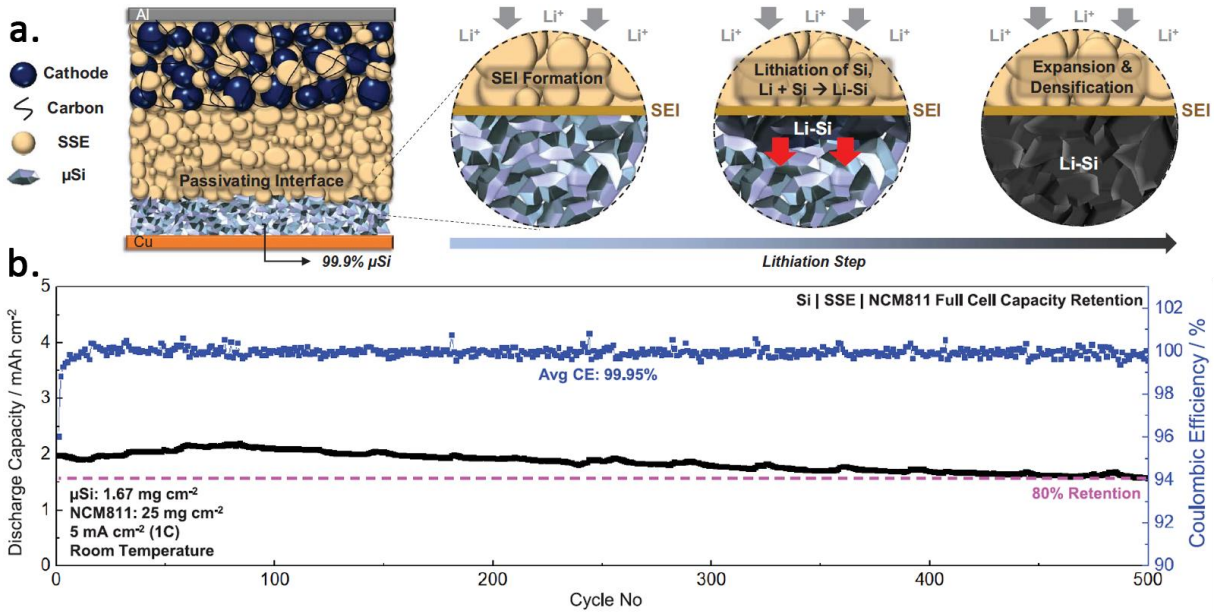

Figure 1.33. (a) Schematic of the NMC811/LPSCl/µSi cell and proposed lithiation mechanism and (b) long cycling performances at RT. Adapted from reference[117].

Another interesting concept, published in 2021, was the use of a SE-free and C-free cathode by revisiting the layered titanium disulphide.[118] Their approach hinged on the mixed

ionic-electronic conductor property of TiS_2, which allowed them to employ the material without any ionic or electronic additives (SE and carbon), which are commonly incorporated into conventional composites (Figure 1.34a). As a result, despite operating at the lower potential range of TiS_2, they managed to reach high energy density of up to 414 $Wh/kg_{electrode}$ by eliminating any electrochemically inactive components. Furthermore, they conducted cycling at high loadings of up to 45.6 mg_{AM}/cm^2, which translated to a practical areal capacity of approximately 9.43 mAh/cm^2 (Figure 1.34b). The same group also work on the same concept for anode material, of which they chose graphite and silicon.[119,120] Using these anodes, they achieved relatively stable cycling at high areal capacities of nearly 3 mAh/cm^2 while also having high energy density at electrode level owing to the SE-free anode design.

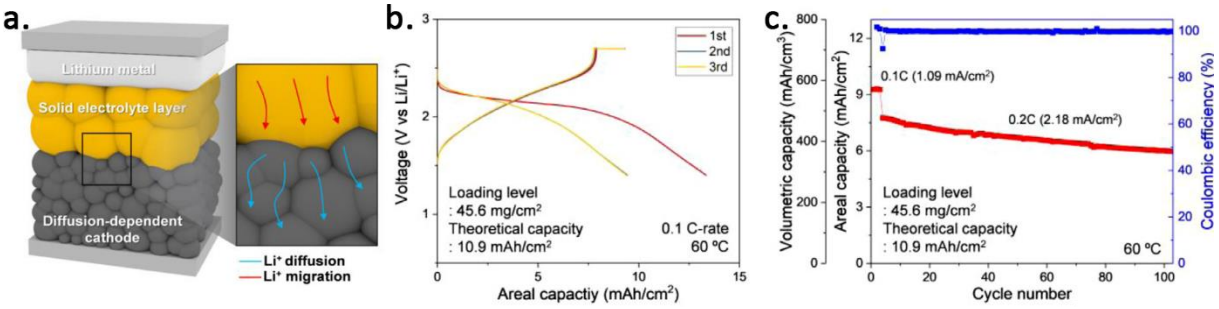

Figure 1.34. (a) Cell schematic, (b) galvanostatic cycling and (c) capacity retention of the TiS2/LPSCl/Li^0 cell. Adapted from reference[118].

The notion of SE-free cathodes, relying solely on the intrinsic conduction properties of the AM is of particular interest. This concept is closely related to other studies mentioned earlier, such as the utilisation of µSi[117] anodes and full halide[116] cells based on Li_3TiCl_6. The potential of this approach in reducing the required stack pressure for ASSBs will also be investigated within the scope of this thesis.

○ The progress toward low pressure cycling

Mitigating the need for high stack pressure during cycling is a crucial challenge in scaling up ASSBs. In recent years, noteworthy research works have explored various strategies aimed at addressing this issue.

A problem when attempting to decrease the stack pressure is to maintain particle contacts and percolation in the cathode composite. In that context, in 2023, a group used a processing technique that they newly applied to ASSB composite preparation, known as solvent-free mechano-fusion (MF) process. This process consists in subjecting the AM/SE

mixture to high shear and compression forces to form a thin and robust coating layer of SE on the surface of the AM (Figure 1.35a). Through this process, NMC particles were effectively coated with a thin and uniform layer of Li_6PS_5Cl SE (Figure 1.35b). The outcomes were remarkable, as outstanding cycling performance was achieved with composites containing as little as 20% and 10% SE. Typically, such low SE content would be insufficient to ensure percolation thus leading to poor AM utilisation and low capacity. The coated NMC@LPSCl composites, prepared in 80:20 and 90:10 ratios, exhibited initial discharge capacities of 163 and 148.5 mAh/g, respectively, performances significantly surpassing those of the regular NMC+LPSCl composites which only registered 148 and 38 mAh/g in the same ratios, respectively (Figure 1.35c-e). Moreover, the improved percolation translated into enhanced rate capabilities compared to regular composites. Beyond enhancing cycling performance and rate capabilities, this technique also contributed to the possibility of substantially lowering the cycling pressure. The authors demonstrated that pressures of 20 or 3 MPa had no impact on reversible capacity when using MF-prepared composites. In contrast, with bare NMC composites, lowering the pressure to 3 MPa resulted in a substantial 65% decrease in the first cycle discharge capacity.

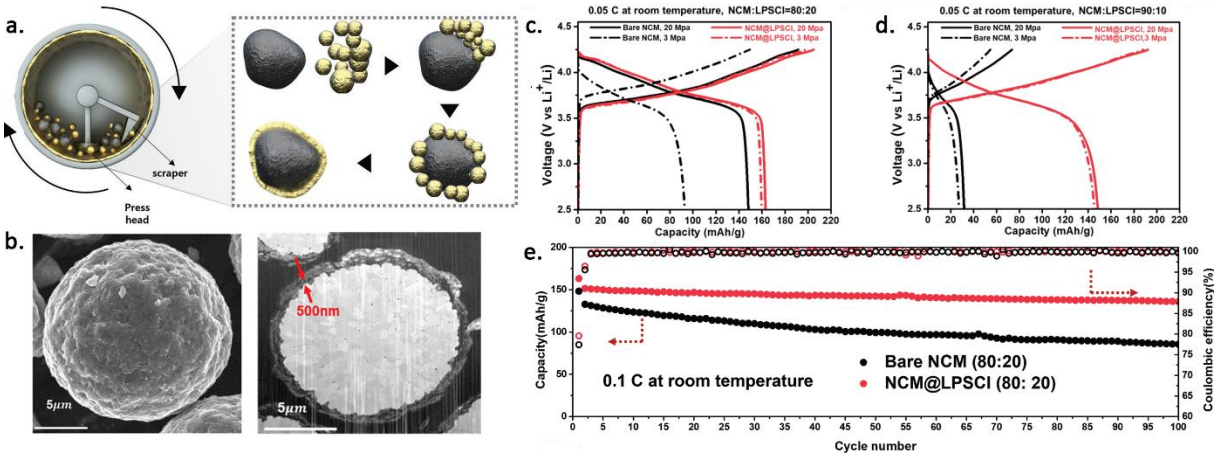

Figure 1.35. (a) Illustration of the mechano-fusion process and (b) surface and cross-section SEM images of the obtained Li_6PS_5Cl-coated NMC (NMC@LPSCl) particles. First galvanostatic cycles of bare NMC composite electrode and NMC@LPSCl composite electrode at 20 and 3 MPa with NMC to LPSCl ratios of (c) 80:20 and (d) 90:10 and (e) capacity retention of the 80:20 ratios. Adapted from reference[94].

Another noteworthy contribution to low-pressure cycling of NMC composites was presented by Peter Bruce's research group in 2022. They capitalized on the high ionic conductivity and excellent high potential stability of halide SE integrated into the cathode composite. This enabled them to achieve cycling at remarkably low pressures, as low as 2 MPa. However, it is important to note that they still required high-temperature operation at 80°C

to reach similar performance as the high-pressure ones. The mention of the choice of SE, the composite composition, the temperature and rates highlight how important these factors become when trying to decrease the cycling pressure.

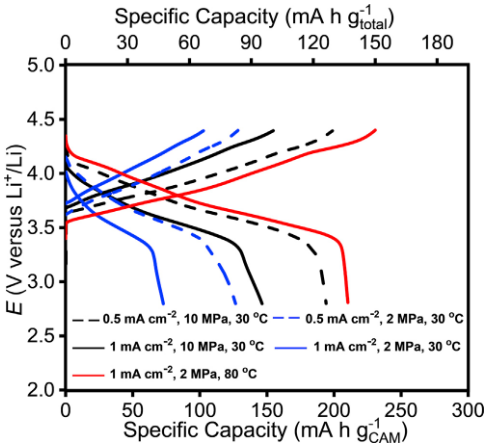

Figure 1.36. Comparisons of the first cycle performance of the composite cathode NMC811/Li_3InCl_6/CNF in 65/30/5 weight ratio under different current densities, temperatures and stack pressures. Reproduced from reference[121].

1.5 – Chapter conclusion

In conclusion, Chapter 1 has provided an in-depth exploration of the landscape of today's battery technologies and the renewed interest in ASSBs. We explored the historical development of solid electrolytes, tracing the evolution from early inorganic conductors to the emergence of high-performance lithium-ion conductors.

The potential benefits that ASSBs can offer in terms of safety, energy density, and overall battery performance were discussed. However, we recognised that despite the promises, ASSBs come with their own set of challenges. The chemical and electrochemical interfacial reactivity within these batteries presents a complex set of issues that need to be addressed for achieving stable and long-lasting performance. The formulation, processing, and integration of various components, such as cathode composites and solid electrolytes, add complexity that must be carefully considered. Moreover, the quest for decreased stack pressures and the integration of high-capacity lithium metal anodes underscore the pressing need for innovative solutions. We explored strategies to address these challenges, ranging from new solid electrolyte materials to advanced processing techniques, highlighting the cutting-edge advancements in the field.

Looking ahead, Chapters 2 and 3 will delve deeper into strategies aimed at lowering cathode-side cycling pressure, providing an overview of innovative approaches and their implications. In addition, Chapter 4 will focus on the incorporation of lithium metal anodes into these previously explored solutions, with the aim of further increasing the energy density of ASSB systems and paving the way for scalability.

Chapter 2 – **Atmospheric-Pressure Operation of All-Solid-State Batteries enabled by Halide-based Solid Electrolyte**[1]

[1]This chapter includes the following publication: Hennequart, B. *et al.* Atmospheric-Pressure Operation of All-Solid-State Batteries Enabled by Halide Solid Electrolyte. *ACS Energy Lett*. **9**, 454–460 (2024). And a patent application (EP23305141, pending)

2.1 – Chapter Introduction

Despite the potential for high energy density in all-solid-state batteries (ASSBs), research efforts are still needed to overcome fundamental issues that prevent their commercialisation. As introduced in the previous chapter, a critical requirement for achieving the promised energy densities is the use of a lithium metal anode (LMA) that requires the considerable reduction of cycling or stack pressure.[91] However, to date, achieving high cyclability under low pressures has proven to be challenging. This difficulty stems from a multitude of interfacial issues that give rise to inadequate contacts in the cathode. Indeed, in an ASSB, the cathode usually being a composite of cathode active material (CAM), solid electrolyte (SE) and carbon additive, new challenges emerge as the pressure is decreased. Most notably is the volume variation that the CAM undergo during charge and discharge cycles of 6 to 8% for the typical $LiNi_xMn_yCo_{1-x-y}O_2$ (NMC)[92], which can lead to loss of contact between the CAM and SE particles and result in poor cyclability. Consequently, most studies in current literature on cathodes for ASSBs tend to overlook this issue by conducting cycling experiments at high stack pressures, typically exceeding 50 MPa. These pressures are definitely incompatible with real-world applications or Li metal integration.

Current strategies to enable low pressure cycling include increasing cycling temperature, lowering upper cut-off potential to limit CAM volume changes[92], optimising CAM and SE particle sizes to improve percolation[81,80], or using solid electrolyte-free cathode systems[118] to minimise interfaces. More recently Gao *et al.*[121] utilised the chloride-based Li_3InCl_6 SE and NMC to reach pressures of 2 MPa at 30°C when having a limited oxidation cut-off of 4.2 V vs. Li^+/Li.

This chapter aims at proposing a new strategy to overcome this pressure limitation that is based on consideration of chemical and mechanical properties of the SE present in the composite. We will first benchmark the performance of a typical sulphide-based (NMC:LPSCl) cathode composite under different pressure conditions and see the effect of the composite formulation on the cyclability. Then we will explore the halide-based SE Li_3InCl_6 as a promising candidate for low-pressure cycling. Finally, we will introduce $Li_3YBr_2Cl_4$, a mixed halide SE displaying improved reduction stability and impressive mechanical properties.

2.2 – The low pressure cycling of argyrodite-based NMC composites

To establish a baseline for future experiments involving various SEs, we conducted a performance assessment using a commercial argyrodite Li_6PS_5Cl SE (NEI Corporation, Fine LPSCl) stated having a particle size of 1 µm but that turns to contain few larger chunks in the range of 10 to 20 µm, as deduced by SEM measurements (Figure 2.1a). Additionally, through electrochemical impedance spectroscopy (EIS), we determined an ionic conductivity of 1.62 mS/cm at a pressure of 100 MPa for this SE.

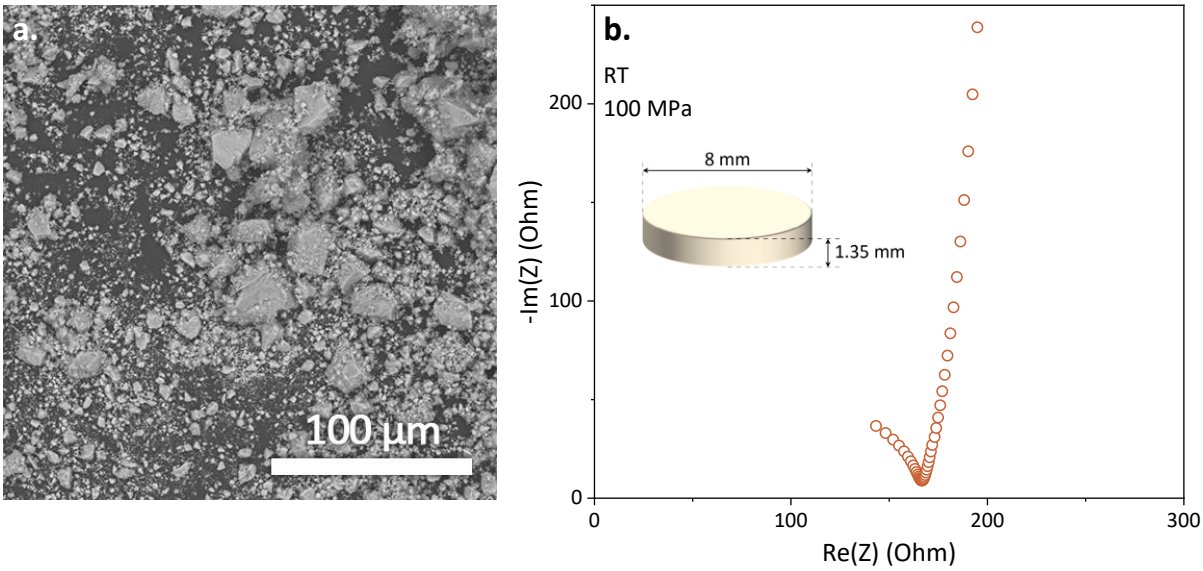

Figure 2.1. Commercial argyrodite Li_6PS_5Cl properties. (a) SEM image of the material and (b) conductivity measurement by EIS.

○ A high pressure reference

Initially, we assessed the performance at a high pressure of 100 MPa within a homemade ASSB cell device as represented in Figure 2.2. This ASSB cell is composed of a LPSCl separator, a lithium-indium alloy/LPSCl composite anode (LiIn, in a 1/2 atomic ratio to obtain a stable 0.62 V vs. Li^+/Li) and a cathode composite comprising an 4 µm in size uncoated monolithic $LiNi_{0.6}Mn_{0.2}Co_{0.2}O_2$ (referred to as NMC622 hereafter) active material, the same LPSCl SE and vapour-grown carbon fibre (VGCF) as a conducting additive.

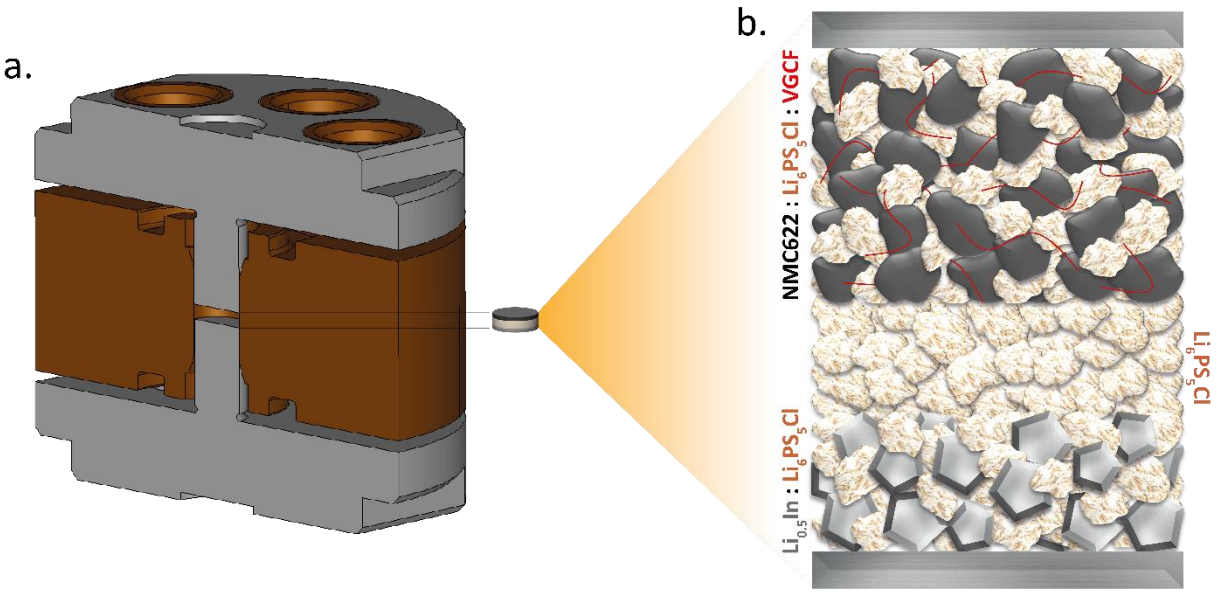

Figure 2.2. Schematic of (a) the homemade cell used for ASSB tests and (b) the ASSB pellet stack composition used for cycling.

The assembly procedure of such solid-state battery involves the sequential densification at 400 MPa of the powders used for the different layers of the battery, *i.e.* the LPSCl separator, the $Li_{0.5}In$/LPSCl anode and the NMC622:LPSCl:VGCF cathode composites. Subsequently, the galvanostatic cycling process for these high-pressure cells is conducted at 100 MPa by tightening the six screws at 2.3 N.m using a torque wrench. A more comprehensive and detailed procedure for the preparation of the composite and the assembly of the cells is available in the Appendix Section A2.1.

Galvanostatic cycling in the potential window 2.1-3.6 V vs. Li^+/LiIn (or 2.7-4.2 V vs. Li^+/Li) was performed on this LPSCl-based ASSB configuration. Figure 2.3 shows the galvanostatic profile of the first cycle and the capacity retention of this cell subjected to cycling at C/20 under 100 MPa with a loading of 12 mg_{NMC}/cm^2.

This system exhibit charge and discharge capacities of 180 and 138 mAh/g on first cycle resulting in a 77% initial coulombic efficiency (ICE). In addition, from Figure 2.3b, such cell shows a retention of 88% after 20 cycles. This high irreversibility and poor retention are typical of sulphide-based composites, known to undergo oxidation reactions at high potential.[67] It is usually mitigated by the use of a thin coating on the AM particles, such as zirconium, cobalt or niobium-based oxide coatings. As an example, a Zr-coated NMC622 was also tested in this configuration and an improved ICE of 81% was obtained (Appendix Figure A2.2). However, in

our study, only bare NMC622 will be used. Altogether, these achieved results will serve as a reference for studying the effect of low-pressure conditions on cycling.

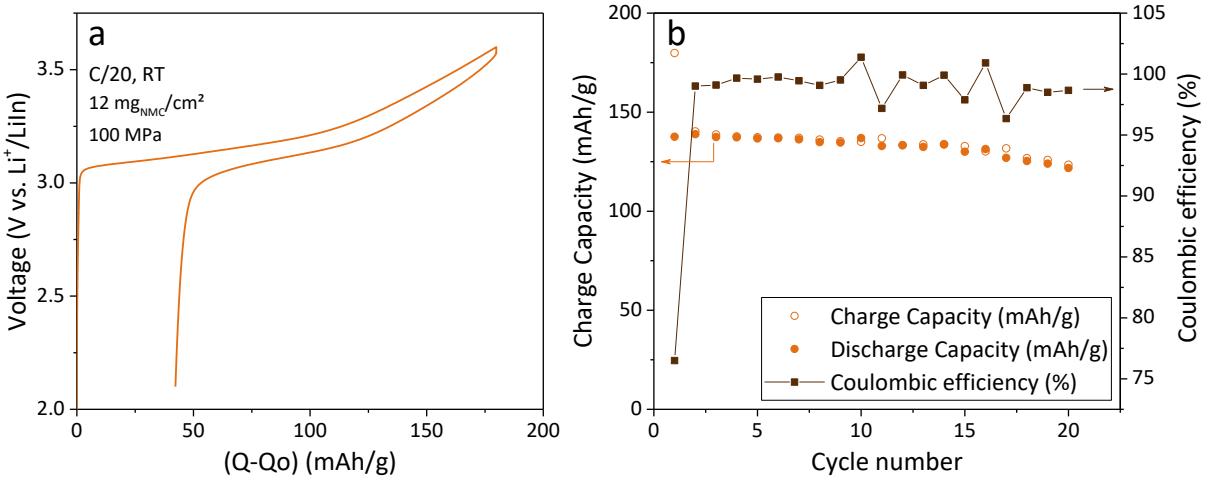

Figure 2.3. Galvanostatic cycling performance of a NMC622/LPSCl/VGCF cathode composite at a pressure of 100 MPa in a LPSCl-based ASSB architecture. (a) Voltage profile of the first galvanostatic cycle and (b) capacity retention and coulombic efficiency evolution.

○ Low pressure performance and the importance of formulation

To investigate the low-pressure performance, we used the same cell composition as previously but modified the cycling device to accommodate a broader pressure range. As illustrated in Figure 2.4, it comprises a frame in which the prepared cell is positioned for cycling. Pressure monitoring is achieved through a force sensor located beneath the cell, and pressure adjustments are made by tightening a screw that secures the cell in place during the experiment. This design is a fixed-gap system having a constant volume but for which the pressure can vary throughout the cycling process. This is in opposition to a constant pressure setup that can accommodate volume changes while keeping the pressure nearly constant by the use of a spring. Noteworthy is that this design is not air-tight and must be employed inside a glovebox, which exposes it to larger temperature variations and vibrations that can disturb low pressure performance.

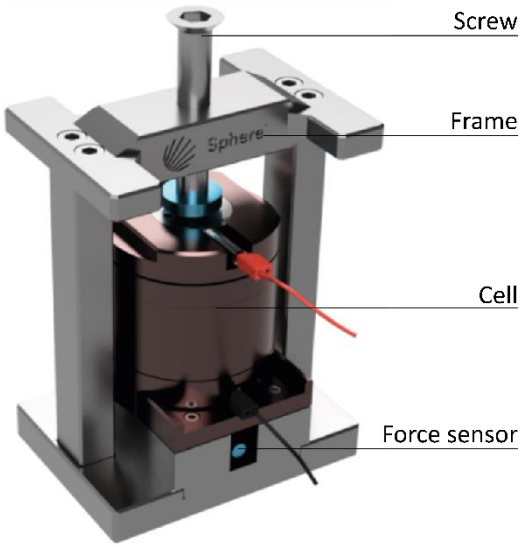

Figure 2.4. Schematic of the fixed-gap cell design used for low pressure cycling.

Low-pressure cycling experiments were carried out employing the same cycling protocol, but with an initial pressure set to 10 MPa and a reduced loading of 5 mg_{NMC}/cm^2. During the initial cycle, depicted in Figure 2.5, the achieved capacities are similar to those observed in the high-pressure tests, attaining 137.6 mAh/g on the first discharge, with a typical ICE of 76.5%. However, affected by this lower stack pressure, the CE decreases from an average of 99.15% to 94.22%.

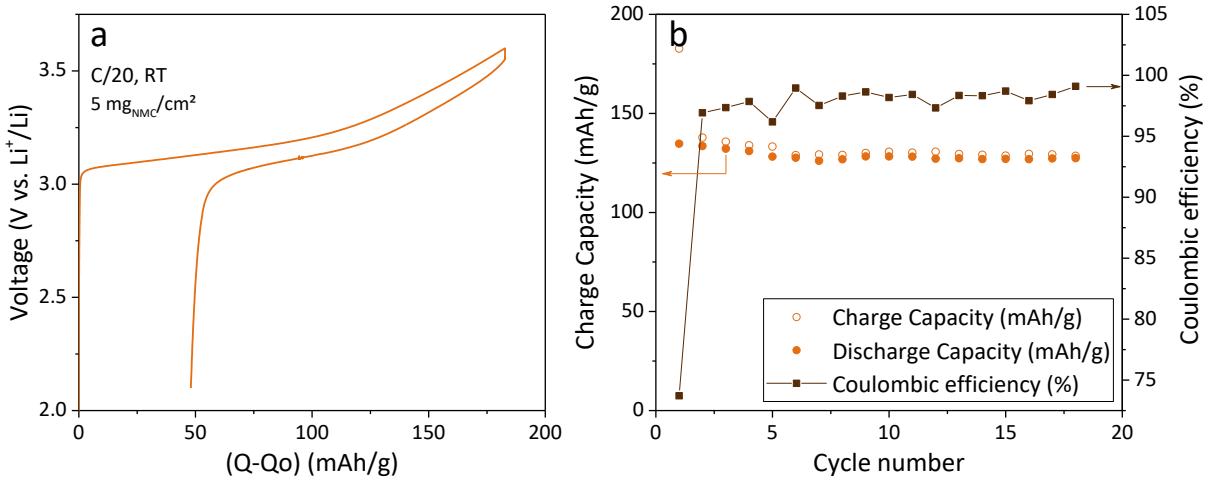

Figure 2.5. Galvanostatic cycling performance of a NMC622/LPSCl/VGCF cathode composite at a pressure of 10 MPa in a LPSCl-based ASSB architecture. (a) Voltage profile of the first galvanostatic cycle and (b) capacity retention and coulombic efficiency evolution.

Subsequently, we further reduced the testing pressure. To this end, we conducted two formation cycles at 10 MPa, after which the pressure was systematically changed every 3 cycles, ranging from 10 to 0.1 MPa, by adjusting the top screw. Figure 2.6 shows that at 10 MPa, the cell displays a nominal charge capacity of 174 mAh/g with an ICE of 74%, slightly

lower than before. However, further lowering the pressure resulted in a rapid decay in reversible capacity, reaching values of 94 and 88 mAh/g at 1 and 0.1 MPa, respectively.

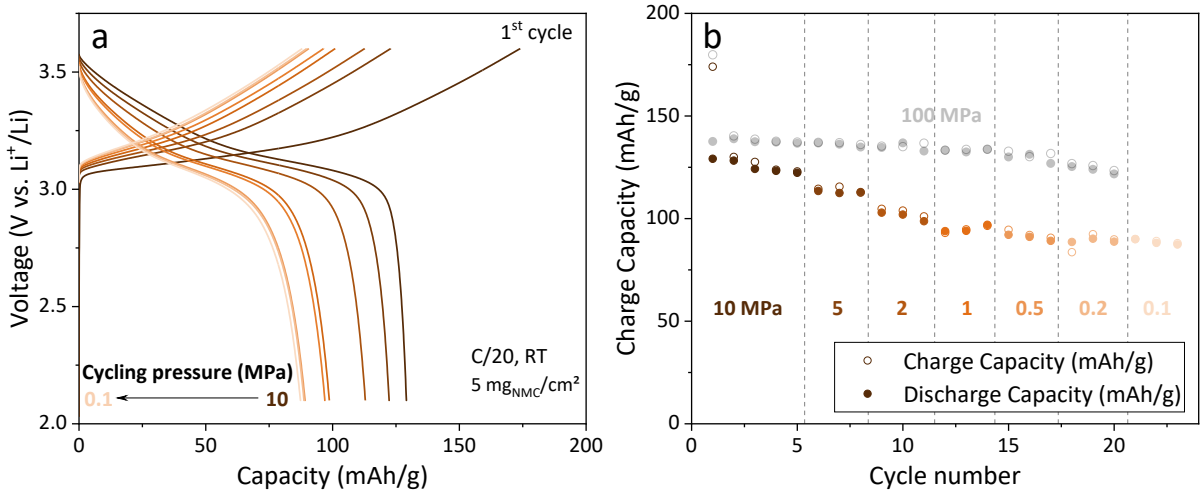

Figure 2.6. (a) First galvanostatic cycle and last cycle at each pressure and (b) capacity retention of a solid state cell comprising a LPSCl-based cathode composite (NMC622:LPSCl:VGCF) cell cycled versus a LiIn anode as a function of the stack pressure (from 10 to 0.1 MPa) and the reference at 100 MPa, cycled at RT and a C/20 rate

This capacity decline can be attributed to various factors, including percolation issues arising from a poor optimisation of the particles sizes of the AM and the SE. In an earlier report, Ceder showed both via simulations and experimental data that cathode utilisation in ASSBs is controlled by percolation, and that a higher ratio of cathode to SE particle size facilitates greater cathode loading.[80] The same rationalisation could explain the deteriorating performance observed when pressure is reduced, as an insufficiently optimised particle size ratio may contribute to increased percolation issues and contact losses. To assess the significance of this metric in low-pressure cycling performance, we conducted experiments at 10 MPa using argyrodite with two different particle sizes. The commercial LPSCl having particle of approximately 1 µm, with a few larger chunks of around 10 to 20 µm (Figure 2.1a) was compared to another LPSCl prepared in-house through a solid-state synthesis, referred to SS-LPSCl hereafter. A detailed procedure can be found in Appendix Section A2.1.

Compared to the commercial LPSCl, this SS-LPSCl displays significantly larger particle sizes with the largest chunks ranging from 50 to 200 µm; however, its ionic conductivity was higher at around 3.2 mS/cm.

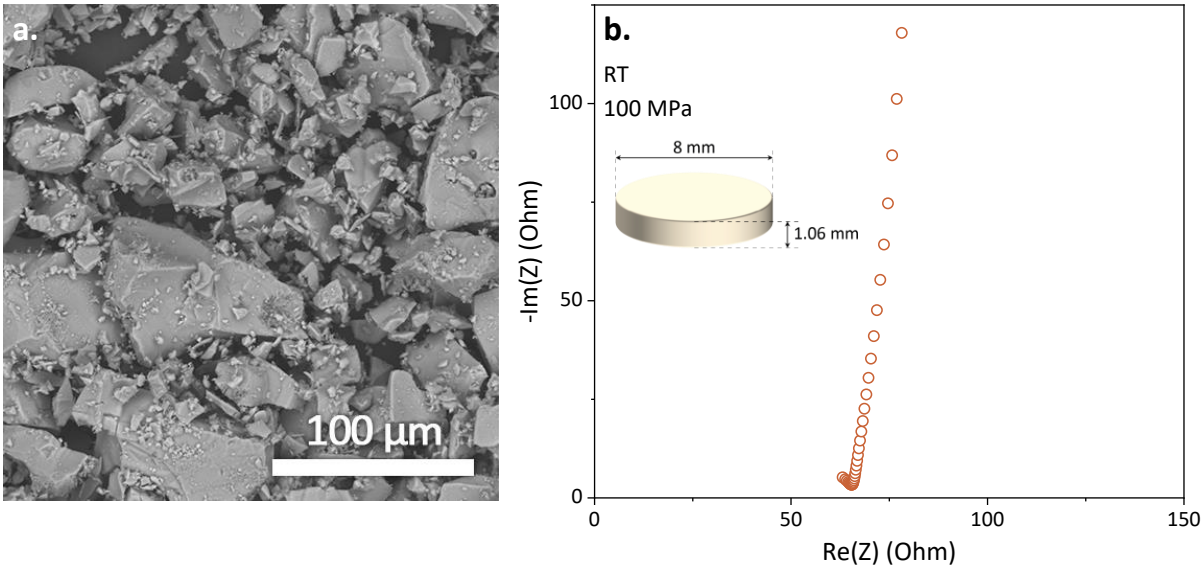

Figure 2.7. Homemade solid-state argyrodite SS-Li_6PS_5Cl properties. (a) SEM image of the material and (b) conductivity measurement by EIS.

Figure 2.8 compares the first cycle capacities at C/20 of composite made with either of these two argyrodites. Note that at high-pressure (100 MPa on the top in Figure 2.8), the performance is not affected by the particle size. However, decreasing the pressure to 10 MPa (bottom part in Figure 2.8) we observed that the fine LPSCl has a much higher reversible capacity compared to the SS-LPSCl. This highlights the importance of having the proper formulation and of adjusting the particle size ratio between the SE and the AM in the composite when performing low pressure cycling experiments.

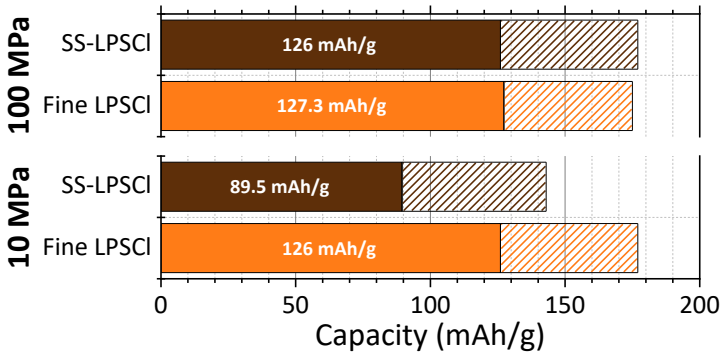

Figure 2.8. First cycle capacities at C/20 as a function of pressure and SE/AM particle size ratio, either with the fine or the larger SS-LPSCl. Solid coloured bars corresponds to the first discharge capacity and the hashed parts to the irreversible on the first cycle. The cumulative value represents the first charge capacity. All data are averaged over the capacities of 2 or 3 identical cells.

Besides the particle size ratio, the presence of an electronic conductor also significantly influences the cycling performance when pressure is decreased. Notably, when cycling a carbon-free composite under high pressure, the percolated NMC network provides a

sufficiently high electronic conductivity at low C-rates to achieve the full capacity under these conditions. As our group previously reported, this behaviour can be exploited in sulphide-based composite to mitigate the catalytic impact of carbon additives on SE decomposition.[122] However, as illustrated in Figure 2.9, the decrease in the initial cycling pressure results in a substantial capacity loss within this carbon-free system, reaching only 26 mAh/g at 10 MPa. This is notably lower than the 130 mAh/g achieved with the carbon-containing composite shown in Figure 2.6. This outcome can be explained by the diminishing contacts between the NMC particles under low-pressure conditions, resulting in a disrupted electronic percolation network in C-free composites.

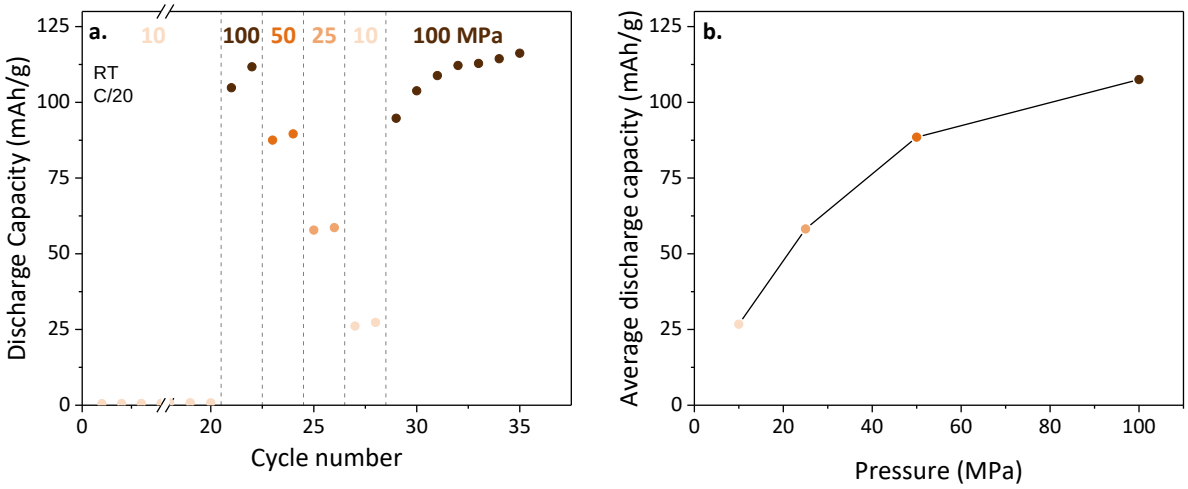

Figure 2.9. Capacity retention of a C-free composite cycled at various stack pressure from 10 to 100 MPa. (a) Capacity retention of a NMC/LPSCl composite cycled against a LiIn/LPSCl anode at different pressure and (b) average discharge capacity for each pressure tested.

Altogether, our exploration of the low-pressure performance of LPSCl-based composites reveals that their performance deteriorates notably below 10 MPa. Nonetheless, given the widespread utilisation of LPSCl in high-pressure studies in the literature, these findings establish a valuable reference point for our future investigations into lower pressure conditions. Moreover, we have confirmed the importance of optimising the particle sizes and the necessity of using a conductive additive to provide adequate ionic and electronic percolation within the composite, particularly in the context of low-pressure measurement where the percolation issues are exacerbated. Building on that we have decided to explore different SE chemistries available to us. In that context, we turned towards halide-based SE.

2.3 – Li_3InCl_6: A good candidate for low pressure cycling

From the LPSCl systems, we shifted our focus to explore alternative SEs. In particular, we turned to the halide SE family due to their favourable attributes, including enhanced oxidation stability, low hardness, and low elastic moduli. These mechanical properties become especially significant when lowering stack pressures, as ductile SEs tend to outperform brittle SEs in handling the strains and stresses that arise at the interface between SEs and electrode active materials during cycling.[107] Being the most widely used among the halide-based SE, we started with the Li_3InCl_6 phase.

○ Electrochemical and chemical stability of Li_3InCl_6

As previously reported by our group[123,124], the Li_3InCl_6 SE, hereafter referred to as LIC, is synthesized through a water-assisted method. Detailed synthesis protocols are available in the Appendix Section A2.1. We previously reported this LIC SE to display an ionic conductivity of 1.81 mS/cm and to exhibit crystalline particles smaller than 2 µm, which tend to loosely agglomerate into larger secondary particles.[123,124] These characteristics render LIC a suitable choice as a SE for the preparation of cathode composites. Its conductivity meets the necessary requirements, and its particle size aligns well with the 4 µm-large NMC particles. Consequently, a cathode composite consisting of the same monolithic uncoated NMC622 as previously used, this LIC SE, and VGCF conductive additive was manually prepared through hand grinding, with a weight ratio of 66.5%, 28.5%, and 5%, respectively.

As discussed in Section 1.3 of the previous chapter, due to their limited reduction stability, halide SEs decompose at low potentials, resulting in the formation of a detrimental mixed ionic-electronic interphase that lead to rapid cell deterioration. A straightforward approach to prevent this issue would be to employ a hetero-structure design, wherein another solid electrolyte, such as LPSCl, is utilised as the separator (Figure 2.10b). However, even with such an architecture, there is a notable degradation in cycling performance (Figure 2.10e). This decay has been ascribed to an increase in resistance at the interface, triggered by the formation of insulating species which may be catalysed by the electronic conductive species present at the triple point between LIC, LPSCl, and NMC or C.[125,126] As a result, an alternative strategy involving a dual solid electrolyte separator design, as depicted in Figure 2.10c, is commonly employed. In this approach, a bilayer consisting of LIC and LPSCl is utilised as the

separator. While this strategy generally leads to more stable cycling[46,48,49,54], it is important to note that in this particular SE pairing (LIC and LPSCl), a chemical incompatibility has been identified.[125,126] Through ToF-SIMS, Janek's group reported[126] this chemical incompatibility to result in an increase in the separator resistance by the formation of In_2S_3, $LiInS_2$ and LiCl decomposition products. Our research group has previously demonstrated the feasibility of implementing a nanometric interlayer composed of Li_3PO_4 or Al_2O_3, fabricated via atomic layer deposition (ALD), to prevent any reactivity between the two SEs.[125] However, for the sake of simplicity, in the subsequent study, a dual-SE architecture will be employed without any protective coating. Consequently, it is anticipated that there will be a continuous degradation of capacity over time.

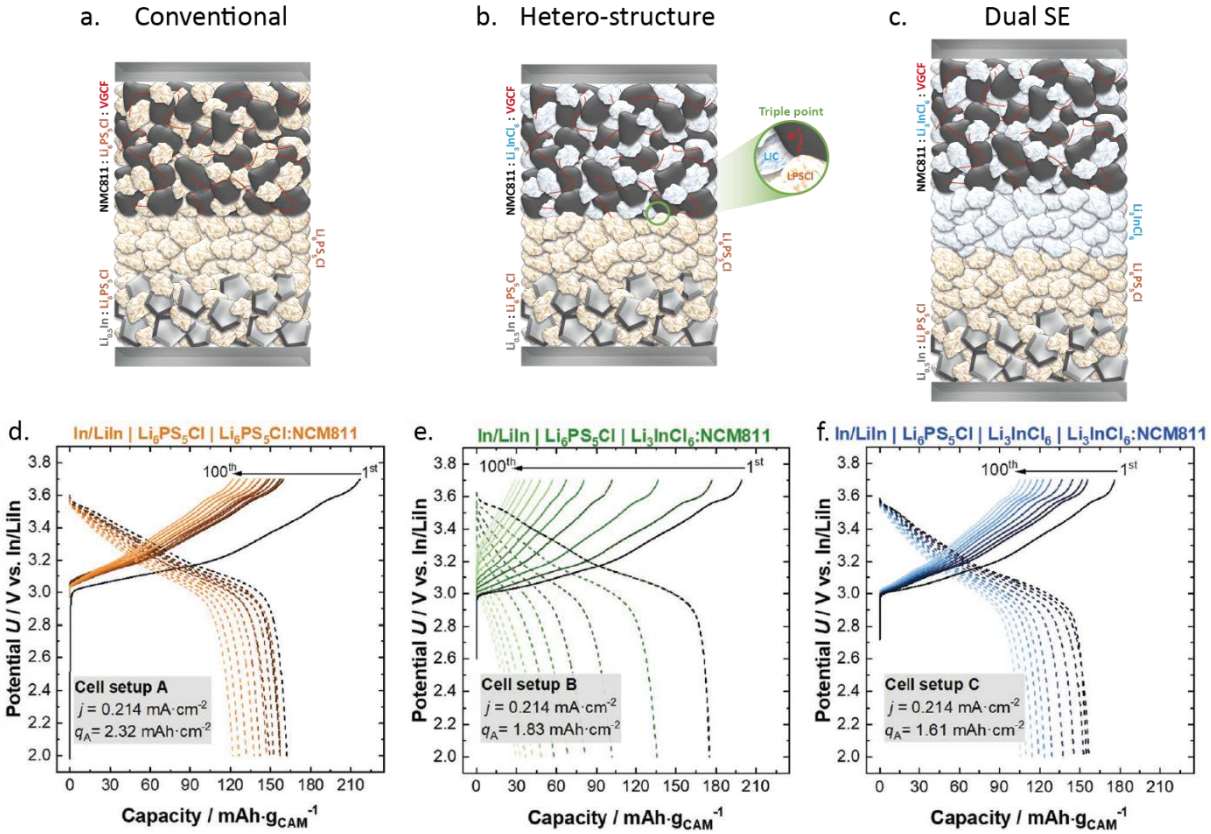

Figure 2.10. Cycling performances of the different cell architecture, *i.e.* conventional, hetero-structure and dual solid electrolyte cell architecture. (a-c) Schematics of the tested architecture and (d-f) their galvanostatic cycling performance at high pressure. Inset in (b) shows the triple point between the LIC, LPSCl and the electronic conductive pathway. Parts d-f reproduced from reference[126].

○ Performances of Li_3InCl_6-based cathode composites under various pressures

The galvanostatic cycling performance of the previously mentioned cathode composite was systematically investigated in conjunction with a LiIn/LPSCl composite anode within a dual-SE separator cell design. ASSB cells were assembled and their cycling performance,

shown in Figure 2.11, was evaluated under different pressure conditions. Interestingly, both cells, whether cycled at a high pressure of 100 MPa or at a relatively low pressure of 9 MPa, exhibit comparable first cycle capacities and retentions, reaching 152 and 145 mAh/g with initial coulombic efficiencies of 89.4% and 88.2% respectively. This stands in contrast to the poor capacity observed when decreasing stack pressure in LPSCl-based systems (Figure 2.6). Moreover, a continuous decay that we ascribe to the SEs incompatibility is present and examining the discharge capacity variations (Figure 2.11c), both cells show a similar trend with a decay rate, at this low C/20 cycling rate, of 0.98 and 0.83%/cycle et 100 and 9 MPa, respectively. Important to note is the low-pressure decay that seems to be more scattered, we attribute this to the effect of environmental conditions (temperature variation, vibrations in the glovebox, etc.) which have a stronger impact on performance at low pressure. This variability is often reflected on low-pressure cells in their capacities, coulombic efficiencies, decay rates as well as their polarizations.

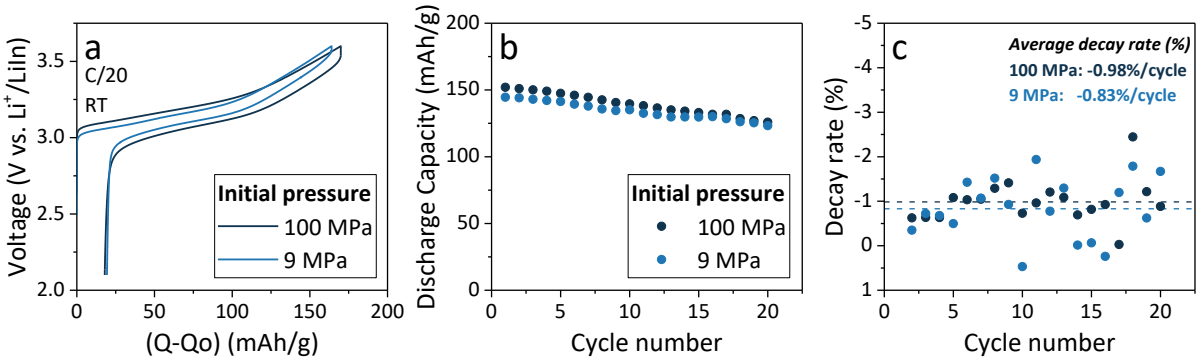

Figure 2.11. Galvanostatic performance of the LIC-based cathode composite at both high and low pressure. (a) First galvanostatic cycle profile, (b) capacity retention and (c) discharge capacity decay rate at 100 MPa and at 9 MPa. Both cells are cycled at C/20 under RT condition.

At this point, we successfully achieved cycling pressures ten times lower than those previously used, with no discernible impact on cycling performance. Nevertheless, it is important to note that even though we reached 9 MPa, this pressure level is still relatively high. For practical applications and the implementation of lithium metal anodes, it is imperative to operate at pressures below 5 MPa, ideally even lower than 2 MPa. In this context, the same cell was subjected to further cycling at successively lower pressures by adjusting the top screw of the frame setup as illustrated in Figure 2.4. First, 50 cycles were performed at 9 MPa before decreasing to 6, 2.5, 1.5, 0.5, 0.3 and finally 0.1 MPa. The results are presented in Figure 2.12. While it appears that the decay rate slows down after approximately 30 cycles, decreasing the pressure does not significantly influence the retention

or the average decay rate. Most of the capacity drop occurs in the cycles immediately following pressure changes, as highlighted by the filled circles in Figure 2.12b. This is due to the necessary cell manipulation required to change pressure, which effect becomes particularly pronounced at low pressures, where maintaining good contact with the current collector is crucial. Moreover, similar to the increased variability at low pressures mentioned above, we also observe an increase in the decay rate variations when decreasing the pressure. This is illustrated by the increase in standard deviation, as indicated by the filled area in Figure 2.12b.

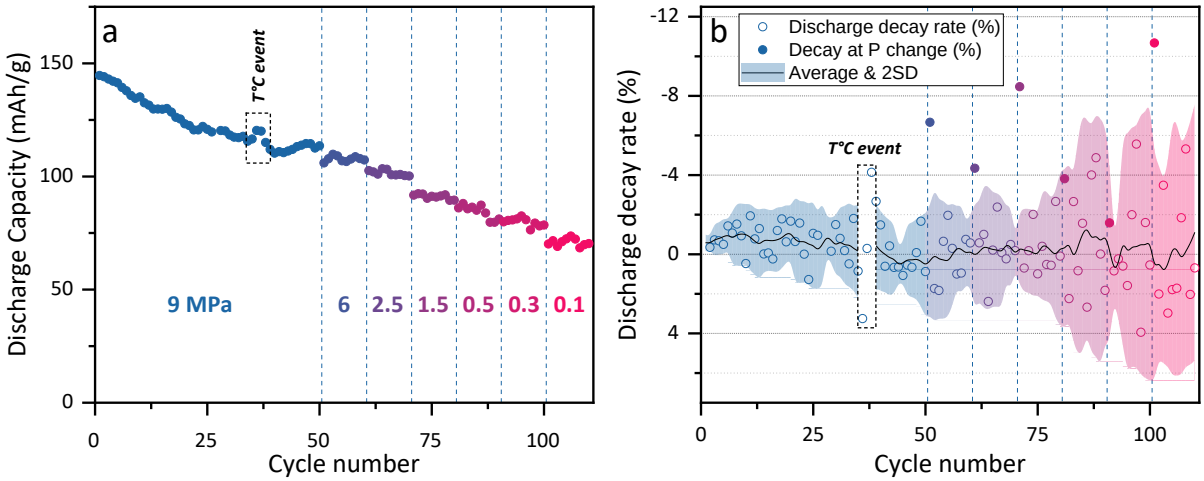

Figure 2.12. (a) Capacity retention and (b) decay rate of a LIC-based cathode composite at decreasing pressures from 9 to 0.1 MPa. Filled circles in the decay rate highlight the larger capacity drop after each pressure change and the filled area highlighting the larger variations at low pressure corresponds to two standard deviations and does not include the data points after the pressure changes in its calculation. The temperature event that occurred at around cycle 35 was due to an unusual important increase in the RT and was therefore remove for the calculation of the standard deviation.

To ensure that cyclability remains consistent at lower pressures, we conducted another experiment in which the cell was initially subjected to five formation cycles at 9 MPa, followed by an immediate reduction of the stack pressure to 1 MPa. The results of this experiment, depicted in Figure 2.13, indicate a capacity of 144 mAh/g for both cells on the first discharge at 9 MPa, and show that they exhibit a similar decay rate throughout cycling, eventually reaching 111 mAh/g after 50 cycles at either 9 or 1 MPa. Collectively, these results provide clear evidence that cycling LIC-based composites at 100, 10 or 1 MPa does not hinder the performance.

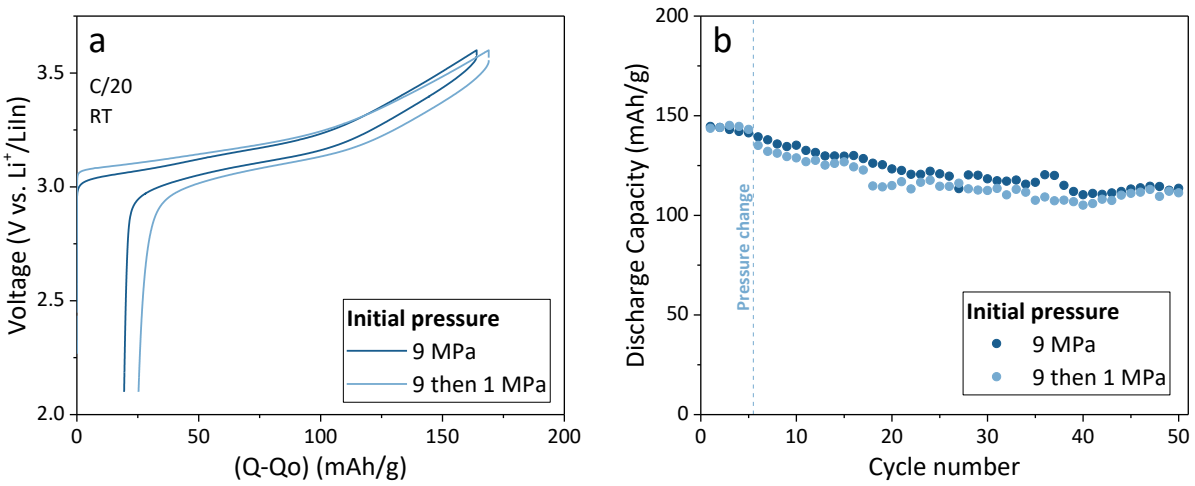

Figure 2.13. (a) First galvanostatic cycle and (b) capacity retention of a LIC-based cathode cell cycled either at 9 MPa or at 1 MPa after 5 cycles at 9 MPa. Both cells were cycled at a C/20 rate under RT conditions with loading of 5 mg_{NMC}/cm^2.

○ The importance of the composite preparation process

It is important to emphasize the polarization difference observed on first cycle between cells in Figure 2.11a and Figure 2.13a. This discrepancy can be attributed to the fact that these cells were constructed using cathode composites from two distinct batches. Following initial experiments (Appendix Figure A2.3a), a notable decline in performance and reproducibility of subsequent LIC-based composites was observed (Appendix Figure A2.3b and c). The issue was traced back to the degradation of the SE, likely caused by solvent vapours in the glovebox atmosphere hence gaining valuable insights into the fabrication process of such composites, which can be influenced by factors such as the operator, grinding time, and applied force. Moreover, it highlights a significant challenge in the production of ASSBs that rely on reactive SEs like halides. These SEs have a tendency to react with air, moisture, and many solvents, posing a significant obstacle to their widespread utilisation in industrial applications.

Altogether, we were able to cycle ASSB cells composed of a halide-based cathode composite at pressures as low as 0.1 MPa or 1 bar. Such low pressure could therefore enable their use in larger pouch cells design that would be cycled under atmospheric pressure. In addition, it shows that halide SEs outperform the sulphide LPSCl SE when cycled under low-pressure conditions, however, we used Li_3InCl_6, which is not an ideal choice. Indeed, it is costly to produce due to the scarcity of indium and has a poor reduction stability that leads to the necessity of using a dual-solid electrolyte cell architecture to prevent its reduction. In that

regard, we turned our interest towards other types of halide SE, in particular, the yttrium-based halide SEs.

2.4 – Introducing $Li_3YBr_2Cl_4$: a mixed halide SE with enhanced reduction stability and low hardness

Yttrium-based halides were selected for their appropriate properties. In particular, Li_3YCl_6 (LYC) displays a theoretically predicted cathodic limit as low as 0.62 V vs. Li^+/Li (as shown in Figure 2.14), limit much lower than the calculated 2.38 V vs. Li^+/Li of the Li_3InCl_6 used in the previous Section 2.3. Such low reduction stability falls within the range that allows for compatibility with a Li-In alloy anode.[127] However, Asano *et al.* reported a lower conductivity of 0.51 mS/cm for LYC compared to Li_3InCl_6.[45] Later, this conductivity was shown to be improved through the partial substitution of Cl by Br anions and the mixed halide $Li_3YBr_3Cl_3$ was reported to display an ionic conductivity of 1.6 mS/cm which can be further improved to 7.2 mS/cm through a hot-pressing process at 150°C.[46] However, as depicted in Figure 2.14, a higher content in Br results in a decrease in the predicted anodic stability from 4.25 V vs. Li^+/Li for LYC to 3.15 V vs. Li^+/Li for Li_3YBr_6 (LYB).

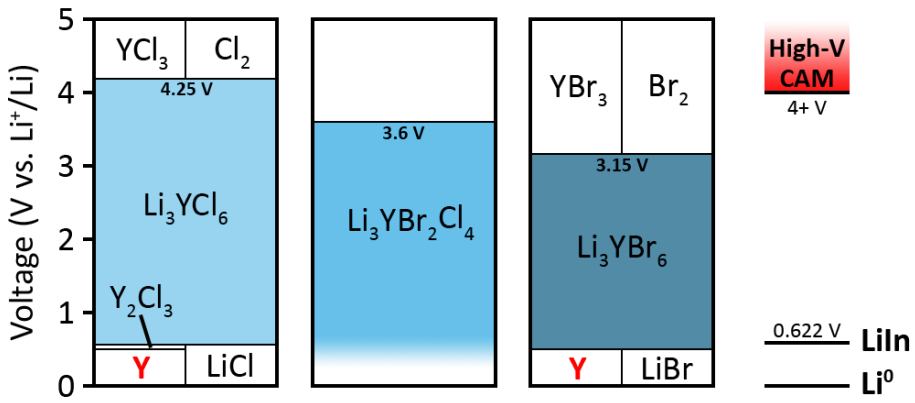

Figure 2.14. Calculated phase equilibria for (left and right) Li_3YCl_6 and Li_3YBr_6 based on first-principle calculations (DFT, adapted from reference[127]) and potential stability window of $Li_3YBr_2Cl_4$ obtained experimentally through linear sweep voltammetry (see Figure 2.15a). Potential of Li metal, LiIn alloy and high potential CAMs on the right. Stable potential window of SEs are coloured and electronically conductive species are in red.

○ Physical, chemical and electrochemical properties of $Li_3YBr_2Cl_4$ SE

In our study, we utilised the mixed Br-Cl $Li_3YBr_2Cl_4$ SE, denoted LYBC hereafter. This halide was kindly provided to us by Saint-Gobain Recherche Paris. LYBC crystallises with particle size ranging from 1 to 4 µm (Figure 2.15a) and has an ionic conductivity of 1.27 mS/cm

(Figure 2.15c). Its electrochemical stability window was determined by linear sweep voltammetry (LSV) in oxidation and reduction separately (Figure 2.15b). Similar to the observations previously[46] reported with $Li_3YBr_3Cl_3$ and compared to LYC and LYB, we denote an intermediate oxidative current onset starting at 3.6 V vs. Li^+/Li, which was associated to Br^- oxidation by calculation.[127] In reduction, a small onset at 1.4 V and a larger current starting from 0.4 V vs. Li^+/Li are observed. The reduction stability observed in LYBC and the reversibility of the electrochemical process between OCV and the LiIn potential (Figure A2.4) suggest that, unlike Li_3InCl_6, LYBC may remain stable when in contact with a LiIn counter electrode with its potential of 0.622 V vs. Li^+/Li. Thus considerably simplifying the experimental procedure, as there would be no need for the protective layer of LPSCl in this case.

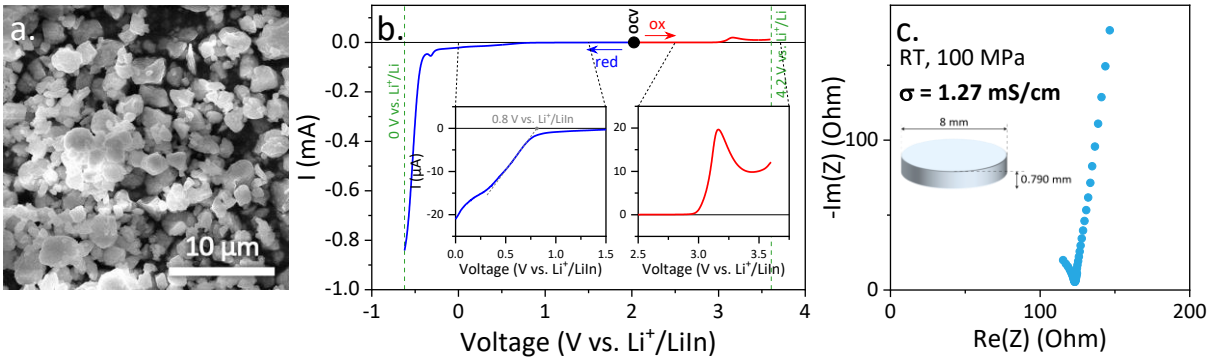

Figure 2.15. LYBC characteristics. (a) Micrograph of LYBC, (b) linear sweep voltammetry in oxidation and reduction of LYBC/VGCF (95/5wt.%) composite and (c) impedance spectroscopy on LYBC pellet at 100 MPa.

The cycling performances of NMC622 with the LYBC SE were then evaluated. In that regard, a cathode composite was prepared through a ball milling process. The same monolithic uncoated NMC622 as previously used, LYBC, and VGCF in a ratio of 66.5 : 28.5 : 5 wt.% were weighted and transferred to a 45 mL zirconia jar. Five 10 mm ZrO_2 balls were used to reach a 36/1 powder-to-ball mass ratio and the composite was prepared through planetary ball milling at 150 RPM for 30 minutes.

Next, to assess the stability of LYBC with our LiIn alloy anode, two cells were constructed and their galvanostatic performance at a rate of C/20 under a pressure 100 MPa were assessed and compared. The first consists in a dual-SE architecture NMC//LYBC//LPSCl//LiIn and the second in a full-halide system NMC//LYBC//LiIn as illustrated by the schematics in Figure 2.16a.

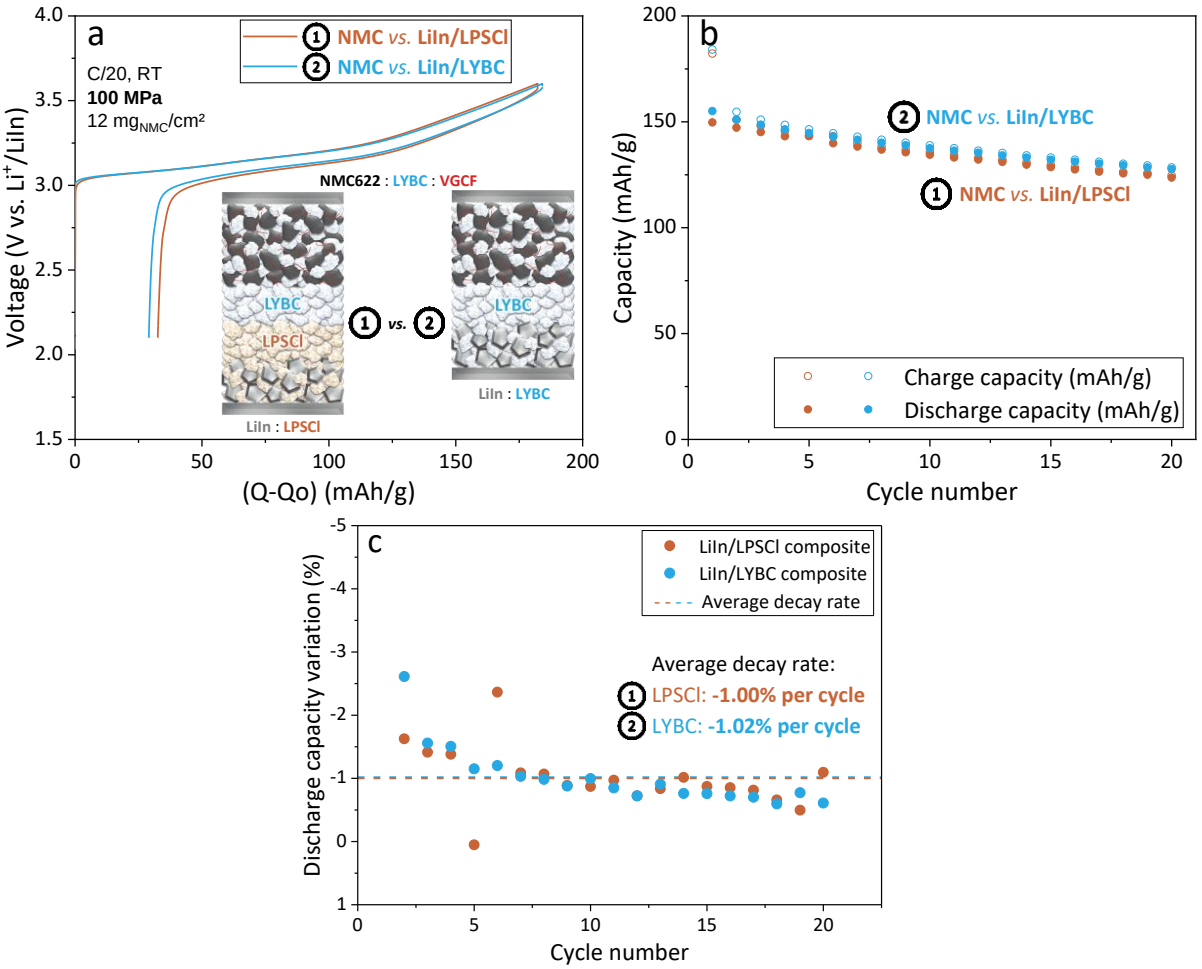

Figure 2.16. (a) First galvanostatic cycle, (b) capacity retention and (c) discharge capacity decay rate of both (in brown, denoted *1*) the dual-SE design and (in blue, denoted *2*) the full-halide cells cycled at RT at a C/20 rate and a stack pressure of 100 MPa. Dashed lines in (c) represent the average decay rate over the 20 first cycles.

Initial capacities of 182 and 184 mAh/g in charge, 150 and 155 mAh/g in discharge with ICEs of 82.2% and 84.2% are obtained for the dual-SE and full-halide cells, respectively. This demonstrates the compatibility of LYBC with LiIn anodes. Comparing the capacity retention of the two systems, no difference is observed (Figure 2.16b). They both show a decrease in capacity of about 1%/cycle at C/20 (Figure 2.16c). For the full LYBC cell (denoted "2" in Figure 2.16), this observed behaviour is unexpected if the previously mentioned halide/sulphide SE incompatibility (Figure 2.10) is considered as the sole source of degradation. To interrogate this aspect, we measured the impedance evolution of a SE bilayer LYBC//LPSCl under accelerated conditions at 80°C. Nyquist plots (Figure 2.17) were obtained at 25°C in the pristine state and after various heating durations. Notably, within 103 hours of heating, the impedance reached a plateau with a final increase in the total resistance of only 25%, result in stark contrast to the four-fold increase our group previously reported in the Li_3InCl_6//LPSCl system.[125]

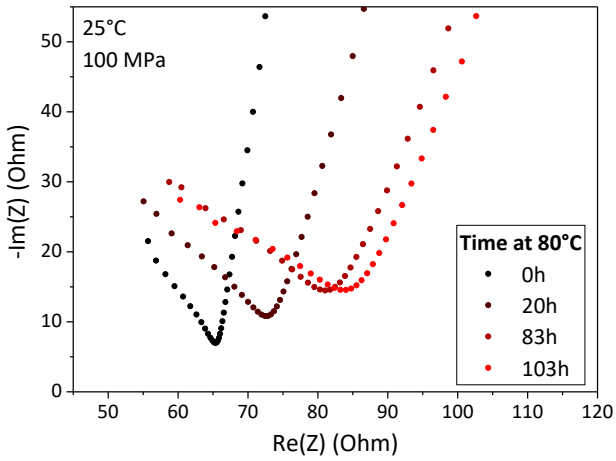

Figure 2.17. Nyquist plots measured at 25°C of a LYBC//LPSCl stack after different 80°C exposure durations.

However, upon further mixing of the powders followed by heating to a temperature of 150°C (a detailed experimental protocol conducted by Maria Platonova from our group is available in the Appendix Section A2.1), a clear evolution of the XRD is observed. Importantly, even though the chosen temperature is well below the respective decomposition temperatures of both SEs, a clear reactivity is evidenced by the disappearance of the LYBC XRD reflections, to the benefit of growing peaks at 29.7, 34.5, and 49.4°, which can be attributed to the formation of LiCl (Figure 2.18a) that is most likely responsible for the degradation of the ionic conductivity of the mixture (Figure 2.18b) after heat treatment. These observations indicate the existence of a thermodynamic instability between our electrolytes, which appears to be kinetically limited at the lower temperatures at which we are cycling cells. Thus explaining the comparable cycling performances observed in Figure 2.16 between the two systems but also raising the question of the origin of this retention decay.

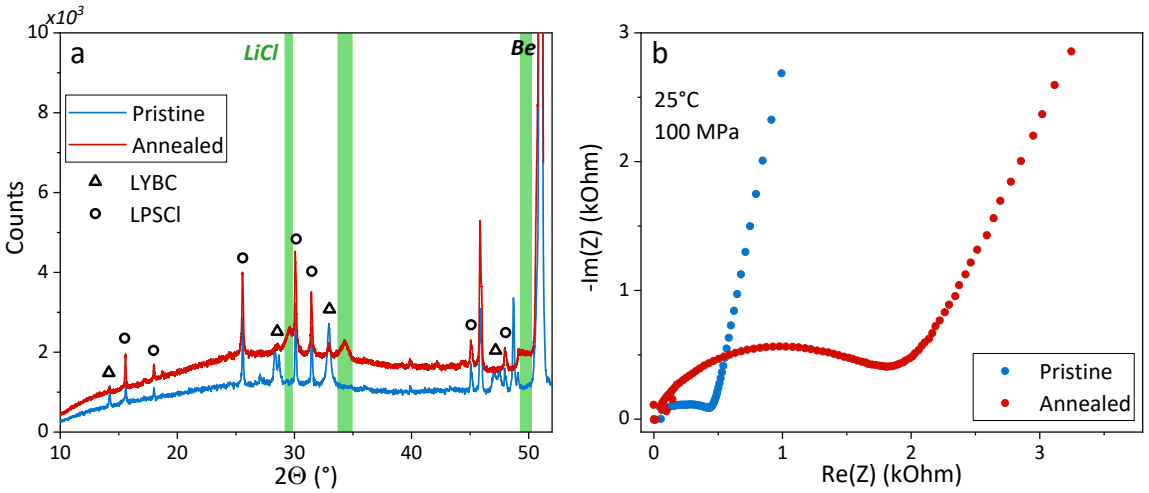

Figure 2.18. (a) Diffractograms and (b) Nyquist plots of the EIS measurement of pristine (in bleu) and annealed at 150°C for 11 days (in red) mixture of LYBC and LPSCl in a 1:1 mass ratio. In part (a), green bands highlight the evolution of two new reflection that can be attributed to LiCl.

Overall, the observed continuous decay upon cycling and the aforementioned SE oxidation above 3.6 V vs. Li^+/Li (Figure 2.15b), suggests a mild incompatibility in the cathode composite itself, which is likely the cause of the increased polarization upon cycling, as evidenced in the Appendix Figure A2.5.

○ The low pressure performance of $Li_3YBr_2Cl_4$-based composites

As mentioned previously, cycling at extremely high pressures (> 100 MPa) is not a scalable option and is completely incompatible with the highly soft and ductile lithium metal anode. Therefore, we investigated the pressure-dependent cycling performance of this new system. In that context, a "full-halide" solid-state NMC//LYBC//LiIn cell with a loading of 4.6 mg_{NMC}/cm^2 was assembled and, similarly to the previous study in pressure of the Li_3InCl_6-based composite, was cycled at successively decreasing stack pressure from 10 MPa to 0.1 MPa (= 1 bar). The results are presented in Figure 2.19a and b. Remarkably, at 10 MPa, this system displayed capacities of 179.6 mAh/g and 150.2 mAh/g in charge and discharge, respectively, with a high ICE of 84% and a low polarization of 37 mV. Overall, the first cycles at 10 and 100 MPa (Figure 2.16a) show very similar performance. The pressure was then gradually decreased down to 0.1 MPa in subsequent cycles and apart from the continuous degradation, no significant drop in capacity was observed. Moreover, as shown by the filled dots in Figure 2.19d, the majority of the capacity decay occurs at the cycle following to pressure changes where the decay rate is higher than the previously determined standard rate of -1%/cycle. As mentioned for the Li_3InCl_6 system in Figure 2.12b, this is due to the cell manipulation required to change pressure. These findings indicate that it is possible to achieve pressures below 1 MPa although the observed decay should be addressed by choosing another SE or introducing coating for example.

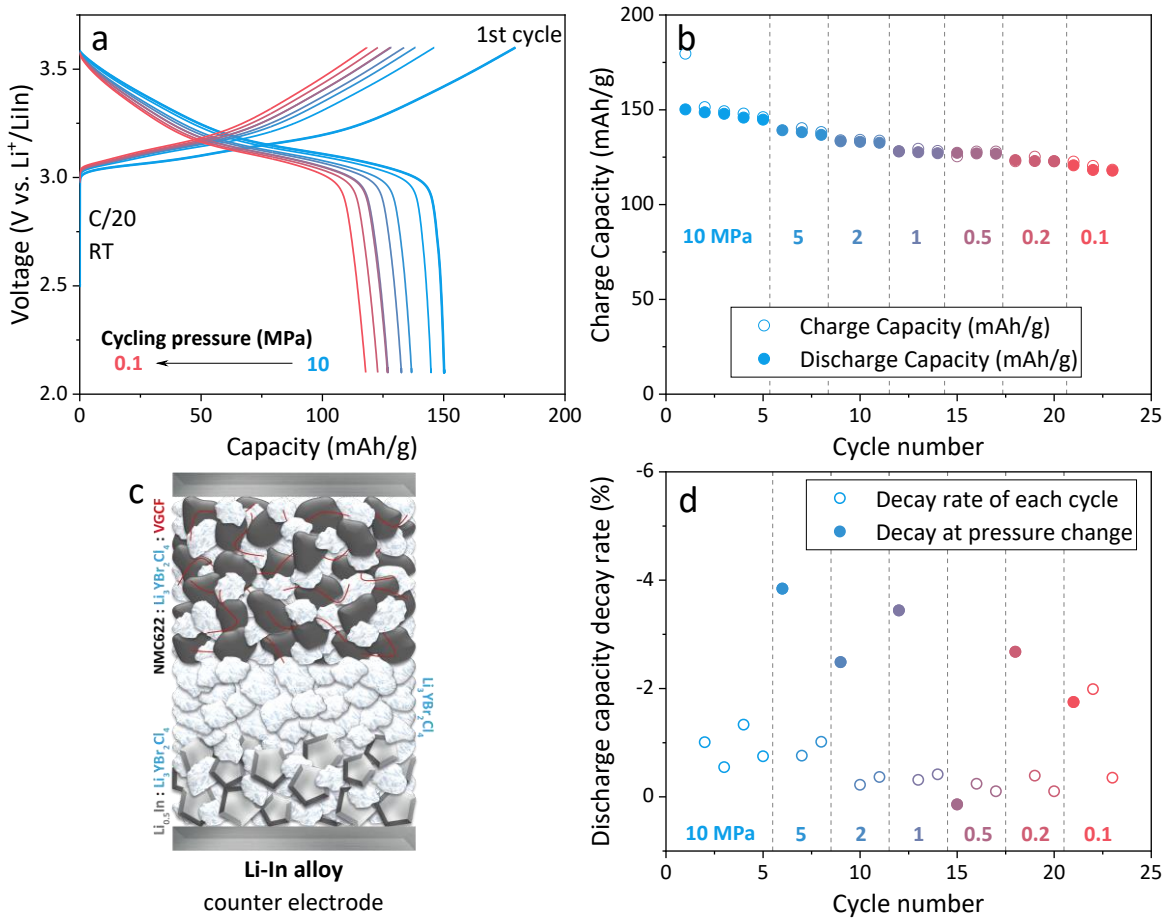

Figure 2.19. (a) Last galvanostatic cycles at each pressure, (b) capacity retention and (d) decay rate of NMC//LYBC//LiIn cell as a function of the stack pressure (from 10 to 0.1 MPa), cycled at RT and a C/20 rate. (c) Schematic of the "full-LYBC" cell architecture tested in this experiment. Filled circles in (d) highlight the larger capacity drop after each pressure change.

At this stage, we have demonstrated that reducing the pressure has little effect on the capacity retention of such composite at a low loading of 4.6 mgNMC/cm² but other figures of merits such as the performance as a function of the pressure, loading, and temperature must be determined.

First the rate capabilities as function of the pressure was estimated (Figure 2.20a). We assembled cells with loadings of approximately 5 mg_{NMC}/cm^2 and conducted cycling experiments according to the following protocol. The first formation cycle was carried out at C/20 under a pressure of 10 MPa and for subsequent cycles, the pressure was decreased and the discharge rate capability was monitored. Rate capability measurements were conducted following by varying the discharge rate from C/20 to 5C, while the charging rate was maintained in Constant Current Constant Voltage (CCCV) mode at C/10 during the CC phase and down to C/50 during the CV phase. Three cycles were performed at each rate, and the average discharge capacity was used to evaluate the rate capability.

The reduction in pressure resulted in a slight decrease in reversible capacity, particularly at higher discharge rates, but showed negligible changes for pressures below 10 MPa. Additionally, after measuring the rate capability, the cells were cycled at C/20, and the calculated capacity decay rate (Appendix Figure A2.6) displayed no clear trend as a function of pressure, with an average decay rate of around -1%/cycle. These results align with previous tests conducted at 100 MPa (Figure 2.16c) and confirm our hypothesis that such halide SE can be used for very low-pressure cycling.

Subsequently, evaluating the rate capabilities as a function of loading, we employed the same cycling protocol but with a stack pressure of 100 MPa. The loading conditions were systematically varied between 5 and 25 mg_{NMC}/cm^2, with the goal of achieving loadings of 5 mAh/cm^2 for future industrial applications of ASSBs.[6] Figure 2.20b clearly illustrates the significant influence of loading on the rate capabilities with the capacity decreasing from 125 to 86, 25, and 16 mAh/g at 1C when increasing the loading from 5 to 12, 20, and 25 mg_{NMC}/cm^2.

Additionally, we examined low-pressure performance of this system as a function of loading. NMC//LYBC//LiIn solid-state cells with loadings of up to 25 mg_{NMC}/cm^2 were cycled at C/20 under a relatively low pressure of around 9 MPa (Figure 2.20d and e). Increasing the loading results in a linear increase in the polarization from 41 mV at a loading of 4.6 mg_{NMC}/cm^2 to 158 mV at a loading of 25 mg_{NMC}/cm^2. Remarkably, there is no significant drop in the first cycle reversible capacity, which remains stable at around 145 mAh/g at this low rate.

Lastly, we studied the performance of such cells over the 0 to 70°C temperature range. Anticipating degradations at high temperature that could affect rate capability (Appendix Figure A2.7b), we have changed our cycling protocol and adopted the "signature curve" technique. Briefly, it consists in discharging the cell at progressively lower currents to a fixed discharge cut-off voltage, so that the resulting cumulative capacities are indicative of the material's rate capabilities. A more detailed explanation of this procedure can be found in the Appendix Section A2.1 and Appendix Figure A2.1. The results, displayed in Figure 2.20c, showed reversible capacities of 165 and 169 mAh/g at a C/20 rate under 50°C and 70°C, respectively. Even at a high rate of 5C, the reversible capacities reached 135 and 138 mAh/g, demonstrating remarkable rate capabilities at high (70°C) and even moderate (50°C)

temperatures. Decreasing the temperature resulted in a drop in reversible capacities, reaching 146, 144, and 133 mAh/g at C/20 under 25°C, 10°C, and 0°C, respectively.

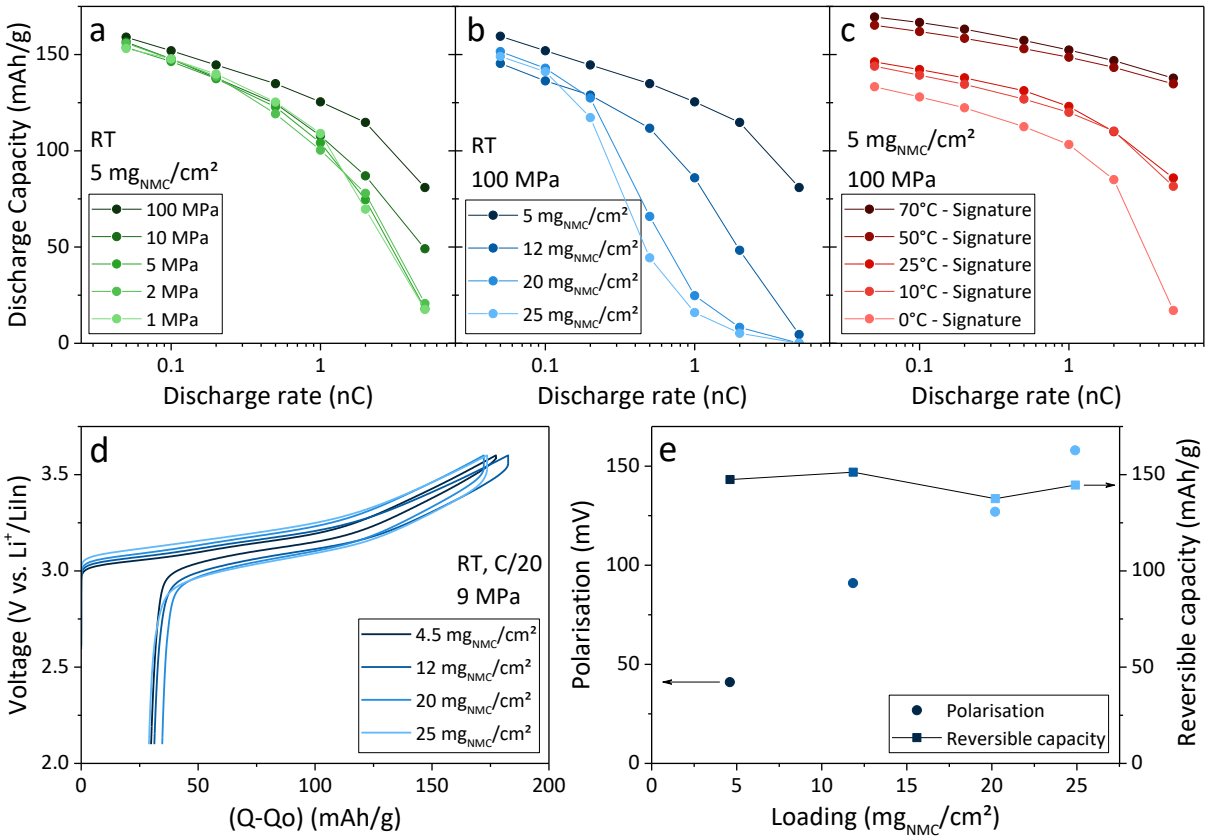

Figure 2.20. Rate capabilities of NMC//LYBC//LPSCl//LiIn cells as a function of (a) stack pressure, (b) loading and (c) temperature. (d) First galvanostatic cycles and (e) first cycle polarization and discharge capacity as a function of the loading, cycled at RT, a stack pressure of 9 MPa and a C/20 rate.

Overall, the low-pressure performance of our halide-based systems highlight the potential of halide SEs for real-world applications although being still limited in terms of achievable loading and temperature due to the relatively low ionic conductivity of 1.27 mS/cm of the LYBC. Comparing the performance of our system to that of LPSCl-based composites shown in Figure 2.9, it becomes evident that, in addition to ionic conductivity of the SE, other mechanisms must be at play in the improved performance under low-pressure conditions.

○ Discussion on the reason underlying the enhanced low-pressure cyclability of halides over Li_6PS_5Cl solid electrolyte

At this stage, a legitimate question regards why cathode composite based on halide SEs exhibit enhanced low-pressure cyclability. There are several reasons for this that may be related to the physical, electrochemical, chemical or mechanical properties of the different components or even from their interaction within the cathode composite. Among them and

in light of our early discussions (Section 1.3), the ability of the SE material to mitigate strain and to accommodate volume changes in the cathode composite while maintaining adequate percolation even at low pressure seems essential.

To explore the issue of percolation in greater depth, we have performed scanning electron microscopy (SEM) imaging and Energy dispersive X-ray (EDX) measurements on composite powder and densified pellets in order to assess the homogeneity and the particle sizes of the different components. Measurements were performed in the *Laboratoire de Réactivité et Chimie des Solides* (LRCS) with the help of Carine Davoisne. The detailed methods can be found in Appendix Section A2.1. Three different composites prepared by hand grinding of composition in NMC622, SE and VGCF of 66.5, 28.5 and 5% were imaged through these techniques. Two of them contained LPSCl electrolytes, more specifically the coarse SS-LPSCl and the fine LPSCl used in Section 2.2 and the third one incorporated the Li_3InCl_6 prepared through a water-based synthesis. Regrettably, due to the high sensitivity to air and moisture of such SEs, we were compelled to outsource these measurements and due to time constraints, we were unable to conduct a parallel study on composites based on LYBC. Analysing the cross-section images presented in Figure 2.21 as well as the EDX mapping of the single elements in Appendix Figure A2.8, it is evident that the SS-LPSCl composite (Figure 2.21a and d) displays regions of large SE particles while concurrently displaying regions devoid of it. This observation correlates with a poor ionic percolation, which provides an explanation for the inferior performance of SS-LPSCl-based composites under low-pressure conditions. In contrast, both the fine LPSCl and LIC composites appear to exhibit a higher level of homogeneity. Based on these results, we concluded that particle sizes and homogeneity of the composites alone are insufficient to fully account for the decrease performance of fine LPSCl compared to LIC under low-pressure conditions. Consequently, it is imperative to explore other contributing factors; namely mechanical properties, as hypothesized earlier.

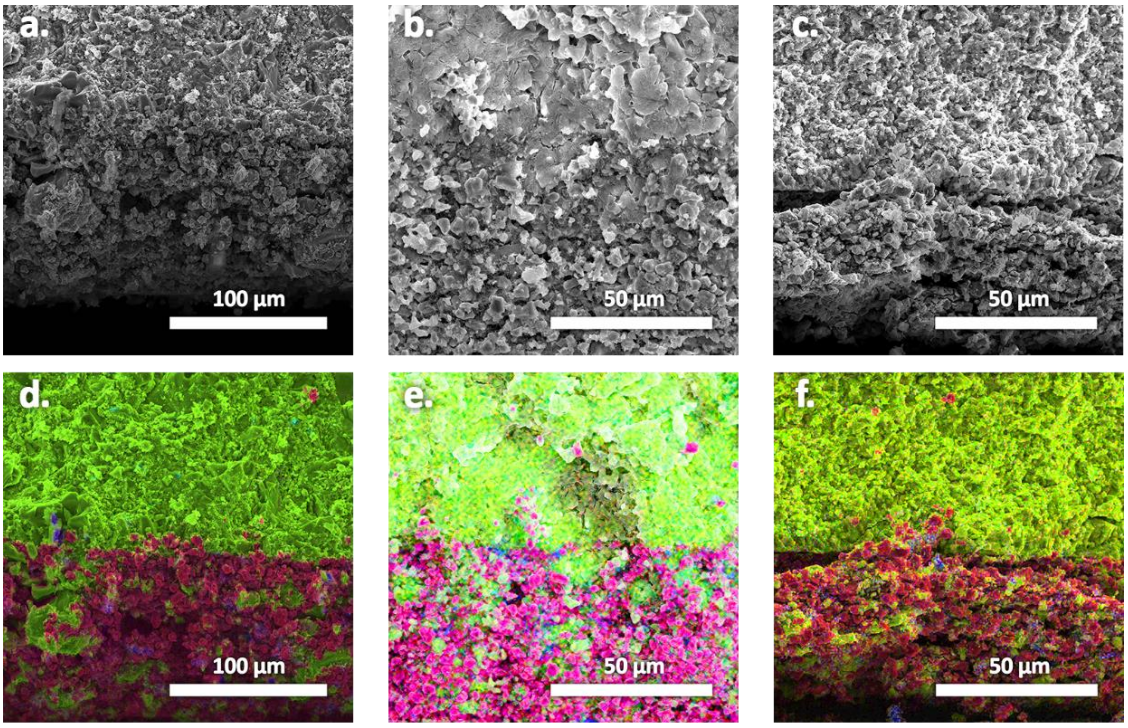

Figure 2.21. Cross-section SEM imaging (a-c) and EDX mapping (d-f) of bilayer pellets made of a SE substrate and the cathode composites. Parts (a) and (d) correspond to SS-Li_6PS_5Cl, (b) and (e) to fine Li_6PS_5Cl and (c) and (f) to Li_3InCl_6-based cathode composites. Green and yellow coloured particles corresponds to SE elements (P, S, Cl and In), pink/red coloured particles corresponds to NMC elements (Ni, Mn, Co, O) and blue regions to VGCF.

To interrogate the mechanical properties of the electrolyte, microindentation measurements were conducted with the help of *Saint-Gobain Recherche Paris*. The results are illustrated in Figure 2.22b. Notably, LYBC exhibits a hardness of 0.302 ± 0.017 GPa, value significantly lower than that previously reported for sulphide or oxide-based SE (Figure 2.22a). Furthermore, it is a hardness value one order of magnitude lower than that reported by Bruce's group with their Li_3InCl_6 halide prepared by ball-milling, although they used a nanoindentation technique and a different synthesis route that can make the comparison not straightforward.[121] A likely explanation to this contrast in hardness values could be nested in the different chemistry of the compounds, in particular in the choice of the Y cation and Br anion. Their larger ionic radius can lead to a more isotropic charge distribution, which lower the pinning of defects, hence favouring an increase in plasticity, as shown in Figure 2.22b where the hardness diminishes with an increase in the proportion of Br content. This low hardness can be advantageous during different phases of the assembly process. Firstly, since it is generally associated with lower stiffness,[128] a lighter load will have to be used during composite preparation process to deform the SE particles in contact with AM as illustrated in Appendix Figure A2.9 . This, in turn, enhances the contact area and promotes the uniformity

of the composite without causing damage to its other constituents. Secondly, during assembly at the densification step, the SE is likely to be denser thus decreasing porosity in both the cathode composite and separator and enabling a good percolation without the need of a sintering step.

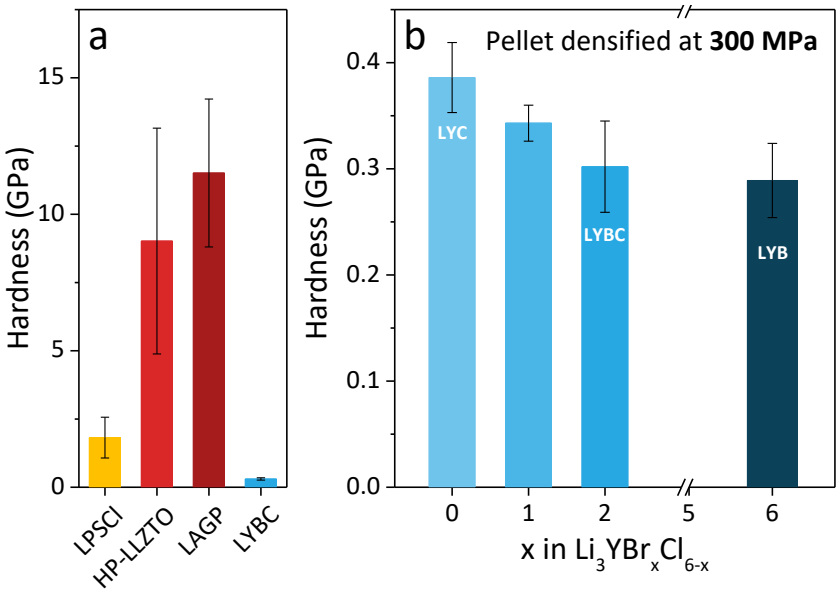

Figure 2.22. Hardness of different SE from the literature and from our study. (a) Hardness of typical SE (adapted from literature[87] for LPSCl, HP-LLZO and LATP) and (b) hardness measurement by microindentation on pellet fabricated at 300 MPa as a function of the bromine content in $Li_3YBr_xCl_{6-x}$ compounds.

In summary, we believe that the material's low hardness plays a pivotal role in facilitating low-pressure cycling. Nonetheless, acknowledging the potential impact of other factors, specifically differences in chemical or electrochemical compatibility between oxide/halide and oxide/sulphide materials is important as the formation of a passivating CEI layer can lead to increase stress and/or contact losses at the interface between the CAM and the SE. In addition, one cannot disregard the potential significance of the adhesion and friction properties of the SE and CAM. Adequate adhesion could significantly help in accommodating volume changes. However, determining adhesion properties is not straightforward and a lack of literature on that subject is clear.

○ A first step towards larger pouch cells

We have successfully demonstrated the low-pressure performance of halide-based SE in cathode composites for ASSB using laboratory-scale equipment with 8 mm diameter cells. The ability to cycle down to 0.1 MPa now allows us to pursue scalability and explore larger cell sizes. In this regard, we have undertaken experiments with a split-body cell of 13 mm in

diameter with a Mylar lining (as illustrated in the Figure 2.23a), which facilitates the unmoulding of the stacked pellet after densification. However, to achieve uniformity over a larger surface area, we adopted a film-based approach for the separator. Specifically, we began by fibrillating LYBC with 0.2 wt.% polytetrafluoroethylene (PTFE) binder by mixing and then rolling and folding the powders using a glass tube until a self-standing membrane was formed. Subsequently, from this membrane, a 13 mm diameter disk with a weight of approximately 150 mg was cut and pressed at 100 MPa within the cell. To address the known decomposition issue of PTFE when in contact with lithium or LiIn, a thin layer of LPSCl argyrodite was then spread and pressed at 100 MPa onto the LYBC separator before introducing the LiIn:LPSCl counter electrode. The working electrode, composed of NMC622:Li_3InCl_6:VGCF in a 66.5:28.5:5 wt.% ratio, was then added and the whole stack was densified at 400 MPa to complete the assembly. Finally, the stack was unmoulded, placed into a pouch cell with aluminium disk and tabs for electric connection and sealed under vacuum (Figure 2.23b).

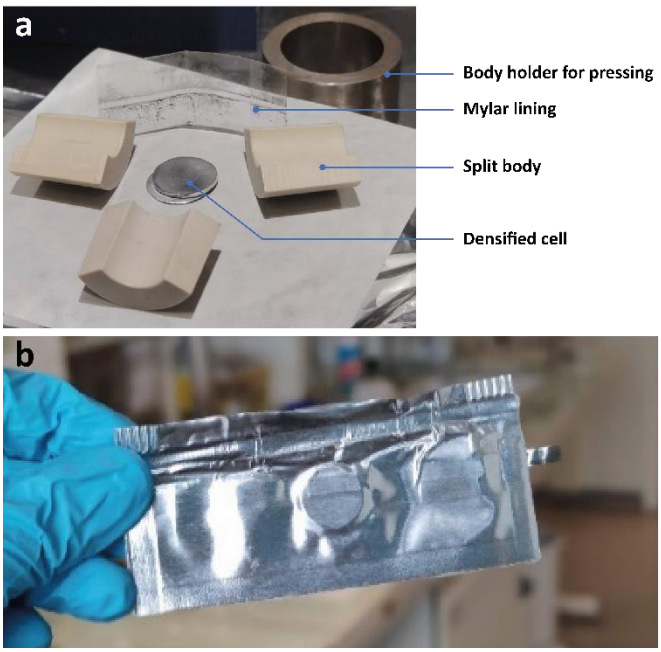

Figure 2.23. (a) Annotated picture of the split cell used for assembly and (b) pouch cell with electric tabs.

Subsequent to the fabrication process, we conducted galvanostatic cycling, and the pouch cell results are illustrated in Figure 2.24a. Note that cycling under atmospheric pressure, equivalent to 0.1 MPa, yielded mediocre results with capacities of only 52 and 33 mAh/g on first charge and discharge respectively, with a rapid decay over cycling. We attributed these poor performances primarily to contact issues with the current collectors

employed in our setup. As an attempt to mitigate this limitation, we also have used different cell configurations, namely a large (2 cm) Swagelock-type cell and a 2032 coin cell. The results, shown in Figure 2.24b and c, respectively, exhibit improved performance, presumably attributed to the better contacts with the current collectors facilitated by the use of higher pressure in these configurations. However, in the coin cell test, some instabilities were observed on the galvanostatic profile, due to pellet damage caused by the crimping pressure applied in the coin cell assembly process.

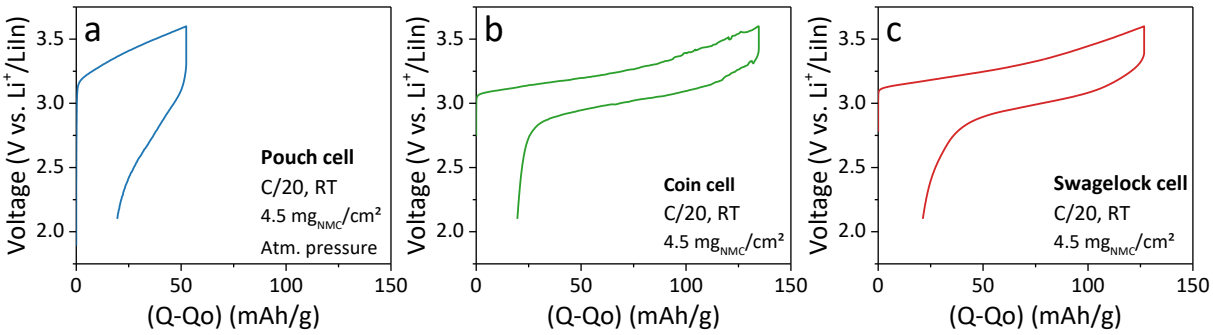

Figure 2.24. (a-c) Galvanostatic cycling and (d-f) capacity retention of a LIC-based composite in 13 mm large cells cycled (left to right) in either a pouch cell under 1 bar, a coin cell or a larger Swagelock-type cell with a small spring inside.

To enhance performance, possible directions include the utilisation of a taped cathode and anode film or the adoption of an isostatic pressing process, among other strategies. In summary, while these results are promising, they underscore the need for further optimisation of the assembly procedure for such cell types.

2.5 – Attempting stable cycling of "full-halide" ASSB

In this chapter, we have seen two halide-type SEs being used in cathode composites. However, in the first case, Li_3InCl_6 (LIC), although demonstrating high oxidation stability, showed poor reduction stability thus necessitating the addition of an LPSCl protective layer with the counter electrode. This layer revealed highly detrimental to the cell stability due to the chemical reactivity of LPSCl and LIC. Secondly, employing a different halide, the LYBC SE, we obtained similar performance in low pressure however, in this case, although being stable with LiIn, its poor oxidation stability led to a decay over cycling due to the reactivity in the cathode. Therefore, we now attempted to solve this issue through different strategies.

○ First strategy: coated NMC particles

The first strategy consists in using a different NMC622 that incorporate nanometric coatings. Materials and detailed protocol for the preparation of these composite can be found in Appendix Section A2.1. These coatings have been demonstrated to be highly efficient in preventing the decay in LPSCl-based cells and may be favourable in mitigating the degradation observed in LYBC-based composites. We chose two different coatings: a zirconium and a cobalt-based coating. Results, illustrated in Figure 2.25, clearly show an improvement in the first cycle reversibility from 82.1% to 86.6% and 87.1% for the Zr and Co-coated materials, respectively. However, the decay over cycling is still present and is not resolved by the use of coatings NMC.

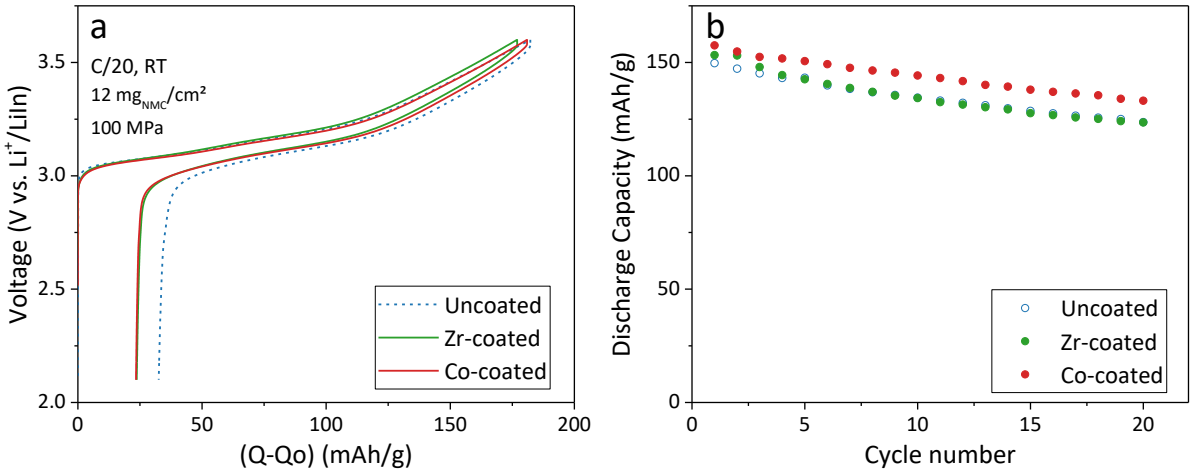

Figure 2.25. Galvanostatic performances of coated NMC in LYBC-based composites. (a) First galvanostatic profile and (b) capacity retention of the Zr-based (in green) and Co-based (in red) coatings compared to the uncoated NMC (in blue) in NMC622:LYBC:VGCF (66.5:28.5:5 wt.%) composites.

○ Second strategy: LIC and LYBC dual-SE architecture

With LYBC showing poor oxidation stability but compatibility with LiIn counter electrodes and LIC demonstrating a high oxidation stability limit but instability at LiIn potential, our second strategy involves creating a dual-SE cell architecture with LIC incorporated into the cathode and LYBC employed in the anode, hence keeping the best of both worlds. An NMC:LIC:VGCF//LIC//LYBC//LYBC:LiIn cell stack was therefore assembled and cycled. As illustrated in Figure 2.26, incorporating such design allowed us to decrease the decay from 17.3% to 10% of decay after 20 cycles at C/20. In addition, employing the same configuration, we prepared and tested a composite consisting of Zr-coated NMC622 with LIC.

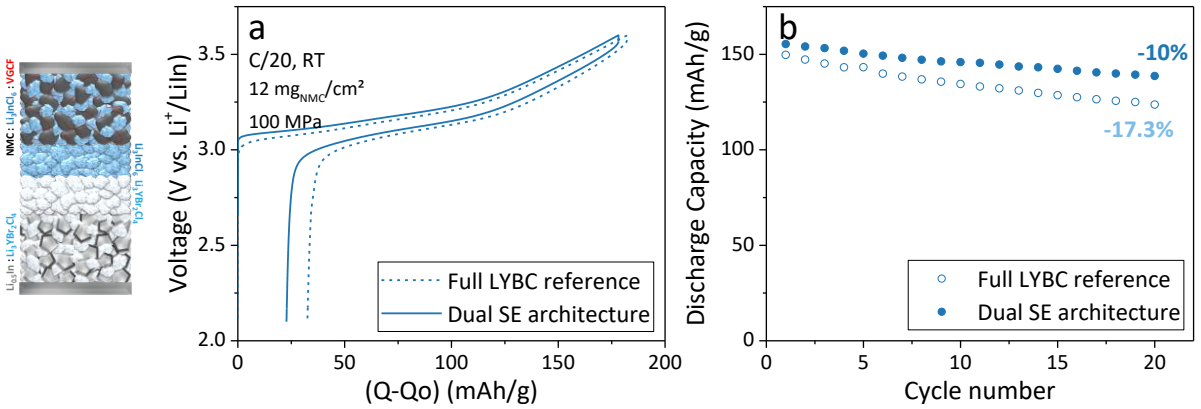

Figure 2.26. (a) Illustration of this dual-SE architecture with LIC and LYBC SEs, (b) first galvanostatic cycle and (c) capacity retention comparison of this system (dotted line) with the previous LYBC cells (solid line), both comprising an uncoated NMC622. Cells were cycled at C/20, at RT under 100 MPa of pressure.

The NMC@Zr:LIC:VGCF composite was prepared through manual hand grinding in an agate mortar with the same ratios as before. Subsequent testing of this composite yielded even better performance at high pressure (100 MPa), as shown in Figure 2.27, achieving a first cycle discharge capacity of 156 mAh/g with an ICE of 90%. The capacity retention was also significantly enhanced, with a notably reduced decay rate, resulting in an 85% retention of the initial discharge capacity after 50 cycles at C/20.

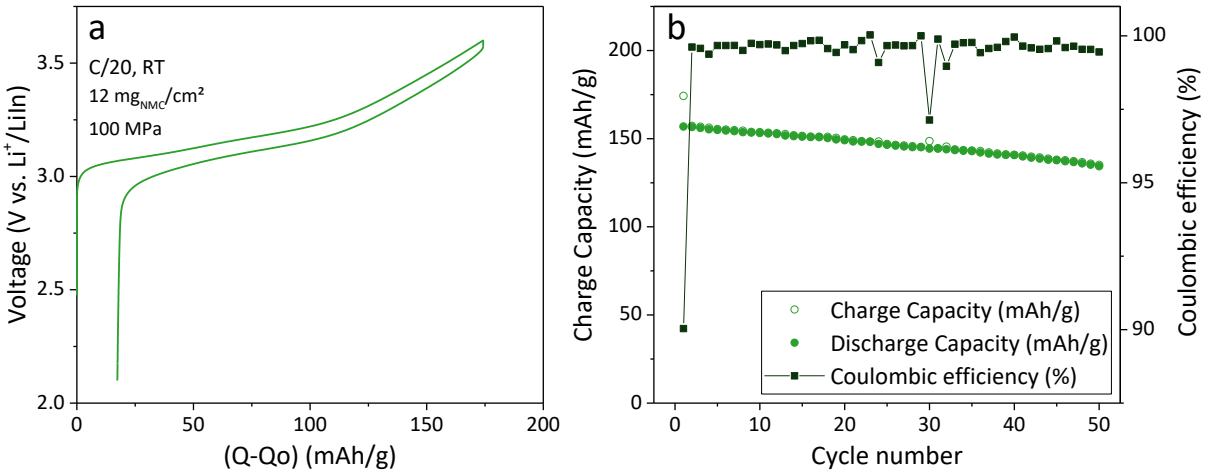

Figure 2.27. (a) First galvanostatic cycle and (b) capacity retention of a Zr-coated NMC622 cycled in the LIC/LYBC dual-SE cell architecture. Tests were performed at C/20, at RT under 100 MPa of pressure.

The improved performance in this configuration at high pressure is promising and subsequent low-pressure tests should be carried out.

2.6 – Chapter conclusion

In conclusion, Chapter 2 has presented a strategy aiming at alleviating the pressure limitation observed in the development of ASSBs. The chapter started by establishing a

baseline reference for high and low pressure cycling, employing an argyrodite-based NMC composite that is typically used in the field. This reference not only highlights the challenges associated with low-pressure cycling but also strengthens the greater significance of composite formulation under low-pressure conditions in achieving high battery performance.

Subsequently, we show that we could partially overcome these limitations by switching to halides-based electrolytes that show more favourable electrochemical and mechanical properties. By investigating the performances of the Li_3InCl_6 (LIC) SE in cathode composites, we demonstrated its ability to enable low pressure cycling down to 0.1 MPa. However, this advantage is negated by its chemical and electrochemical incompatibilities with LPSCl and LiIn, respectively, hence calling for the use of another member of the halide SE family having greater stability.

Along that line we selected a mixed halide $Li_3YBr_2Cl_4$ (LYBC) phase, known for its enhanced reduction stability and low hardness, and demonstrated its similar ability for low-pressure cycling down to 0.1 MPa and high loading of up to 25 mg_{NMC}/cm^2. Moreover, we rationalise such findings based on materials hardness considerations as well as different chemistry of the compounds, in relying on Y cation and Br anion. Altogether, this revealed that further exploring the design space of halides stands as an interesting strategy.

Finally, we demonstrated that stable cycling in "full-halide" ASSBs can be achieved by introducing the dual-SE architecture concept, not by pairing argyrodite and halide SEs, but by pairing two different type of halides, LIC in the cathode and LYBC in the anode. Such a cell was shown to deliver a capacity of 156 mAh/g with a notably improved retention compared to the LYBC system.

In summary, Chapter 2 has opened up a promising route to low-pressure cycling of ASSBs using a LiIn alloy as the anode. This achievement provided the impetus to continue our journey towards the realisation of a complete solid-state battery operating at low pressure in the presence of a Li metal anode.

Chapter 3 – **Solid-Electrolyte-Free Cathode Concept for Low-Pressure Cycling of All-Solid-State Batteries**[1]

[1]This chapter includes the following publication: Hennequart, B. *et al*. Solid-Electrolyte-Free O3-LixTiS2 Cathode for High-Energy-Density All-Solid-State Lithium-Metal Batteries. *ACS Appl. Energy Mater*. **6**, 8521–8531 (2023).

3.1 – Chapter Introduction

Reducing the stack pressure in all-solid-state batteries (ASSBs), as discussed in the preceding chapter, represents a significant challenge in the development, commercialisation, and widespread adoption of this battery technology. Previously, we introduced a method to address this challenge, which is centred on the optimisation of electrode components to enable effective low-pressure cycling. However, the sole fact that the typical high performance cathode active materials (CAMs), such as $LiCoO_2$ or $LiNi_xMn_yCo_{1-x-y}O_2$ (NMC) have inherently limited electronic and ionic conductivities leads to the necessity of implementing them within composite systems. Within these composite structures, the large amount of interfaces created can increase the impact of chemical and electrochemical instabilities between the different components. This issue is particularly pronounced in the case of sulphide-based solid electrolytes (SEs), which are known for their poor stability and their susceptibility to oxidation and decomposition at potentials exceeding 3 V vs. Li^+/Li.[43,67,73,129–132] Moreover, another significant challenge stems from the intrinsic volume changes experienced by the CAM particles during cycling, which we have seen can lead to poor performance in low pressure conditions in the case of an unoptimised composite.[92,133]

In light of all these challenges, advantages of a SE-free electrode design could be exploited. Composite electrodes (Figure 3.1a) mimic the wetting of a liquid electrolyte in conventional lithium-ion batteries by providing ionic percolation in the cathode, whereas a SE-free electrode (Figure 3.1b), predominantly composed of active material, relies solely on interparticle ionic diffusion through the CAM particles. This approach effectively eliminates most of SE/CAM interfacial challenges by containing them at the planar interface between the cathode and SE separator and simultaneously contributes to enhancing the energy density.

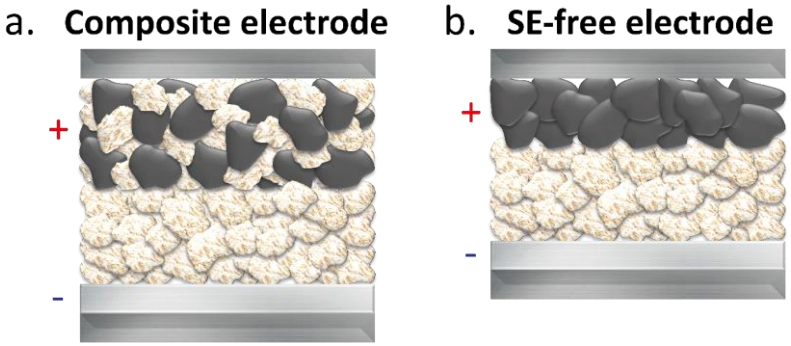

Figure 3.1. Illustration of (a) a composite cathode and (b) a SE-free cathode design in an ASSB.

However, the choice of a suitable active material for a SE-free electrode necessitates the fulfilment of several prerequisites. The materiel must possess adequate ionic and electronic conductivities, exhibit chemical stability regarding the SE, and be mechanically ductile enough to allow densification through a simple cold-pressing process. Typical lamellar transition metal oxides materials, such as NMC, being oxides, tend to exhibit high hardness and are therefore unsuitable for such design implementation. However, sulphide materials, in contrast, are known for their greater ductility. Among them, the lamellar phase of TiS_2 meets all the specified requirements; it is a rapid ionic conductor[134], a semimetallic[135] and exhibits higher ductility and better stability with sulphide-based SEs than conventional oxide CAMs.

In this chapter, we first introduced the performance of the O1-TiS_2 in this SE-free electrode design, and thus confirm the performance reported in an earlier report[118] on this material. Further exploiting this concept, we identified another titanium sulphide, the O3-Li_xTiS_2[136–138] phase that met the above specifications. Through a milling process, this phase enabled us to achieve a high energy density comparable to NMC cathodes while facilitating low-pressure cycling. Additionally, we broaden our scope by extending this concept to a diverse range of CAMs. We embark on two distinct pathways, that have consisted in exploring i) other Ti-based sulphide polymorphs as well as ii) halide-based materials, taking advantage of their low ductility for achieving low pressure operation.

3.2 – The O1-TiS_2 case: a literature benchmark

Initially, we focused on the O1-TiS_2 phase. This phase was shown, by Kim *et al.*[120,119,139,118], to display remarkable performance within a SE-free or "diffusion-dependent" electrode configuration. Notably, it delivered most of its theoretical capacity at a high electrode loading of 45.6 mg/cm², while operating at 60°C. This remarkable performance was achieved through a straightforward milling process of the pristine material. It was hypothesized by the authors that this milling process, by reducing particle size and altering morphology, could effectively reduce the tortuosity within the electrode and therefore enable successful cycling within the SE-free electrode design.

O1-TiS_2 was obtained commercially from Sigma and is referred to as pristine TiS_2 hereafter. In order to reproduce the reported protocol, the pristine material was subsequently milled for 90 minutes in a high-energy milling device. Figure 3.2 summarizes the

morphological, structural and electrochemical performance of the material before and after grinding. As revealed in the SEM images displayed in Figure 3.2a and b, this process effectively reduced the particle size from tens of microns to less than 1 µm and changed the morphology from platelets to a shapeless particle structure. Moreover, the X-ray diffraction (XRD) analysis, as shown in Figure 3.2c, reveals a reduction in crystallinity and an increase in the stresses within the particles as evidenced by the disappearance of certain reflections and the broadening of others. In terms of electrochemical performance, both pristine and ball-milled materials were subjected to testing within the SE-free electrode design (Figure 3.2d). Although not reaching its theoretical capacity of 239 mAh/g, the ball-milled TiS_2 exhibited enhanced reversibility, recovering 0.76 lithium (183 mAh/g), compared to the pristine material which returned only 0.05 Li (11 mAh/g) on the first charge, hence confirming the earlier report.[118]

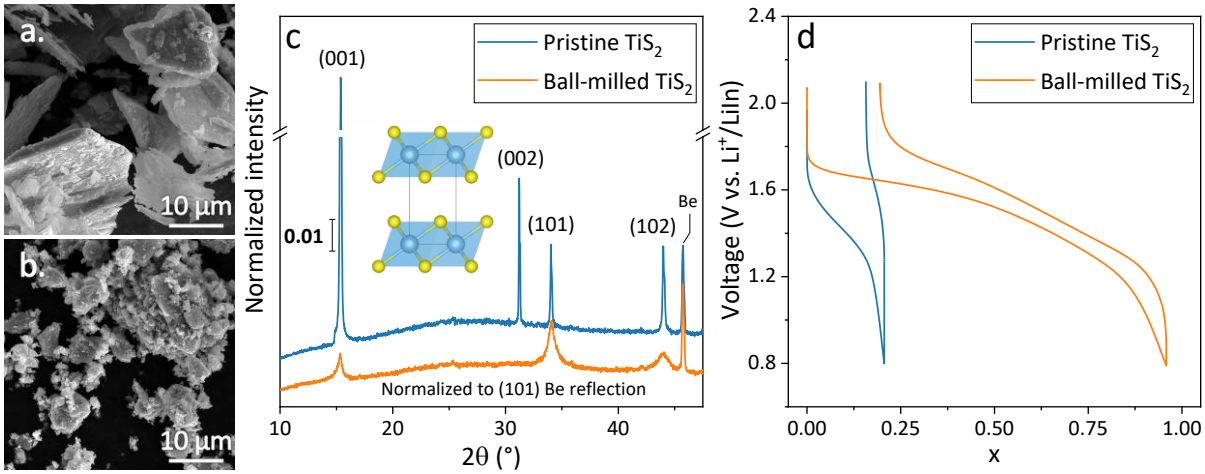

Figure 3.2. Characteristics of the pristine and milled O1-TiS_2. (a) SEM micrographs, (b) X-ray diffractograms with crystallographic structure and (c) first galvanostatic cycle at C/30 in a SE-free cathode of the pristine and ball-milled O1-TiS_2, respectively in blue and orange.

Through galvanostatic intermittent titration technique (GITT, Figure 3.3), we determined a significantly higher apparent Li^+ diffusion coefficient in the milled TiS_2 sample compared to the pristine material. This finding provides additional support for the proposed "diffusion-dependent" electrode model where a decrease in tortuosity of the electrode enables the SE-free electrode to cycle in a solid-state cell.

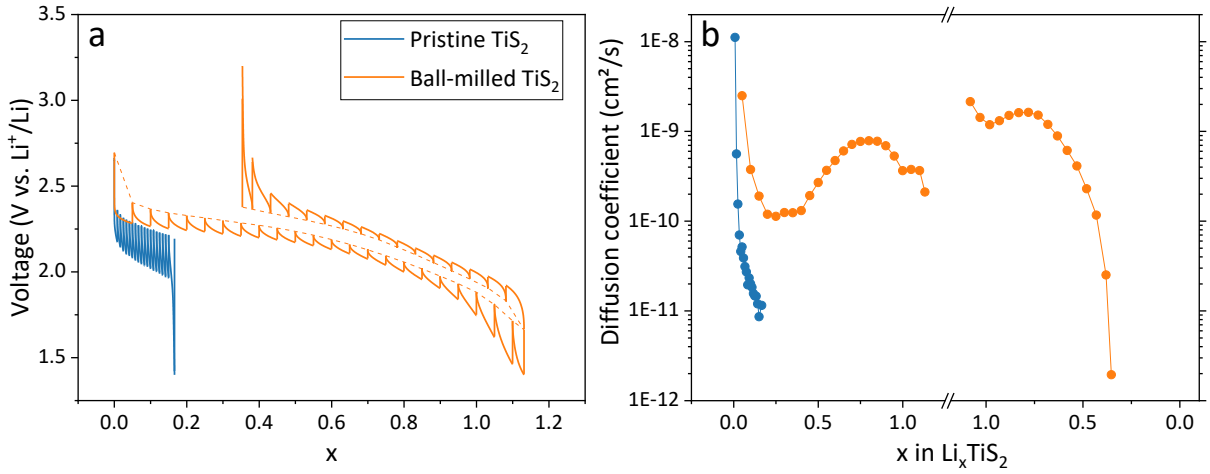

Figure 3.3. (a) Voltage profiles and (b) apparent diffusion coefficient of both pristine and ball-milled O1-TiS_2 calculated from the GITT measurement at different state-of-charge (SOC) in a SE-free cathode system.

The validation of Kim *et al.* work has motivated us to expand the range of materials suitable for such configurations.

3.3 – O3-Li_xTiS_2: A Pre-lithiated lamellar phase enabling low pressure cycling

We conducted further exploration of members of the Ti-based sulphide chemistry, focusing primarily on the metastable O3-Li_xTiS_2. This phase was synthesized from a high temperature (800°C) solid-state synthesis by reacting stoichiometric amounts of thoroughly mixed Ti and Li_2S powders in evacuated quartz tubes. This phase exhibits a comparable lamellar structure to the previously studied O1-TiS_2, as illustrated in Figure 3.4.

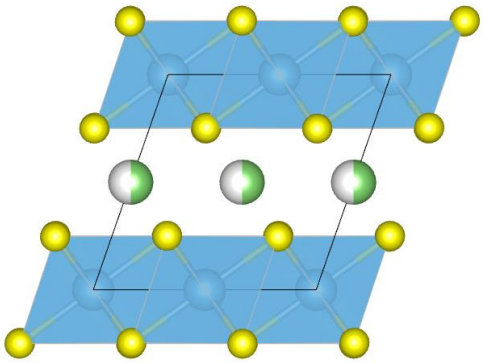

Figure 3.4. Crystallographic structure of the O3-Li_xTiS_2 phase.

○ Characteristics and performances in typical composite cathodes

The formation of the O3-Li_xTiS_2 phase, hereafter referred as LTS, was confirmed through XRD, as shown in Figure 3.5a and, similar to the O1 phase, the resulting powder

consists of large platelets measuring 30 to 50 µm as presented in Figure 3.5b. Its electrochemical signature is somewhat similar to the findings reported by Colbow *et al.*[138] in that it exhibits a step voltage change that can be attributed to an O3 to O1 structural phase transition. Through an operando XRD measurement (Appendix Figure A3.2 and insets in Figure 3.5c), we also confirmed the irreversible disappearance below x=0.5 in the first charge of the (104) reflection of the O3 phase at 36° to the benefit of the (101) reflection of the O1 phase at around 34°.

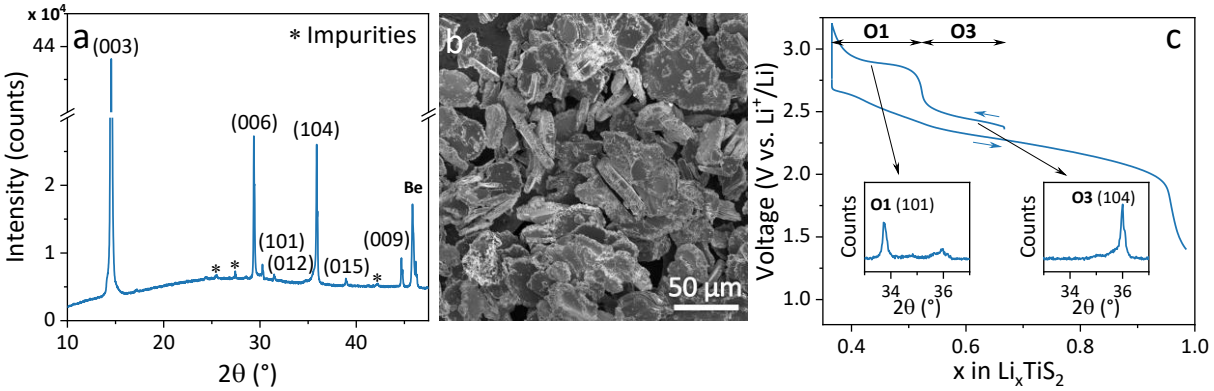

Figure 3.5. Characteristics of the O3-Li_xTiS_2 phase. (a) XRD pattern, (b) SEM image showing the plate shape of the pristine O3-Li_xTiS_2, (c) first galvanostatic cycle in a liquid system and inset of operando XRD measurements showing the structural phase transition

This material also displays a high electronic conductivity of 13.28 S/cm determined through chronopotentiometry (Figure A3.3a). This high electronic conductivity eliminates the need to add an electronic conductive additive in the cathode for the subsequent electrochemical tests. Recognising that structural changes in materials can generally have a negative impact on cell performance, we conducted our initial electrochemical tests by limiting the upper cut-off voltage to 2.6 V vs. Li^+/Li. The material was tested both in liquid cell, with LP30 electrolyte and a Li metal anode, and in solid-state cells with a LPSCl-based cathode composite, a LPSCl separator and a lithium-indium (LiIn) alloy composite anode. The composite preparation and assembly procedure are detailed in the Appendix Section A3.1. The initial discharge results, shown in Figure 3.6, revealed similar reversible capacities for both cells, reaching 134 mAh/g and 142 mAh/g, for the liquid and solid-state cells respectively. However, the latter exhibited a faster capacity decay, reaching 80% of its initial capacity after 20 cycles, while the other cell maintained a nearly constant reversible capacity with only a 5% decay observed during the first two cycles. Moreover, taking into account the composite nature of the solid-state cell cathode, the capacity in relation to the total electrode mass,

represented by the red dots in part d of Figure 3.6, is greatly reduced due to the electrochemically inactive weight associated with the 30 wt.% of SE in the composite. To mitigate this decrease in specific capacity, we naturally opted to leverage the SE-free electrode concept.

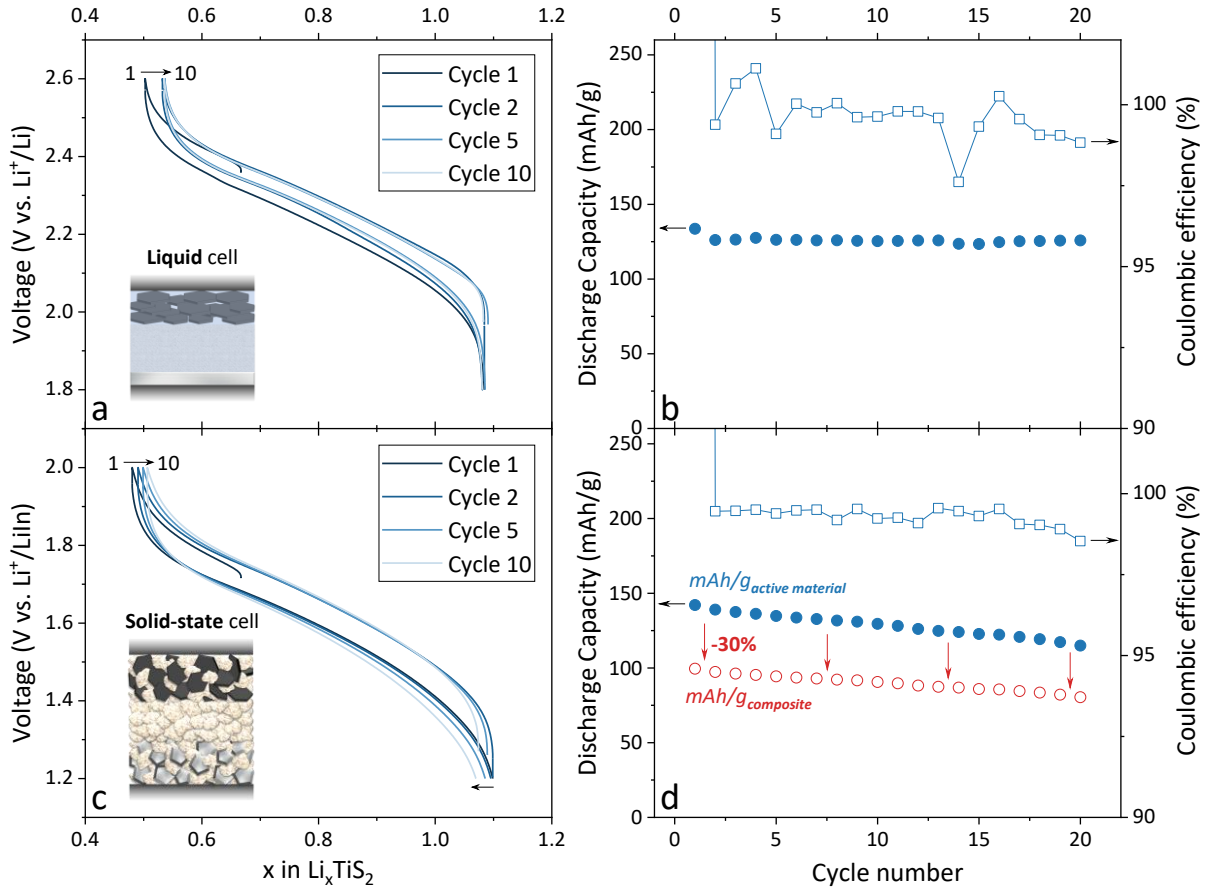

Figure 3.6. Cycling performance in liquid and composite ASSB. (a-c) Galvanostatic cycling and (b-d) capacity retention and coulombic efficiency of the pristine O3-Li_xTiS_2 in liquid (top) and solid-state (bottom) cells with 30 wt.% LPSCl SE in the cathode. Red dots in (d) correspond to the capacity normalized to the total electrode composite mass.

○ Enabling SE-free cycling of O3-Li_xTiS_2 through a milling strategy

Utilising the SE-free electrode design requires sufficient ionic diffusion throughout the entire LTS electrode. In this regard, we investigated the performance of the material within composites with decreasing amounts of SE, ranging from 30 to 0 wt.%. The results presented in Figure 3.7 clearly indicate that reducing the SE content to 15 wt.%, while maintaining a similar first cycle discharge capacity of 145 mAh/g, results in an increased polarization and reduced retention. In addition, completely removing the SE and cycling with this pristine LTS in a SE-free electrode configuration leads to a poor reversible capacity of only 37 mAh/g and high polarization even at this very low rate of C/60 (Figure 3.7d). This demonstrates the limited

apparent diffusion of Li^+ ions, similar to what was observed with O1-TiS_2. Consequently, we then applied the same milling approach to enhance the performance in this SE-free electrode.

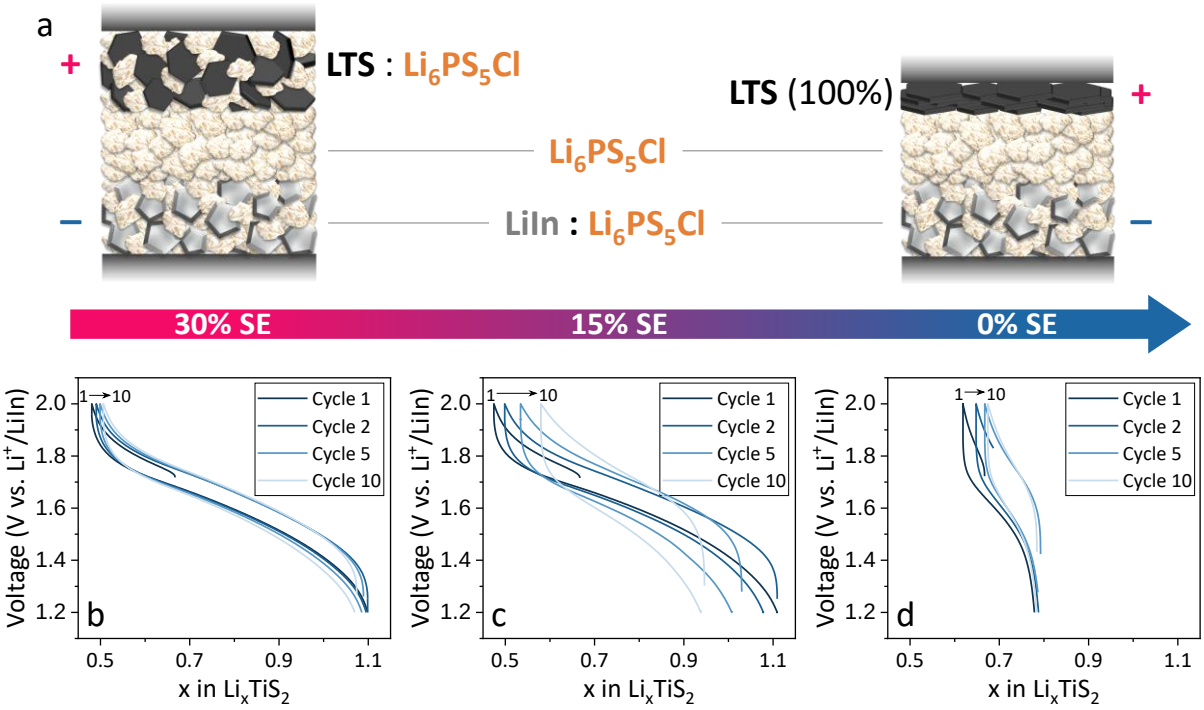

Figure 3.7. (a) Illustration of the composite and SE-free electrode design with pristine LTS active material. (b-d) Galvanostatic performance in ASSB cells of the pristine LTS in electrodes incorporating 30, 15 and 0 wt.% of SE, respectively. Cycling was performed at RT under a pressure of 100 MPa and a C/60 rate.

In order to assess the evolution of the properties and performance as a function of the milling time, four samples were subjected to grinding under the same conditions for 10, 20, 60, and 90 minutes, and are hereafter referred to as BM10, BM20, BM60 and BM90-LTS, respectively. SEM micrographs, presented in Figure 3.8a and b, show a significant change in particle size and morphology with increasing grinding time, transitioning from a plate shape of about 50 µm to shapeless sub-micrometric particle. XRD patterns obtained from the four samples (Figure 3.8c) show an increase in their amorphous character due to milling. This is evident from the gradual decrease in amplitude and increase in broadening of the (003) reflection, along with the complete disappearance of both the (006) and (009) peaks after only 10 minutes of grinding. The reduction in particle size and the increase in strain typically contribute to peak broadening.[140] Due to the featureless nature of the XRD powders patterns for our ground material, we could not estimate by the Williamson-Hall analysis the compression-extension strains in the material. Therefore, considering that only the crystallite

size is involved, we can approximate a reduction in size from several hundreds of nanometres in the pristine sample to 15 nm in the BM90-LTS sample using the Sherrer formula.

In addition, we observe a slight decrease in electronic conductivity from 13.28 to 4.67 S/cm upon milling (Appendix Figure A3.3). This value remains significantly higher than the ionic conduction values of Li^+ ions in the LTS material or the SE itself, which typically reaches up to $6 \cdot 10^{-3}$ S/cm in Li_6PS_5Cl. Based on these findings, we can conclude that electronic conductivity is not a rate-limiting factor in our materials and that the use of carbon additives remains unnecessary even after milling.

Solid-state batteries were then assembled with the different milled materials within a SE-free cathode configuration, and the cells were cycled over the voltage window 1.8 to 2.6 V vs. Li^+/Li at a low current rate of C/60. The voltage-composition curves obtained are shown in Figure 3.8d. Interestingly, the discharge capacity increases progressively from 37 mAh/g for the pristine LTS to 123, 141, 157, and ultimately 163 mAh/g for the BM10, BM20, BM60, and BM90-LTS samples, respectively. In addition, as grinding time increased, we observed lower polarization, leading to higher energy efficiency.

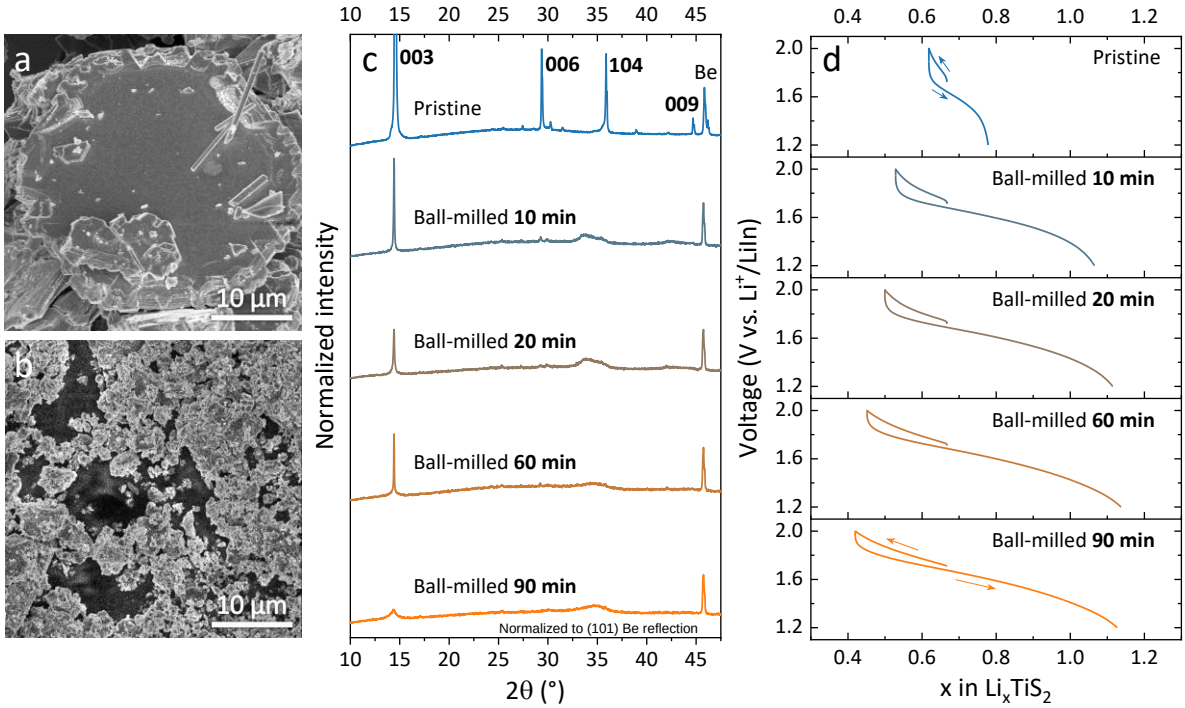

Figure 3.8. Micrographs of (a) the pristine and (b) the BM90-LTS, (c) XRD patterns and (d) first galvanostatic cycle evolution with milling time of the O3-Li_xTiS_2 as a SE-free electrode in solid-state cells at C/60.

For comparison, we tested the same samples in a liquid system (Figure 3.9). They exhibit similar discharge capacities regardless of the milling time, indicating that grinding the material does not introduce new Li^+ sites that would otherwise increase the total capacity of the material. Moreover, this very different behaviour compared to solid-state cells further confirms the positive effect and the necessity of the milling process in achieving the full capacity when using SE-free electrodes based on such layered compounds.

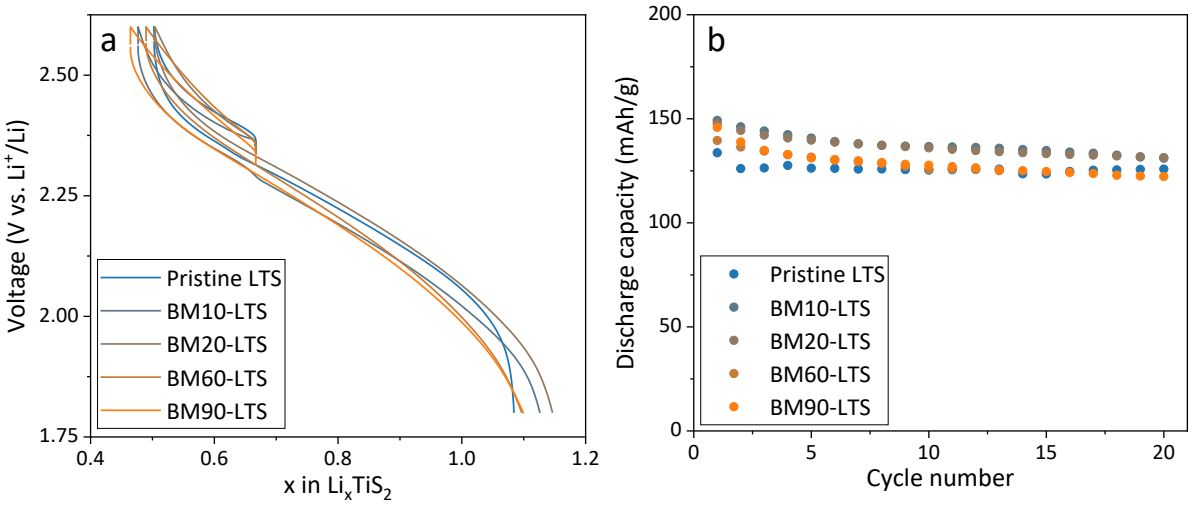

Figure 3.9. Performance of the pristine and milled samples in liquid-based cell. (a) First galvanostatic cycle and (b) capacity retention for different milling time with lithium metal anodes and a C/20 rate in the limited electrochemical window 1.8 to 2.7 V vs. Li^+/Li.

Thus far, we have demonstrated the potential of the SE-free cathode configuration. However, we have limited the potential window to a safe range in order to avoid triggering the O3-O1 structural change above 2.6 V vs. Li^+/Li, which consequently limited the achievable capacity. Therefore, we then expanded the cycling potential window from 1.8-2.6 to 1.4-3.2 V vs. Li^+/Li. The results, illustrated in Figure 3.10, demonstrate a notable enhancement in capacity. Notably, the BM90-LTS can now deliver up to 226 mAh/g in a composite and 175 mAh/g in a SE-free positive electrode when operated at C/20. Interestingly, in contrast to the pristine sample presented in Figure 3.5c, neither of the two systems exhibit the plateau at higher potential associated with the structural change. This phenomenon can be attributed to the increased amorphous nature of the sample induced by ball milling, as elucidated by the cycling behaviour difference of a composite consisting of Pristine LTS:LPSCl (70:30) (Appendix Figure A3.4), which clearly manifests the presence of the aforementioned second plateau. This observation aligns with earlier findings in the literature[141,142], which have consistently reported the broadening or complete disappearance of such salient features in the voltage-

composition curves following a milling process. Moreover, comparison of the galvanostatic curve between the composite and SE-free cell (Figure 3.10a and c), reveals a significant distinction in the high-potential response. Specifically, the composite electrode exhibits the ability to remove 0.4 Li during the initial charge, in contrast to the SE-free electrode, which only removes 0.2 Li.

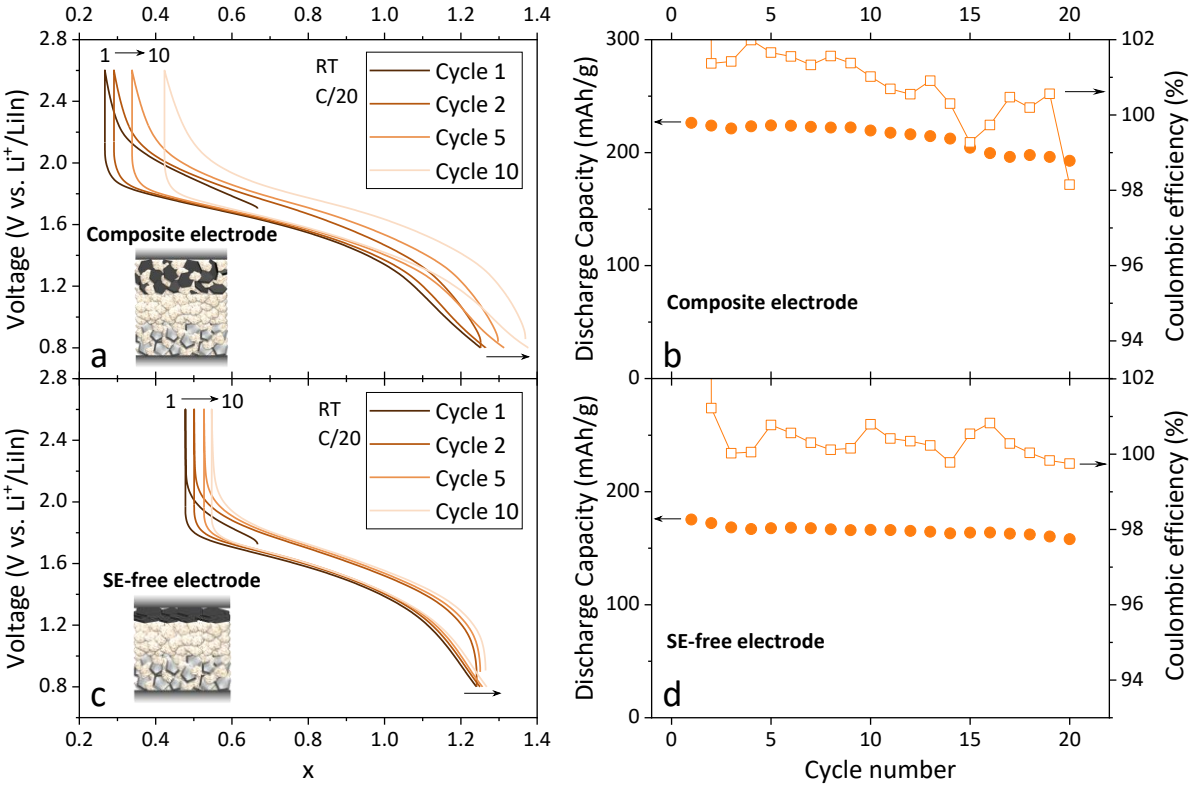

Figure 3.10. (a-c) Galvanostatic cycling and (b-d) capacity retention in the enlarged window of 1.4 to 3.2 V vs. Li^+/Li of BM90-LTS in (top) a composite electrode with 30% SE and (bottom) a SE-free electrode.

In addition, despite demonstrating higher capacities, the composite system (Figure 3.10a) exhibits a more pronounced voltage slip, which can be linked to the previously reported[67] increasing parasitic activity of the LPSCl SE at these potentials. Such effect is further exacerbated in this context due to the increased contact area between the SE and the CAM in comparison to the SE-free system. To test this hypothesis, we conducted experiments by combining the LTS with another SE in both the composite and the separator. In particular, we selected the halide-type $Li_3YBr_2Cl_4$ (LYBC) SE, of which we have demonstrated in Chapter 2 Section 2.4 an electrochemical stability between 3 V and 0.8 V vs. Li^+/LiIn. Notably, as shown in the differential capacity curves in Figure 3.11, using such halide SE lead to no additional capacity at low potential (inset in Figure 3.11b).

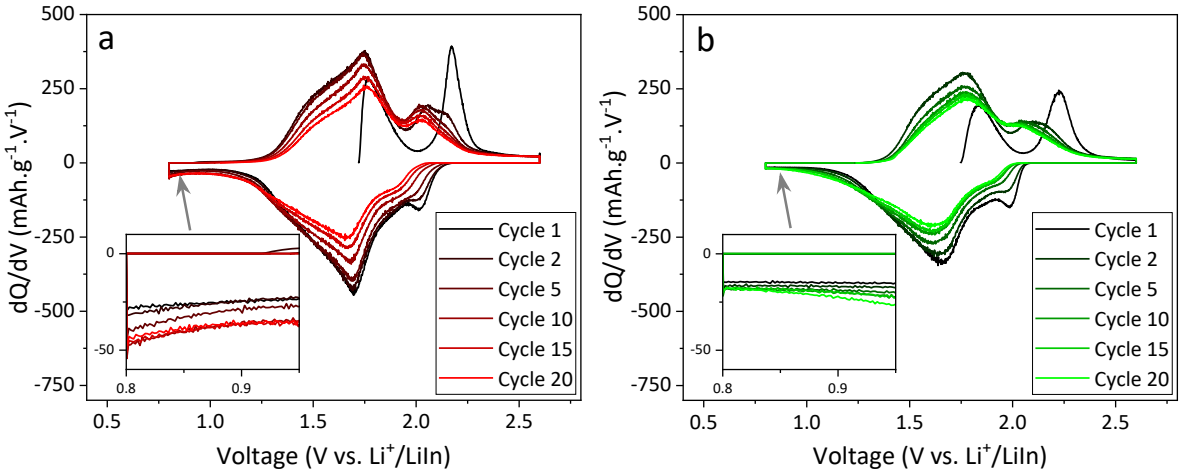

Figure 3.11. Differential capacity plots of a LTS:SE (70:30) composite either with (a) SE=LPSCl or (b) SE=LYBC solid electrolyte. Showing the parasitic reactivity of the argyrodite SE at low potential (in inset a) that its absence in the case of the halide SE (inset b).

Altogether, we have demonstrated that the milling of the pristine material allows us to access a considerably larger capacity in a SE-free electrode. However, we have seen a discrepancy in the electrochemical response at high potential between the SE-free and composite systems that may be attributed to a decrease in the apparent Li^+ diffusion coefficient.

○ Improved performance through lithium ion diffusion coefficient enhancement

To investigate this ionic diffusion hypothesis, we conducted Galvanostatic Intermittent Titration Technique (GITT) measurements on both the Pristine and BM90-LTS samples. The GITT results for the BM90-LTS (shown in orange in Figure 3.12b) reveal that, at high lithium content, the apparent diffusion coefficient averages approximately 10^{-9} cm²/s. However, a substantial decrease occurs, plummeting to 10^{-11} cm²/s when the lithium content drops below x=0.6 during the charging process. Thus somewhat supporting our previous hypothesis and explaining the lower reversible capacity observed for the SE-free cathode.

The evolution of the rate capability with increasing ball-milling time was further examined using the "signature curve" method.[143] A detailed procedure is available in the Appendix Section A3.1. A representative discharge "signature curve" is presented in Figure 3.12c and the cumulative capacity values at various discharge currents are plotted in Figure 3.12b. The extension of ball-milling time resulted in an enhancement in performance from ultimately yielding a peak discharge capacity of 200 mAh/g at a C/50 rate for the BM90-LTS sample.

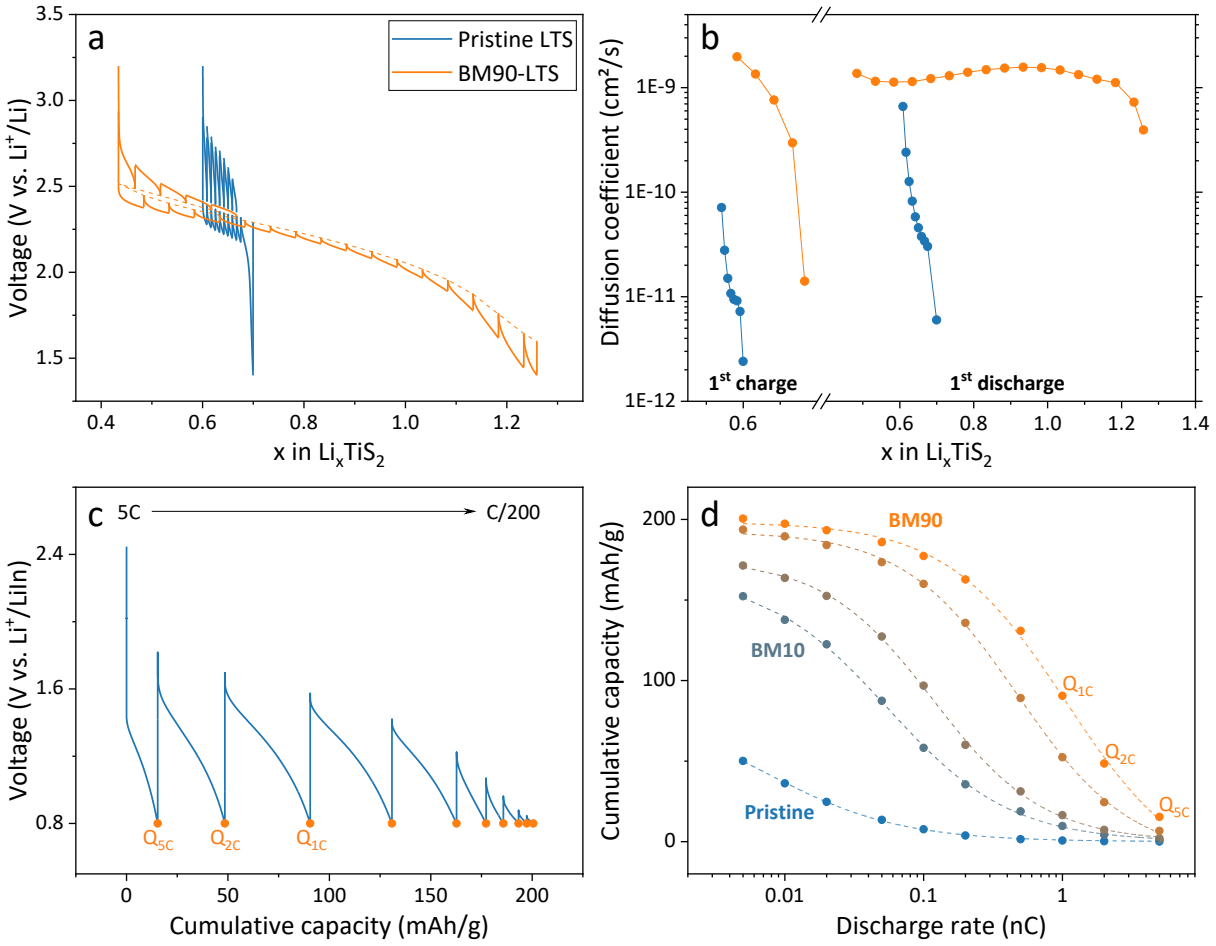

Figure 3.12. (a) Voltage profiles and (b) diffusion coefficient of both pristine and ball-milled O3-LTS calculated from the GITT measurement at different state-of-charge (SOC). (c) Typical galvanostatic response of a signature curve at rates ranging from 5C to C/200 and (d) obtained rate capabilities in a SE-free electrode.

In summary, similarly to the O1-TiS_2, the observed performance enhancement following grinding can be attributed to both the reduction in particle size and morphological changes that facilitate a more isotropic diffusion of Li^+ through the electrode thickness and lead to a lowered tortuosity, as illustrated in Figure 3.13. This interpretation is supported by the results of the GITT (Figure 3.12a and b) conducted on both Pristine and BM90-LTS.

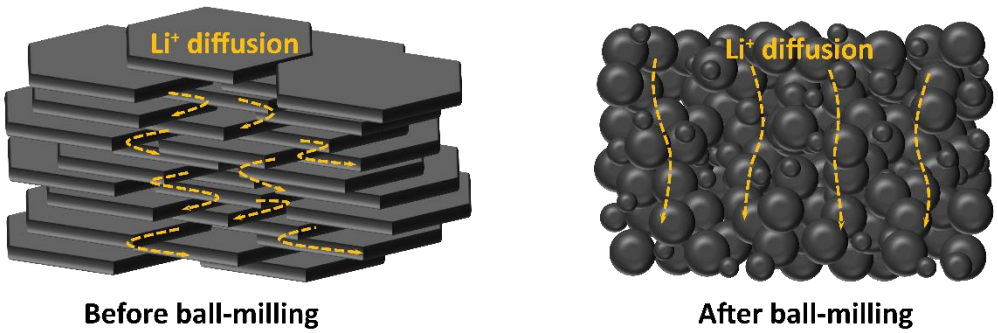

Figure 3.13. Schematic of the electrodes before and after ball-milling illustrating the decreased tortuosity.

However, it is important to note that an increase in the intrinsic diffusion coefficient of the material with extended milling time cannot be ruled out. Consequently, in an attempt to decouple the effects of apparent (*i.e.* at the electrode level) and intrinsic (*i.e.* at material level) diffusion in our system, we conducted, with the help of Michaël Deschamps in the *CEMHTI laboratory*, solid-state nuclear magnetic resonance (ss-NMR) measurements on both pristine and ball-milled LTS samples and assessed the evolution of lithium ion mobility.

^{7}Li Magic Angle Spinning NMR spectra were acquired for the pristine, BM20, BM60, and BM90-LTS samples, as shown in Figure 3.14. Detailed methods and fitting parameters are provided in Appendix Section A3.1 and Appendix Table A3.1, respectively. In the spectrum of the pristine material (Figure 3.14i), two distinct components at chemical shifts of 12 ppm (pink) and 2.1 ppm (blue) are observed, representing 49.3% and 50.7% of the total signal, respectively. Interestingly, when compared to the narrower signal (pink), the broader signal (blue) exhibits slightly more intense spinning sidebands, indicating greater anisotropy and potentially reduced mobility. This discrepancy may signify that the broader signal arises from Li^{+} ions with lower mobility, while the narrower signal is associated with more mobile ions.

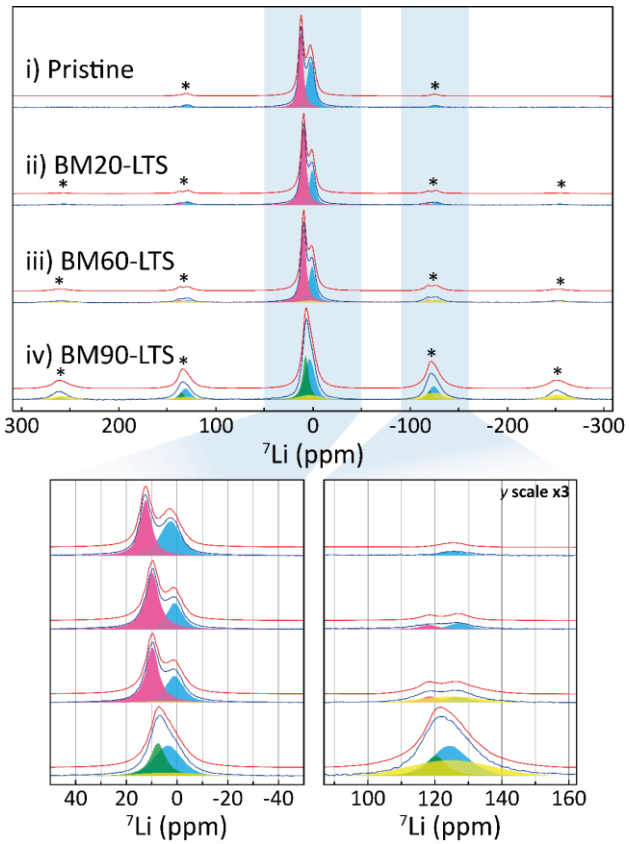

Figure 3.14. ^{7}Li MAS-NMR spectra of (i) pristine, (ii) BM20, (iii) BM60 and (iv) BM90-LTS. The experimental spectrum is shown in blue and the model in red. Spinning sidebands are highlighted by stars. Model parameters can be found in Appendix Table A3.1.

It should be recalled that similar narrow and broad NMR signals were previously reported in the study of ball-milled nanocrystalline O1-$Li_{2/3}TiS_2$ samples using static ^{7}Li NMR.[144,145] At the time, these observations were attributed to a rapid mobility of Li ions at the interface for the narrow band and to a reduced mobility within crystalline domains for the broader signal. To check the validity of this interface/crystalline ionic conduction hypothesis, we employed a straightforward cylindrical geometry model (as illustrated in Figure 3.15), which was previously utilised by Winter *et al.*[144] In this model, calculating the surface-to-bulk ratio is done using the following Equation 3.1.

$$f(d,g,h) = \frac{(d+g)^2(h+g) - d^2h}{(d+g)^2(h+g)} \text{ with } 0.5 \leq g \leq 1\ nm \qquad \text{Equation 3.1}$$

where *g* is the interface thickness, *d* the diameter and *h* the height of the particle. Considering a typical interface thickness between 0.5 and 1 nm (corresponding to 2 to 4 atomic planes), a diameter and a height of 200 nm (minimum crystallite size deduced by XRD), an interface fraction between 0.75 and 1.49% is obtained. Using the same equation, we found that an interface thickness of 25 nm, rather than the typical 0.5 to 1 nm thick interface[144], was necessary to account for the 49.3% obtained by NMR. Such interface thickness is largely improbable. Consequently, we believe that we are in presence of a two-phase system, which could differ in terms of Li stoichiometry, similar to vacancies ordering in Li_xTiS_2[146], where the broad component at 2.1 ppm (in blue) would stem from ordered lithium planes, and the narrow component at 12 ppm (in pink) from a more mobile lithium phase. The change in ^{7}Li shift between the two phases may result from a difference in local electronic density and mobility, which governs the paramagnetic, and Knight shifts.

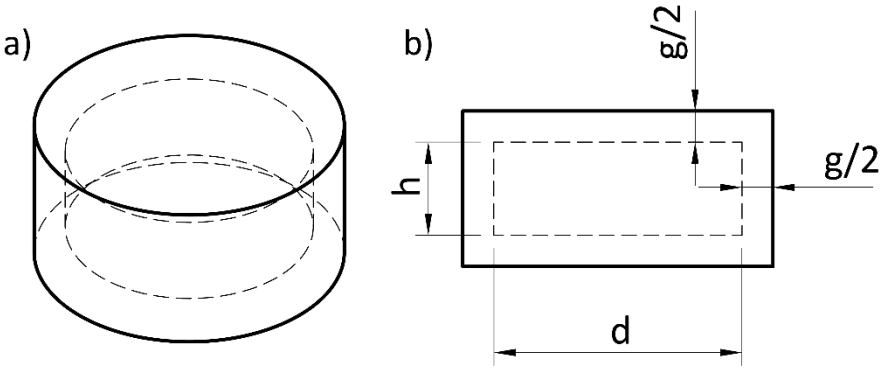

Figure 3.15. Cylindrical model for surface-to-bulk ratio calculation to determine the interface ratio *f* calculated with the Equation 3.1. Adapted from reference[144].

Returning to the ^{7}Li MAS-NMR measurements conducted as a function of the milling time (Figure 3.14), intriguingly, a significant change in the relative proportions of the two phases becomes evident following just 20 minutes of milling (as seen in Figure 3.14ii). Specifically, there is an increase in the signal associated with the mobile lithium phase (pink), which now contributes to 65% of the total signal, while the signal originating from the ordered Li phase (blue) diminishes, accounting for only the remaining 35%. This change may imply a reduction in vacancy ordering (*i.e.* increasing disorder) of the ordered blue phase component, which in turn would increase the Li-ion mobility and hint towards an improved diffusion of the ions after milling.

Concomitantly, longitudinal relaxation times were measured for the BM20 sample as a function of temperature (Figure 3.16a) to investigate nanoscale dynamics. The spin-lattice relaxation time (T_1) for the BM20-LTS sample is found to decrease from 1.5 s to 350 ms over the 25°C – 150°C range. Interestingly, increasing the temperature leads to the collapse of the broad peak, which is attributed to the phase with vacancy ordering. This phenomenon demonstrates a reversibility with temperature, akin to materials displaying a miscibility gap behaviour. Assuming that $1/T_1$ is proportional to the site-to-site jump correlation time τ_c in a simple Bloembergen, Purcell and Pound approach (BPP)[147], we could deduce an activation energy of site-to-site jumps of about 128 meV. Moreover, through a 2D EXchange SpectroscopY (EXSY) measurement with an exchange delay of 50 ms (Figure 3.16b), cross-peaks are observed hence confirming that Li^+ ions are diffusing between the two environments at RT and justifying the observed signal ratio change with increasing temperature.

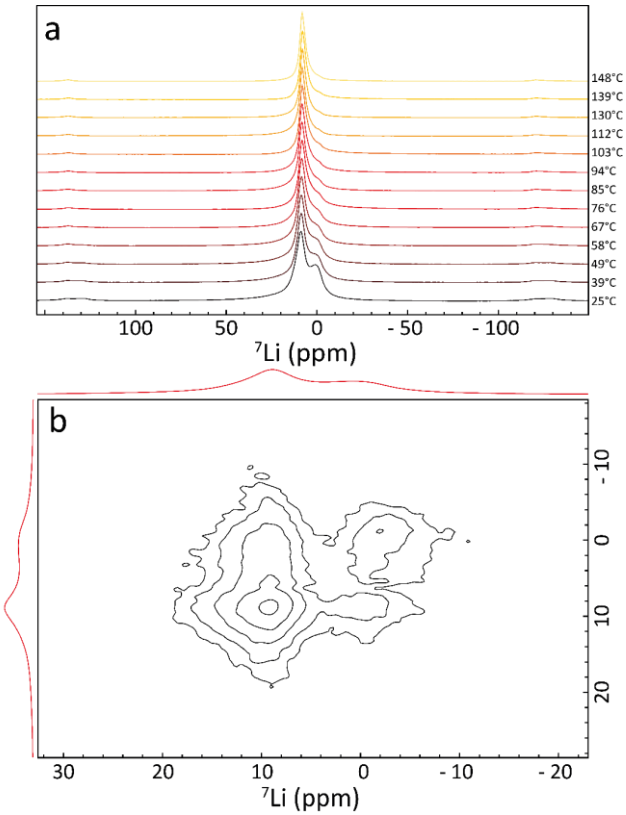

Figure 3.16. (a) ^{7}Li MAS NMR spectrum of BM20-LTS as a function of temperature. (b) 2D ^{7}Li EXSY NMR spectrum obtained for BM20-LTS with a 50 ms mixing time. The cross (off-diagonal) peaks indicate that lithium ions are able to diffuse from the ordered environment to the mobile phase in the 50 ms timescale.

Finally, in the case of samples milled for 60 and 90 minutes (Figure 3.14iii and iv, respectively), a new broad feature (represented in yellow) becomes apparent. This newly observed broad component is likely a consequence of the amorphisation of O3-Li_xTiS_2, which intensifies disorder within the material, creating asymmetric lithium environments. Its signal amplitude is estimated to account for 15.8% and 34.6% of the overall signal for the BM60 and BM90 samples, respectively. This new component leads to a change in the amplitude of the remaining mobile (pink) and ordered (blue) environment signals for BM60, which now accounts for 50.8% and 33.4% of the overall Li signal, respectively. In contrast, BM90-LTS displays a fundamental transformation, as the mobile lithium environment (pink) appears to disappear in favour of a new broader signal (green) shifted to 7 ppm. This green signal accounts for 24.7% of the lithium ions, while the main component (blue), now centred at 2.9 ppm, represents 40.7% of the total signal.

Additionally, the site-to-site jump activation energy for BM90 was retrieved from ^{7}Li longitudinal relaxation times measurements. These relaxation times were shown to decrease from 353 ms to 186 ms as the temperature increased from 23°C to 151°C. From that, the

activation energy was determined to be 51 meV, which is notably lower than the value measured for BM20-LTS (128 meV) and slightly lower than the one reported for amorphous $Li_{2/3}TiS_2$ (70 meV) in a prior study.[145] The decrease in the T_1 value already implies a substantial reduction in the jump time by a factor of 5 between the BM20 and BM90 samples, assuming the same quadrupolar coupling constant. This suggests that a significant portion of the BM90 sample has become amorphous, thus favouring 3D diffusion as well as leading to a lower activation energy for site-to-site jumps (*e.g.* lowering of diffusion barriers) due to both the disappearance of vacancy ordering and crystallite boundaries modifications.

Altogether, our findings support the hypothesis that the amorphisation process coupled with particle size reduction and morphology modification induced by ball milling plays a pivotal role in facilitating isotropic diffusion at the electrode level. This is particularly crucial for layered compounds when used in a SE-free system, where otherwise, a predominant 2D Li^+ diffusion pattern is observed. To test this hypothesis we will investigate, in a later Section 3.4, the potential of employing other materials, such as the cubic spinel Ti_2S_4 that offers a 3D ionic diffusion in a SE-free cathode configuration.

○ The low pressure performance of the SE-free electrode configuration

At this stage, a legitimate question concerns the performance of these SE-free ball-milled electrodes under low-pressure conditions. In that regard, we assembled a solid-state cell comprising a SE-free BM90-LTS electrode, with a loading of 7.76 mg_{AM}/cm^2, and a $Li_{0.8}In$:LPSCl (60:40 wt.%) composite anode. Subsequently, in the same fixed-gap cell setup used in the previous Chapter 2 Figure 2.4, the cell was cycled by successively reducing the cycling pressure, starting from 10 MPa and progressively decreasing to 0.1 MPa.

From Figure 3.17, we observed that the cell exhibits a stable reversible capacity of 165 mAh/g even at 0.1 MPa, which corresponds to approximately 87.5% of the initial discharge capacity obtained at 10 MPa. Moreover, upon returning to a pressure of 5 MPa, the capacity remained stable at 172 mAh/g. Thus demonstrating that the impact of such low pressure is relatively minor, resulting in only a slight 4% decrease in reversible capacity. The same cell was subjected to subsequent cycling at various pressures and rates, as shown in Figure 3.17c. Remarkably, it exhibited consistent performance, maintaining a stable capacity of 129 mAh/g at 5 MPa and 112 mAh/g at 1 MPa when cycled at a C/5 discharge rate.

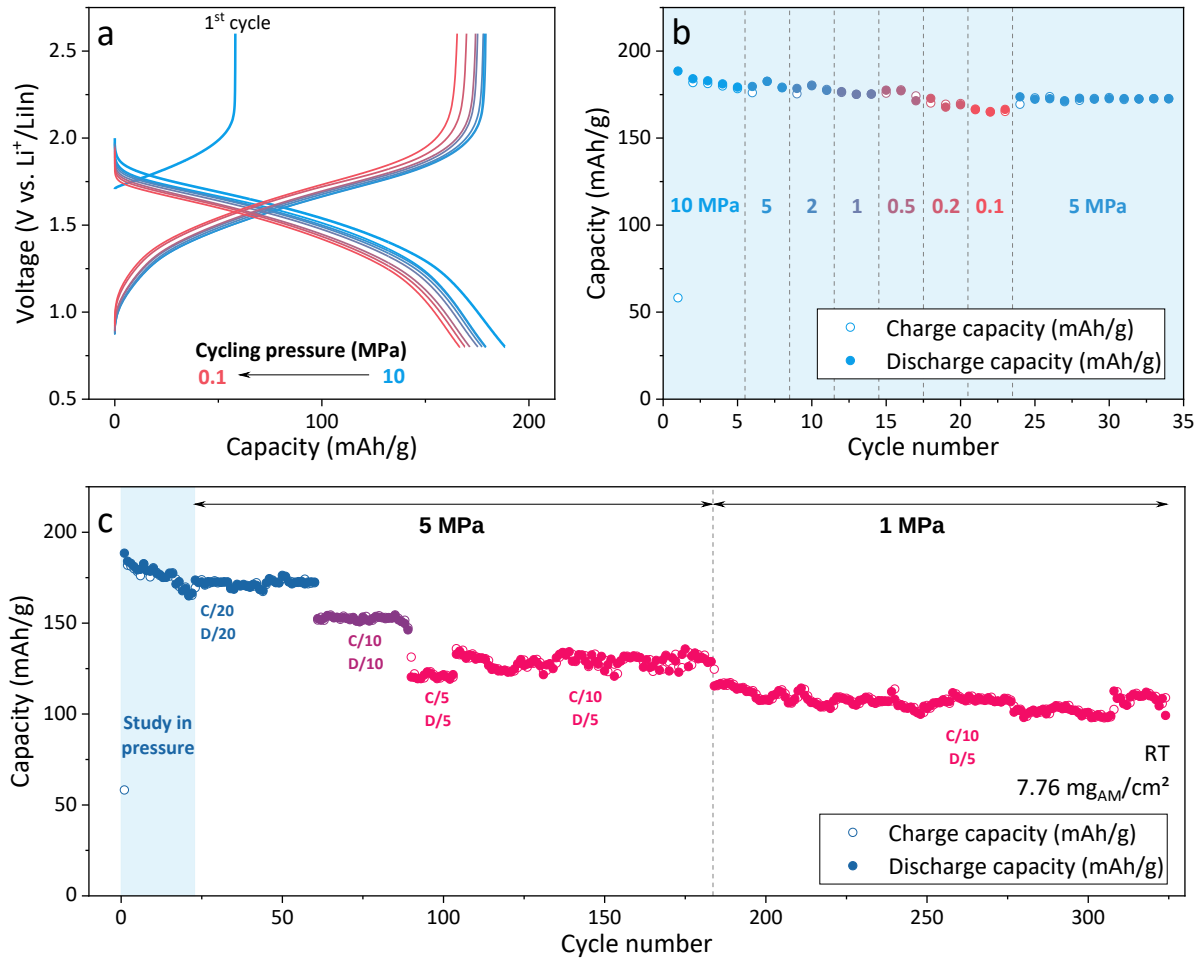

Figure 3.17. (a) Galvanostatic cycling and (b) capacity retention of BM90-LTS in a SE-free electrode cycled at successively lower pressure versus a LiIn anode. (c) Capacity retention at different rates and pressure of the BM90-LTS in a SE-free electrode used for the cycling pressure study from 10 to 0.1 MPa. Blue zone in part (c).corresponds to the study in pressure displayed in panel (b).

Next, we conducted tests on similar cells but having higher electrode loadings, specifically up to 31 mg_{AM}/cm^2 and 12.9 mg_{AM}/cm^2 at pressures of 100 MPa and 10 MPa, respectively. When comparing the first cycle of these cells (as shown in Figure 3.18), it is evident that the cell with a higher loading exhibits lower capacity, which can be attributed to the limited Li^+ conduction. This effect becomes particularly pronounced at high state-of-charge (SOC; for $x<0.6$), where an increased loading results in a significant loss of capacity, which is consistent with the reduced apparent lithium diffusion coefficient at high SOC that we observed earlier.

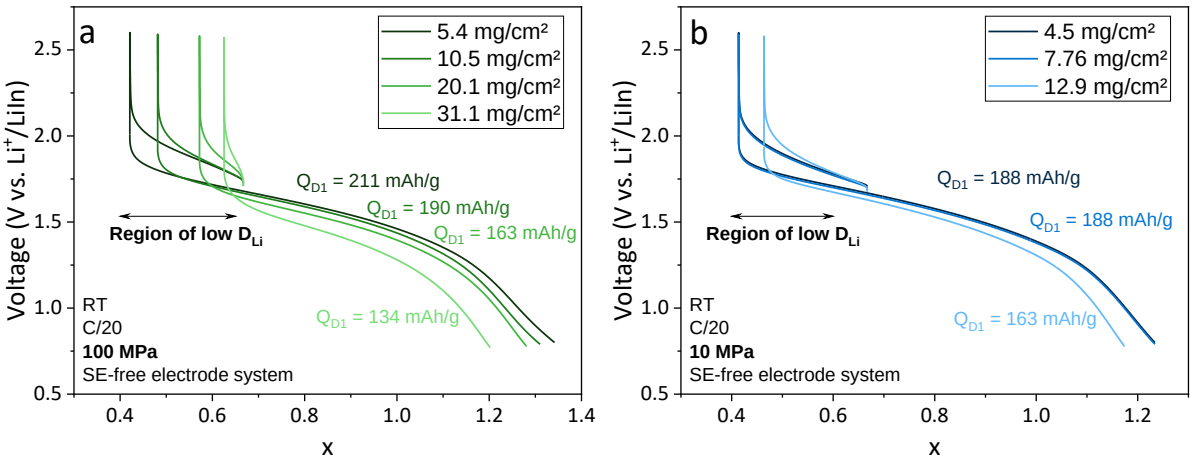

Figure 3.18. First galvanostatic cycle of SE-free cathode in ASSB cells as a function of the loading under (a) 100 MPa and (b) 10 MPa of stack pressure.

In summary, these results underline the feasibility of achieving stable cycling even under low-pressure conditions, despite the inherent volume changes that occur during cycling. This achievement can be attributed to the utilisation of the SE-free cathode configuration, which enables homogeneous volume expansion and contraction across the entire electrode thickness. Standing in contrast to composite systems, where only the CAM contracts often resulting in contact losses with the SE.

To assess the contacts in our electrodes, we conducted ex-situ SEM characterisation (Figure 3.19). We examined a BM90-LTS//LPSCl//LiIn stack in its pristine state, as well as after charging to 2.6 V and discharging to 0.8 V vs. Li^+/LiIn. The findings indicate a coalescence of particles at the surface of the pellet upon lithiation (as observed in Figure 3.19e-g) and the appearance of vertical cracks upon delithiation (Figure 3.19h-j) while interparticle contacts remain preserved. Interestingly, a similar morphological evolution was reported by Meng's group[117] when investigating the lithiation of an anolyte-free silicon anode for ASSBs at high pressure. The fact that both LTS and Si exhibit a Li-driven morphological evolution suggests that the feasibility of cycling LTS even at low pressure and Si only at high pressure is likely more influenced by the difference in material ductility. Additionally, differences in the amorphous nature between these materials could also play a role in their distinct behaviours during lithiation.

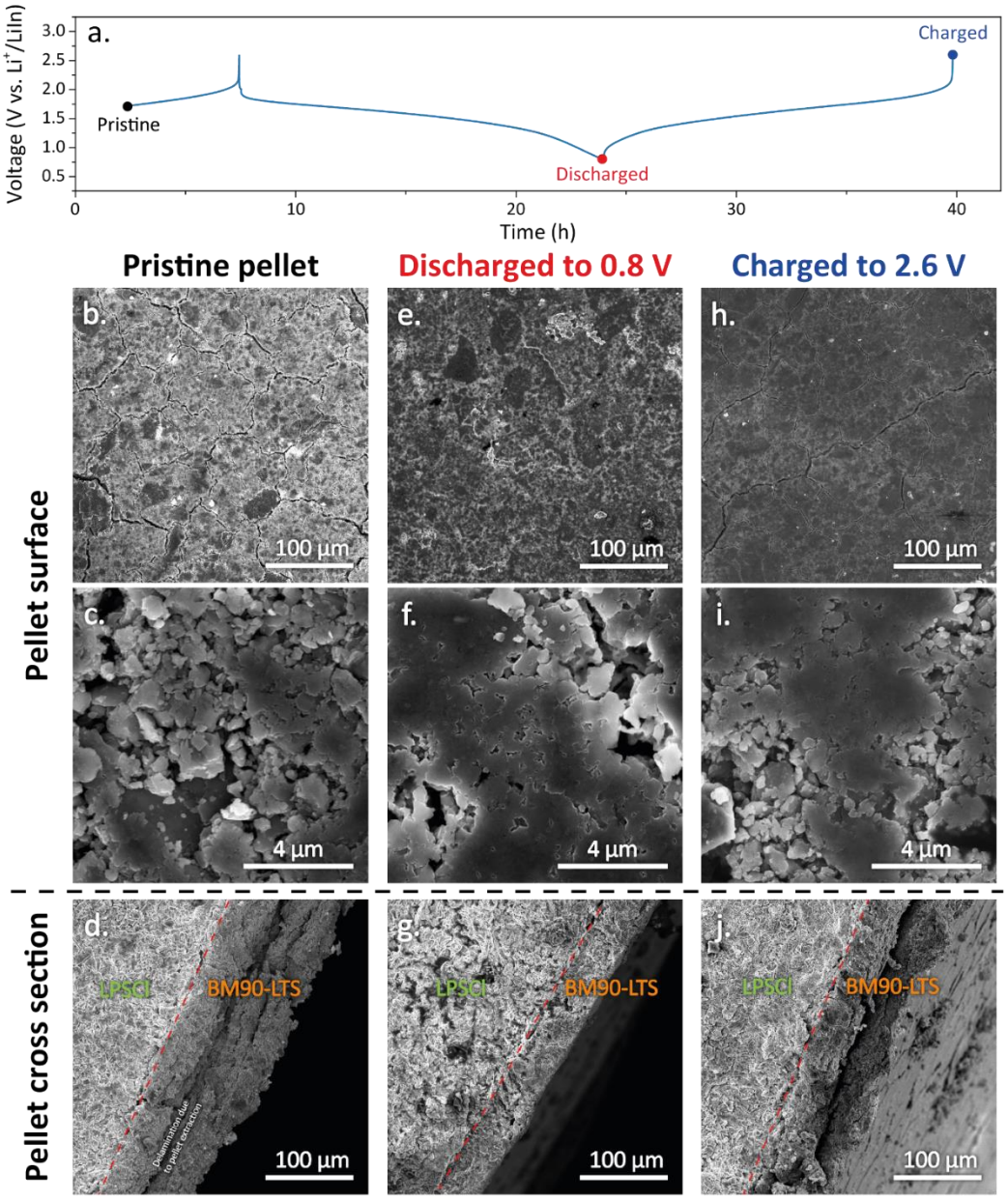

Figure 3.19. (a) Galvanostatic profile and surface and cross section micrographs of pellets (b-c-d) pristine as-densified, (e-f-g) discharged to 0.8 V and (h-i-j) charged to 2.6 V vs. Li^+/LiIn.

For comparative purposes, Figure 3.20 displays the energy densities of solid-state cells cycled at a C/20 rate, utilising various positive electrodes (sulphides and oxides), while employing the same electrolyte and counter electrode (LiIn:LPSCl composite). Notably, the cell utilising NMC622 delivers 530 Wh/kg at the material level, but, due to the necessity of incorporating 30% of electrochemically inactive SE and carbon additives to ensure proper operation, this translates to only 375 Wh/kg at the electrode level. This additional SE is not required in our BM90-LTS SE-free electrode configuration thus leading to an energy at the electrode level of 305 Wh/kg within the limited potential window of 1.8-2.6 V vs. Li^+/Li, and

up to 366 Wh/kg (as shown in Figure 3.20) by enlarging the potential window to 1.4-3.2 V vs. Li^+/Li. In summary, these values are highly competitive with those obtained using NMC622/SE electrode composites in ASSBs, underscoring that SE-free electrodes stand as a serious contender for the next generation of solid-state batteries.

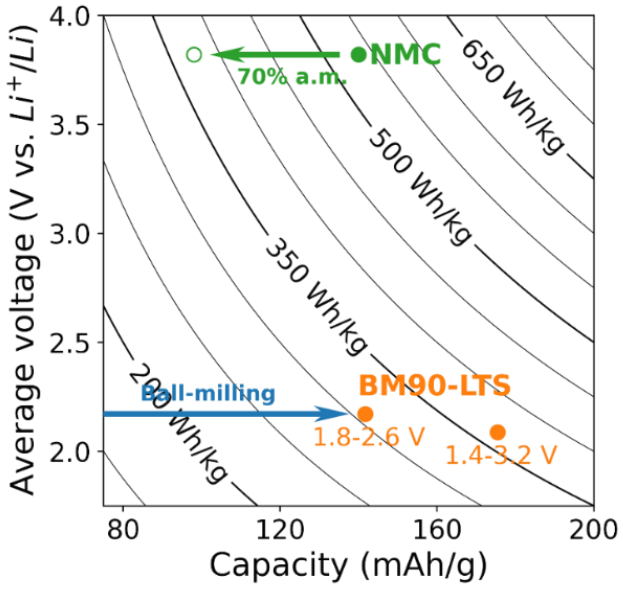

Figure 3.20. Obtained energy densities with a typical NMC622 material (cut-off at 4.2 V vs. Li^+/Li) and the BM90-LTS at different potential cut-offs in ASSBs.

Altogether, we have investigated the use of Li-containing Ti-based sulphides as a promising cathode material for operating ASSB under low-pressure conditions. For proof of concept, we have selected the O3-Li_xTiS_2 phase and reported that this phase, when milled, can be directly used as positive electrode in solid-state batteries as a SE-free cathode, thereby achieving higher energy densities. Moreover, we have shown exceptional cyclability of such electrode under pressure as low as 0.1 MPa.

Expanding on these findings, there are several avenues worth exploring. In the upcoming Section 3.4, we evaluate the performance of various materials, with a specific focus on compounds that offer 3D ionic diffusion pathways with the objective being the possibility to eliminate the ball-milling step. Moreover, we explore the feasibility of leveraging the ductile properties of halide materials discussed in the previous chapter to develop SE-free electrodes utilising halide CAM, hence reuniting in one the two strategies employed in this thesis to enable cycling under very low-pressure conditions.

3.4 – Applying the SE-free concept to other CAMs for low pressure cycling

From an industrial perspective, although being used is the battery manufacturing, the process of ball milling remains an additional expensive step. Until now, we used it in order to improve the ionic diffusion through particle downsizing and morphology change of the layered compounds. However, one such process could be unnecessary in the case that the material already provides a 3D ionic diffusion pathway. Identifying such materials could lead to more efficient and cost-effective production processes for SE-free electrode.

○ Exploring other titanium-based sulphide polymorphs

In the same Ti-based sulphide family, several compounds, such as the spinel Ti_2S_4 or the rock-salt Li_2TiS_3 phases (Figure 3.21), having a 3D ionic diffusion could be considered.

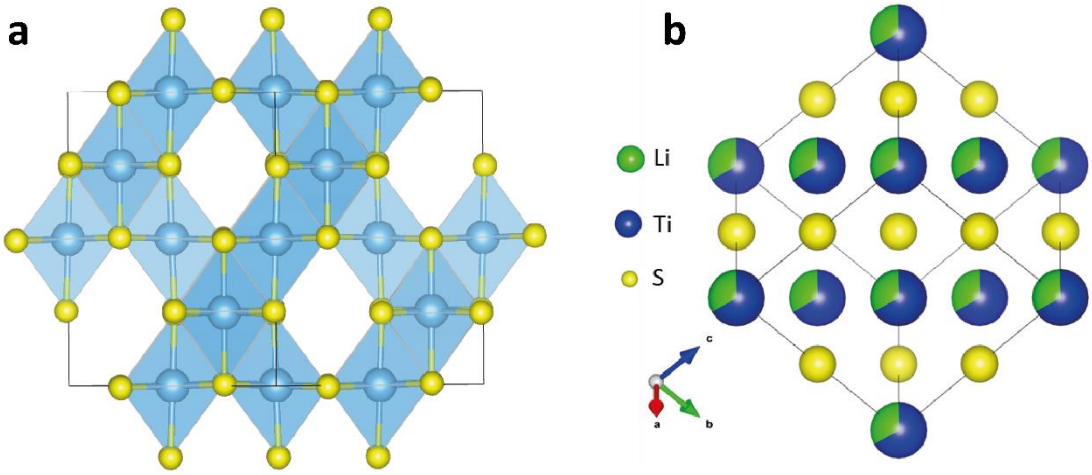

Figure 3.21. Crystallographic structure of (a) the spinel Ti_2S_4 and (b) of the disordered rock-salt Li_2TiS_3.

We first explored the cubic spinel Ti_2S_4, which was obtained by removing Cu from $CuTi_2S_4$ using Br_2,following the previously published[148] protocol detailed in Appendix Section A3.1. When using this phase, it is important to keep in mind that the activation energy of diffusion in the cubic phase has been shown to be less favourable than in the layered one[147] which could hinder the performance in a SE-free electrode configuration. Similar to the experiments with the O3-Li_xTiS_2, a solid-state cell was assembled and cycled. However, no notable improvement was observed in the SE-free system until the sample underwent ball milling, as shown in Figure 3.22. This suggests either that the diffusion coefficient in this spinel phase is insufficient or that achieving nanoscale powders, from synthesis or through milling, may be more crucial than an intrinsic isotropic diffusion in designing usable electrodes free of

SE additives. One potential improvement of this spinel phase involves focusing on the synthesis of nanoscale particles that seems to be necessary in this case.

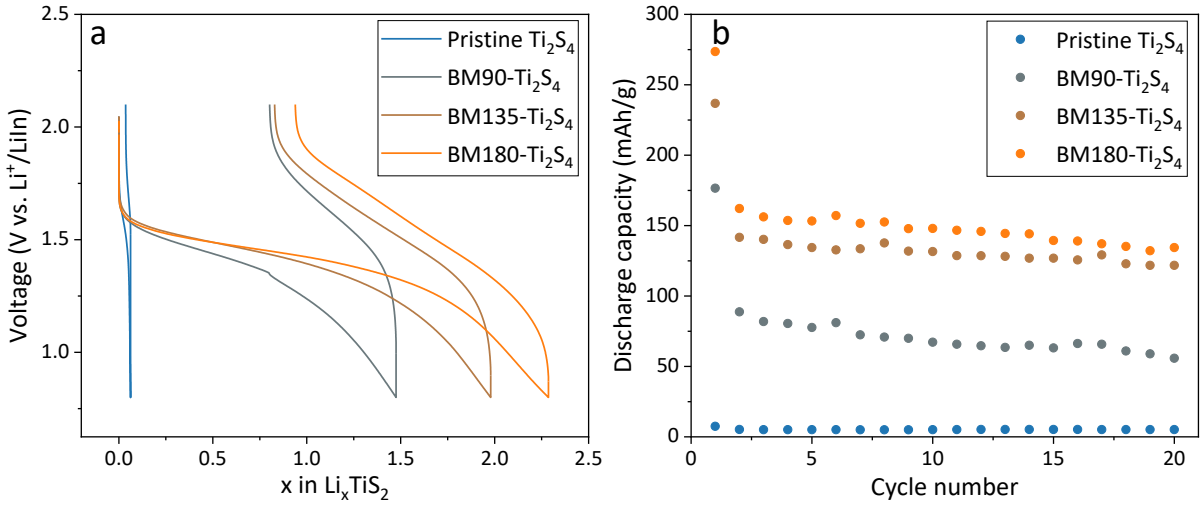

Figure 3.22.Performance of the Spinel Ti_2S_4 as a function of the milling time in a SE-free electrode configuration. (a) First galvanostatic cycle at C/20 and (b) capacity retention of the Spinel Ti_2S_4 with different milling time (0, 90, 135 and 180 minutes) in SE-free ASSBs with a LiIn anode at RT under a pressure of 100 MPa.

Following the same idea, we explored the potential of several other phases to be used as SE-free cathode materials, some of which were prelithiated. Specifically, we investigated the rock-salt Li_2TiS_3 phase with its high reported capacity of 425 mAh/g, the lithium-rich layered $Li_{1.2}Ti_{0.4}^{4+}Ti_{0.4}^{3+}S_2$, the chemically lithiated layered O1-$LiTiS_2$, the selenium-based layered O1-$LiTiSe_2$. Detailed procedures for their preparation are provided in Appendix Section A3.1. However, it is worth noting that none of these phases allowed for SE-free cycling, as indicated by the results displayed in Figure A3.5. The layered phases encountered similar challenges and required a ball-milling step, while the rock-salt phase did not exhibit sufficient ionic diffusion to support SE-free cycling even at a high pressure of 100 MPa.

In summary, results from our investigations involving various Ti-based chalcogenide phases highlight the challenge of identifying materials that exhibit a sufficiently high 3D ionic diffusion, possess a small particle size, and exhibit the necessary ductility to facilitate effective interparticle contacts within the SE-free electrode.

○ Leveraging the ductility of halide-based materials

In addition to chalcogenides, other compounds are known for their ductility. In the previous chapter, we have harnessed this property from halide-based SE to enable low

pressure cycling. In the upcoming section, we intend to explore halide-based cathode active materials that exhibit high ionic conduction.

Our initial exploration focused on the potential of the cubic Li_2FeCl_4 (LFC) phase to serve as a SE-free electrode material, enabling low-pressure cycling. This phase not only is expected to be ductile but also possess 3D ionic conduction pathways and a higher electrochemical potential than sulphides. In a previous study by Tanibata *et al.*, this phase was used in a similar context, where an electrode composed of 95 wt.% LFC and 5 wt.% carbon was employed in a LPSCl-based cell.[149] The authors reported an ionic conduction of $2.1 \cdot 10^{-5}$ S/cm for the LFC prepared through a mechano-synthesis process. They demonstrated a one-electron full charge reaction with a high operating voltage of 3.6 V vs. Li^+/Li in an ASSB at a pressure of 100 MPa.

In our study, we synthesized the material following the same protocol by subjecting a stoichiometric mixture of LiCl and $FeCl_2$ to high-speed (500 RPM) ball milling for 10 hours. A more comprehensive protocol is available in Appendix Section A3.1. Our electrochemical impedance spectroscopy measurements revealed an ionic conductivity of $1.80 \cdot 10^{-5}$ S/cm, while DC polarization measurements indicated an electronic conductivity of $4.48 \cdot 10^{-8}$ S/cm.

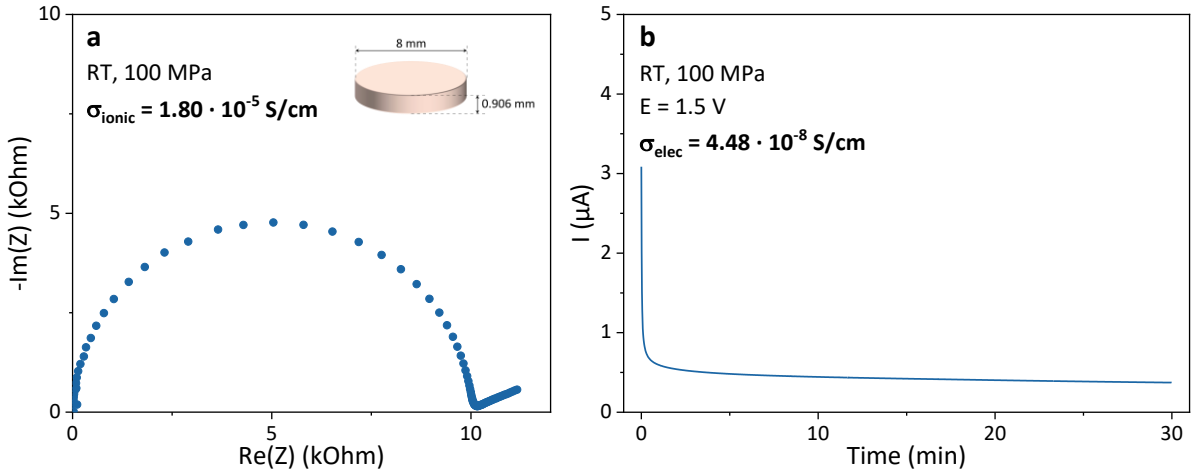

Figure 3.23. Characteristics of the as-synthesized cubic LFC. (a) Diffractogram on LFC powder, (b) EIS and (c) DC polarization measurement on a LFC pellet.

Following the synthesis and characterisation, we proceeded with galvanostatic cycling of the material. Initially, we incorporated it within a composite electrode consisting of LFC, LYBC ($Li_3YBr_2Cl_4$), and VGCF in a mass ratio of 66.5:28.5:5 wt.% and cycled it at 100 MPa to assess its nominal performance. The potential window was limited to the range 2.7 to 3.3 V

vs. Li^+/Li corresponding to a one-electron reaction. Such limitation in potential was to avoid the plateau corresponding to the irreversible second lithium deintercalation upon charge (Figure A3.6). Results presented in Figure 3.24a and b demonstrate a reversible capacity of around 115 mAh/g on the first discharge, with a substantial capacity decay upon cycling. Next, we assessed the material in a SE-free electrode configuration by mixing it with only 5 wt.% VGCF. Cycling this composite resulted in a relatively good discharge capacity of 104 mAh/g in the first cycle. However, the capacity decay was also present on subsequent cycles.

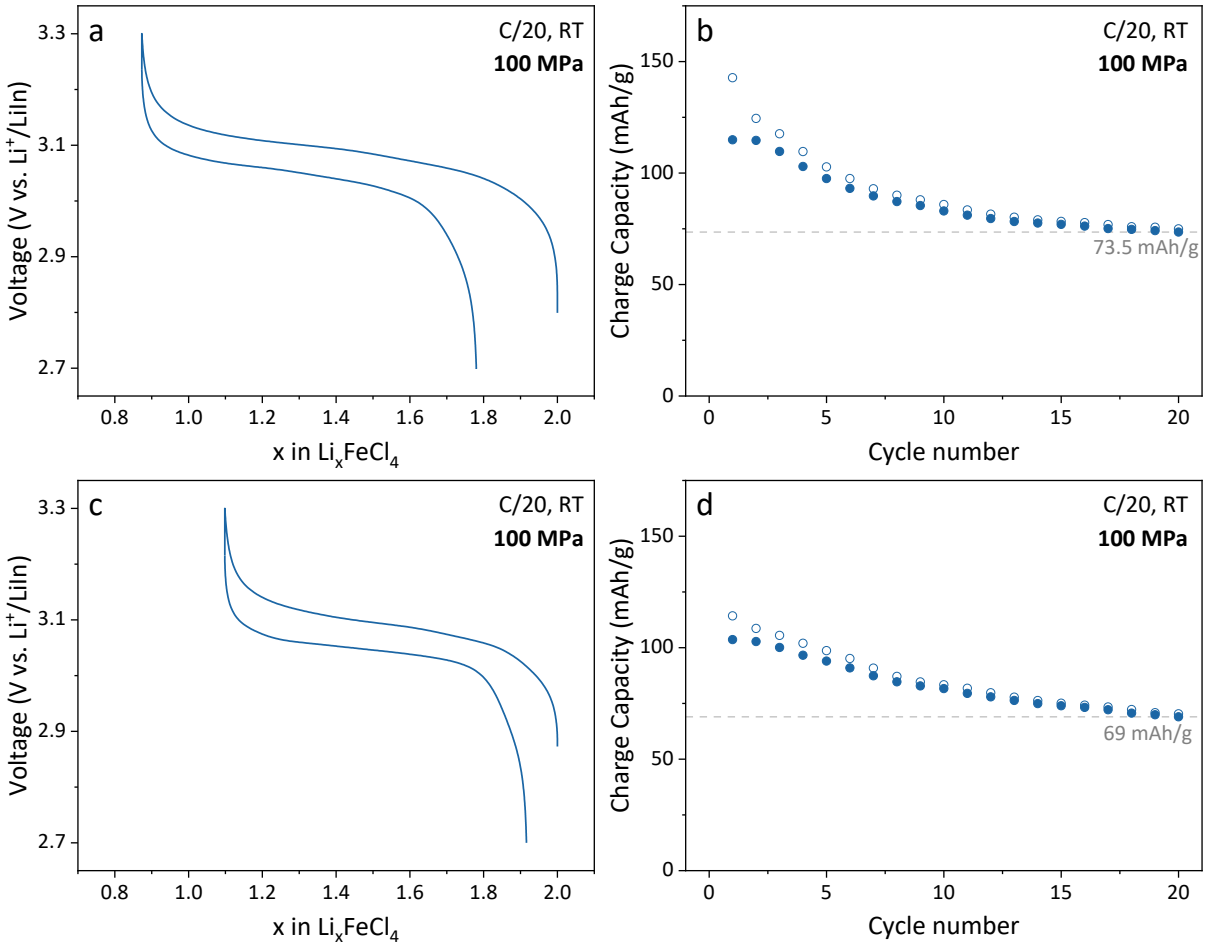

Figure 3.24. Cycling performance of the cubic LFC against a LiIn anode in high pressure. (a and c) First galvanostatic cycle and (b and d) capacity retention in (a-b) a LFC:LYBC:VGCF and (c-d) a LFC:VGCF composite in a solid-state cell cycled at a rate of C/20, at RT and a pressure of 100 MPa.

The performance being assessed at high pressure, we then tested the material under low-pressure conditions. To this end, similar to tests of the BM-LTS, we assembled cells with either a composite composed of LFC, LYBC and VGCF or LFC and VGCF and we cycled them in a fixed gap setup with an initial pressure of 10 MPa. Results shown in Figure 3.25 clearly

demonstrate a lower capacity of first cycle compared to the high-pressure tests as well as a larger decay.

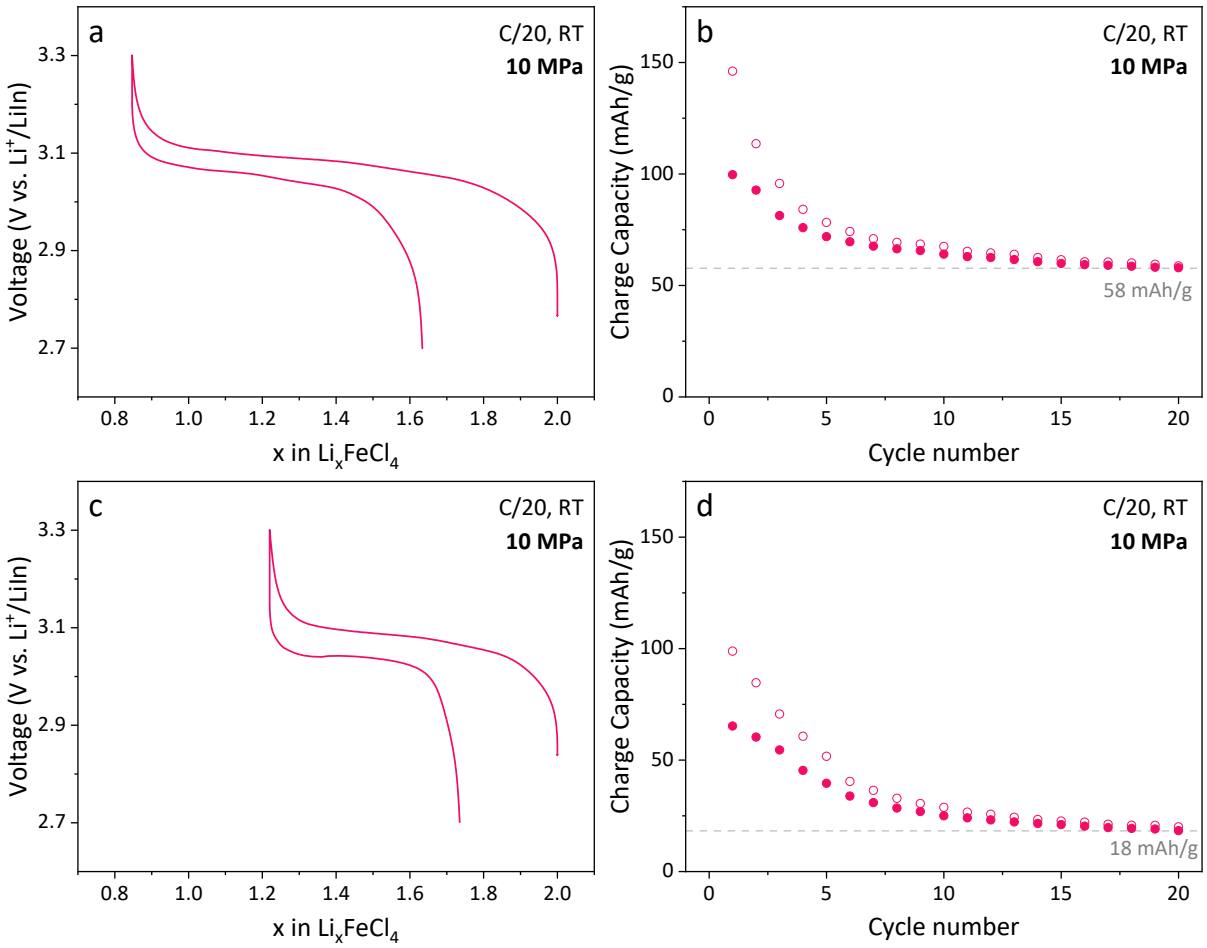

Figure 3.25. Cycling performance of the cubic LFC in a composite cathode and against a LiIn anode at low pressure. (a and c) First galvanostatic cycle and (b and d) capacity retention in (a-b) a LFC:LYBC:VGCF and (c-d) a LFC:VGCF composite in a solid-state cell cycled at a rate of C/20, at RT and an initial pressure of 10 MPa.

In summary, the performance of this halide-based active material in a SE-free cathode configuration demonstrates poor performance under this reduced operating pressure. Building upon these results, one avenue for further exploration could involve investigating the low-pressure performance of the recently reported Li_3TiCl_6 halide-based CAM. Although this material has demonstrated a relatively low reversible capacity of approximately 90 mAh/g, it showed remarkable cycling retention in a SE-free cathode under high-pressure conditions. Moreover, owing to its high ionic conductivity of 1.04 mS/cm, it showed high rate capabilities.[116] Finally, exploring the performance of other halide CAMs based on different metal cations like Mn or V could also be a valuable area of investigation.

3.5 – Chapter conclusion

In conclusion, Chapter 3 presented a detailed exploration of an innovative concept of a SE-free electrode configuration for achieving low pressure cycling in ASSBs, a strategy that promises to simplify ASSB design and manufacturing processes.

The chapter began by evaluating the case of the O1-TiS_2 as a literature reference to establish a foundation for our investigation on SE-free cathode systems. We then focus on the evaluation of the O3-Li_xTiS_2 material, a pre-lithiated lamellar phase similar to the O1 phase. We conducted a comprehensive examination of the characteristics and performance of this material in typical composite cathodes. Subsequently, we introduced a milling strategy that enabled SE-free cycling of O3-Li_xTiS_2 through particle size downsizing and morphology change that resulted in a decreased tortuosity and an enhanced Li^+ ion diffusion through the electrode thickness.

Continuing on this research trajectory, we have demonstrated that the ball-milled material possesses the remarkable capability of cycling even under extremely low pressures, as low as 0.1 MPa. This outstanding performance can be attributed to the material's ability to expand and contract uniformly during cycling, resulting in minimal contact losses inside the electrode. This contrasts with typical composite materials that can exhibit performance degradation under low-pressure conditions due to contact-related issues.

Expanding on the SE-free concept, we explored its applicability to other CAMs for low-pressure cycling. This included exploring of other Ti-based sulphide polymorphs and leveraging the ductility of halide-based materials to widen the range of materials that can benefit from SE-free configurations.

Overall, Chapter 3 has presented a SE-free electrode concept whose experimental results can collectively contribute to the advancement of ASSB. This concept offers a promising avenue to address the challenges associated with low-pressure cycling. Moving forward, having demonstrated stable cycling under low-pressure conditions, we opened new opportunities among which the use lithium metal anodes (LMA), a necessary step towards making ASSBs more practical and applicable, which has not been done so far. In that regard, the next chapter will explore this possibility and will discuss current strategies and limitations that remain to be solved for enabling the use of LMAs in solid-state batteries.

Chapter 4 – **Lithium Metal Anode: Strategies, Critiques and Perspectives on its Implementation**

4.1 – Chapter Introduction

The use of a lithium metal anode (LMA) is essential to achieve high energy levels in solid-state batteries (SSBs). Traditionally, LMAs have been considered unsafe due to their tendency to form dendritic Li deposits that can penetrate the cell, resulting in short-circuits and subsequent thermal runaway events. The use of a solid electrolyte (SE) was seen as a promising solution to the problem due to its ability to mechanically prevent dendrite growth. In previous chapters, we have discussed the need to reduce the stack pressure to enable the implementation of this ductile lithium metal. By employing diverse engineering strategies within the positive electrode, we have illustrated the achievement of high capacity and stable cycling of cathode materials at pressures as low as 0.1 MPa. However, it should be noted that we have not yet used LMA as the counter electrode.

In this chapter, our study begins with the integration of LMAs into the two previously studied systems: the cathode composite employing a halide-based SE, as discussed in Chapter 2, and the SE-free cathode strategy detailed in Chapter 3. Both of these systems have previously demonstrated their ability to sustain cycling under extremely low-pressure conditions. Consequently, we aim to evaluate their performance when paired with a lithium counter electrode and to empirically highlight the critical challenges associated with LMAs. This section will serve as the culmination of our examination of lithium metal all-solid-state battery (Li-ASSB) systems within this thesis and will allow us to move into a discussion and critique of the current methodologies employed to assess the viability and performance of LMAs. To conclude, we will provide an overview of the current and most promising strategies emerging in the literature for their integration

4.2 – Implementing Li metal anodes in low pressure systems

In Chapter 2 and 3, although demonstrating cycling of positive electrodes under very low-pressure conditions, we have been using an alternative anode composed of an alloy of lithium and indium. As illustrated in the In/Li binary phase diagram in Figure 4.1, this alloy has several biphasic domains characterised by a voltage plateau, with the one occurring at 0.622 V vs. Li^+/Li that corresponds to the formation of the intermetallic InLi phase from Li and In. With its long and stable potential, it is an ideal candidate to serve as an alternative counter electrode for half-cell measurements. Moreover, in contrast to pure lithium or indium, which are ductile, this alloy shows a brittle nature once formed, making it particularly advantageous for cycling at high pressures, as it does not lead to mechanical extrusion through the SE. However, due to the high content of the heavy and electrochemically inactive indium, coupled with its higher potential, the utilisation of this anode in a full-cell system is impractical, as it would significantly hamper the cell's energy density. In that context, returning to the use of low-potential anodes becomes evident. Consequently, we have opted to employ a pure lithium anode for low-pressure cycling in both of the previously investigated systems.

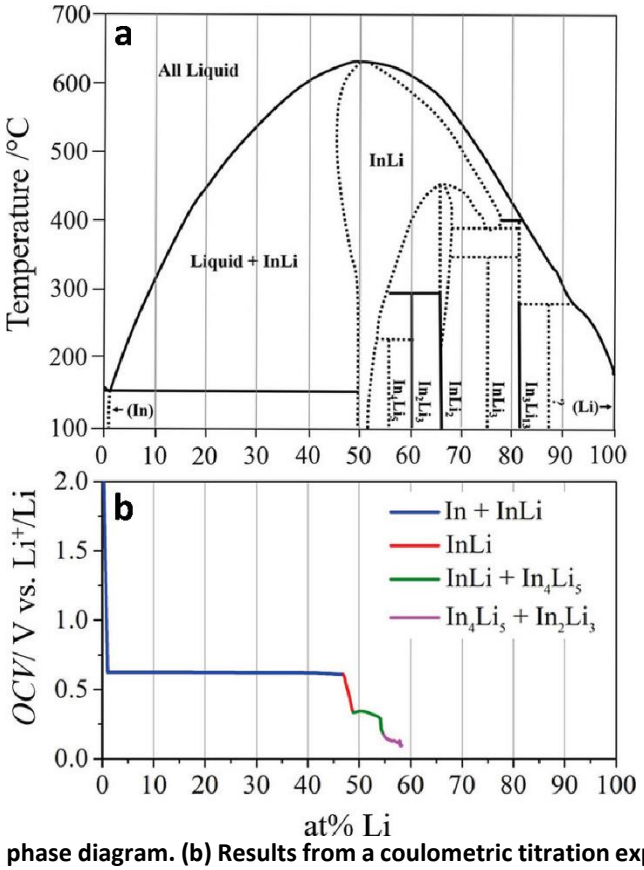

Figure 4.1. (a) Binary In–Li phase diagram. (b) Results from a coulometric titration experiment at RT. The graph shows the electrochemically determined open circuit voltage (OCV) over the lithiation from In to the phase In_2Li_3. Reproduced from reference[150].

○ Applicability to the halide-based composite system

Focussing on the halide-based composite of NMC622, studied in Chapter 2, we investigated the performance of a bi-electrolyte NMC//$Li_3YBr_2Cl_4$//Li_6PS_5Cl//Li cell (Figure 4.2c) with a loading of 4.5 mg_{NMC}/cm^2. It should be noted that, unlike the previous study where a "full-halide" NMC//$Li_3YBr_2Cl_4$//LiIn cell could be constructed, in this case, due to the low reduction stability of LYBC (Figure 2.15b), the use of the LMA requires the incorporation of a Li_6PS_5Cl (LPSCl) protective layer with the $Li_3YBr_2Cl_4$ (LYBC) material. The cell was cycled at decreasing stack pressures from 10 to 0.2 MPa. Remarkably, on the first cycle at 10 MPa (Figure 4.2a), this system displayed very similar performance as for the half-cell experiment (Figure 2.19) with capacities of 177.2 and 150.2 mAh/g in charge and discharge, respectively, and a high ICE of 84.7%. Gradually decreasing the pressure on subsequent cycles did not lead to an increased capacity decay maintaining an average of -1%/cycle at C/20 (Figure 4.2d). A pressure of 0.2 MPa was reached but instabilities most likely originating from the Li//LPSCl interface began to appear below.

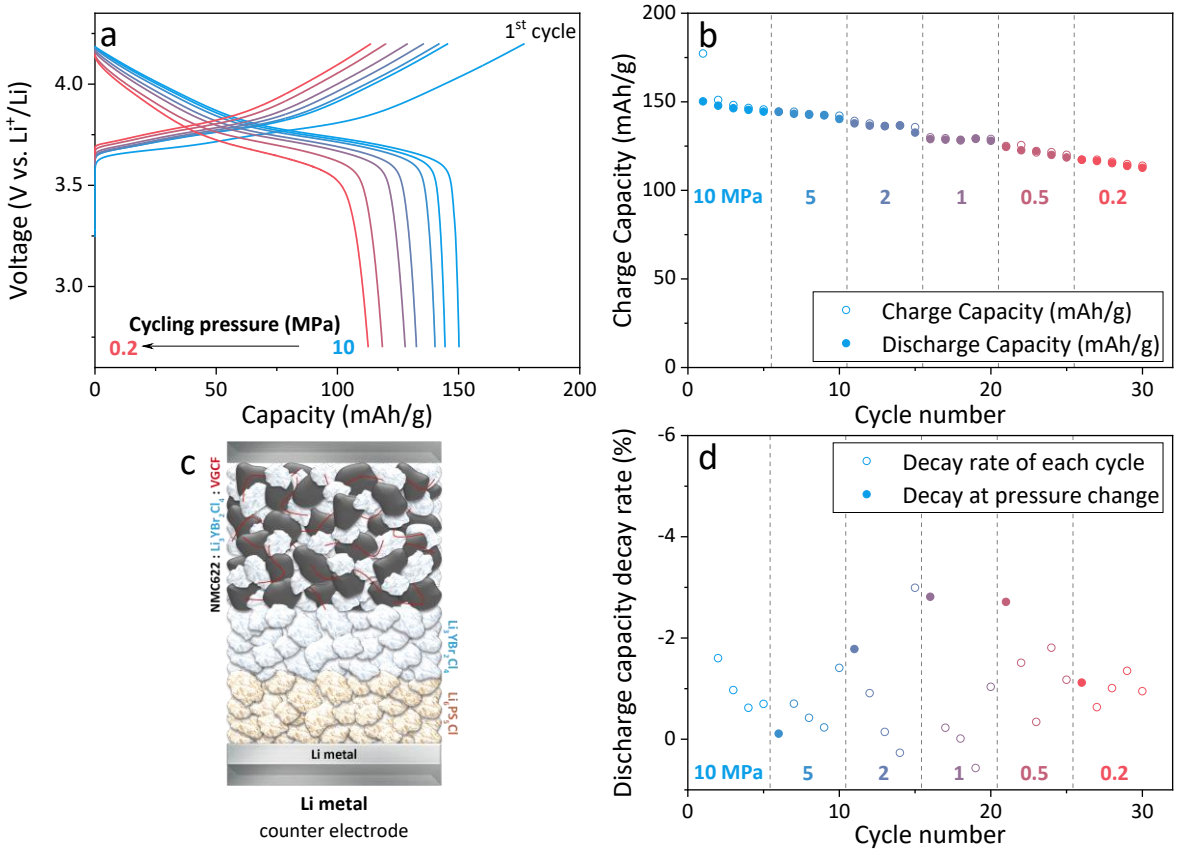

Figure 4.2. (a) Last galvanostatic cycles at each pressure, (b) capacity retention and (d) decay rate of NMC//LYBC//LPSCl//Li cell as a function of the stack pressure (from 10 to 0.2 MPa), cycled at RT and a C/20 rate. (c) Schematic of the Li metal dual-SE cell architecture tested in this experiment. Filled circles in (d) highlight the larger capacity drop after each pressure change.

Instabilities in systems that incorporate LMA are frequently encountered. Despite achieving a remarkably low pressure of 0.2 MPa in the previous experiment, various problems quickly become apparent when attempting to replicate low-pressure cells using LMA. Some cells exhibit diminished performance as soon as the pressure is reduced (as shown in Figure 4.3a and b), while others experience short-circuits after just a few cycles (Figure 4.3c).

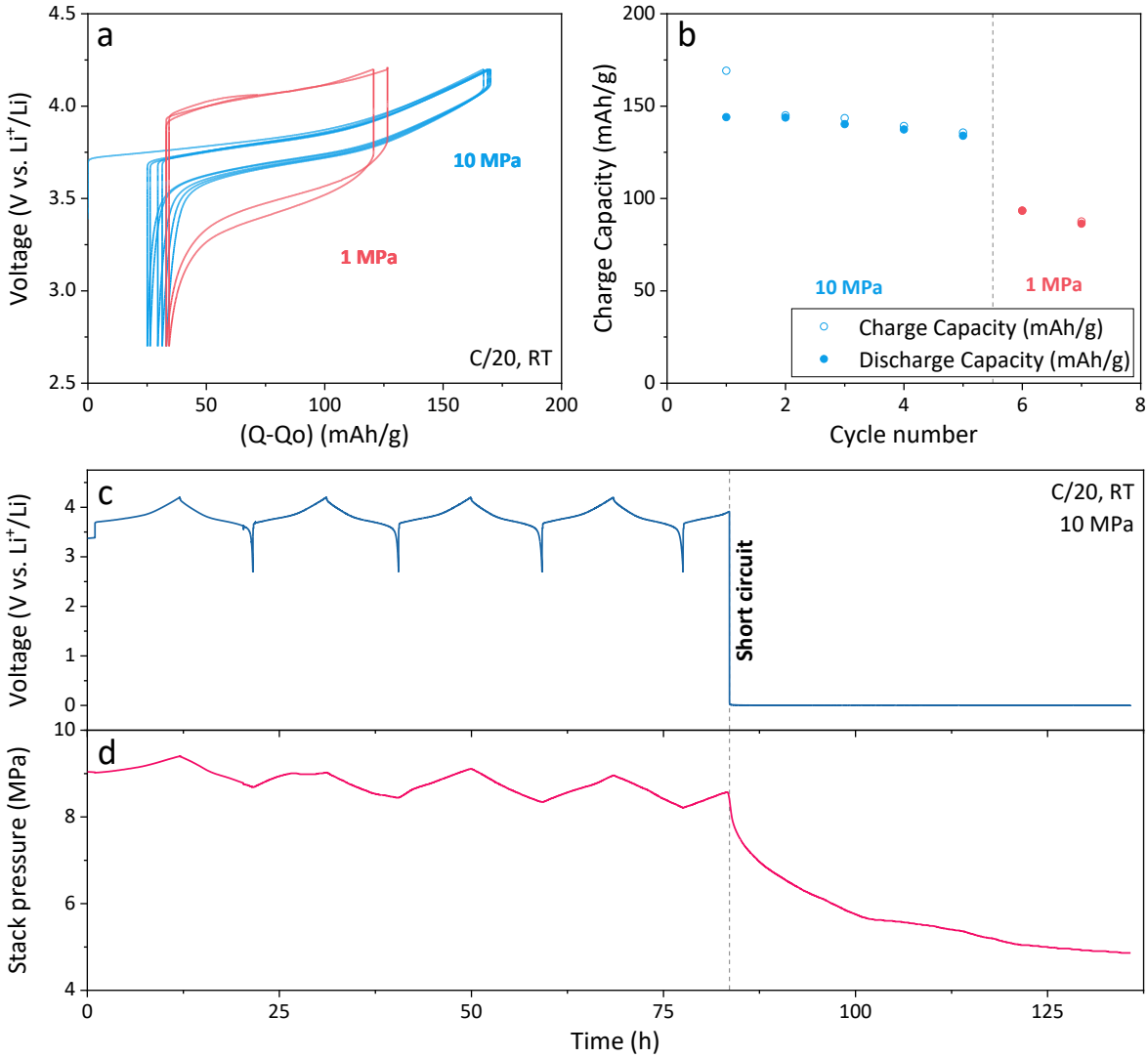

Figure 4.3. (a and b) Galvanostatic profiles and capacity retention of an NMC//LYBC//LPSCl//Li cell with decreasing pressure and (c and d) galvanostatic curve and recorded stack pressure as a function of cycling time. The sudden drop in potential highlighted by a dashed line in part c corresponds to a short-circuit of the cell.

○ Lithium metal anode in the SE-free cathode system

Exploring the second strategy addressed in this thesis, we then focused on the implementation of this LMA in a SE-free cathode of milled O3-Li_xTiS_2 (referred to as BM90-LTS). A lithium metal solid-state BM90-LTS//LPSCl//Li cell with a loading of around 4.5 mg_{AM}/cm^2 was constructed by simply pressing a lithium disk on the surface of the cell's SE

separator and was cycled at a relatively low initial pressure of 8 MPa. Lower pressures were not attempted with this system due to the previously observed instabilities. As shown in Figure 4.4, this cell displays a first cycle discharge capacity of 195 mAh/g with an average polarization as low as 85 mV. Impressively, this configuration exhibited a remarkable capacity retention of 94.2% after 25 cycles at C/20 and an energy density at electrode level of over 400 Wh/kg was reached. Similar to our previous observations, instabilities in the form of lithium dendrites started appearing at the 28th cycle as indicated in Figure 4.4c.

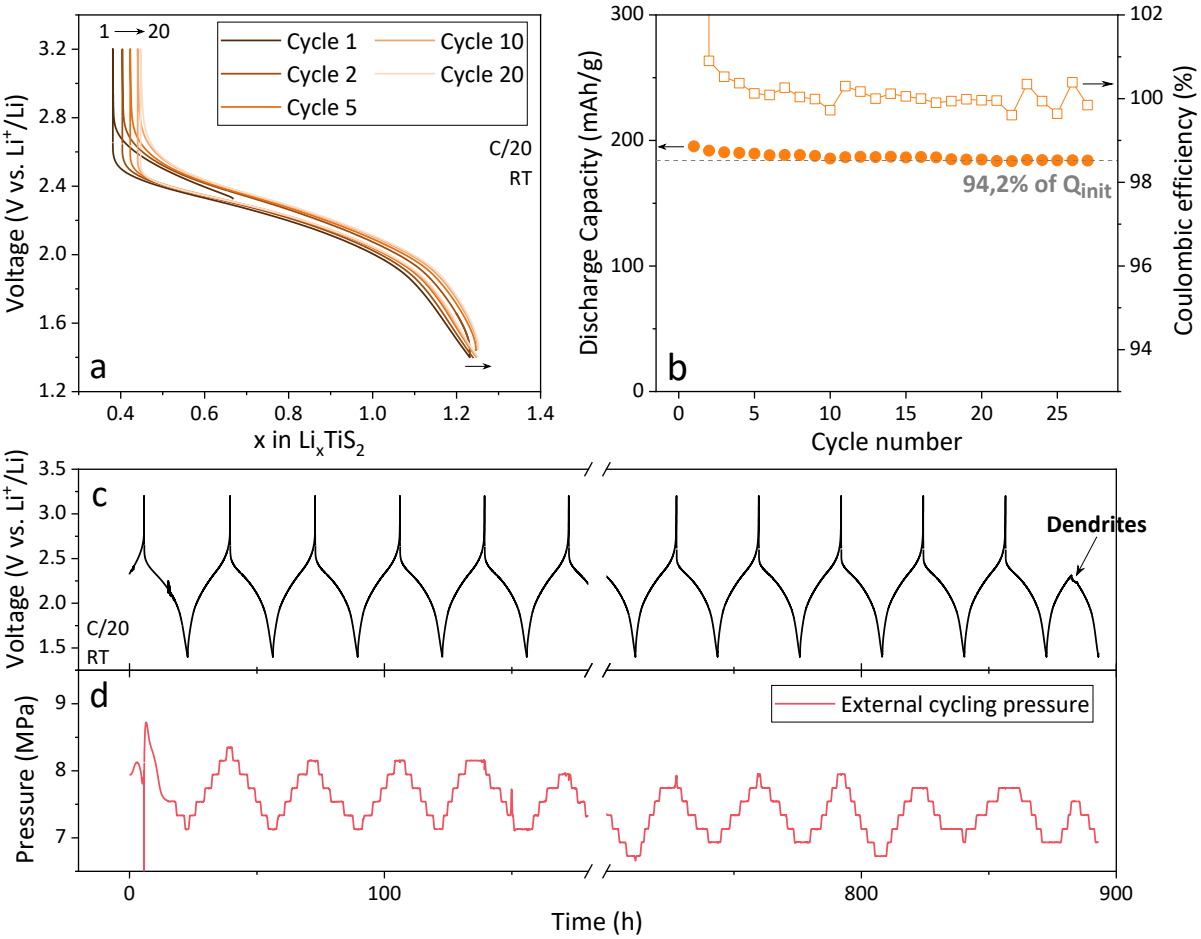

Figure 4.4. (a) Galvanostatic profile, (b) capacity retention and (c-d) pressure evolution (in red) upon cycling (in black) of the BM90-LTS in the SE-free electrode system with a lithium metal anode in the 1.4 to 3.2 V vs. Li$^+$/Li electrochemical window.

Interestingly, using our cell configuration, which included an external force sensor, we monitored the evolution of the cell's pressure (Figure 4.4d). Due to lithium plating/stripping, we found that the cell's pressure mimics the galvanostatic curve and varies reversibly with pressures oscillating from 6.6 to 8 MPa between the end of charges and discharges, respectively. It is worth mentioning that, in this particular cell configuration, efforts to increase the loading beyond 4.5 mg_{AM}/cm^2 often result in cell failure. This outcome is not entirely

unexpected, as higher loadings induce greater pressure fluctuations due to lithium plating until reaching a critical threshold where the cell experiences a short circuit due to the mechanical extrusion of Li metal through the SE. This is an intrinsic problem of fixed-gap cell setups, not fully appreciated by the battery community. Such an issue could be mitigated using a spring-loaded constant pressure setup, presently under development in our group.

Altogether, results obtained with an LMA from either of our two strategies are promising although a substantial amount of research and engineering on the Li//SE interface is still required to effectively stabilise it. The well-documented[66,103] issues associated to the use of lithium in ASSBs, that have been comprehensively addressed in Chapter 1 Section 1.3 and that are summarised in the following Figure 4.5, are often limiting the achievable areal capacities and power output of the cells to prevent failures. However, the development of Li-ASSB reaching capacities of more than 5 mAh/cm² and capable of cycling at current of 5 to 10 mA/cm² is imperative for future industrial application and commercialisation of the technology.[16,151] In that context, it is imperative to be able to quantify the performance of the Li//SE interface and to assess the strategies employed to enhance it.

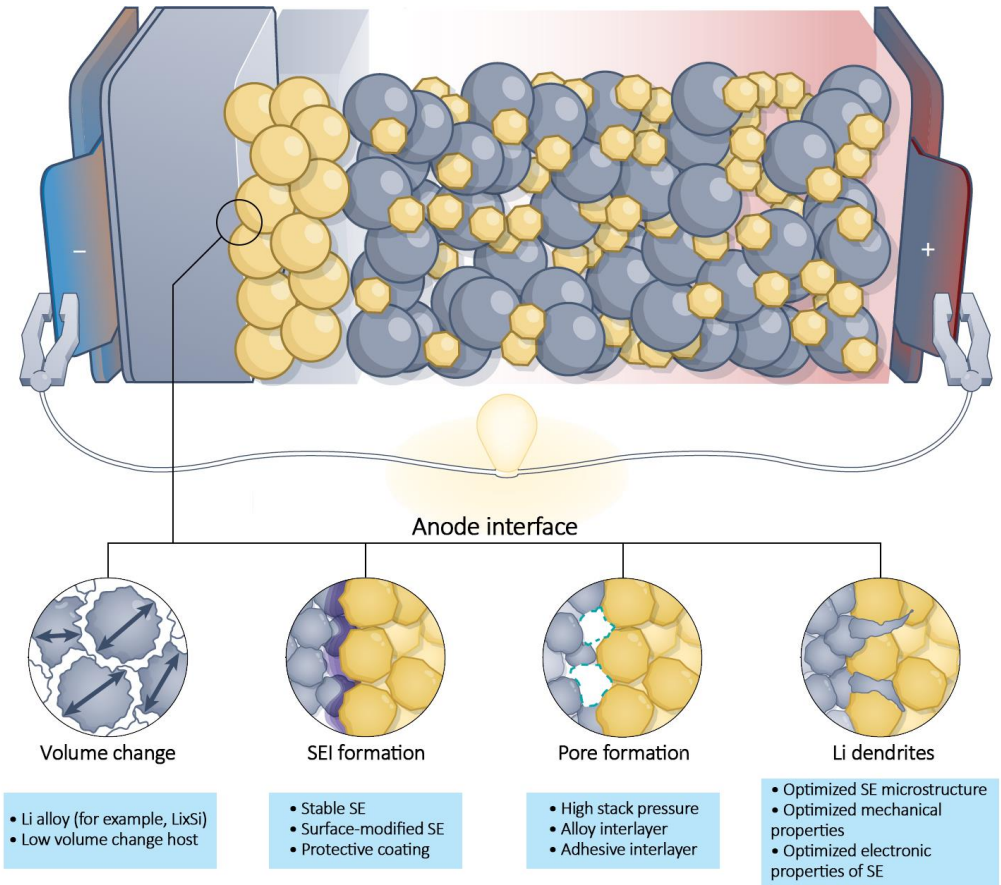

Figure 4.5. Known anode interface-related issues in ASSBs and potential solutions (highlighted in blue). SEI stands for solid electrolyte interphase and MCI for mixed-conducting interphase**.** Adapted from reference[66].

4.3 – How accurate is the evaluation of the SE//Li interface?

An important metric to evaluate the performance of a Li-ASSB is the critical current density (CCD) that can be defined as the maximum achievable current density at which a cell can cycle stably without any failure occurring. However, as we will see in this section, its assessment is not straightforward.

○ Evaluating the critical current density with our electrolytes

A common approach for determining the CCD, involves the use of lithium symmetric cells. As illustrated in Figure 4.6b, this assessment typically consists in a bidirectional plating/stripping galvanostatic staircase test, which is characterised by a gradual increment in the current with a fixed hold duration at each step. Through this method, researchers have explored various systems and methods to enhance the CCD of Li-ASSBs. However, the CCD is influenced by multiple factors such as cell chemistry, stack pressure or temperature and it is important to note that significant variations in CCD have been reported, even for similar cell configurations.[152,153]

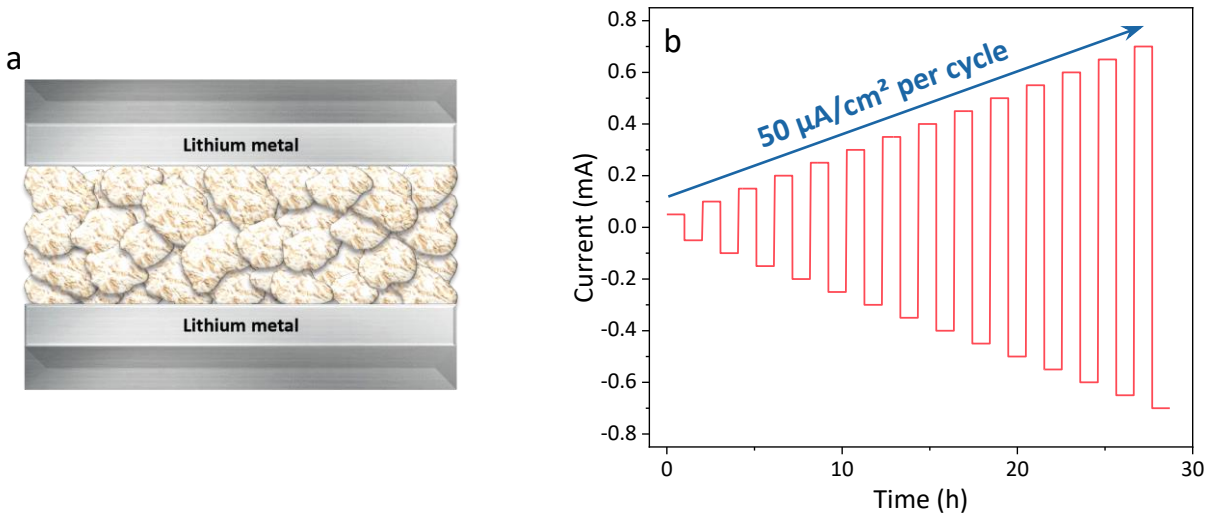

Figure 4.6. (a) Schematic of a lithium symmetrical cell stack and (b) typical current staircase test protocol.

To evaluate the performance of our pristine Li systems, meaning a SE separator with a lithium metal anode, we conducted CCD staircase test measurements using two different sulphide SEs: the β-Li_3PS_4 (LPS) and the LPSCl argyrodite. Symmetric cells were assembled according to the protocol available in the Appendix Section A4.1, and were then cycled with a starting current and rate increase of 50 µA/cm² under 9 MPa in cells comprising a spring-loaded current collector to maintain a nearly constant pressure (Figure 4.7).

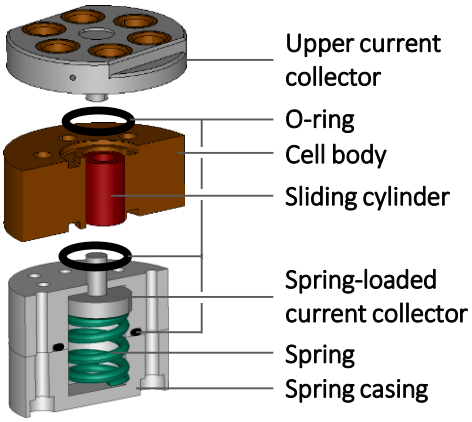

Figure 4.7. Schematic of a constant pressure spring-loaded cell setup. The spring can be changed to modify the stack pressure. Courtesy of Dr. Romain Dugas.

A typical potential profile resulting from a CCD of 0.75 mA/cm² is presented in Figure 4.8a. Following a linear increase, the plating/stripping polarization ranges from 3.8 to 43 mV when increasing the current from 50 µA/cm² to the CCD of 750 µA/cm². On average, the CCD obtained were 0.58 and 0.68 mA/cm² for the LPS and the LPSCl SE, respectively. These observed values are consistent with previously reported findings for these sulphide SEs.[152] However, as evident from the box plot in Figure 4.8b, substantial variations exist between cells within the same SE system, with CCD spanning the range of 0.3 to 1.3 mA/cm² for the LPSCl SE. Such variations have also been observed in recent works by both Meng's[152] and Janek's[153] groups and in our experience, at first, we attributed these large variations to the challenge of achieving consistent, flat, and uniform separator surfaces in contact with the Li. However, it is crucial to note that numerous assembly and cycling parameters can also influence the measured CCD in Li-ASSBs.

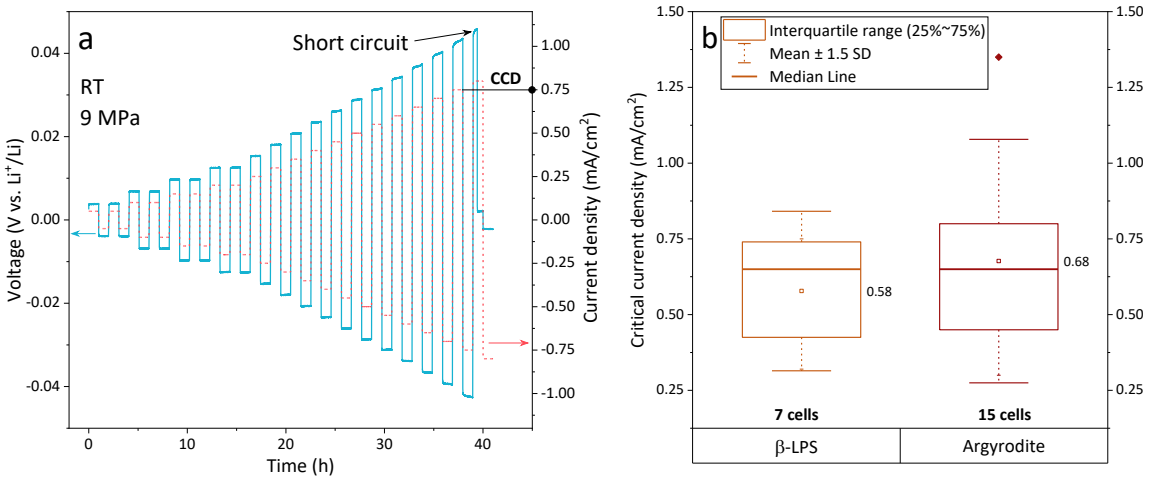

Figure 4.8. (a) Typical current staircase test (in red) and resulting potential profile (in blue) of a Li//LPSCl//Li cell and (b) whisker plot of the obtained CCD values for symmetrical cells with either a β-Li_3PS_4 or LPSCl electrolyte. In part (b) the box corresponds to the interquartile 25-75%, the line to the median value, the average is the square point, the whiskers to 1.5 standard deviation while the diamond points are outliers of the 1.5 SD.

○ Parameters influencing the critical current density

Firstly, in line with observations made in liquid LIBs cells, higher temperatures lead to substantial improvements in Li-ASSB cell stability. With our LPSCl system, measuring the CCD at either 25°C or 55°C resulted in an improvement of the average CCD from 0.68 to 1.1 mA/m². This trend is also depicted in the values agglomerated from the literature in Figure 4.9b, where most CCD values exceeding 1 mA/cm² are achieved for temperatures above 60°C.

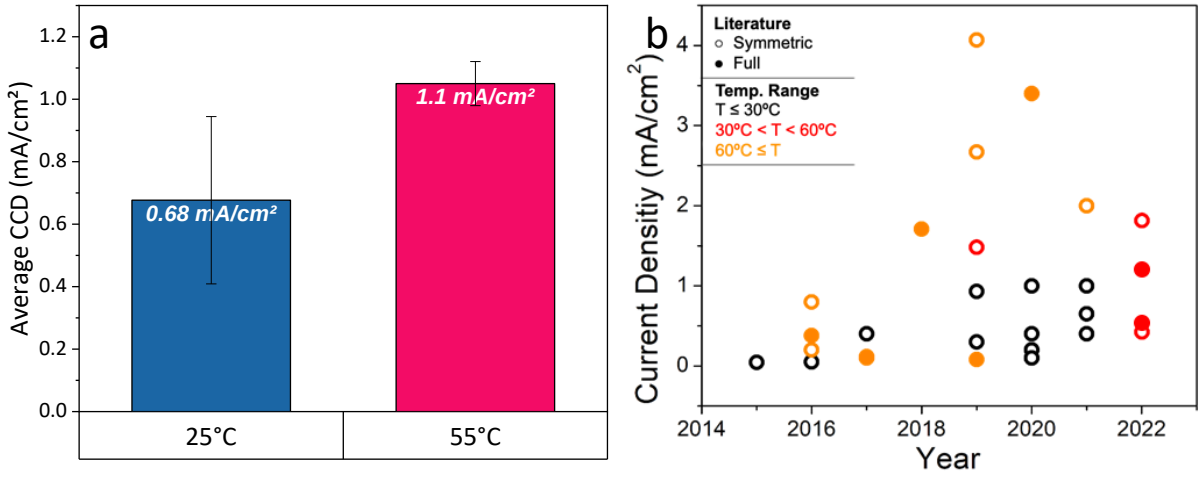

Figure 4.9. CCD variation with temperature. (a) CCD measurement of the Li//LPSCl//Li symmetric cell system at either 25°C or 55 °C and (b) current densities of Li-ASSB cells reported in the literature in different configurations and temperatures. Part (b) is adapted from reference[152].

Moreover, prior investigations have indicated that relatively small changes in stack pressures can significantly affect the CCD. It has been reported to improve with increasing stack pressure from 0.4 to 7 MPa (Figure 4.10a), as adjusting the pressure can help mitigate void formation upon stripping by deforming the lithium.[154] In that regard, different stack pressure can leads to two different failure mechanism, either through dendrite growth and subsequent short-circuit, as observed in Figure 4.8a, or void formation and contact loss, as illustrated in Figure 4.10a with the drastic increase in the polarization at low pressure.

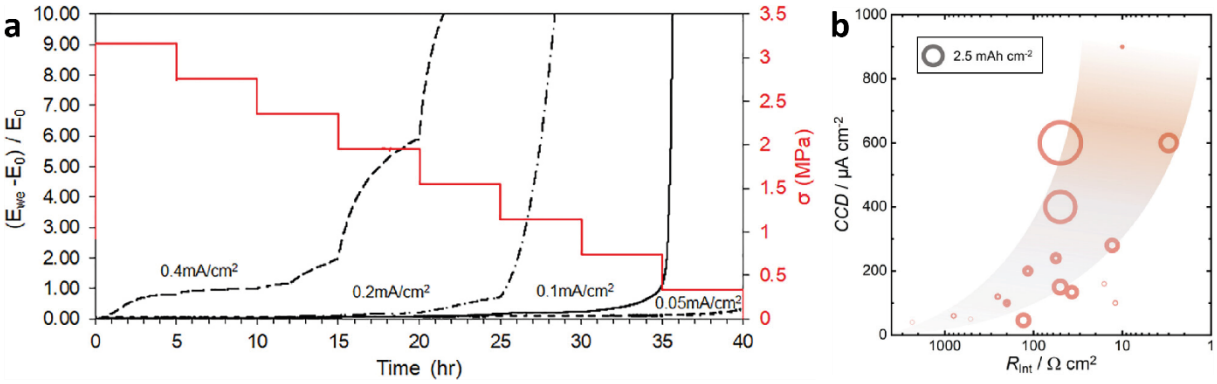

Figure 4.10. (a) Potential response to a constant current density at varying stack pressures and (b) CCD results are taken from various reports on Li//LLZO//Li symmetric cells plotted versus the interfacial resistance. The area of the circles represents the cumulative charge that was cycled until a short circuit occurred. To quantify this capacity, compare the area of the 2.5 mAh/cm² grey circle on the top left corner. Reproduced from references[153,154].

In addition, the CCD measured in Li symmetrical cells does not often translate to full cell performance where lower values are typically observed. A significant contributing factor is the areal capacity, especially considering that CCD measurements in symmetrical cells often use low capacities compared to the full-cell loading (< 1 mAh/cm² versus > 3 mAh/cm²). This highlights the importance of the separator thickness, which acts as a buffer for dendrite during their formation. Therefore, a low areal capacity or a thick separator can thus artificially increase the CCD by preventing the dendrite from reaching the other electrode. Moreover, a conditioning step consisting in the application of a relatively low assembly pressure[152] and a mild heat-treatment (Figure 4.11a and b-c, respectively) can effectively decrease the initial interfacial resistance which is particularly significant as previous research have indicated that it is one of the most critical parameters influencing the obtained CCD (Figure 4.10b).[153]

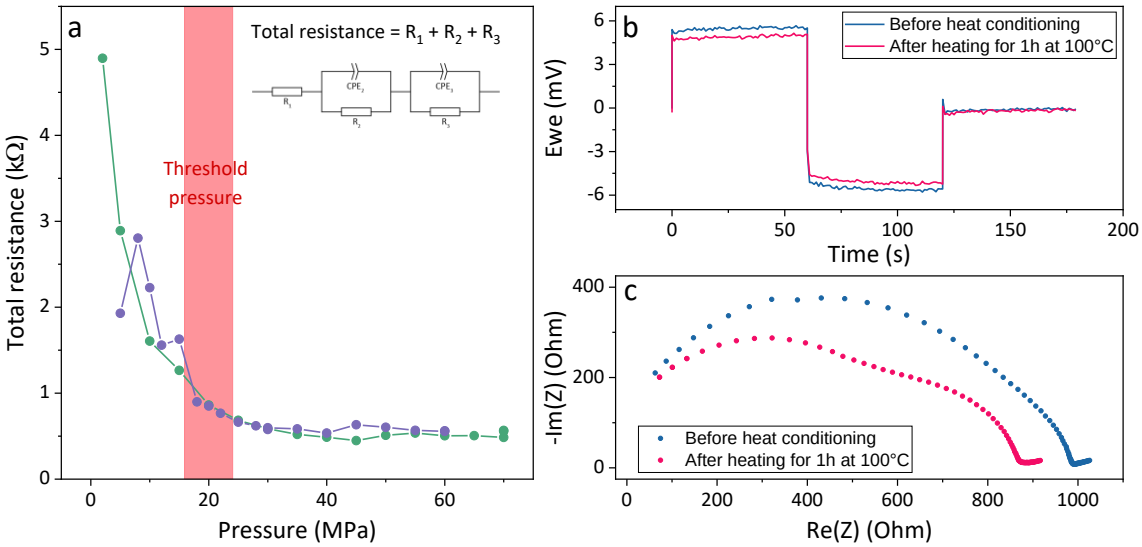

Figure 4.11. (a) Total resistance evolution as a function of the conditioning pressure used, (b) symmetric galvanostatic imposition at 10 µA/cm² and (c) Nyquist plots of a Li//SE//Li symmetric cell before and after a temperature conditioning at 100°C for 1h.

The cell setup is also important, as a fixed-gap configuration will inevitably lead to a pressure build-up during charge possibly leading to the mechanical extrusion of lithium through the SE. In contrast, Meng's group reported significantly improved CDD in a constant pressure system.[152]

Overall, although the use of this technique can be traced back to the development of sodium ASSB in the 1980's[155], in light of the large variability observed in the literature today, one might question the effectiveness of this method to measure accurate CCD. Specifically, it is essential to note that the staircase test can introduce certain biases. The test results may be influenced by the duration of the current hold, as a longer hold allows for more lithium plating. Additionally, dendrite formation is significantly influenced by the presence of locally high current densities. While model systems typically assume a uniform current density across the electrode surface, real-world factors like surface roughness and electrode edges play a substantial role. Therefore, the conventional use of symmetrical cells with identical-sized lithium electrodes may lead to premature dendrite growth due to edge effects.[156]

○ How to improve the measure of the CCD?

Altogether we have seen that assessing the critical current density of a Li//SE interface, being influenced by various parameters, is not straightforward. Therefore, the next section will provide a concise list of recommendations to enhance the accuracy of CCD measurements.

1. Material Control:
    - Ensure stringent control over Li surface contamination and bulk purity or use an anodeless configuration.
    - Maintain a flat, low-roughness surface for the SE separator, with uniform bulk density. In that regard, if pistons are used for densification, make sure they are flat and polished.
    - Consider employing isostatic pressing to enhance the SE bulk density homogeneity.
2. Setup Considerations:
    - Choose a constant pressure setup over typical fixed-gap systems.
    - Ensure that the thickness of the SE is coherent with the target for the full cell.
    - Design the sizes of the different components (Li electrode, separator) to prevent edge effects, which depending on the system and protocol used may not be applicable in symmetric cells.
3. Procedure Enhancements:
    - Consider a cell pre-conditioning, involving the application of higher pressure (20 to 25 MPa for a few seconds) at assembly to establish good Li//SE contact and potentially a mild heat-treatment to facilitate Li flow and improve wetting of the separator's surface, thereby reducing interfacial resistance.
    - Conduct a careful impedance analysis to examine the initial state of the cell, ensuring that the assembly or pre-conditioning did not result in a mechanical formation of lithium filaments that may lead to a "fake-stable phenomenon" and yield erroneously high CCD values.[153]
    - When assessing CCD, if the goal is to compare to full-cell performance, confirm that the areal capacities, temperature and pressure used align with the targeted full-cell characteristics to ensure the obtained CCDs accurately translate to full cell.
    - Consider alternative procedures in addition to the bidirectional staircase test, such as the measurement of the short-circuit times (Figure 4.12a and b) which consists in an unidirectional galvanostatic polarization at constant current until a failure occurs.[157,158] Moreover, a unidirectional staircase test implementing resting times can also be considered. Such test can help deconvolute the effect of cycling and cell failure mechanisms (Figure 4.12c and d).[153]

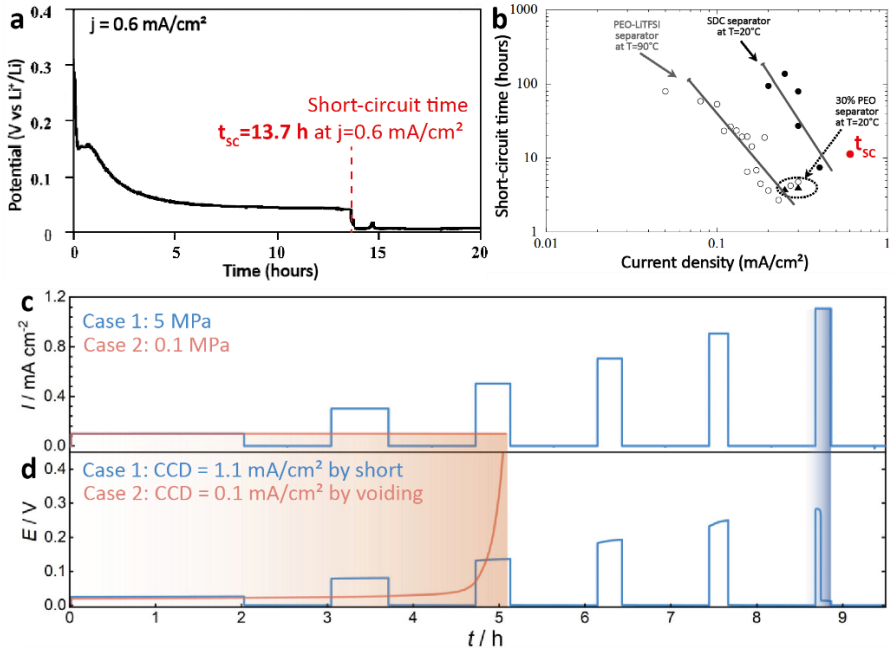

Figure 4.12. (a) Typical short-circuit observed on a Li symmetric cell polarized at 0.6 mA/cm² and (b) current density vs. short-circuit time for different systems and corresponding t_{SC} from part (a). (c) Current and (d) polarization of Li//LLZO//Li cells for a unidirectional staircase CCD measurement, which also highlights the influence of pressure on the failure mechanisms. Adapted from references[153,157,158].

While these recommendations provide a basis for improving the accuracy of CCD measurements, it is essential to acknowledge that the Li//SE interface is a complex system with many influencing factors. Further research and exploration are likely to reveal additional parameters and nuances that affect the CCD. These recommendations provide a starting point for evaluating the performance of different strategies to ensure stable Li-ASSB, and ongoing research will continue to expand our understanding of this interface. Several approaches have been explored in order to increase the stability of Li-ASSB cells. In that regard, the next section will be devoted to highlight some of these promising strategies.

4.4 – Promising strategies and perspectives to enable the use of lithium metal anodes

○ Design of solid electrolytes

From a chemical perspective, most of the SEs easily react at low potential when contacted with lithium metal. Such a decomposition results in the formation of a resistive interphases of which the thickness have been reported by Janek's group to be often largely underestimated.[159] Approaches to tackle this issue are various and a straightforward solution would be through the design of a SE that displays a thermodynamic stability at the lithium

potential. However, these are uncommon and, thus far, are not the most performing in terms of conductivity or mechanical properties.[25,26,160]

○ Alloy anodes

Alloying lithium with another metal is a technique of significant interest. While it is commonly employed in laboratory-scale studies of ASSBs using lithium-indium alloy as an anode, it is not a viable choice for constructing high-energy-density ASSBs, as previously discussed. However, given the array of lithium alloys available, some alternatives may hold potential.

In particular, for reasons similar to those of LIBs, the use of silicon as an anode may be a promising option although it has shown difficulties in cycling under low pressures.[117] Magnesium-lithium alloy is also of particular interest as Mg undergoes a kinetically favourable solid-solution reaction with Li compared to the sluggish intermetallic reaction of other metals (Si, Au, Zn, etc.).[161] Furthermore, as shown in Figure 4.13, this solid-solution domain extends over a wide range of compositions both on the Mg-rich and Li-rich sides. Moreover, research into lithium alloys has been extensive, extending beyond binary systems. Various ternary and quaternary systems that incorporate lithium have been thoroughly investigated and could be considered as potential candidates for such alloy anodes.[162] In particular, a recent work showed promising results in the use of a Li-Mg-Bi ternary alloy.[163]

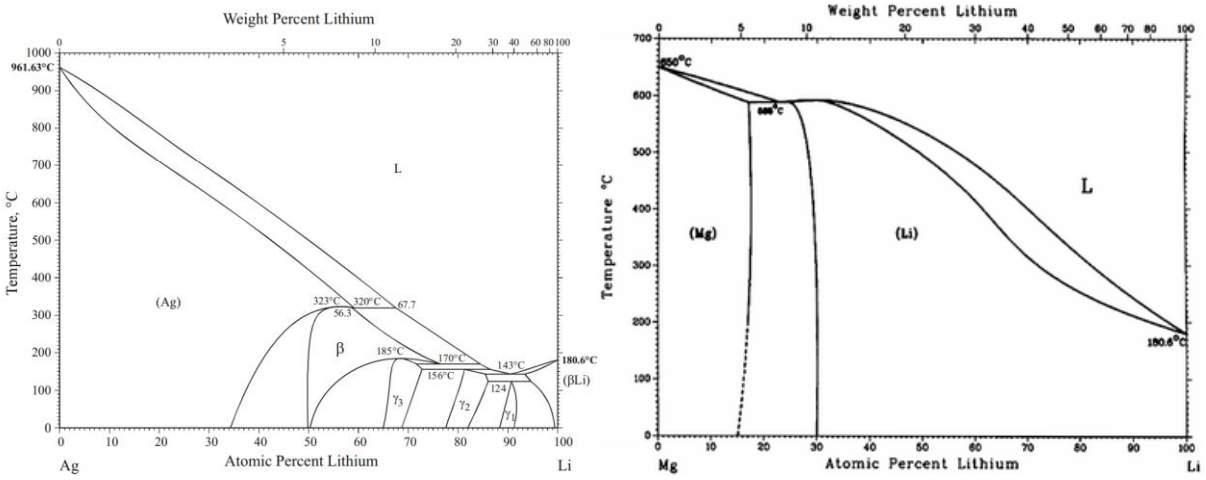

Figure 4.13. Binary Li-Ag (left) and Li-Mg (right) phase diagrams. Reproduced from references[164,165].

Although promising, forming such alloys typically leads to substantial volume changes with lithium content, which can be detrimental to the cycling performance of ASSBs. In that regard, one might seek alloys with minimal volume changes. An example of this is the open

metallic framework of $LaNi_5$, capable of hosting 6 hydrogen atoms per formula unit with just a 20% volume expansion.[164]

○ Coatings and interlayers

As most solid electrolytes form a passivating SEI or a detrimental MCI, a better approach involves the utilisation of coatings or interlayers. By tailoring the chemistry at the interface, this approach offers several advantages, including greater thermodynamic stability but also improved wettability or adhesion of Li with SE and provides a uniform mechanical barrier to dendrites.[107,166,167] Coatings and interlayers are an effective strategy to improve uniformity of plating and stripping thus preventing the formation of dendrites and pores, respectively. The most notable enhancement comes from the incorporation of a 5 µm-thin Ag-C interlayer that demonstrates remarkable effectiveness in allowing a uniform plating and stripping at current densities of up to 3.4 mA/cm² at 60°C.[101,108,110,168]

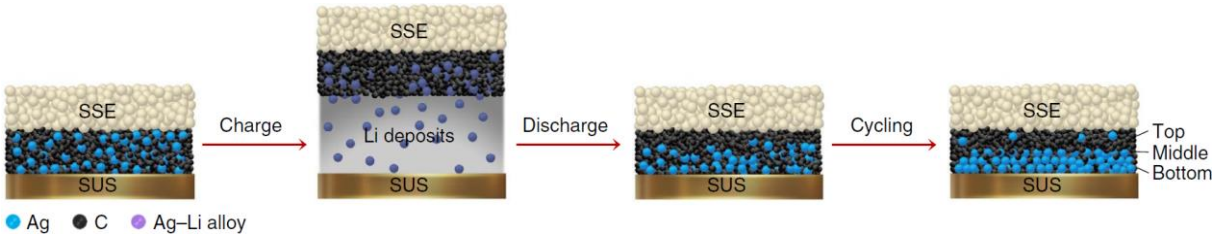

Figure 4.14. Schematic of Li plating–stripping on the current collector with an Ag–C nanocomposite layer during charging and discharging processes.

Based on this idea, it would be necessary to replace the silver in the Ag-C layer and explore the use of other materials known to be soluble in lithium or to form alloys with it. The use of Zn, Al, Sn, and Ni have been attempted without reaching the performance of the silver[169], however, owing to its wide solid-solution range, magnesium is also a promising candidate here. The exploration of other multi element systems mentioned before can also be of interest.[162]

Moreover, we can recall the use of metal fluoride MF_x at the interface that upon lithiation undergo a conversion reaction into LiF and M with subsequent alloying of Li-M (Figure 4.15).[170] With an AgF interlayer, the stable operation at RT and 20 MPa of a Li-ASSB cell with a high areal capacity of 9.7 mAh/cm² was reported. Similarly, another group used CuF_2 in a PVDF-HFP matrix that was laminated as an interlayer with a Li foil to form LiF and Cu to protect the Li.[171]

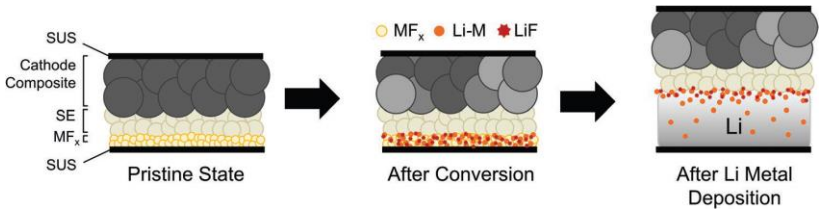

Figure 4.15. Schematic of Li plating on a current collector with a MF interlayer. Reproduced from reference[170].

○ In-situ formed and self-healing coating

The application of a coating at SE/Li interface can be achieved through various techniques, such as atomic layer deposition, sputtering, and more. Additionally, these coatings can be applied to different components, either the SE particles, a densified separator, or directly onto the Li metal itself. However, such a strategy inherently adds complexity and raises the cost associated with constructing an ASSB. Similar to the use of vinyl carbonate in lithium-ion batteries, an alternative strategy involves incorporating an electrolyte or an additive that, in contact with lithium, decomposes to create a controlled electronically insulating and ionically conductive stable interphase that would healed itself if ever damaged.

A notable example of this type of design can be found in the Li-Iodine primary cells, mentioned in Chapter 1 Section 1.2, where Li and I_2 were directly placed in contact to create the LiI SE separator. In addition, halide-based SEs, when partially substituted with fluorine, create a LiF-rich interphase that stabilises the interface despite their expected decomposition at Li potential. The use of additive for that purpose is less common but one could potentially incorporate additives like MF_x or others like Cu_3N into the SE to control the SEI formation.[172]

○ Lithium reservoir-free cell configuration

From a materials standpoint, the processing of lithium metal poses its own set of challenges. It readily reacts with various atmospheric components, even in trace amounts, leading to the formation of a contamination layer on its surface that, in turn, can have detrimental effects on its interaction with the SE. In addition, the purity of the lithium metal is also an issues, its bulk composition frequently contains elevated levels of sodium and oxygen that can significantly change its mechanical and electrochemical properties. Some report have also indicated the presence of a significant number of defect in the bulk that upon cycling tend to accumulate at the interface with the SE, thereby impacting the overall performance.[173–175] An adequate solution could involve adopting a Li reservoir-free cell alternative configuration,

where metallic lithium is not initially incorporated at assembly. This design, commonly referred to as anode-free or anodeless, leads to higher energy density at cell level and, with the SE serving as a filter, ensures the deposition of pure lithium during the charging process, effectively addressing the mentioned issues.[175] This configuration can also be coupled to an interlayer strategy as illustrated for the Ag-C and MF_x strategies in Figure 4.14 and Figure 4.15 respectively.

In summary, historical research efforts have focused on several strategies to achieve a stable cycling behaviour for LMAs, as summarised in Figure 4.16. The most remarkable improvements have arisen from optimising the uniformity of lithium plating and stripping, with a significant milestone accomplished through the incorporation of interlayers in anodeless configurations. Specifically, the utilisation of an Ag-C interlayer[101,108,110,168,176] enables to reach currents of up to 3.4 mA/cm², while an AgF conversion-type interlayer achieved capacities of up to 9.7 mAh/cm² at room temperature.[170] Consequently, future efforts to achieve higher current densities with LMAs should focus on the study of similar micrometric interlayers M-C, MF_x or MN_x, with other metal M such as Mg, Si, Al, etc., that can easily be spray coated[168] onto the SE or current collector.

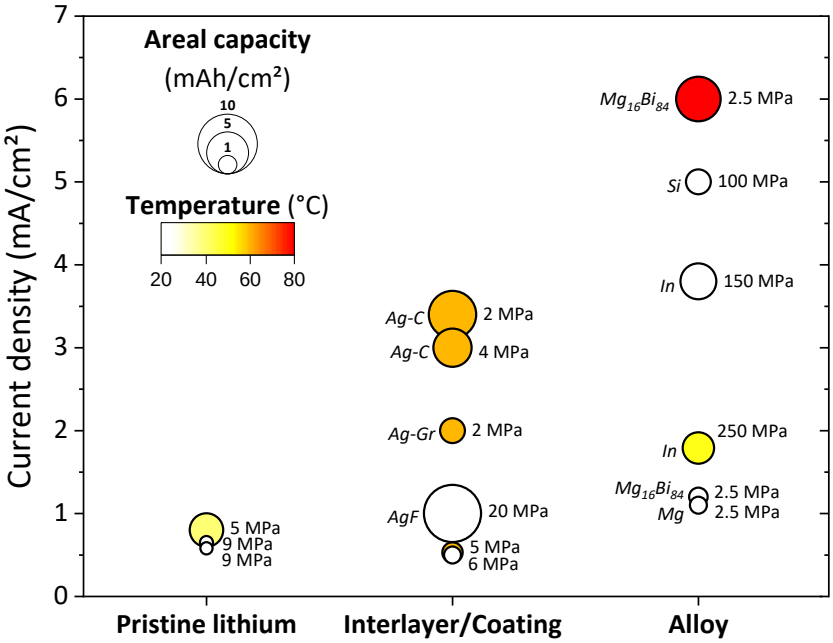

Figure 4.16. Current densities reported in the literature for the LPSCl-based systems depending on the strategy adopted for stabilising the Li//SE interface (pristine lithium, interlayer or alloy). Data is agglomerated from our experimental data and references[101,108,110,117,150,163,168,169,177–180].

4.5 – Chapter conclusion

In summary, Chapter 4 has provided a comprehensive exploration of strategies and considerations related to the integration of lithium metal anodes (LMAs) into ASSBs. We have presented direct evidence of the ability to cycle low pressure ASSB with a Li anode. This was made possible by the use of cathodes capable of cycling under very low pressures that we have previously explored in Chapter 2 and Chapter 3. Despite this achievement, such a study had the merit to highlight the challenges associated with the implementation of LMAs.

Faced with these challenges, based on our own experience, we drawn attention to the accuracy of critical current density (CCD) measurements in ASSBs, a key metric often used to assess the improved SE//Li interface performance resulting from various strategies. Understanding the parameters influencing the CCD, we then provided in all modesty recommendations to enhance the accuracy of its measurement. Finally, we looked at current strategies and promising perspectives for enabling the use of LMAs in ASSBs. This encompassed the design of new solid electrolytes, the use of alloy anodes, and the application of coatings and interlayers from which the latter showed the most remarkable improvements in performance, with the use of Ag-based interlayers.

General conclusions and perspectives

Through this thesis, we investigated strategies to enable **low-pressure operation** of positive electrodes and we reported on two different approaches, which enable to significantly decrease the necessary cycling pressure in all-solid-sate batteries.

Given the susceptibility of composite electrodes to contact losses between the solid electrolytes and the active material, we begin by incorporating a **halide-based solid electrolyte**. This choice was motivated by the collective advantages of its highly ductile nature, good ionic conductivity, robust potential stability and fine particle size, all of which were expected to improve interfacial contacts within the electrode during cycling. In particular, our investigation demonstrated that the incorporation of a fine $Li_3YBr_2Cl_4$ halide solid electrolyte in conjunction with the NMC622 active material in the cathode composite enables the remarkable achievement of cycling ASSBs at room temperature with a stack pressure as low as 0.1 MPa. This stands in stark contrast to the poor performance we observed for the typical sulphide argyrodite electrolyte-based solid-state batteries under low-pressure conditions.

Despite achieving remarkably low cycling pressures, this study clearly showed signs of electrochemical degradation between the solid electrolyte and the high-potential cathode materials used. Consequently, future research endeavours may benefit from directing their efforts toward the development of novel ductile solid electrolytes characterised by wider potential stability windows.

Inspired by the **solid electrolyte-free concept** developed in various existing literature works, we have applied this approach to low-pressure cycling. The notable advantage of this design stems from the expectation that, in contrast to composite electrodes, a solid electrolyte-free electrode should exhibit uniform volume changes throughout the entire electrode thickness, thereby mitigating interparticle contact losses. Necessitating a ductile active material for sufficient compaction through cold pressing, we settled on a Ti-based sulphide active material, in particular the O3-Li_xTiS_2 (LTS) phase, which upon milling transformed from a crystalline platelet-like shape of tens of micron in size to an amorphous shapeless submicrometric particle morphology. The alteration in morphology was imperative to reduce the tortuosity of Li^+ pathways within the electrode. Employing this modified material, our study demonstrated that a milling duration of 90 minutes was sufficient to achieve performance levels comparable to those attained with a composite electrode

comprising solid electrolyte and the pristine LTS. Furthermore, when cycled at progressively decreasing stack pressures, we observed no discernible decrease in capacity retention associated with pressure changes down to 0.1 MPa.

On the basis of these remarkable results, we subsequently extended our survey to evaluate this concept with other materials that displayed high ductility. Encouraged by the low-pressure results obtained with halide solid electrolyte-based composites, we sought to incorporate halide-based cathode material in a solid electrolyte-free system. As an initial proof of concept, we explored the utilisation of the cubic Li_2FeCl_4 phase, which displays an operating voltage higher than Ti-based sulphides while theoretically having an ionic conductivity sufficiently high to bypass the use of an ionic conductor in our composites. Although our initial attempts were unsuccessful, this concept deserves further exploration with other materials displaying low hardness. In this regard, we propose the consideration of other halide-based active materials. Notably, one compelling idea is to explore the utilisation of the Li_3TiCl_6 phase, which exhibits an even higher ionic conductivity, comparable to that of conventional solid electrolytes.

Having demonstrated the good cyclability of cathodes under very low-pressure conditions, we then adventured into the next step in line, which is the incorporation of a high capacity anode, in particular, the **lithium metal anode**. Utilising the cathode systems employed throughout this thesis to facilitate low-pressure cycling, we successfully incorporated and cycled lithium anodes. Nonetheless, this achievement has also highlighted remaining challenges associated with cycling lithium metal, namely dendrites growth. This observation brought back the problem of existing analytical methods for assessing the performance of the solid electrolyte/lithium metal interface, which traditionally revolve around the determination of the critical current density. Our experience, coupled with insights from recent research, brought to light the clear limitations of this technique in assessing the stability of this interface. As a result, we propose a series of recommendations to mitigate this issue. We conclude by offering a brief overview of the existing strategies employed to effectively integrate and consistently cycle lithium metal anodes within all-solid-state batteries, spanning from bare SE//Li interface to alloys, coatings and interlayers.

Moving forward, it is evident that novel strategies regarding the design of interfaces will be necessary in the successful implementation of high capacity anodes. As a perspective,

it becomes apparent that alloy-based approaches call for further investigations. In particular, in light of recent literature reports, we suggest the exploration of magnesium, either as an alloying compound or in small quantities in a carbonaceous interlayer to improve the uniformity of the plating and stripping.

Finally, the advances made in this PhD have strengthened confidence in the practical feasibility of building all-solid-state batteries over the next decade. These advancements are particularly significant at a time when the development of all-solid-state batteries often faces compromises in favour of intermediate solutions that incorporate either liquids, gels, or polymers in their design.

Appendix

A2 – Supplementary information for Chapter 2

A2.1 – Materials and methods

Materials. $Li_3YBr_2Cl_4$ (LYBC) was kindly provided by Saint-Gobain Recherche Paris. Fine Li_6PS_5Cl (LPSCl) solid electrolyte was obtained from NEI Corporation.

SS-LPSCl was prepared through a solid-state synthesis consisting in the annealing of a stoichiometric mixture of Li_2S, P_2S_5 and LiCl. The powders were first thoroughly mixed in an agate mortar before being transferred to alumina crucibles. The crucibles were then sealed under vacuum in a quartz tube before being heated at 550°C (5°C/min heating rate) for 72h. The resulting product was recovered and crushed by hand in a mortar before being used in cells.

Li_3InCl_6 (LIC) was synthesized by a water-assisted synthesis. A stoichiometric quantity of the precursors (LiCl and $InCl_3$) was first dissolved in water and stirred overnight; the solution was then natural dried in air at 100°C and subsequently under a dynamic vacuum at 100°C and then at 200°C for 24h each.

$LiNi_{0.6}Mn_{0.2}Co_{0.2}O_2$ (NMC622 uncoated, monolithic, d_{10} = 3.21 µm, d_{50} = 5.28 µm and d_{90} = 8.47 µm, BET = 0.5 m^2/g) as well as the Co-coated (monolithic, d_{10} = 2.94 µm, d_{50} = 4.91 µm and d_{90} = 7.97 µm, BET = 0.45 m^2/g) and Zr-coated NMC622 (monolithic, ~4 µm) were kindly provided by UMICORE.

Composite preparation. The cathode composites were prepared by mixing NMC622, SE and VGCF in a 66.5/28.5/5 wt.% ratio using two different techniques. Either by hand grinding in a mortar or by planetary ball-milling (Pulverisette 7, FRITSCH) in a 45 mL zirconia jar. In the latter case, the composite was milled for 30 min at 150 rpm with a ball-to-powder mass ratio of 36/1 (5 ZrO_2 balls of 10 mm in diameter for 400 mg of powder). The resulting composite powder was then recuperated and stored in an argon-filled glovebox until further use.

Lithium-indium composites were prepared in a two-step process. Firstly, the appropriate amount of Li and In foils was weighed to achieve a $Li_{0.5}In$ stoichiometry. The foils were then laminated and folded together using a glass tube until the resulting alloy became

brittle. Subsequently, the obtained alloy was mixed with SE (either LPSCl or LYBC) in a 60% LiIn to 40% SE weight ratio in an agate mortar, until a homogeneous fine powder was obtained.

All-solid-state cell assembly. ASSBs were fabricated within a homemade two-electrode cell developed in-house consisting in a cylindrical polyetherimide body and two stainless steel pistons of 8 mm diameter as current collector.

In the case of cells based on solely LPSCl or LYBC, the assembly procedure is as follows. First, 30 mg of SE was cold-pressed in the cell body at 1 t/cm² for a few seconds. Then, the adequate amounts of NMC cathode and LiIn anode composites prepared with the same SE were homogeneously spread on opposite sides of the separator and the stack was densified at 4 t/cm² for 15 minutes.

For cells made with LIC//LPSCl, LYBC//LPSCl or LIC//LYBC bilayer separators (with electrolytes designated as SE1//SE2 hereafter), a similar protocol is adopted. First 35 mg of SE1 was cold-pressed in the cell at 1 t/cm², the inside of cell was then cleaned of any remaining loose SE1 powder before adding 15 mg of SE2 and pressing at 1 t/cm². Following that, the anode composite prepared with SE2 was spread and pressed on the SE2 surface layer. The SE1-based cathode composite was then added on the opposite side of the separator (on the SE1 surface) and the whole stack was densified at 4 t/cm² for 15 minutes. Loadings are specified in the main text for each measurement and the typical weight ratio for cathode/anode composites is 10/35.

Finally, the cells were closed differently depending on the stack pressures desired. High-pressure cells were closed at 100 MPa by tightening the six top cell screws at a torque of 2.3 N.m. The low-pressure cells were cycled using the homemade frame comprising a force sensor and a screw allowing us to set the initial stack pressure (Figure 2.4). All assembly procedures were carried out in an Argon-filled glovebox ([O2] < 1 ppm, [H2O] < 1 ppm).

Ionic conductivity measurement was performed as follow. A pellet of about 100 mg (~1 mm thick) was densified at 4 t/cm² for 3 min in a die set and the obtained pellet was then recovered, measured and weighted before being transferred to a cell with carbon paper on each side to improve contacts. Electrochemical impedance spectroscopy (PEIS) was then performed with an excitation amplitude of 10 mV in the frequency range 5 MHz – 1 Hz under

a pressure of 100 MPa on a Biologic MTZ-35 device. The impedance spectra were fitted with a simple R/CPE-CPE model and the conductivity was calculated with the following equation.

$$\sigma_{ion} = \frac{l}{R \cdot A} \qquad \text{Equation A2.1}$$

where *l* is the pellet thickness, *R* the total resistance measured by EIS and *A* the surface area of the pellet.

Electrochemical stability window determination. To determine the electrochemical potential window of LYBC, linear sweep voltammetry (LSV) was conducted. 8 mg of LYBC:VGCF composite, prepared by hand grinding LYBC and VGCF in a 95:5 wt.% ratio using an agate mortar, was utilised. The measurement was performed in the previously mentioned typical cell setup, consisting of LYBC:VGCF//LYBC//$Li_{0.5}In$:LYBC at a pressure of 100 MPa.

Galvanostatic cycling, unless specified, were conducted at room temperature within the potential range of 2.1-3.6 V vs. Li^+/LiIn, employing a C/20 rate (where C represents 1 mole of Li per mole of active material in 1 hour).

Cell polarization *ΔV* were obtained through the difference of the charge and discharge average potentials calculated using the following equation.

$$\Delta V = \frac{\int_0^{Q_{charge}} V dQ}{Q_{charge}} - \frac{\int_0^{Q_{discharge}} V dQ}{Q_{discharge}} \qquad \text{Equation A2.2}$$

where Q_{charge} and $Q_{discharge}$ represent charge and discharge capacity respectively.

Capacity decay was calculated from one cycle to the other using the following equation, for cycle *n*:

$$Decay\ (\%) = \frac{Q_{n-1} - Q_n}{Q_n} * 100 \qquad \text{Equation A2.3}$$

where Q_n corresponds to the discharge capacity of cycle *n*.

Standard rate capability measurements were conducted by initially performing a cycle at C/20, followed by varying the discharge rate from C/20 to 5C, while the charging rate was kept in CCCV mode (C/10 in CC and down to C/50 in CV). Three cycles were conducted at each rate, and the average discharge capacity was utilised to assess the rate capability. For the study in pressure, the first cycle was always performed at 10 MPa (except for pressure > 10 MPa) to ensure successful cell assembly.

"Signature curve" method for rate capability. This method consists in discharging the material at incrementally lower currents. Then the obtained cumulative capacities correspond to the rate capabilities of the material. Experimentally, the cell was first charged to 3.6 V vs Li^+/LiIn in CCCV mode (C/10 in CC and down to C/50 in CV). Then the cell was discharged down to 2.1 V vs Li^+/LiIn with incrementally lower currents, starting from 5C to C/20, with 30 seconds rest between each current pulse.

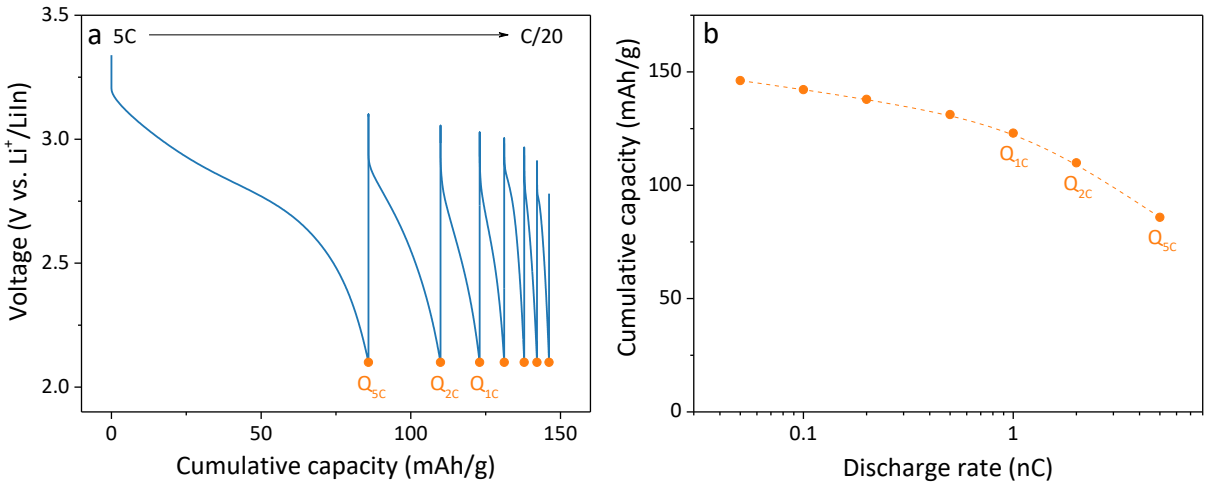

Figure A2.1. (a) Typical galvanostatic response of a signature curve at rates ranging from 5C to C/20 and (b) corresponding rate capabilities obtained by extracting the cumulative capacities from the signature curve.

SE compatibility. The compatibility of SEs was assessed using two different methods. On one hand, in a LYBC//LPSCl bilayer through impedance evolution. The bilayer was prepared by first cold-pressing 30 mg of LYBC followed by the addition of 30 mg of LPSCl. The stack was then densified at 4 t/cm² for 3 min and transferred into a cell, which was closed at 100 MPa. Subsequently, the cell underwent aging at 80°C for varying durations, and the impedance evolution was monitored using PEIS at 25°C, following the aforementioned protocol. On another hand, a mixture of LPSCl and LYBC was prepared by hand grinding the SEs in a 1:1 weight ratio. The powder was then pressed at 4 t/cm² for 3 minutes and the recovered pellet was placed in a quartz tube that was subsequently sealed under high vacuum. The tube was then heated at 150°C for 11 days to reach the thermodynamic equilibrium between the two SE. Their reactivity was then assessed through XRD and conductivity measurements.

Scanning electron microscopy (SEM) and **Energy Dispersive X-ray (EDX) mapping** were performed on pellet cross sections. The pellets were cut by simply braking them. Micrographs were obtained on a FEI Quanta200F scanning electron microscope equipped with a CPER AGROBIO 2012 EDX detector for chemical analysis. Samples were prepared and placed

on the holder inside an Ar-filled glovebox and subsequently transferred using a special homemade transfer chamber to avoid exposure to air and moisture.

Powder X-ray diffraction (XRD) analysis was conducted utilizing an airtight holder fitted with a beryllium (Be) window. The XRD patterns were recorded in reflection mode, employing the Bragg−Brentano geometry, and data acquisition was carried out with a Bruker D8 ADVANCE diffractometer. A copper (Cu) Kα X-ray source (λ_1 = 1.54056 Å and λ_2 = 1.54439 Å) was utilized in conjunction with a LynxEye detector for data collection.

A2.2 – Supplementary figures

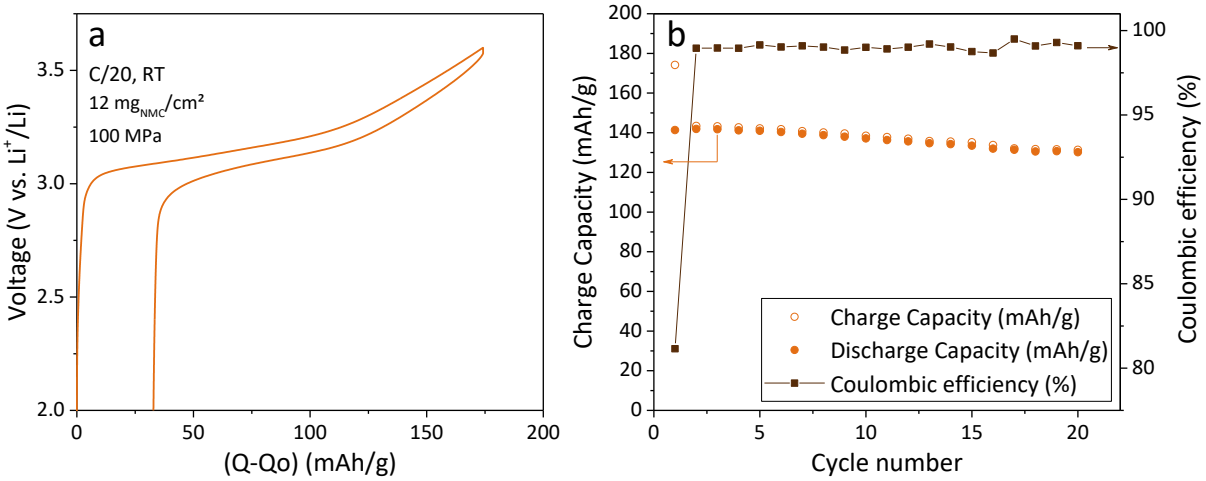

Figure A2.2. (a) First galvanostatic cycle and (b) capacity retention of a Zr-coated NMC622 cycled in the LPSCl-based cell. Tests were performed at C/20, at RT under 100 MPa of pressure.

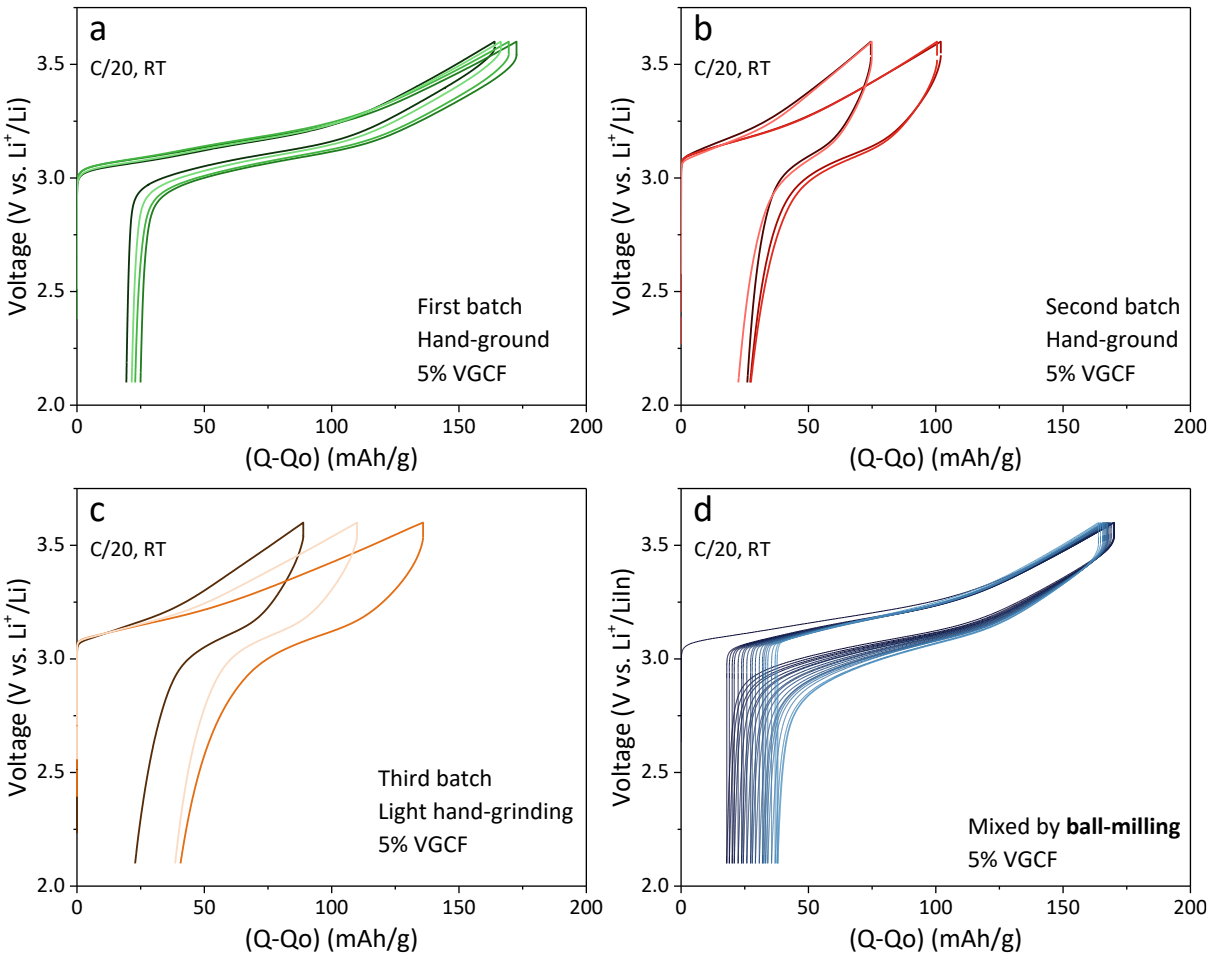

Figure A2.3. First galvanostatic cycles of LIC-based composites cells at low pressure of 10 MPa as a function of the composite batch used. The composites used were: (a) the first, (b) second and (c) third composite batches prepared by hand grinding using the same procedure and (d) a composite prepared by planetary ball milling. These results highlight the importance of the composite preparation process on the performances and repeatability of cells.

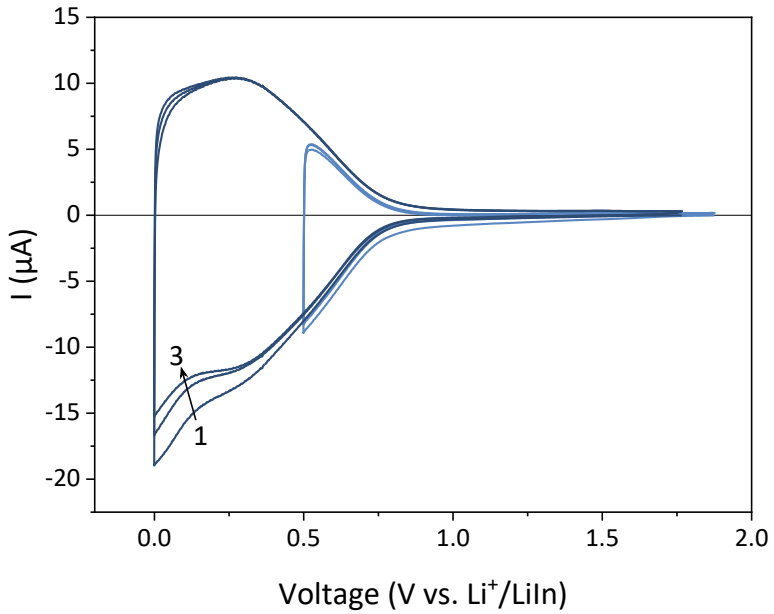

Figure A2.4. Cyclic voltammetry measurement of LYBC/VGCF (95/5wt.%) composite from OCV to 0.5 V (in light blue) and to 0 V vs. Li^+/Li (dark blue).

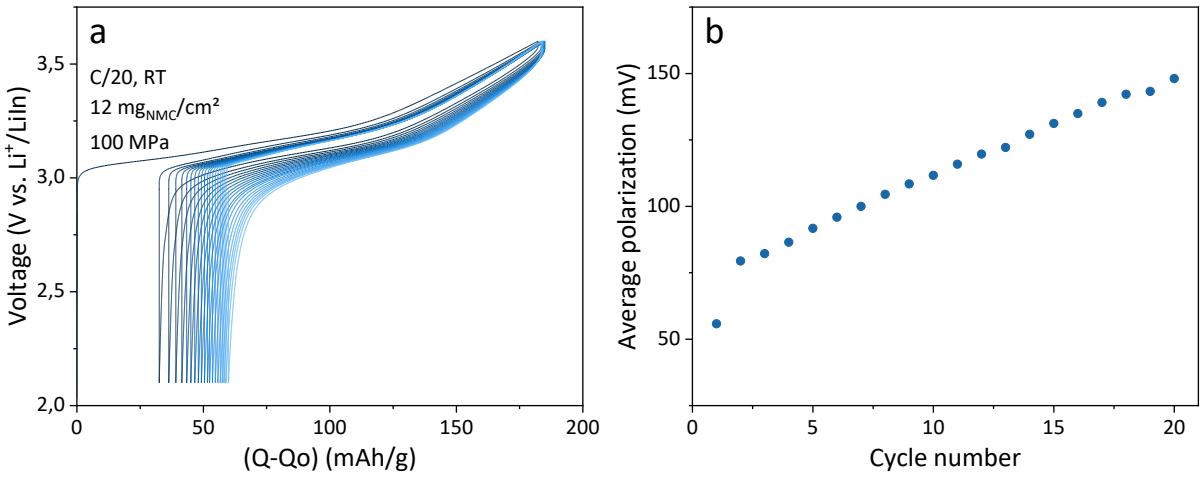

Figure A2.5. (a) Galvanostatic cycling and (b) polarization over cycling of an LYBC-based cathode composite cycled at C/20 and a pressure of 100 MPa at RT.

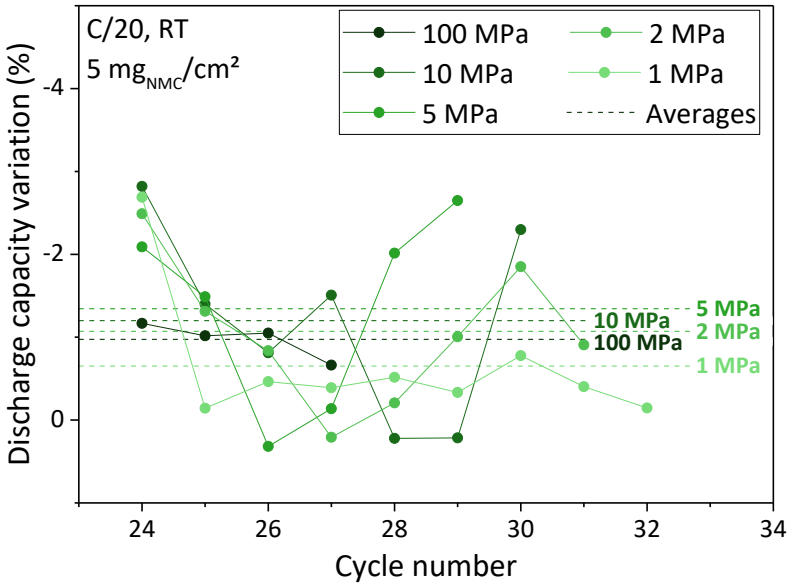

Figure A2.6. Decay rate of NMC//LYBC//LPSCl//LiIn cells as a function of the pressure. Dash lines represent the averages over the entire dataset for each cell. Measurements were performed after rate capability measurements.

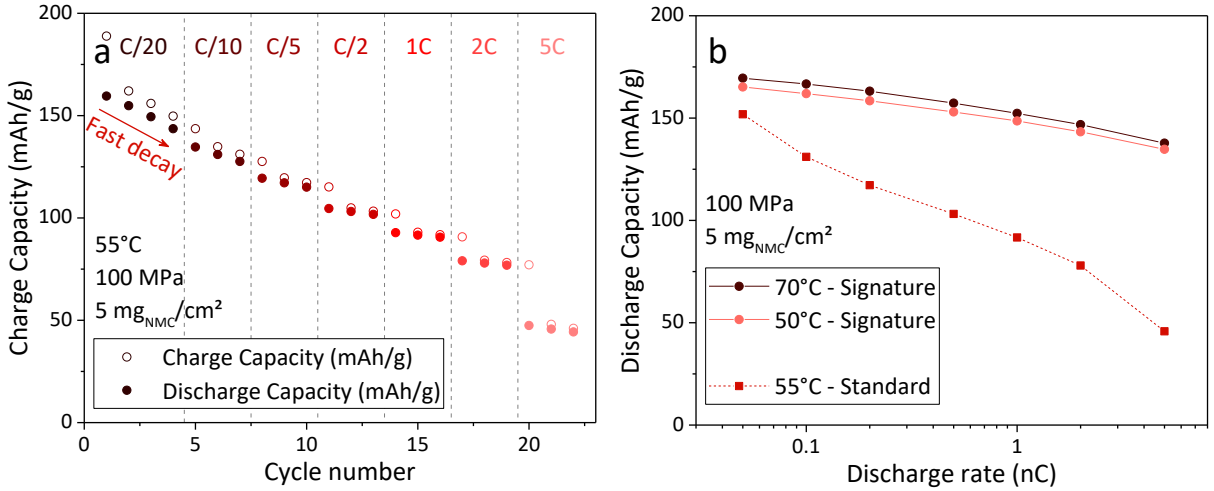

Figure A2.7. (a) Capacity retention of the rate capability measurement at 55°C using the standard protocol and (b) associated rate capabilities at 55°C compared to the rate capabilities at 50°C and 70°C measured using the signature curve protocol. The standard rate capability measurement at 55°C clearly displays a fast decay at C/20, much larger than the nominal 1%/cycle at RT.

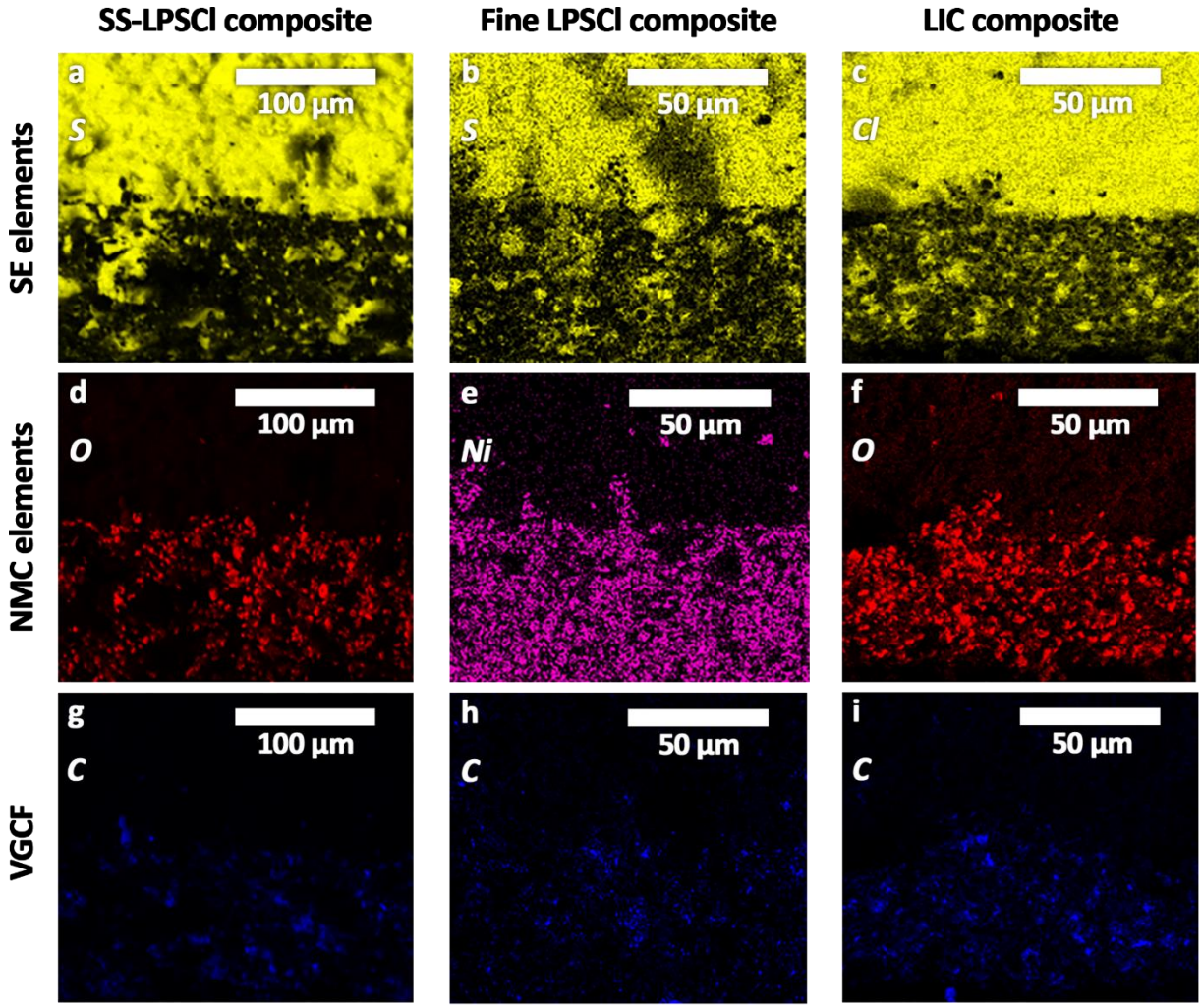

Figure A2.8. EDX mapping of single elements for the cross section pellets imaging. (a-c), (d-f) and (g-i) correspond to SE (LPSCl or LIC), NMC and VGCF elements, respectively, in composite based on SS-LPSCl (in a,d and g), fine LPSCl (in b, e and h) and LIC (in c, f and i).

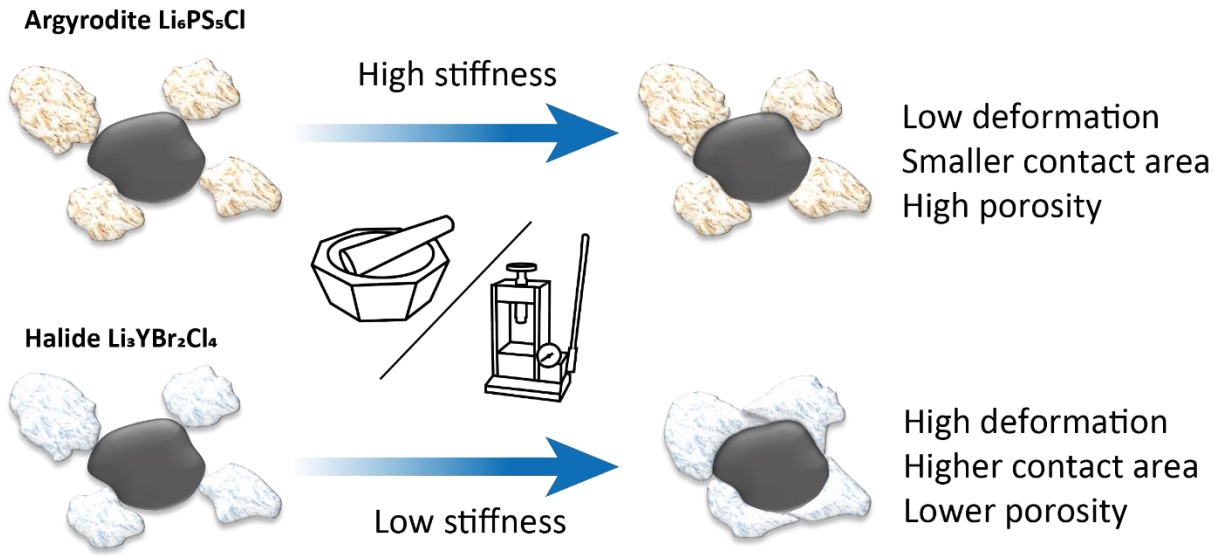

Figure A2.9. Schematic of SE (LPSCl at the top and LYBC at the bottom) deformation during composite preparation or densification depending on the stiffness of the material.

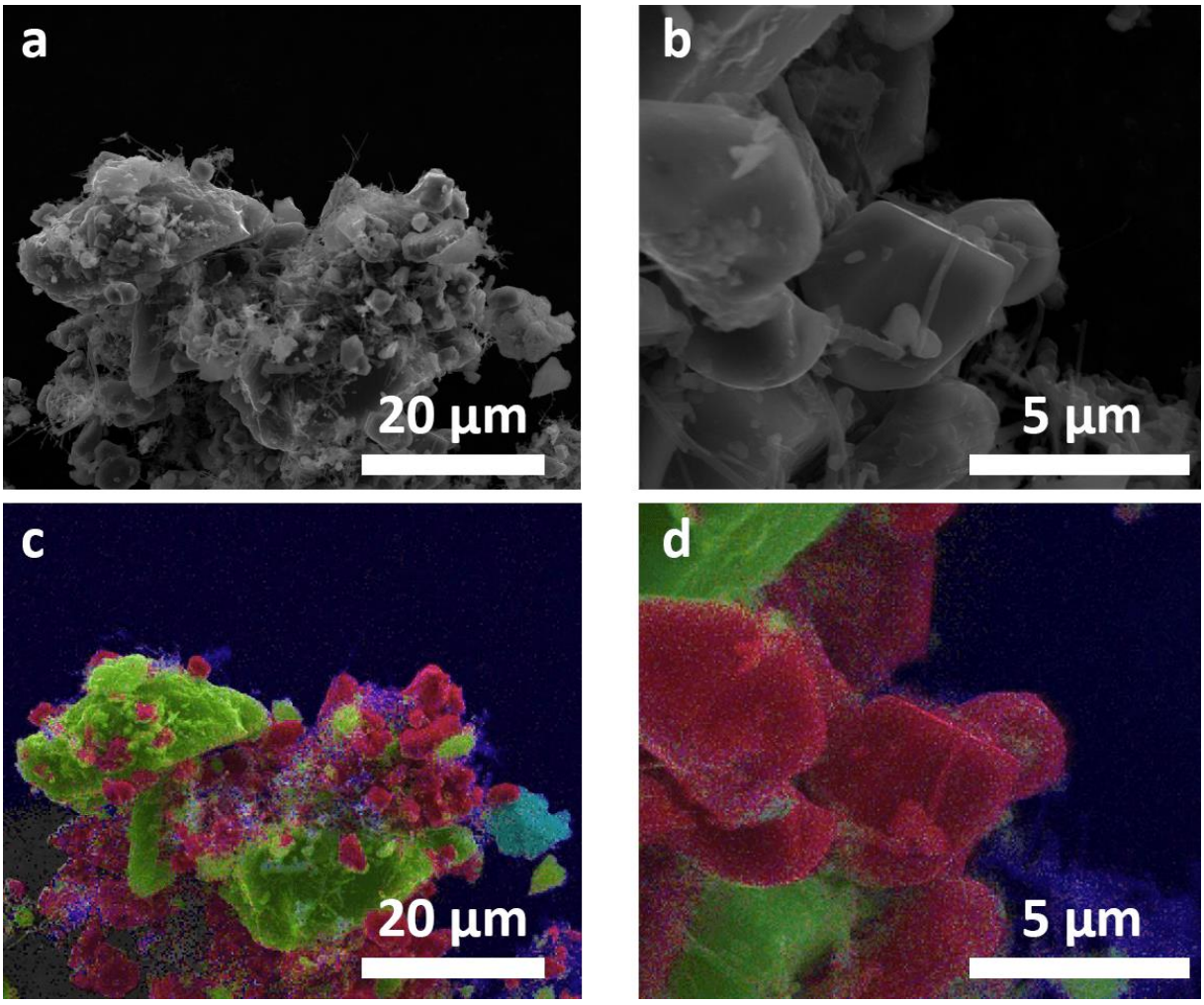

Figure A2.10.SEM and EDX imaging of SS-LPSCl-based cathode composite powders to assess adhesion. Green and yellow coloured particles corresponds to SE elements (P, S, Cl and In), pink/red coloured particles corresponds to NMC elements (Ni, Mn, Co, O) and blue regions to C.

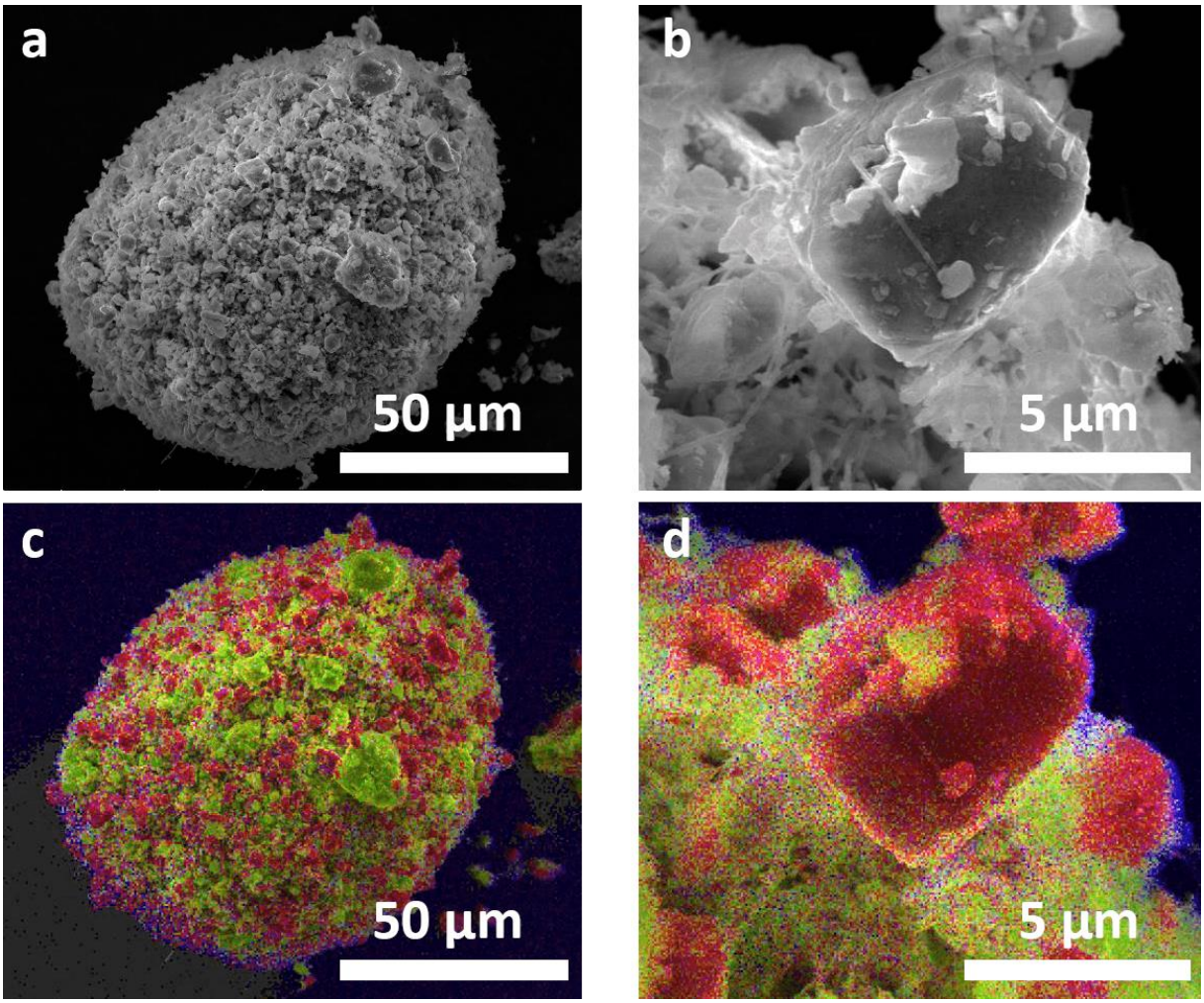

Figure A2.11. SEM and EDX imaging of LIC-based cathode composite powders to assess adhesion. Green and yellow coloured particles corresponds to SE elements (P, S, Cl and In), pink/red coloured particles corresponds to NMC elements (Ni, Mn, Co, O) and blue regions to C.

A3 – Supplementary information for Chapter 3

A3.1 – Materials and methods

Materials. O1-TiS_2 was purchased from Sigma. O3-Li_xTiS_2 phase was synthesized, following Colbow *et al.* methodology,[138] from a high temperature (800°C) solid-state synthesis by reacting stoichiometric amounts of thoroughly mixed Ti and Li_2S powders in evacuated quartz tubes. Ti_2S_4 was obtained through the removal of Cu from the $CuTi_2S_4$ phase using Br_2 in acetonitrile.[181]

Rock-salt Li_2TiS_3 was prepared through a mechanochemical synthesis, reacting stoichiometric amount of Li_2S and TiS_2 following the previously described protocol.[182] In brief, 500 mg of a stoichiometric mixture of commercially available Li_2S and TiS_2 were milled for 25 hours at 500 RPM in a 45 mL ZrO_2 jar with 12 balls (10 mm in diameter) in a Pulverisette 7 planetary ball-mill from FRITSCH.

Lithium-rich layered $Li_{1.2}Ti_{0.4}^{4+}Ti_{0.4}^{3+}S_2$ was synthesized following the procedure previously reported[183] by reacting stoichiometric amount of Li_2S, and TiS_2 in a vacuum-sealed quartz tube at 750 °C for 48 hours with a heating rate of 1°C/min.

O1-$LiTiSe_2$ was prepared through a solid-sate synthesis by reacting a stoichiometric amount of in-house made $LiSe_2$ and commercial Ti and Se powders in a vacuum-sealed quartz tube at 750°C for 48 hours with a heating rate of 1°C/min. The homemade $LiSe_2$ was synthesized by solid-state synthesis, reacting Li and Se powders at 500°C for 48 hours with a heating rate of 1°C/min.

Cubic Li_2FeCl_4 was prepared through a mechano-chemical synthesis. A stoichiometric amount of LiCl and $FeCl_2$ were weighted and transferred to a 45mL ZrO2 ball-milling jar along with 72 balls of 5 mm in diameter, achieving a 30/1 ball-to-powder mass ratio. The mixture was then subjected to ball milling (in a Pulverisette 7, FRITSCH) at a rotation speed of 500 RPM for a duration of 10 hours.

Li_6PS_5Cl (LPSCl) was prepared as described previously in the literature[123]. Briefly, a solid-state synthesis was carried out by reacting stoichiometric amounts of Li_2S, P_2S_5 and LiCl reagent at 550°C for 72h in evacuated quartz tubes. $Li_3YBr_2Cl_4$ (LYBC) was kindly provided by Saint-Gobain Recherche Paris.

Ball milling of AM. Materials were milled in a stainless steel SPEX grinder for the adequate amount of time by 200 mg batches using 2 stainless steel balls (8 mm in diameter) corresponding to a ball-to-powder mass ratio of 20/1.

Composite preparation. The cathode composite of Ti-based sulphides were prepared by mixing the AM and SE in a 70/30 wt.% ratio by hand grinding for around 10 minutes until an homogeneous mixture was obtained. Composites of halide-based cathode materials were composed of either AM, SE and VGCF or AM and VGCF in ratios of 66.5/28.5/5 or 95/5 wt.% and fabricated by hand grinding. The resulting composites powder was then recuperated and stored in an argon-filled glovebox until further use.

Lithium-indium composite was prepared in a two-step process. Firstly, the appropriate amount of Li and In foils was weighed to achieve either a $Li_{0.5}In$ or $Li_{0.8}In$ stoichiometry. The foils were then laminated and folded together using a glass tube until the resulting alloy became brittle. Subsequently, the obtained alloy was mixed with SE (either LPSCl or LYBC) in a 60% LiIn to 40% SE weight ratio in an agate mortar, until a homogeneous powder was obtained.

Liquid cells were assembled using Swagelock hardware and are made of the O3-Li_xTiS_2 (100%) as positive electrode, either in the pristine or ball-milled state, with a Li metal disk as counter electrode and both were separated by a glass fiber Whattman separator soaked in an LP30 electrolyte solution (1M $LiPF_6$ in EC:DMC (1:1 vol)) obtained from Dodochem.

All-solid-state cell assembly. ASSBs were fabricated within a homemade two-electrode cell developed in-house consisting in a cylindrical polyetherimide body and two stainless steel pistons of 8 mm diameter as current collector. Fabrication consists in sandwiching LPSCl SE powder (30 mg) between LiIn/LPSCl (in 60:40 wt.%) composite as counter electrode and the positive electrode. The layers are successively pressed at 1 t/cm² before being densified at 4 t/cm² for 15 min. Finally, following the same protocol as for the cell in Chapter 2, the cells were closed differently depending on the stack pressures desired. High-pressure cells were closed at 100 MPa by tightening the six top cell screws at a torque of 2.3 N.m. The low-pressure cells were cycled using the homemade frame comprising a force sensor and a screw allowing us to set the initial stack pressure.

Three-electrode solid-state cells were fabricated for GITT measurements. They were assembled in an homemade 3-electrode setup modified from the 2-electrode setup as previously published by our group.[184] Unlike in ref[184], first, lithium metal was rolled down to 100 µm and, as depicted in the Figure A3.1, a ring (13 and 8 mm in outer and inner diameter respectively) was punched and clamped between the reference current collector and the plastic body to use as a reference electrode. Then, the cell stack was constructed as described above for the two-electrode cell setup making sure that enough SE was used to entirely cover the Li metal ring reference electrode.

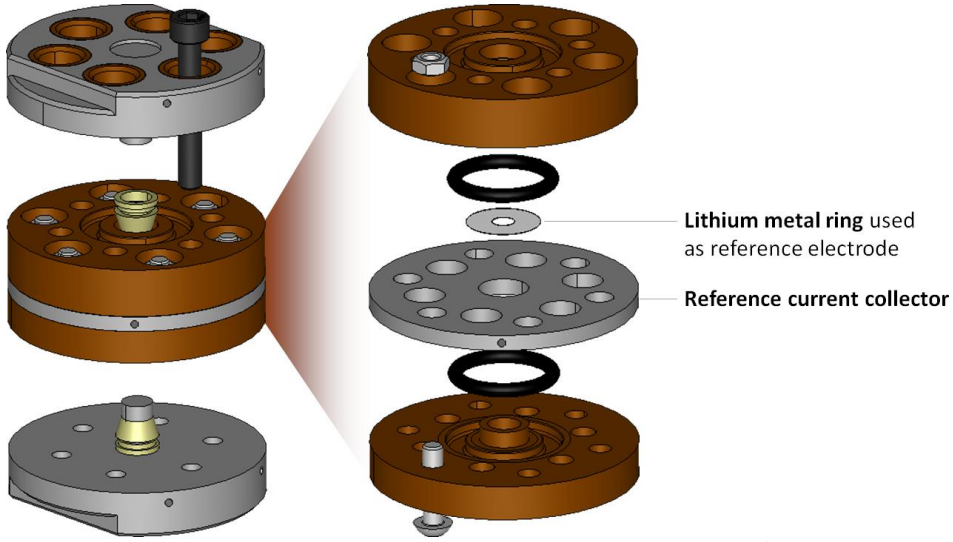

Figure A3.1. Schematic of the three-electrode cell inner parts. Adapted from ref[184].

All assembly procedures were carried out in an Argon-filled glovebox ([O2] < 1 ppm, [H2O] < 1 ppm).

Ionic conductivity measurement was performed as follow. A pellet of about 100 mg (~1 mm thick) was densified at 4 t/cm² for 3 min in a die set and the obtained pellet was then recovered, measured and weighted before being transferred to a cell with carbon paper on each side to improve contacts. Electrochemical impedance spectroscopy (PEIS) was then performed with an excitation amplitude of 10 mV in the frequency range 5 MHz – 1 Hz under a pressure of 100 MPa on a Biologic MTZ-35 device. The impedance spectra were fitted with a simple R/CPE-CPE model and the conductivity was calculated with the following equation.

$$\sigma_{ion} = \frac{l}{R \cdot A} \qquad \text{Equation A3. 1}$$

where *l* is the pellet thickness, *R* the total resistance measured by EIS and *A* the surface area of the pellet.

Electronic conductivity measurements were conducted using either of the specified technique: the chronopotentiometry or DC polarization technique under a pressure of 100 MPa.

For Ti-based sulphide materials, the chronopotentiometry technique was employed. Pellets consisting of CAM fibrillated with 1.3 wt.% PTFE to enhance their mechanical strength were pressed under 4 t/cm². To accurately assess the electronic conductivity, 4-wire measurements were employed, which effectively eliminated any impedance contribution from the cable. Additionally, a blank measurement was carried out to eliminate any influence from the cell itself.

For halide-based CAM, the DC polarization technique was adopted and pellets of around 100 mg of material were densified for 3 minutes under 4 t/cm².

Galvanostatic cycling was carried out at room temperature and at desired potential window and C-rates (with C corresponding to 1 mol of Li per mole of active material in 1 h). Unless specified, cycling was performed with loadings of 12-13 mg_{AM}/cm^2 and a stack pressure of 100 MPa.

Galvanostatic intermittent titration technique. Two different pulse durations were used for the pristine and the ball-milled samples due to the much lower diffusion of the first. Pulses at a rate of C/20 were applied for 10 or 30 minutes for the pristine or ball-milled samples respectively, followed by a rest period of 5 hours. The apparent Li^+ diffusion coefficient D_{app} was then calculated via Equation A3.2.

$$D_{app} = \frac{4}{\pi\tau}\left(\frac{mV_m}{MS}\right)^2\left(\frac{\Delta E_s}{\Delta E_t}\right)^2 \qquad \text{Equation A3.2}$$

where m is the mass, V_m the molar volume and M the molar mass of the active material, S the contact area between the SE and the cathode layer (in SE-free electrode), ΔE_s the steady-state voltage change, ΔE_t the transient voltage change when current is applied and τ the current pulse duration.

"Signature curve" method for rate capability. Rate capabilities were measured on typical 2-electrode cells by the "Signature curve" method that consists in discharging the material at incrementally lower currents. Then the obtained cumulative capacities correspond to the rate capabilities of the material. Experimentally, the cell was first charged to 2.6 V vs

Li^+/LiIn in CCCV mode (C/20 in CC and down to C/200 in CV). Then the cell was discharged down to 0.8 V vs Li^+/LiIn with incrementally lower currents, starting from 5C to C/200, with 30 minutes rest between each current pulse.

All electrochemical measurements were conducted on Biologic devices (VMP3 potentiostats or BCS-805 cyclers) devices controlled by EC-Lab or BT-Lab software.

Scanning electron microscopy (SEM) was performed on powders and pellet cross sections. For ex-situ measurements, cells were cycled to the desired potential, then disassembled and pellets were finally extracted. The pellets were cut by simply braking them. Micrographs were obtained on a FEI Quanta200F scanning electron microscope equipped. Samples were prepared and placed on the holder inside an Ar-filled glovebox and subsequently transferred into the SEM chamber. The transfer was as fast as possible to limit the exposure to air and moisture.

Powder X-ray diffraction (XRD) analysis was conducted utilising an airtight holder fitted with a beryllium (Be) window. The XRD patterns were recorded in reflection mode, employing the Bragg−Brentano geometry, and data acquisition was carried out with a Bruker D8 ADVANCE diffractometer. A copper (Cu) Kα X-ray source (λ_1 = 1.54056 Å and λ_2 = 1.54439 Å) was utilised in conjunction with a LynxEye detector for data collection.

***Operando* X-ray powder diffraction** (XRD) was performed in an airtight electrochemical cell equipped with a Be window. XRD patterns were recorded using the same methods as described above.

Solid-state NMR experiments were performed on a 4.7 T (200 MHz for ^{1}H) Bruker Avance HD spectrometer equipped with 4 mm Magic Angle Spinning (MAS) probehead tuned to ^{7}Li at 77.8 MHz. The MAS rate was set to 10 kHz, and the bearing and drive gas were 100% N_2, the temperature was regulated and calibrated with the ^{207}Pb shift in lead nitrate. The radiofrequency field was set to 58.5 kHz at 100 W amplifier output power. The ^{7}Li shift was calibrated with a 1 M LiCl aqueous solution and the longitudinal relaxation times were measured with a saturation recovery sequence. The spectra were recorded with 16 transients, with at least 5 T_1 magnetization recovery delays between each. The EXSY spectrum was recorded with 128 transients separated by a 2s delay, and 256 t_1 increments in the indirect

dimension. The sweepwidth of the indirect dimension was set to 10 kHz and the exchange delay was set to 50 ms.

A3.2 – Supplementary figures

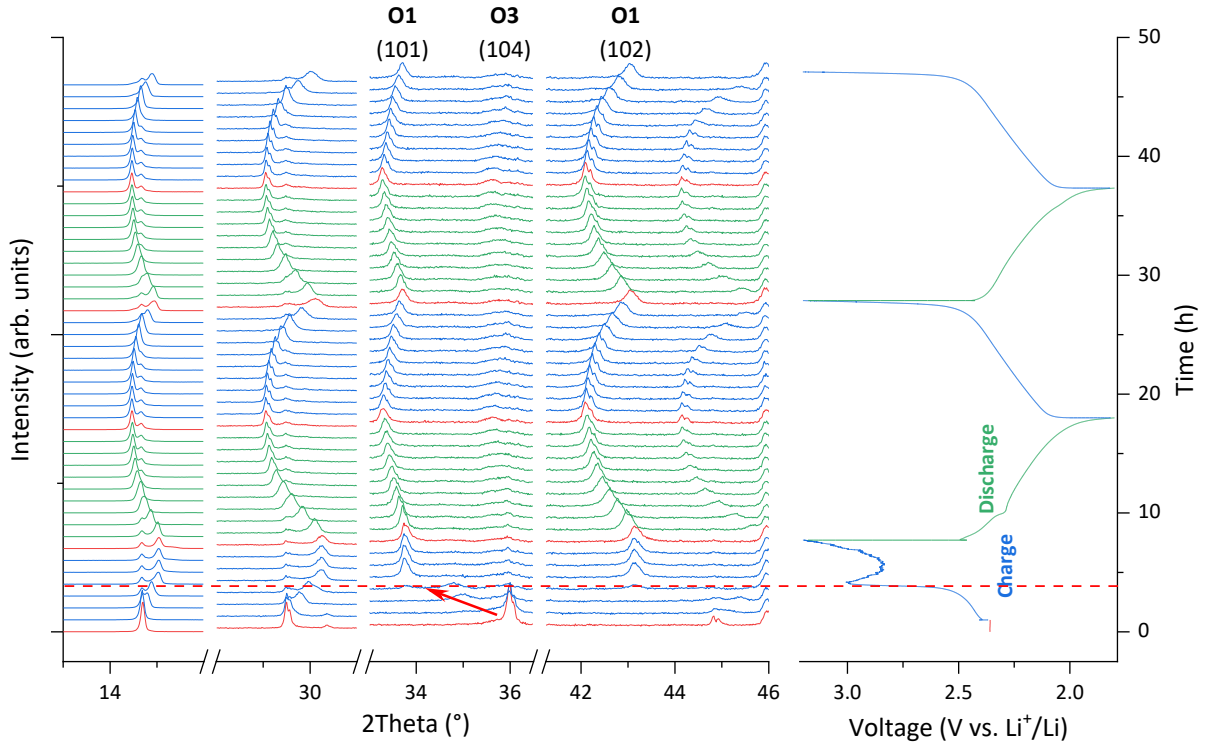

Figure A3.2. Operando X-ray diffraction operando cycling measurement of a Pristine LTS electrode in liquid cell.

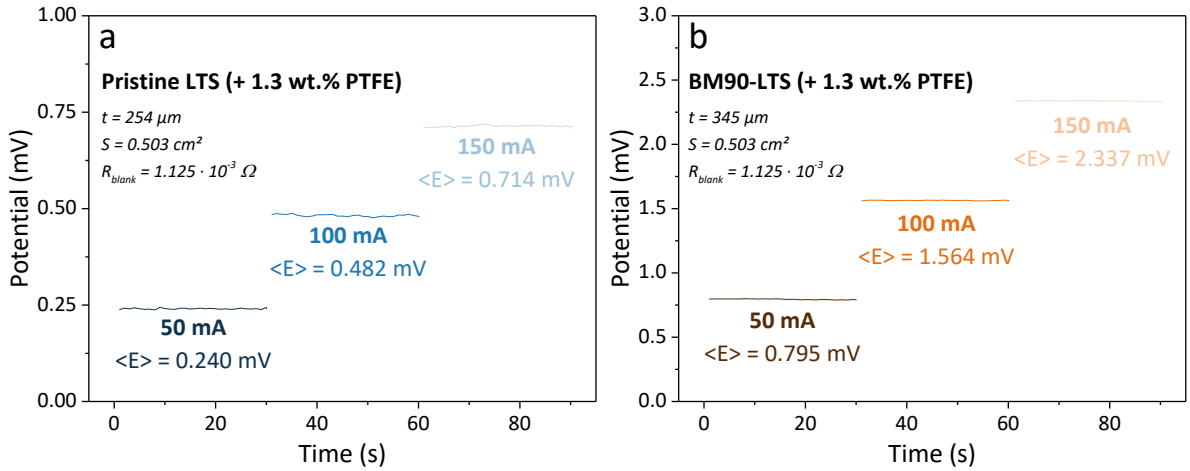

Figure A3.3. Chronopotentiometry measurements for electronic conductivity determination of (a) a pristine LTS and (b) a BM90-LTS pellet. Tests were performed at RT under 100 MPa of pressure.

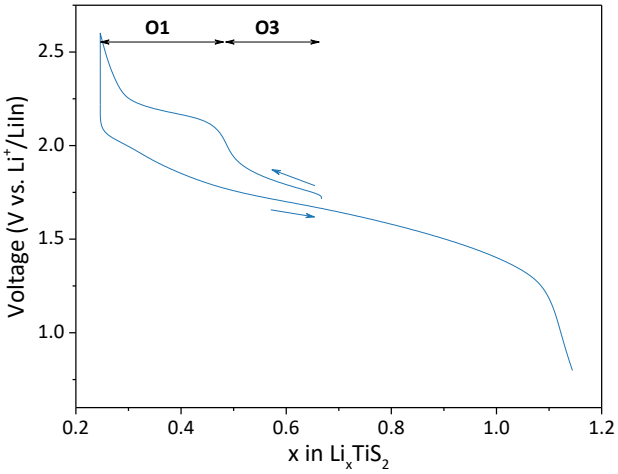

Figure A3.4. First galvanostatic cycle at C/20 of the pristine LTS:LPSCl (70:30) composite against a $Li_{0.8}In$:LPSCl counter electrode in ASSB, revealing two plateaus on the first charge attributed to the O3-O1 phase transition or the LTS.

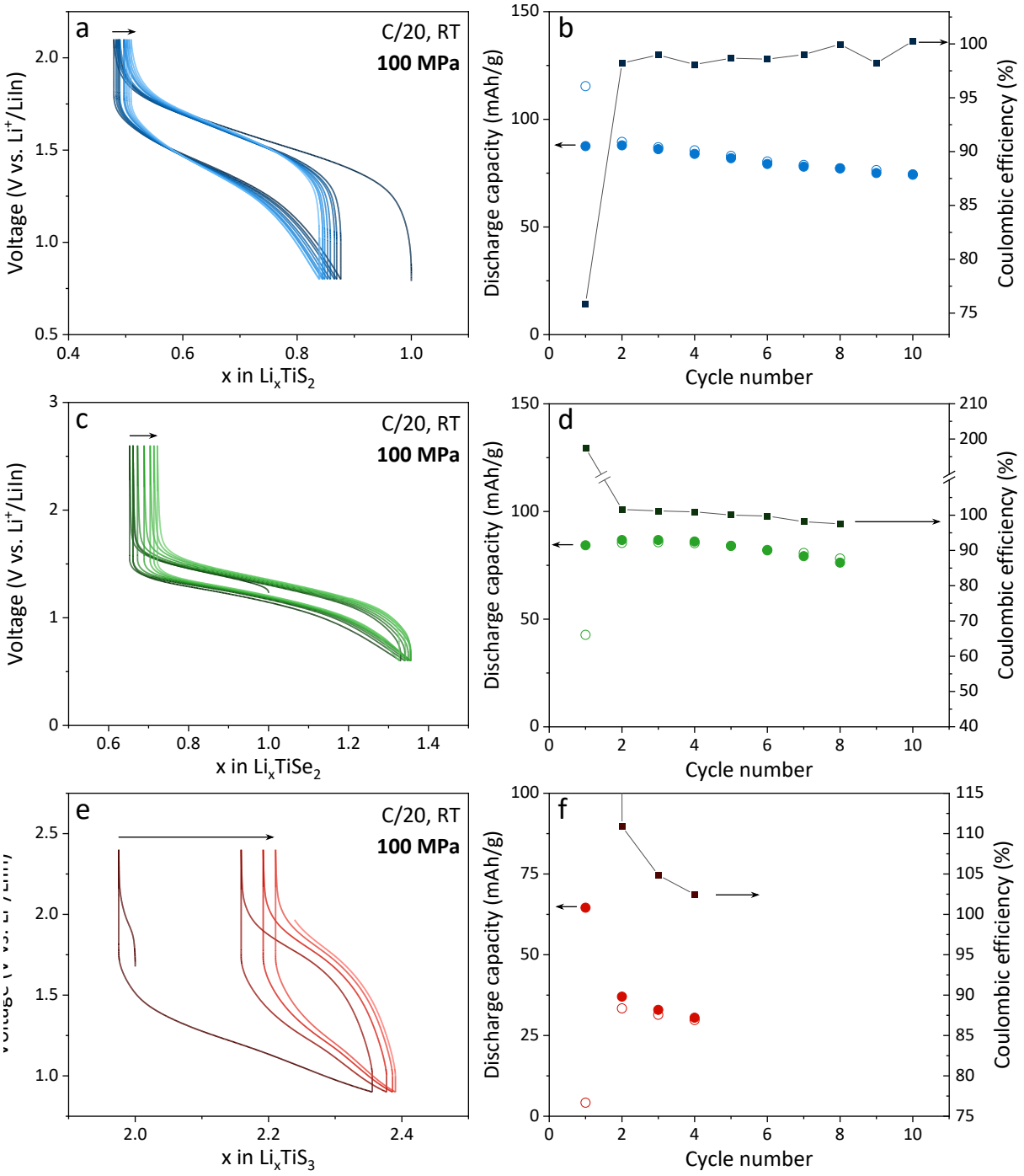

Figure A3.5. Cycling performances in a SE-free configuration of (a and b) a chemically lithiated TiS_2 after ball milling, (c and d) a ball-milled $LiTiSe_2$ and (e and f) a rock-salt Li_2TiS_3. (a-c) Galvanostatic cycling and (d-f) capacity retention of solid-state cells cycling in a SE-free configuration at 100 MPa, RT and a rate of C/20.

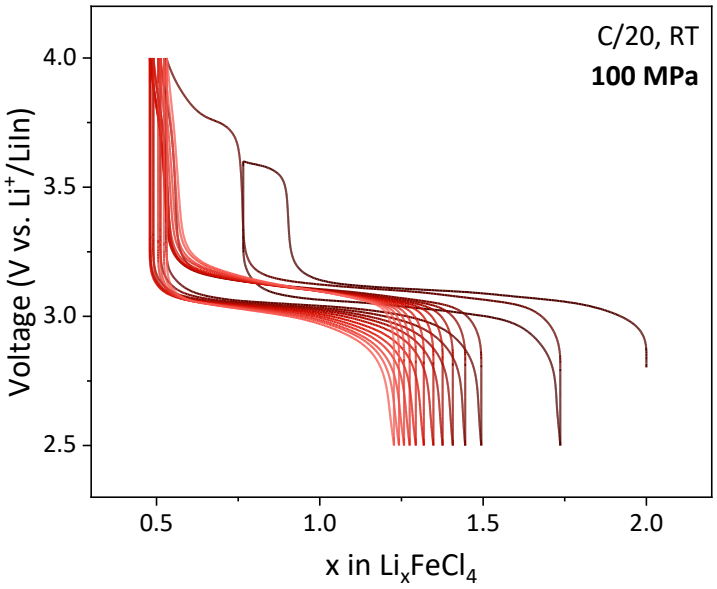

Figure A3.6. Galvanostatic cycling of the LFC material in a LFC:LYBC:VGCF composite in the range 2.5-4.0 V vs. Li^+/LiIn

A3.3 – Supplementary tables

Table A3.1. NMR fitting parameters for the ^{7}Li NMR spectra of pristine, BM20, BM60 and BM90-LTS recorded at RT

	Environment	Fraction of Li signal	Chemical shift	FWHM	Gaussian / Lorentzian
Pristine	Mobile (pink)	49.3%	12.0 ppm	5.6 ppm	17% / 83%
	Ordered Li (blue)	50.7%	2.1 ppm	9.5 ppm	46% / 54%
BM20	Mobile (pink)	65%	9.0 ppm	6.1 ppm	0% / 100%
	Ordered Li (blue)	35%	0.2 ppm	7.4 ppm	40% / 60%
BM60	Mobile (pink)	50.8%	9.1 ppm	5.9 ppm	0% / 100%
	Ordered Li (blue)	33.4%	0.3 ppm	8.6 ppm	34% / 66%
	“Amorphous“ (yellow)	15.8%	2.8 ppm	22 ppm	100% / 0%
BM90	New env. (green)	24.7%	7 ppm	7.1 ppm	0% / 100%
	Ordered Li (blue)	40.7%	2.9 ppm	13 ppm	61% / 39%
	“Amorphous” (yellow)	34.6%	2.9 ppm	29.4 ppm	100% / 0%

A4 – Supplementary information for Chapter 4

A4.1 – Materials and methods

Materials. $LiNi_{0.6}Mn_{0.2}Co_{0.2}O_2$ (NMC622 uncoated, monolithic, d10 = 3.21 µm, d50 = 5.28 µm and d90 = 8.47 µm, BET = 0.5 m^2/g) was kindly provided by UMICORE.

O3-Li_xTiS_2 phase was synthesized, following Colbow *et al.* methodology,[138] from a high temperature (800°C) solid-state synthesis by reacting stoichiometric amounts of thoroughly mixed Ti and Li_2S (Alfa Aesar, purity 99 w/w %) powders in evacuated quartz tubes.

$Li_3YBr_2Cl_4$ (LYBC) was kindly provided by Saint-Gobain Recherche Paris. Li_6PS_5Cl (LPSCl) solid electrolyte was obtained from NEI Corporation. β-Li_3PS_4 was prepared through a solvent-mediated synthesis in tetrahydrofuran (THF). Stoichiometric amounts of Li_2S (Alfa Aesar, purity 99 w/w %) and P_2S_5 (Acros Organics, purity > 98 w/w %) were dispersed in THF (Sigma Aldrich, 99.9 % v/v) and then, continuously stirred for 48 h at room temperature. The obtained powder was later recovered by centrifugation at 600 rpm for 3 min. Next, the powder was dried in a cylindrical Schlenk flask at 100°C (heating rate 5°C/min) for 24 h and subsequently at 155°C for 24 h under dynamic vacuum (P < 0.1mbar).

BM90-LTS preparation. Pristine O3-Li_xTiS_2 was milled in a stainless steel SPEX grinder for 90 minutes by 200 mg batches using 2 stainless steel balls (8 mm in diameter) corresponding to a ball-to-powder mass ratio of 20/1.

Composite preparation. Composites of NMC and LYBC were composed of AM, SE and VGCF in ratios of 66.5/28.5/5 wt.% and fabricated by hand grinding.

Li metal all-solid-state cell assembly. Low pressure Li-ASSB cells were fabricated within a homemade two-electrode cell developed in-house consisting in a cylindrical polyetherimide body and two stainless steel pistons of 8 mm diameter as current collector. Fabrication consists in first pressing LPSCl SE powder (30 mg) into a separator then the cathode was added with a loading of 4.5 to 5 mg_{AM}/cm^2 on one side and the stack was densified at 4 t/cm^2 for 15 minutes. Finally, a lithium foil was cleaned and rolled to a thickness of 80-100 µm before being punched at 8 mm diameter and placed in the cell against the LPSCl layer. The low-pressure cells were cycled using the homemade frame comprising a force sensor and a screw allowing us to set the initial stack pressure.

Li symmetric cell were assembled by first densifying 30 mg of LPSCl or β-LPS into the sliding cylinder of the spring-loaded cell (illustrated in Figure 4.7) and then adding on both side of the separator Li disks of 8 mm in diameter punched from a lithium foil that was cleaned and rolled to a thickness of 80-100 µm. To add the Li disks, they were first stuck onto stainless steel (304 type) disks of 8mm in diameter and 0.5 mm in thickness by pressing them into each other's by hand.

All assembly procedures were carried out in an Argon-filled glovebox ([O2] < 1 ppm, [H2O] < 1 ppm).

Galvanostatic cycling was carried out at room temperature and at desired potential window and C-rates (with C corresponding to 1 mol of Li per mole of active material in 1 h). Unless specified, cycling was performed with loadings of 4.5-5 mg_{AM}/cm^2 and a stack pressure of 100 MPa.

CCD measurements on Li symmetrical cell were carried out at room temperature following a staircase test with pulses of 1 hour from a starting current of 50 µA/cm² and step increase of 50 µA/cm² per cycle. If not specified, the pressure was applied through a spring and set to 9 MPa

All electrochemical measurements were conducted on Biologic devices (VMP3 potentiostats or BCS-805 cyclers) devices controlled by EC-Lab or BT-Lab software.

A5 – Additional supplementary information

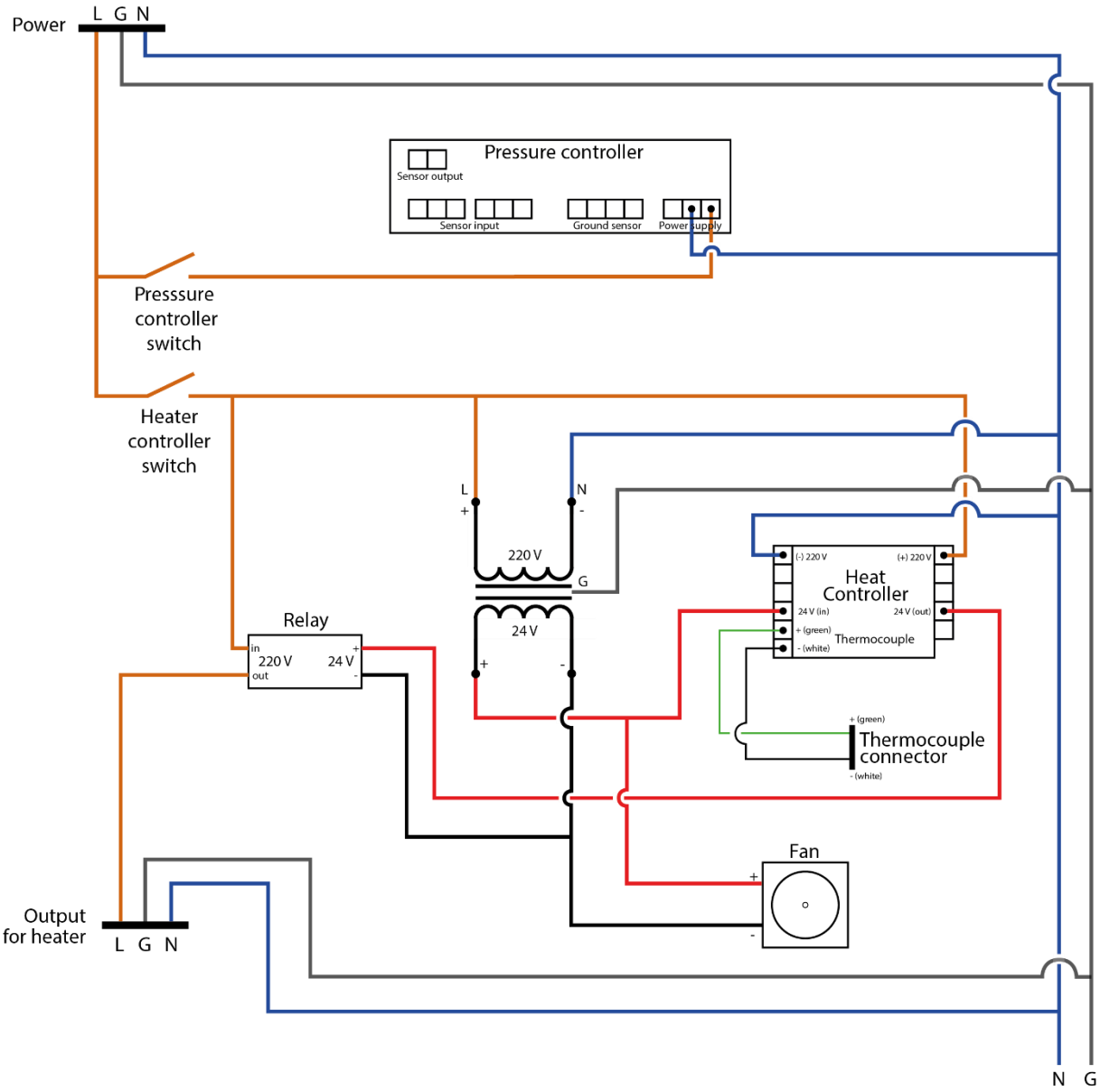

Figure A5.1. Electric circuit of the control boxes used for pressure and temperature control.

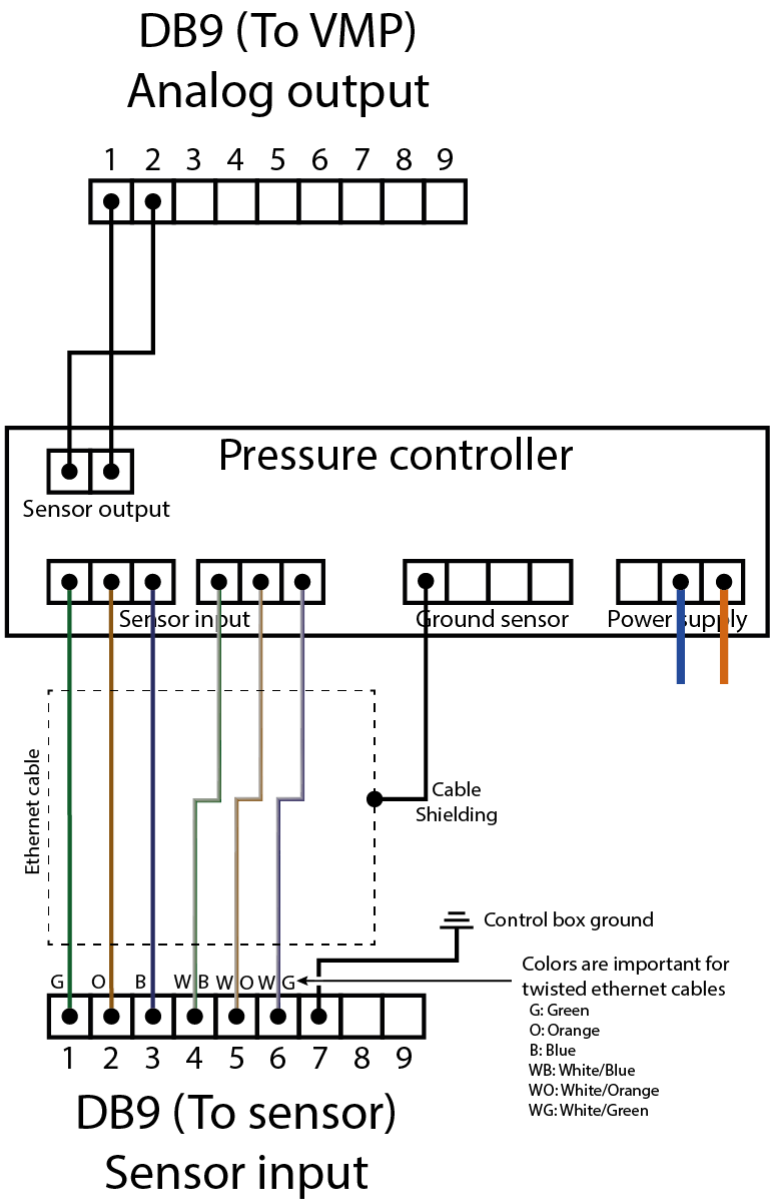

Figure A5.2. Electric circuit of the pressure controller connection to the analogue output and the force sensor input.

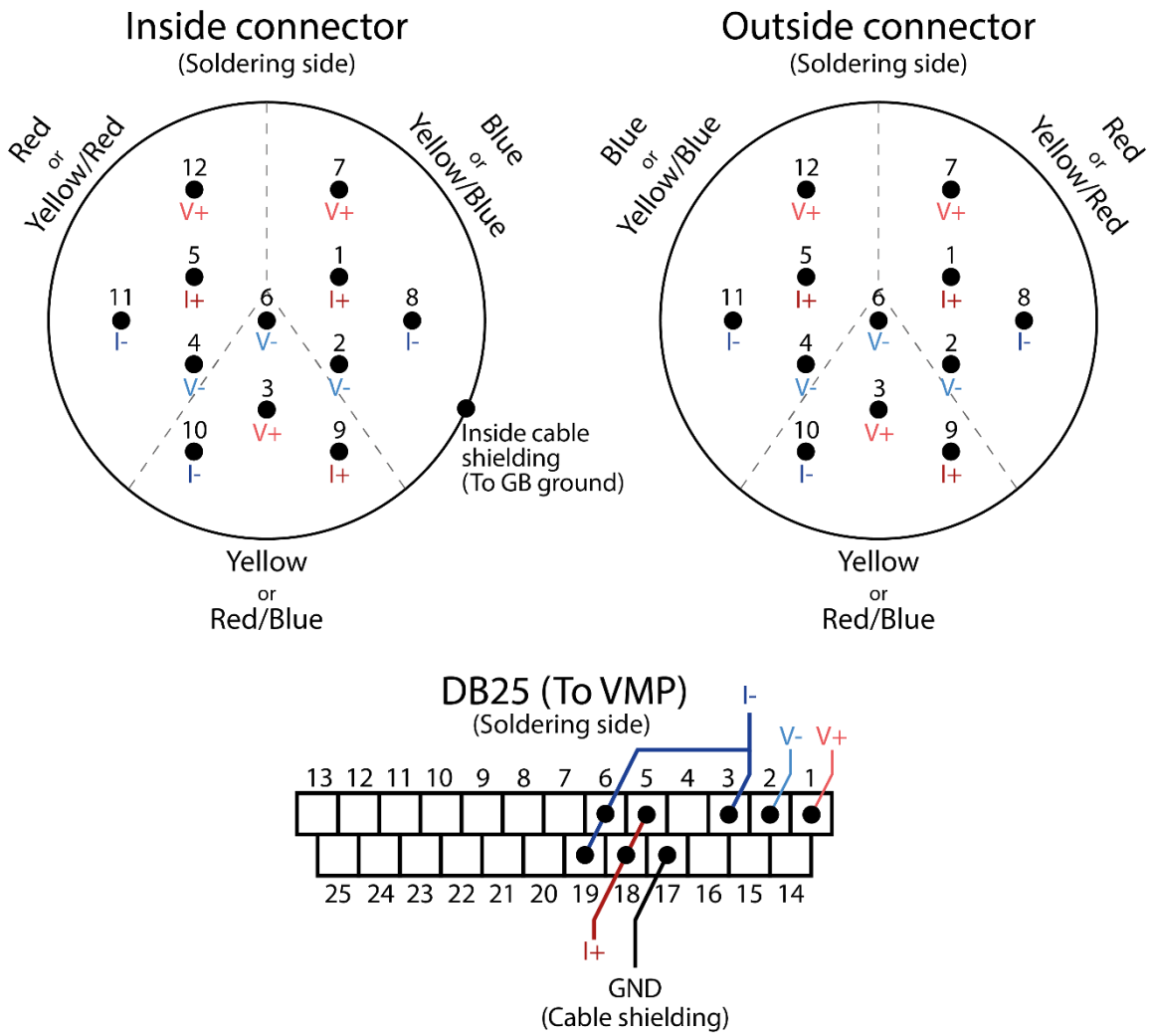

Figure A5.3. Soldering connections diagram for the cables connecting the potentiostat to the cell through the glovebox.

References

(1) Calvin, K. IPCC, 2023: Climate Change 2023: Synthesis Report. Contribution of Working Groups I, II and III to the Sixth Assessment Report of the Intergovernmental Panel on Climate Change [Core Writing Team, H. Lee and J. Romero (Eds.)]. IPCC, Geneva, Switzerland., First.; Intergovernmental Panel on Climate Change (IPCC), 2023. https://doi.org/10.59327/IPCC/AR6-9789291691647.

(2) Thomas, T. Pumped Storage: Proceedings of the Conference Organized by the Institution of Civil Engineers at Imperial College of Science, Technology and Medicine, London; 1990.

(3) Rehman, S.; Al-Hadhrami, L. M.; Alam, Md. M. Pumped Hydro Energy Storage System: A Technological Review. Renewable and Sustainable Energy Reviews **2015**, 44, 586–598. https://doi.org/10.1016/j.rser.2014.12.040.

(4) Tarascon, J.-M.; Armand, M. Issues and Challenges Facing Rechargeable Lithium Batteries. Nature **2001**, 414 (6861), 359–367. https://doi.org/10.1038/35104644.

(5) Li, Q.; Yang, Y.; Yu, X.; Li, H. A 700 W·h·kg−1 Rechargeable Pouch Type Lithium Battery. Chinese Phys. Lett. **2023**, 40 (4), 048201. https://doi.org/10.1088/0256-307X/40/4/048201.

(6) Randau, S.; Weber, D. A.; Kötz, O.; Koerver, R.; Braun, P.; Weber, A.; Ivers-Tiffée, E.; Adermann, T.; Kulisch, J.; Zeier, W. G.; Richter, F. H.; Janek, J. Benchmarking the Performance of All-Solid-State Lithium Batteries. Nat Energy **2020**, 5 (3), 259–270. https://doi.org/10.1038/s41560-020-0565-1.

(7) Pile voltaïque. Wikipédia; 2023.

(8) Goodenough, J. B.; Park, K.-S. The Li-Ion Rechargeable Battery: A Perspective. J. Am. Chem. Soc. **2013**, 135 (4), 1167–1176. https://doi.org/10.1021/ja3091438.

(9) Rouxel, J.; Danot, M.; Bichon, M. Les Composites Intercalaires NaxTiS2. Etude Générale Des Phases NaxTiS2 et KxTiS2. Bull. Soc. Chim **1971**, 11, 3930–3936.

(10) Funke, K. Solid State Ionics: From Michael Faraday to Green Energy—the European Dimension. Sci Technol Adv Mater **2013**, 14 (4), 043502. https://doi.org/10.1088/1468-6996/14/4/043502.

(11) Fast Ion Transport in Solids; Scrosati, B., Magistris, A., Mari, C. M., Mariotto, G., Eds.; Springer Netherlands: Dordrecht, 1993. https://doi.org/10.1007/978-94-011-1916-0.

(12) International Energy Agency. Global EV Outlook 2023: Catching up with Climate Ambitions; Global EV Outlook; OECD, 2023. https://doi.org/10.1787/cbe724e8-en.

(13) Assat, G.; Tarascon, J.-M. Fundamental Understanding and Practical Challenges of Anionic Redox Activity in Li-Ion Batteries. Nat Energy **2018**, 3 (5), 373–386. https://doi.org/10.1038/s41560-018-0097-0.

(14) Li, Q.; Yang, Y.; Yu, X.; Li, H. A 700 W·h·kg−1 Rechargeable Pouch Type Lithium Battery. Chinese Phys. Lett. **2023**, 40 (4), 048201. https://doi.org/10.1088/0256-307X/40/4/048201.

(15) Louli, A. J.; Eldesoky, A.; deGooyer, J.; Coon, M.; Aiken, C. P.; Simunovic, Z.; Metzger, M.; Dahn, J. R. Different Positive Electrodes for Anode-Free Lithium Metal Cells. J. Electrochem. Soc. **2022**, 169 (4), 040517. https://doi.org/10.1149/1945-7111/ac62c4.

(16) Janek, J.; Zeier, W. G. A Solid Future for Battery Development. Nat Energy **2016**, 1 (9), 16141. https://doi.org/10.1038/nenergy.2016.141.

(17) Pang, M.-C.; Wei, Y.; Wang, H.; Marinescu, M.; Yan, Y.; Offer, G. J. Large-Format Bipolar and Parallel Solid-State Lithium-Metal Cell Stacks: A Thermally Coupled Model-Based Comparative Study. J. Electrochem. Soc. **2021**, 167 (16), 160555. https://doi.org/10.1149/1945-7111/abd493.

(18) Faraday, M. I. Experimental Researches in Electricity. —Fifteenth Series. Phil. Trans. R. Soc. **1839**, 129, 1–12. https://doi.org/10.1098/rstl.1839.0002.

(19) O'Keeffe, M. Phase Transitions and Translational Freedom in Solid Electrolytes. In Superionic Conductors; Mahan, G. D., Roth, W. L., Eds.; Springer US: Boston, MA, 1976; pp 101–114. https://doi.org/10.1007/978-1-4615-8789-7_9.

(20) Nernst, W.; Dolesalek, F. Über die Gaspolarisation im Bleiakkumulator. Z. Elektrotech. Elektrochem. **1900**, 6 (45), 549–550. https://doi.org/10.1002/bbpc.19000064502.

(21) Wagner, C. Über den Mechanismus der elektrischen Stromleitung im Nernststift. Naturwissenschaften **1943**, 31 (23), 265–268. https://doi.org/10.1007/BF01475685.

(22) Tubandt, C.; Lorenz, E. Molekularzustand und elektrisches Leitvermögen kristallisierter Salze. Zeitschrift für Physikalische Chemie **1914**, 87U (1), 513–542. https://doi.org/10.1515/zpch-1914-8737.

(23) Owens, B. B.; Argue, G. R. High Conductivity Solid Electrolyte System Rbl - Agl. J. Electrochem. Soc. **1970**, 117 (7), 898. https://doi.org/10.1149/1.2407666.

(24) Whittingham, M. S.; Huggins, R. A. Beta Alumina-Prelude to a Revolution in Solid State Electrochemistry. NBS Special Publications **1972**, 364, 139–154.

(25) Alpen, U. v. Li3N: A Promising Li Ionic Conductor. Journal of Solid State Chemistry **1979**, 29 (3), 379–392. https://doi.org/10.1016/0022-4596(79)90195-6.

(26) Ginnings, D. C.; Phipps, T. E. TEMPERATURE-CONDUCTANCE CURVES OF SOLID SALTS. III. HALIDES OF LITHIUM. J. Am. Chem. Soc. **1930**, 52 (4), 1340–1345. https://doi.org/10.1021/ja01367a006.

(27) Owens, B. B.; Salkind, A. J. Key Events in the Evolution of Implantable Pacemaker Batteries. In Batteries for Implantable Biomedical Devices; Owens, B. B., Ed.; Springer US: Boston, MA, 1986; pp 37–49. https://doi.org/10.1007/978-1-4684-9045-9_2.

(28) Owens, B. B. Solid State Electrolytes: Overview of Materials and Applications during the Last Third of the Twentieth Century. Journal of Power Sources **2000**, 90 (1), 2–8. https://doi.org/10.1016/S0378-7753(00)00436-5.

(29) akram, ghalia. Pacemaker!! A Marvel Called Artificial Heart. Envirocivil.com. https://envirocivil.com/health-and-wellness/pacemaker-a-marvel-called-artificial-heart/ (accessed 2023-08-17).

(30) Root, M. J. Medical Device Batteriesmedical Device Battery. In Encyclopedia of Sustainability Science and Technology; Meyers, R. A., Ed.; Springer: New York, NY, 2012; pp 6498–6519. https://doi.org/10.1007/978-1-4419-0851-3_658.

(31) Goodenough, J. B.; Hong, H. Y.-P.; Kafalas, J. A. Fast Na+-Ion Transport in Skeleton Structures. Materials Research Bulletin **1976**, 11 (2), 203–220. https://doi.org/10.1016/0025-5408(76)90077-5.

(32) Wright, P. V. Electrical Conductivity in Ionic Complexes of Poly(Ethylene Oxide). Brit. Poly. J. **1975**, 7 (5), 319–327. https://doi.org/10.1002/pi.4980070505.

(33) Geng, H.; Mei, A.; Lin, Y.; Nan, C. Effect of Sintering Atmosphere on Ionic Conduction and Structure of Li0.5La0.5TiO3 Solid Electrolytes. Materials Science and Engineering: B **2009**, 164 (2), 91–95. https://doi.org/10.1016/j.mseb.2009.07.011.

(34) Sun, Y.; Guan, P.; Liu, Y.; Xu, H.; Li, S.; Chu, D. Recent Progress in Lithium Lanthanum Titanate Electrolyte towards All Solid-State Lithium Ion Secondary Battery. Critical Reviews in Solid State and Materials Sciences **2019**, 44 (4), 265–282. https://doi.org/10.1080/10408436.2018.1485551.

(35) Murugan, R.; Thangadurai, V.; Weppner, W. Fast Lithium Ion Conduction in Garnet-Type Li7La3Zr2O12. Angewandte Chemie International Edition **2007**, 46 (41), 7778–7781. https://doi.org/10.1002/anie.200701144.

(36) Thangadurai, V.; Narayanan, S.; Pinzaru, D. Garnet-Type Solid-State Fast Li Ion Conductors for Li Batteries: Critical Review. Chem. Soc. Rev. **2014**, 43 (13), 4714–4727. https://doi.org/10.1039/C4CS00020J.

(37) Fahys, B.; Robert, G. SUPERIONIC CONDUCTION IN Li2S - P2S5 - LiI - GLASSES.

(38) Minami, T.; Hayashi, A.; Tatsumisago, M. Recent Progress of Glass and Glass-Ceramics as Solid Electrolytes for Lithium Secondary Batteries. Solid State Ionics **2006**, 177 (26), 2715–2720. https://doi.org/10.1016/j.ssi.2006.07.017.

(39) Kanno, R.; Hata, T.; Kawamoto, Y.; Irie, M. Synthesis of a New Lithium Ionic Conductor, Thio-LISICON–Lithium Germanium Sulfide System. Solid State Ionics **2000**, 130 (1), 97–104. https://doi.org/10.1016/S0167-2738(00)00277-0.

(40) Kamaya, N.; Homma, K.; Yamakawa, Y.; Hirayama, M.; Kanno, R.; Yonemura, M.; Kamiyama, T.; Kato, Y.; Hama, S.; Kawamoto, K.; Mitsui, A. A Lithium Superionic Conductor. Nature Mater **2011**, 10 (9), 682–686. https://doi.org/10.1038/nmat3066.

(41) Kato, Y.; Hori, S.; Saito, T.; Suzuki, K.; Hirayama, M.; Mitsui, A.; Yonemura, M.; Iba, H.; Kanno, R. High-Power All-Solid-State Batteries Using Sulfide Superionic Conductors. Nat Energy **2016**, 1 (4), 1–7. https://doi.org/10.1038/nenergy.2016.30.

(42) Deiseroth, H.-J.; Kong, S.-T.; Eckert, H.; Vannahme, J.; Reiner, C.; Zaiß, T.; Schlosser, M. Li6PS5X: A Class of Crystalline Li-Rich Solids With an Unusually High Li+ Mobility. Angewandte Chemie International Edition **2008**, 47 (4), 755–758. https://doi.org/10.1002/anie.200703900.

(43) Walther, F.; Koerver, R.; Fuchs, T.; Ohno, S.; Sann, J.; Rohnke, M.; Zeier, W. G.; Janek, J. Visualization of the Interfacial Decomposition of Composite Cathodes in Argyrodite-Based All-Solid-State Batteries Using Time-of-Flight Secondary-Ion Mass Spectrometry. Chem. Mater. **2019**, 31 (10), 3745–3755. https://doi.org/10.1021/acs.chemmater.9b00770.

(44) Nie, X.; Hu, J.; Li, C. Halide-Based Solid Electrolytes: The History, Progress, and Challenges. Interdisciplinary Materials **2023**, 2 (3), 365–389. https://doi.org/10.1002/idm2.12090.

(45) Asano, T.; Sakai, A.; Ouchi, S.; Sakaida, M.; Miyazaki, A.; Hasegawa, S. Solid Halide Electrolytes with High Lithium-Ion Conductivity for Application in 4 V Class Bulk-Type All-Solid-State Batteries. Advanced Materials **2018**, 30 (44), 1803075. https://doi.org/10.1002/adma.201803075.

(46) Liu, Z.; Ma, S.; Liu, J.; Xiong, S.; Ma, Y.; Chen, H. High Ionic Conductivity Achieved in Li3Y(Br3Cl3) Mixed Halide Solid Electrolyte via Promoted Diffusion Pathways and Enhanced Grain Boundary. ACS Energy Lett. **2021**, 6 (1), 298–304. https://doi.org/10.1021/acsenergylett.0c01690.

(47) Li, X.; Liang, J.; Luo, J.; Banis, M. N.; Wang, C.; Li, W.; Deng, S.; Yu, C.; Zhao, F.; Hu, Y.; Sham, T.-K.; Zhang, L.; Zhao, S.; Lu, S.; Huang, H.; Li, R.; Adair, K. R.; Sun, X. Air-Stable Li3InCl6 Electrolyte with High Voltage Compatibility for All-Solid-State Batteries. Energy Environ. Sci. **2019**, 12 (9), 2665–2671. https://doi.org/10.1039/C9EE02311A.

(48) Liang, J.; Li, X.; Wang, S.; Adair, K. R.; Li, W.; Zhao, Y.; Wang, C.; Hu, Y.; Zhang, L.; Zhao, S.; Lu, S.; Huang, H.; Li, R.; Mo, Y.; Sun, X. Site-Occupation-Tuned Superionic LixScCl3+xHalide Solid Electrolytes for All-Solid-State Batteries. J. Am. Chem. Soc. **2020**, 142 (15), 7012–7022. https://doi.org/10.1021/jacs.0c00134.

(49) Zhou, L.; Zuo, T.; Li, C.; Zhang, Q.; Janek, J.; Nazar, L. F. Li3–xZrx(Ho/Lu)1–xCl6 Solid Electrolytes Enable Ultrahigh-Loading Solid-State Batteries with a Prelithiated Si Anode. ACS Energy Lett. **2023**, 8 (7), 3102–3111. https://doi.org/10.1021/acsenergylett.3c00763.

(50) Yin, Y.-C.; Yang, J.-T.; Luo, J.-D.; Lu, G.-X.; Huang, Z.; Wang, J.-P.; Li, P.; Li, F.; Wu, Y.-C.; Tian, T.; Meng, Y.-F.; Mo, H.-S.; Song, Y.-H.; Yang, J.-N.; Feng, L.-Z.; Ma, T.; Wen, W.; Gong, K.; Wang, L.-J.; Ju, H.-X.; Xiao, Y.; Li, Z.; Tao, X.; Yao, H.-B. A LaCl3-Based Lithium Superionic Conductor Compatible with Lithium Metal. Nature **2023**, 616 (7955), 77–83. https://doi.org/10.1038/s41586-023-05899-8.

(51) Tuo, K.; Sun, C.; López, C. A.; Fernández-Díaz, M. T.; Alonso, J. A. New Superionic Halide Solid Electrolytes Enabled by Aliovalent Substitution in Li3−xY1−xHfxCl6 for All-Solid-State Lithium Metal Based Batteries. J. Mater. Chem. A **2023**, 11 (29), 15651–15662. https://doi.org/10.1039/D3TA02781C.

(52) Kwak, H.; Han, D.; Lyoo, J.; Park, J.; Jung, S. H.; Han, Y.; Kwon, G.; Kim, H.; Hong, S.; Nam, K.; Jung, Y. S. New Cost-Effective Halide Solid Electrolytes for All-Solid-State Batteries: Mechanochemically Prepared Fe3+-Substituted Li2ZrCl6. Adv. Energy Mater. **2021**, 11 (12), 2003190. https://doi.org/10.1002/aenm.202003190.

(53) Zhou, L.; Kwok, C. Y.; Shyamsunder, A.; Zhang, Q.; Wu, X.; Nazar, L. F. A New Halospinel Superionic Conductor for High-Voltage All Solid State Lithium Batteries. Energy Environ. Sci. **2020**, 13 (7), 2056–2063. https://doi.org/10.1039/D0EE01017K.

(54) Zhou, L.; Zuo, T.-T.; Kwok, C. Y.; Kim, S. Y.; Assoud, A.; Zhang, Q.; Janek, J.; Nazar, L. F. High Areal Capacity, Long Cycle Life 4 V Ceramic All-Solid-State Li-Ion Batteries Enabled by Chloride Solid Electrolytes. Nat Energy **2022**, 7 (1), 83–93. https://doi.org/10.1038/s41560-021-00952-0.

(55) Liang, J.; Li, X.; Adair, K. R.; Sun, X. Metal Halide Superionic Conductors for All-Solid-State Batteries. Acc. Chem. Res. **2021**, 54 (4), 1023–1033. https://doi.org/10.1021/acs.accounts.0c00762.

(56) Kwak, H.; Wang, S.; Park, J.; Liu, Y.; Kim, K. T.; Choi, Y.; Mo, Y.; Jung, Y. S. Emerging Halide Superionic Conductors for All-Solid-State Batteries: Design, Synthesis, and Practical Applications. ACS Energy Lett. **2022**, 7 (5), 1776–1805. https://doi.org/10.1021/acsenergylett.2c00438.

(57) Braga, M. H.; Ferreira, J. A.; Stockhausen, V.; Oliveira, J. E.; El-Azab, A. Novel Li3ClO Based Glasses with Superionic Properties for Lithium Batteries. J. Mater. Chem. A **2014**, 2 (15), 5470–5480. https://doi.org/10.1039/C3TA15087A.

(58) Numan-Al-Mobin, A. M.; Schmidt, B.; Lannerd, A.; Viste, M.; Qiao, Q.; Smirnova, A. Interdigitated Cathode–Electrolyte Architectural Design for Fast-Charging Lithium Metal Battery with Lithium Oxyhalide Solid-State Electrolyte. Mater. Adv. **2022**, 3 (24), 8947–8957. https://doi.org/10.1039/D2MA00512C.

(59) Zhang, S.; Zhao, F.; Chen, J.; Fu, J.; Luo, J.; Alahakoon, S. H.; Chang, L.-Y.; Feng, R.; Shakouri, M.; Liang, J.; Zhao, Y.; Li, X.; He, L.; Huang, Y.; Sham, T.-K.; Sun, X. A Family of Oxychloride Amorphous Solid Electrolytes for Long-Cycling All-Solid-State Lithium Batteries. Nat Commun **2023**, 14 (1), 3780. https://doi.org/10.1038/s41467-023-39197-8.

(60) Tanaka, Y.; Ueno, K.; Mizuno, K.; Takeuchi, K.; Asano, T.; Sakai, A. New Oxyhalide Solid Electrolytes with High Lithium Ionic Conductivity >10 mS Cm $^{-1}$ for All-Solid-State Batteries. Angewandte Chemie **2023**, 135 (13). https://doi.org/10.1002/ange.202217581.

(61) Hu, L.; Wang, J.; Wang, K.; Gu, Z.; Xi, Z.; Li, H.; Chen, F.; Wang, Y.; Li, Z.; Ma, C. A Cost-Effective, Ionically Conductive and Compressible Oxychloride Solid-State Electrolyte for Stable All-Solid-State Lithium-Based Batteries. Nat Commun **2023**, 14 (1), 3807. https://doi.org/10.1038/s41467-023-39522-1.

(62) Landgraf, V.; Famprikis, T.; de Leeuw, J.; Bannenberg, L. J.; Ganapathy, S.; Wagemaker, M. Li5NCl2: A Fully-Reduced, Highly-Disordered Nitride-Halide Electrolyte for Solid-State

Batteries with Lithium-Metal Anodes. ACS Appl. Energy Mater. **2023**, 6 (3), 1661–1672. https://doi.org/10.1021/acsaem.2c03551.

(63) Liu, J.; Zhou, F.; Wang, S.; Zeng, R. Novel Nitride-Based Electrodes for Solid-State Batteries. In Solid State Batteries Volume 2: Materials and Advanced Devices; ACS Symposium Series; American Chemical Society, 2022; Vol. 1414, pp 15–38. https://doi.org/10.1021/bk-2022-1414.ch002.

(64) Sharafi, A.; Meyer, H. M.; Nanda, J.; Wolfenstine, J.; Sakamoto, J. Characterizing the Li–Li7La3Zr2O12 Interface Stability and Kinetics as a Function of Temperature and Current Density. Journal of Power Sources **2016**, 302, 135–139. https://doi.org/10.1016/j.jpowsour.2015.10.053.

(65) Yu, T.; Liang, J.; Luo, L.; Wang, L.; Zhao, F.; Xu, G.; Bai, X.; Yang, R.; Zhao, S.; Wang, J.; Yu, J.; Sun, X. Superionic Fluorinated Halide Solid Electrolytes for Highly Stable Li-Metal in All-Solid-State Li Batteries. Advanced Energy Materials **2021**, 11 (36), 2101915. https://doi.org/10.1002/aenm.202101915.

(66) Janek, J.; Zeier, W. G. Challenges in Speeding up Solid-State Battery Development. Nat Energy **2023**, 8 (3), 230–240. https://doi.org/10.1038/s41560-023-01208-9.

(67) Tan, D. H. S.; Wu, E. A.; Nguyen, H.; Chen, Z.; Marple, M. A. T.; Doux, J.-M.; Wang, X.; Yang, H.; Banerjee, A.; Meng, Y. S. Elucidating Reversible Electrochemical Redox of Li_6PS_5Cl Solid Electrolyte. ACS Energy Lett. **2019**, 4 (10), 2418–2427. https://doi.org/10.1021/acsenergylett.9b01693.

(68) Wang, C.; Adair, K.; Sun, X. All-Solid-State Lithium Metal Batteries with Sulfide Electrolytes: Understanding Interfacial Ion and Electron Transport. Acc. Mater. Res. **2022**, 3 (1), 21–32. https://doi.org/10.1021/accountsmr.1c00137.

(69) Song, S.; Hori, S.; Li, Y.; Suzuki, K.; Matsui, N.; Hirayama, M.; Saito, T.; Kamiyama, T.; Kanno, R. Material Search for a Li10GeP2S12-Type Solid Electrolyte in the Li–P–S–X (X = Br, I) System via Clarification of the Composition–Structure–Property Relationships. Chem. Mater. **2022**. https://doi.org/10.1021/acs.chemmater.2c01608.

(70) Riegger, L. M.; Schlem, R.; Sann, J.; Zeier, W. G.; Janek, J. Lithium-Metal Anode Instability of the Superionic Halide Solid Electrolytes and the Implications for Solid-State Batteries. Angew. Chem. Int. Ed. **2021**, 60 (12), 6718–6723. https://doi.org/10.1002/anie.202015238.

(71) Wenzel, S.; Leichtweiss, T.; Krüger, D.; Sann, J.; Janek, J. Interphase Formation on Lithium Solid Electrolytes—An in Situ Approach to Study Interfacial Reactions by Photoelectron Spectroscopy. Solid State Ionics **2015**, 278, 98–105. https://doi.org/10.1016/j.ssi.2015.06.001.

(72) Zhu, Y.; He, X.; Mo, Y. Origin of Outstanding Stability in the Lithium Solid Electrolyte Materials: Insights from Thermodynamic Analyses Based on First-Principles Calculations. ACS Appl. Mater. Interfaces **2015**, 7 (42), 23685–23693. https://doi.org/10.1021/acsami.5b07517.

(73) Walther, F.; Randau, S.; Schneider, Y.; Sann, J.; Rohnke, M.; Richter, F. H.; Zeier, W. G.; Janek, J. Influence of Carbon Additives on the Decomposition Pathways in Cathodes of Lithium Thiophosphate-Based All-Solid-State Batteries. Chem. Mater. **2020**, 32 (14), 6123–6136. https://doi.org/10.1021/acs.chemmater.0c01825.

(74) Zhang, X.; Li, X.; Weng, S.; Wu, S.; Liu, Q.; Cao, M.; Li, Y.; Wang, Z.; Zhu, L.; Xiao, R.; Su, D.; Yu, X.; Li, H.; Chen, L.; Wang, Z.; Wang, X. Spontaneous Gas–Solid Reaction on Sulfide Electrolytes for High-Performance All-Solid-State Batteries. Energy Environ. Sci. **2023**, 10.1039.D2EE03358E. https://doi.org/10.1039/D2EE03358E.

(75) Nikodimos, Y.; Su, W.-N.; Hwang, B. J. Halide Solid-State Electrolytes: Stability and Application for High Voltage All-Solid-State Li Batteries. Advanced Energy Materials **2023**, 13 (3), 2202854. https://doi.org/10.1002/aenm.202202854.

(76) Rajendran, S.; Pilli, A.; Omolere, O.; Kelber, J.; Arava, L. M. R. An All-Solid-State Battery with a Tailored Electrode–Electrolyte Interface Using Surface Chemistry and Interlayer-Based Approaches. Chem. Mater. **2021**, 33 (9), 3401–3412. https://doi.org/10.1021/acs.chemmater.1c00747.

(77) Walther, F.; Strauss, F.; Wu, X.; Mogwitz, B.; Hertle, J.; Sann, J.; Rohnke, M.; Brezesinski, T.; Janek, J. The Working Principle of a Li2CO3/LiNbO3 Coating on NCM for Thiophosphate-Based All-Solid-State Batteries. Chem. Mater. **2021**, 33 (6), 2110–2125. https://doi.org/10.1021/acs.chemmater.0c04660.

(78) Hood, Z. D.; Mane, A. U.; Sundar, A.; Tepavcevic, S.; Zapol, P.; Eze, U. D.; Adhikari, S. P.; Lee, E.; Sterbinsky, G. E.; Elam, J. W.; Connell, J. G. Multifunctional Coatings on Sulfide-Based Solid Electrolyte Powders with Enhanced Processability, Stability, and Performance for Solid-State Batteries. Advanced Materials **2023**, 35 (21), 2300673. https://doi.org/10.1002/adma.202300673.

(79) Wang, S.; Xu, X.; Cui, C.; Zeng, C.; Liang, J.; Fu, J.; Zhang, R.; Zhai, T.; Li, H. Air Sensitivity and Degradation Evolution of Halide Solid State Electrolytes upon Exposure. Advanced Functional Materials **2022**, 32 (7), 2108805. https://doi.org/10.1002/adfm.202108805.

(80) Shi, T.; Tu, Q.; Tian, Y.; Xiao, Y.; Miara, L. J.; Kononova, O.; Ceder, G. High Active Material Loading in All-Solid-State Battery Electrode via Particle Size Optimization. Advanced Energy Materials **2020**, 10 (1), 1902881. https://doi.org/10.1002/aenm.201902881.

(81) Doerrer, C.; Capone, I.; Narayanan, S.; Liu, J.; Grovenor, C. R. M.; Pasta, M.; Grant, P. S. High Energy Density Single-Crystal NMC/Li6PS5Cl Cathodes for All-Solid-State Lithium-Metal Batteries. ACS Appl. Mater. Interfaces **2021**, 13 (31), 37809–37815. https://doi.org/10.1021/acsami.1c07952.

(82) Kim, K. J.; Rupp, J. L. M. All Ceramic Cathode Composite Design and Manufacturing towards Low Interfacial Resistance for Garnet-Based Solid-State Lithium Batteries. Energy Environ. Sci. **2020**, 13 (12), 4930–4945. https://doi.org/10.1039/D0EE02062A.

(83) Bielefeld, A.; Weber, D. A.; Janek, J. Modeling Effective Ionic Conductivity and Binder Influence in Composite Cathodes for All-Solid-State Batteries. ACS Appl. Mater. Interfaces **2020**, 12 (11), 12821–12833. https://doi.org/10.1021/acsami.9b22788.

(84) Kim, S. Y.; Cha, H.; Kostecki, R.; Chen, G. Composite Cathode Design for High-Energy All-Solid-State Lithium Batteries with Long Cycle Life. ACS Energy Lett. **2023**, 8 (1), 521–528. https://doi.org/10.1021/acsenergylett.2c02414.

(85) Ke, X.; Wang, Y.; Ren, G.; Yuan, C. Towards Rational Mechanical Design of Inorganic Solid Electrolytes for All-Solid-State Lithium Ion Batteries. Energy Storage Materials **2020**, 26, 313–324. https://doi.org/10.1016/j.ensm.2019.08.029.

(86) Jiang, M.; Mukherjee, S.; Chen, Z. W.; Chen, L. X.; Li, M. L.; Xiao, H. Y.; Gao, C.; Singh, C. V. Materials Perspective on New Lithium Chlorides and Bromides: Insights into Thermo-Physical Properties. Phys. Chem. Chem. Phys. **2020**, 22 (39), 22758–22767. https://doi.org/10.1039/D0CP02946G.

(87) Papakyriakou, M.; Lu, M.; Liu, Y.; Liu, Z.; Chen, H.; McDowell, M. T.; Xia, S. Mechanical Behavior of Inorganic Lithium-Conducting Solid Electrolytes. Journal of Power Sources **2021**, 516, 230672. https://doi.org/10.1016/j.jpowsour.2021.230672.

(88) Deng, Z.; Wang, Z.; Chu, I.-H.; Luo, J.; Ong, S. P. Elastic Properties of Alkali Superionic Conductor Electrolytes from First Principles Calculations. J. Electrochem. Soc. **2015**, 163 (2), A67. https://doi.org/10.1149/2.0061602jes.

(89) Bucci, G.; Talamini, B.; Renuka Balakrishna, A.; Chiang, Y.-M.; Carter, W. C. Mechanical Instability of Electrode-Electrolyte Interfaces in Solid-State Batteries. Phys. Rev. Materials **2018**, 2 (10), 105407. https://doi.org/10.1103/PhysRevMaterials.2.105407.

(90) Bucci, G.; Swamy, T.; Chiang, Y.-M.; Carter, W. C. Modeling of Internal Mechanical Failure of All-Solid-State Batteries during Electrochemical Cycling, and Implications for Battery Design. J. Mater. Chem. A **2017**, 5 (36), 19422–19430. https://doi.org/10.1039/C7TA03199H.

(91) Doux, J.; Nguyen, H.; Tan, D. H. S.; Banerjee, A.; Wang, X.; Wu, E. A.; Jo, C.; Yang, H.; Meng, Y. S. Stack Pressure Considerations for Room-Temperature All-Solid-State Lithium Metal Batteries. Adv. Energy Mater. **2020**, 10 (1), 1903253. https://doi.org/10.1002/aenm.201903253.

(92) Koerver, R.; Zhang, W.; de Biasi, L.; Schweidler, S.; Kondrakov, A. O.; Kolling, S.; Brezesinski, T.; Hartmann, P.; Zeier, W. G.; Janek, J. Chemo-Mechanical Expansion of Lithium Electrode Materials – on the Route to Mechanically Optimized All-Solid-State Batteries. Energy Environ. Sci. **2018**, 11 (8), 2142–2158. https://doi.org/10.1039/C8EE00907D.

(93) Culver, S. P.; Koerver, R.; Zeier, W. G.; Janek, J. On the Functionality of Coatings for Cathode Active Materials in Thiophosphate-Based All-Solid-State Batteries. Advanced Energy Materials **2019**, 9 (24), 1900626. https://doi.org/10.1002/aenm.201900626.

(94) Kim, J.; Kim, M. J.; Kim, J.; Lee, J. W.; Park, J.; Wang, S. E.; Lee, S.; Kang, Y. C.; Paik, U.; Jung, D. S.; Song, T. High-Performance All-Solid-State Batteries Enabled by Intimate Interfacial Contact Between the Cathode and Sulfide-Based Solid Electrolytes. Advanced Functional Materials n/a (n/a), 2211355. https://doi.org/10.1002/adfm.202211355.

(95) Lee, K.; Kim, S.; Park, J.; Park, S. H.; Coskun, A.; Jung, D. S.; Cho, W.; Choi, J. W. Selection of Binder and Solvent for Solution-Processed All-Solid-State Battery. J. Electrochem. Soc. **2017**, 164 (9), A2075. https://doi.org/10.1149/2.1341709jes.

(96) Jing, S.; Shen, H.; Huang, Y.; Kuang, W.; Zhang, Z.; Liu, S.; Yin, S.; Lai, Y.; Liu, F. Toward the Practical and Scalable Fabrication of Sulfide-Based All-Solid-State Batteries: Exploration of Slurry Process and Performance Enhancement Via the Addition of LiClO4. Advanced Functional Materials n/a (n/a), 2214274. https://doi.org/10.1002/adfm.202214274.

(97) Lee, J.; Lee, T.; Char, K.; Kim, K. J.; Choi, J. W. Issues and Advances in Scaling up Sulfide-Based All-Solid-State Batteries. Acc. Chem. Res. **2021**, 54 (17), 3390–3402. https://doi.org/10.1021/acs.accounts.1c00333.

(98) Boaretto, N.; Garbayo, I.; Valiyaveettil-SobhanRaj, S.; Quintela, A.; Li, C.; Casas-Cabanas, M.; Aguesse, F. Lithium Solid-State Batteries: State-of-the-Art and Challenges for Materials, Interfaces and Processing. Journal of Power Sources **2021**, 502, 229919. https://doi.org/10.1016/j.jpowsour.2021.229919.

(99) Xiao, Y.; Turcheniuk, K.; Narla, A.; Song, A.-Y.; Ren, X.; Magasinski, A.; Jain, A.; Huang, S.; Lee, H.; Yushin, G. Electrolyte Melt Infiltration for Scalable Manufacturing of Inorganic All-Solid-State Lithium-Ion Batteries. Nat. Mater. **2021**, 20 (7), 984–990. https://doi.org/10.1038/s41563-021-00943-2.

(100) Kim, D. H.; Oh, D. Y.; Park, K. H.; Choi, Y. E.; Nam, Y. J.; Lee, H. A.; Lee, S.-M.; Jung, Y. S. Infiltration of Solution-Processable Solid Electrolytes into Conventional Li-Ion-Battery Electrodes for All-Solid-State Li-Ion Batteries. Nano Lett. **2017**, 17 (5), 3013–3020. https://doi.org/10.1021/acs.nanolett.7b00330.

(101) Lee, Y.-G.; Fujiki, S.; Jung, C.; Suzuki, N.; Yashiro, N.; Omoda, R.; Ko, D.-S.; Shiratsuchi, T.; Sugimoto, T.; Ryu, S.; Ku, J. H.; Watanabe, T.; Park, Y.; Aihara, Y.; Im, D.; Han, I. T. High-Energy Long-Cycling All-Solid-State Lithium Metal Batteries Enabled by Silver–Carbon Composite Anodes. Nat Energy **2020**, 5 (4), 299–308. https://doi.org/10.1038/s41560-020-0575-z.

(102) Tan, D. H. S.; Meng, Y. S.; Jang, J. Scaling up High-Energy-Density Sulfidic Solid-State Batteries: A Lab-to-Pilot Perspective. Joule **2022**, 6 (8), 1755–1769. https://doi.org/10.1016/j.joule.2022.07.002.

(103) Krauskopf, T.; Richter, F. H.; Zeier, W. G.; Janek, J. Physicochemical Concepts of the Lithium Metal Anode in Solid-State Batteries. Chem. Rev. **2020**, 120 (15), 7745–7794. https://doi.org/10.1021/acs.chemrev.0c00431.

(104) Jeppson, D. W.; Ballif, J. L.; Yuan, W. W.; Chou, B. E. Lithium Literature Review: Lithium's Properties and Interactions; HEDL-TME-78-15; Hanford Engineering Development Lab., Richland, WA (United States), 1978. https://doi.org/10.2172/6885395.

(105) Chang, K.; Hallstedt, B. Thermodynamic Assessment of the Li–O System. Calphad **2011**, 35 (2), 160–164. https://doi.org/10.1016/j.calphad.2011.02.003.

(106) Kasemchainan, J.; Zekoll, S.; Spencer Jolly, D.; Ning, Z.; Hartley, G. O.; Marrow, J.; Bruce, P. G. Critical Stripping Current Leads to Dendrite Formation on Plating in Lithium Anode Solid Electrolyte Cells. Nat. Mater. **2019**, 18 (10), 1105–1111. https://doi.org/10.1038/s41563-019-0438-9.

(107) Kalnaus, S.; Dudney, N. J.; Westover, A. S.; Herbert, E.; Hackney, S. Solid-State Batteries: The Critical Role of Mechanics. Science **2023**, 381 (6664), eabg5998. https://doi.org/10.1126/science.abg5998.

(108) Kim, J.-S.; Yoon, G.; Kim, S.; Sugata, S.; Yashiro, N.; Suzuki, S.; Lee, M.-J.; Kim, R.; Badding, M.; Song, Z.; Chang, J.; Im, D. Surface Engineering of Inorganic Solid-State Electrolytes via Interlayers Strategy for Developing Long-Cycling Quasi-All-Solid-State Lithium Batteries. Nat Commun **2023**, 14 (1), 782. https://doi.org/10.1038/s41467-023-36401-7.

(109) Fu, K. (Kelvin); Gong, Y.; Fu, Z.; Xie, H.; Yao, Y.; Liu, B.; Carter, M.; Wachsman, E.; Hu, L. Transient Behavior of the Metal Interface in Lithium Metal–Garnet Batteries. Angewandte Chemie International Edition **2017**, 56 (47), 14942–14947. https://doi.org/10.1002/anie.201708637.

(110) Spencer-Jolly, D.; Agarwal, V.; Doerrer, C.; Hu, B.; Zhang, S.; Melvin, D. L. R.; Gao, H.; Gao, X.; Adamson, P.; Magdysyuk, O. V.; Grant, P. S.; House, R. A.; Bruce, P. G. Structural Changes in the Silver-Carbon Composite Anode Interlayer of Solid-State Batteries. Joule **2023**, 7 (3), 503–514. https://doi.org/10.1016/j.joule.2023.02.001.

(111) Cui, C.; Yang, H.; Zeng, C.; Gui, S.; Liang, J.; Xiao, P.; Wang, S.; Huang, G.; Hu, M.; Zhai, T.; Li, H. Unlocking the in Situ Li Plating Dynamics and Evolution Mediated by Diverse Metallic Substrates in All-Solid-State Batteries. Science Advances **2022**, 8 (43), eadd2000. https://doi.org/10.1126/sciadv.add2000.

(112) Adeli, P.; Bazak, J. D.; Park, K. H.; Kochetkov, I.; Huq, A.; Goward, G. R.; Nazar, L. F. Boosting Solid-State Diffusivity and Conductivity in Lithium Superionic Argyrodites by Halide Substitution. Angewandte Chemie International Edition **2019**, 58 (26), 8681–8686. https://doi.org/10.1002/anie.201814222.

(113) Peng, L.; Yu, C.; Zhang, Z.; Ren, H.; Zhang, J.; He, Z.; Yu, M.; Zhang, L.; Cheng, S.; Xie, J. Chlorine-Rich Lithium Argyrodite Enabling Solid-State Batteries with Capabilities of High Voltage, High Rate, Low-Temperature and Ultralong Cyclability. Chemical Engineering Journal **2022**, 430, 132896. https://doi.org/10.1016/j.cej.2021.132896.

(114) Umeshbabu, E.; Maddukuri, S.; Hu, Y.; Fichtner, M.; Munnangi, A. R. Influence of Chloride Ion Substitution on Lithium-Ion Conductivity and Electrochemical Stability in a

Dual-Halogen Solid-State Electrolyte. ACS Appl. Mater. Interfaces **2022**, 14 (22), 25448–25456. https://doi.org/10.1021/acsami.2c04160.

(115) Ganesan, P.; Soans, M.; Cambaz, M. A.; Zimmermanns, R.; Gond, R.; Fuchs, S.; Hu, Y.; Baumgart, S.; Sotoudeh, M.; Stepien, D.; Stein, H.; Groß, A.; Bresser, D.; Varzi, A.; Fichtner, M. Fluorine-Substituted Halide Solid Electrolytes with Enhanced Stability toward the Lithium Metal. ACS Appl. Mater. Interfaces **2023**, 15 (32), 38391–38402. https://doi.org/10.1021/acsami.3c03513.

(116) Wang, K.; Gu, Z.; Xi, Z.; Hu, L.; Ma, C. Li3TiCl6 as Ionic Conductive and Compressible Positive Electrode Active Material for All-Solid-State Lithium-Based Batteries. Nat Commun **2023**, 14 (1), 1396. https://doi.org/10.1038/s41467-023-37122-7.

(117) Tan, D. H. S.; Chen, Y.-T.; Yang, H.; Bao, W.; Sreenarayanan, B.; Doux, J.-M.; Li, W.; Lu, B.; Ham, S.-Y.; Sayahpour, B.; Scharf, J.; Wu, E. A.; Deysher, G.; Han, H. E.; Hah, H. J.; Jeong, H.; Lee, J. B.; Chen, Z.; Meng, Y. S. Carbon-Free High-Loading Silicon Anodes Enabled by Sulfide Solid Electrolytes. Science **2021**, 373 (6562), 1494–1499. https://doi.org/10.1126/science.abg7217.

(118) Kim, J. Y.; Park, J.; Kang, S. H.; Jung, S.; Shin, D. O.; Lee, M. J.; Oh, J.; Kim, K. M.; Zausch, J.; Lee, Y.-G.; Lee, Y. M. Revisiting TiS2 as a Diffusion-Dependent Cathode with Promising Energy Density for All-Solid-State Lithium Secondary Batteries. Energy Storage Materials **2021**, 41, 289–296. https://doi.org/10.1016/j.ensm.2021.06.005.

(119) Kim, J. Y.; Jung, S.; Kang, S. H.; Park, J.; Lee, M. J.; Jin, D.; Shin, D. O.; Lee, Y.-G.; Lee, Y. M. Graphite–Silicon Diffusion-Dependent Electrode with Short Effective Diffusion Length for High-Performance All-Solid-State Batteries. Advanced Energy Materials **2022**, 12 (3), 2103108. https://doi.org/10.1002/aenm.202103108.

(120) Kim, J. Y.; Park, J.; Lee, M. J.; Kang, S. H.; Shin, D. O.; Oh, J.; Kim, J.; Kim, K. M.; Lee, Y.-G.; Lee, Y. M. Diffusion-Dependent Graphite Electrode for All-Solid-State Batteries with Extremely High Energy Density. ACS Energy Lett. **2020**, 5 (9), 2995–3004. https://doi.org/10.1021/acsenergylett.0c01628.

(121) Gao, X.; Liu, B.; Hu, B.; Ning, Z.; Jolly, D. S.; Zhang, S.; Perera, J.; Bu, J.; Liu, J.; Doerrer, C.; Darnbrough, E.; Armstrong, D.; Grant, P. S.; Bruce, P. G. Solid-State Lithium Battery Cathodes Operating at Low Pressures. Joule **2022**, 6 (3), 636–646. https://doi.org/10.1016/j.joule.2022.02.008.

(122) Quemin, E.; Dugas, R.; Koç, T.; Hennequart, B.; Chometon, R.; Tarascon, J.-M. Decoupling Parasitic Reactions at the Positive Electrode Interfaces in Argyrodite-Based Systems. ACS Appl. Mater. Interfaces **2022**. https://doi.org/10.1021/acsami.2c13150.

(123) Koç, T.; Marchini, F.; Rousse, G.; Dugas, R.; Tarascon, J.-M. In Search of the Best Solid Electrolyte-Layered Oxide Pairing for Assembling Practical All-Solid-State Batteries. ACS Appl. Energy Mater. **2021**, 4 (12), 13575–13585. https://doi.org/10.1021/acsaem.1c02187.

(124) Koç, T. In Search of the Best Solid Electrolyte-Layered Oxide Pair in All-Solid-State Batteries. PhD Thesis, Sorbonne Université, Laboratoire Chimie du Solide et Energie, Collège de France, 2022. https://theses.hal.science/tel-04137255 (accessed 2023-09-19).

(125) Koç, T.; Hallot, M.; Quemin, E.; Hennequart, B.; Dugas, R.; Abakumov, A. M.; Lethien, C.; Tarascon, J.-M. Toward Optimization of the Chemical/Electrochemical Compatibility of Halide Solid Electrolytes in All-Solid-State Batteries. ACS Energy Lett. **2022**, 7 (9), 2979–2987. https://doi.org/10.1021/acsenergylett.2c01668.

(126) Rosenbach, C.; Walther, F.; Ruhl, J.; Hartmann, M.; Hendriks, T. A.; Ohno, S.; Janek, J.; Zeier, W. Visualizing the Chemical Incompatibility of Halide and Sulfide-Based Electrolytes in Solid-State Batteries. Advanced Energy Materials **2023**, 13 (6), 2203673. https://doi.org/10.1002/aenm.202203673.

(127) Wang, S.; Bai, Q.; Nolan, A. M.; Liu, Y.; Gong, S.; Sun, Q.; Mo, Y. Lithium Chlorides and Bromides as Promising Solid-State Chemistries for Fast Ion Conductors with Good Electrochemical Stability. Angewandte Chemie International Edition **2019**, 58 (24), 8039–8043. https://doi.org/10.1002/anie.201901938.

(128) Ziegenhain, G.; M. Urbassek, H. Effect of Material Stiffness on Hardness: A Computational Study Based on Model Potentials. Philosophical Magazine **2009**, 89 (26), 2225–2238. https://doi.org/10.1080/14786430903022697.

(129) Auvergniot, J.; Cassel, A.; Ledeuil, J.-B.; Viallet, V.; Seznec, V.; Dedryvère, R. Interface Stability of Argyrodite Li6PS5Cl toward LiCoO2, LiNi1/3Co1/3Mn1/3O2, and LiMn2O4 in Bulk All-Solid-State Batteries. Chem. Mater. **2017**, 29 (9), 3883–3890. https://doi.org/10.1021/acs.chemmater.6b04990.

(130) Dewald, G. F.; Ohno, S.; Kraft, M. A.; Koerver, R.; Till, P.; Vargas-Barbosa, N. M.; Janek, J.; Zeier, W. G. Experimental Assessment of the Practical Oxidative Stability of Lithium Thiophosphate Solid Electrolytes. Chem. Mater. **2019**, 31 (20), 8328–8337. https://doi.org/10.1021/acs.chemmater.9b01550.

(131) Deng, S.; Sun, Y.; Li, X.; Ren, Z.; Liang, J.; Doyle-Davis, K.; Liang, J.; Li, W.; Norouzi Banis, M.; Sun, Q.; Li, R.; Hu, Y.; Huang, H.; Zhang, L.; Lu, S.; Luo, J.; Sun, X. Eliminating the Detrimental Effects of Conductive Agents in Sulfide-Based Solid-State Batteries. ACS Energy Lett. **2020**, 5 (4), 1243–1251. https://doi.org/10.1021/acsenergylett.0c00256.

(132) Jung, S.-K.; Gwon, H.; Lee, S.-S.; Kim, H.; Lee, J. C.; Chung, J. G.; Park, S. Y.; Aihara, Y.; Im, D. Understanding the Effects of Chemical Reactions at the Cathode–Electrolyte Interface in Sulfide Based All-Solid-State Batteries. J. Mater. Chem. A **2019**, 7 (40), 22967–22976. https://doi.org/10.1039/C9TA08517C.

(133) Liu, X.; Zheng, B.; Zhao, J.; Zhao, W.; Liang, Z.; Su, Y.; Xie, C.; Zhou, K.; Xiang, Y.; Zhu, J.; Wang, H.; Zhong, G.; Gong, Z.; Huang, J.; Yang, Y. Electrochemo-Mechanical Effects on Structural Integrity of Ni-Rich Cathodes with Different Microstructures in All Solid-State Batteries. Adv. Energy Mater. **2021**, 11 (8), 2003583. https://doi.org/10.1002/aenm.202003583.

(134) Whittingham, M. S. Chemistry of Intercalation Compounds: Metal Guests in Chalcogenide Hosts. Progress in Solid State Chemistry **1978**, 12 (1), 41–99. https://doi.org/10.1016/0079-6786(78)90003-1.

(135) Umrigar, C.; Ellis, D. E.; Wang, D.-S.; Krakauer, H.; Posternak, M. Band Structure, Intercalation, and Interlayer Interactions of Transition-Metal Dichalcogenides: Ti S 2 and LiTi S 2. Phys. Rev. B **1982**, 26 (9), 4935–4950. https://doi.org/10.1103/PhysRevB.26.4935.

(136) Nakhal, S.; Lerch, M.; Koopman, J.; Islam, M. M.; Bredow, T. Crystal Structure of 3R-LiTiS2 and Its Stability Compared to Other Polymorphs. Zeitschrift für anorganische und allgemeine Chemie **2013**, 639 (15), 2822–2825. https://doi.org/10.1002/zaac.201300330.

(137) Zhang, Z.; Dong, C.; Guan, C.; Yang, L.; Luo, X.; Li, A. Sealed-Tube Synthesis and Phase Diagram of LixTiS2 (0≤x≤1). Materials Research Bulletin **2015**, 61, 499–503. https://doi.org/10.1016/j.materresbull.2014.10.045.

(138) Colbow, K. M.; Dahn, J. R.; Haering, R. R. The 3R Phase of LixTiS2. Journal of Power Sources **1989**, 26 (3–4), 301–307. https://doi.org/10.1016/0378-7753(89)80138-7.

(139) Kim, J. Y.; Jung, S.; Kang, S. H.; Lee, M. J.; Jin, D.; Shin, D. O.; Lee, Y.-G.; Lee, Y. M. All-Solid-State Hybrid Electrode Configuration for High-Performance All-Solid-State Batteries: Comparative Study with Composite Electrode and Diffusion-Dependent Electrode. Journal of Power Sources **2022**, 518, 230736. https://doi.org/10.1016/j.jpowsour.2021.230736.

(140) Suryanarayana, C. Mechanical Alloying and Milling. Progress in Materials Science **2001**, 46 (1), 1–184. https://doi.org/10.1016/S0079-6425(99)00010-9.

(141) Tarascon, J.-M.; Morcrette, M.; Saint, J.; Aymard, L.; Janot, R. On the Benefits of Ball Milling within the Field of Rechargeable Li-Based Batteries. Comptes Rendus Chimie **2005**, 8 (1), 17–26. https://doi.org/10.1016/j.crci.2004.12.006.

(142) Sivakkumar, S. R.; Milev, A. S.; Pandolfo, A. G. Effect of Ball-Milling on the Rate and Cycle-Life Performance of Graphite as Negative Electrodes in Lithium-Ion Capacitors. Electrochimica Acta **2011**, 56 (27), 9700–9706. https://doi.org/10.1016/j.electacta.2011.06.060.

(143) Doyle, M.; Newman, J.; Reimers, J. A Quick Method of Measuring the Capacity versus Discharge Rate for a Dual Lithium-Ion Insertion Cell Undergoing Cycling. Journal of Power Sources **1994**, 52 (2), 211–216. https://doi.org/10.1016/0378-7753(94)02012-4.

(144) Winter, R.; Heitjans, P. Intergranular Structure of Nanocrystalline Layered LixTiS2 as Derived from 7Li NMR Spectroscopy. Journal of Non-Crystalline Solids **2001**, 293–295, 19–24. https://doi.org/10.1016/S0022-3093(01)00640-8.

(145) Winter, R.; Heitjans, P. Li+ Diffusion and Its Structural Basis in the Nanocrystalline and Amorphous Forms of Two-Dimensionally Ion-Conducting LixTiS2. J. Phys. Chem. B **2001**, 105 (26), 6108–6115. https://doi.org/10.1021/jp011200f.

(146) Thompson, A. H. Lithium Ordering in LixTiS2. Phys. Rev. Lett. **1978**, 40 (23), 1511–1514. https://doi.org/10.1103/PhysRevLett.40.1511.

(147) Küchler, W.; Heitjans, P.; Payer, A.; Schöllhorn, R. 7Li NMR Relaxation by Diffusion in Hexagonal and Cubic LixTiS2. Solid State Ionics **1994**, 70–71, 434–438. https://doi.org/10.1016/0167-2738(94)90350-6.

(148) Bodenez, V.; Dupont, L.; Morcrette, M.; Surcin, C.; Murphy, D. W.; Tarascon, J.-M. Copper Extrusion/Reinjection in Cu-Based Thiospinels by Electrochemical and Chemical Routes. Chem. Mater. **2006**, 18 (18), 4278–4287. https://doi.org/10.1021/cm060436z.

(149) Tanibata, N.; Kato, M.; Takimoto, S.; Takeda, H.; Nakayama, M.; Sumi, H. High Formability and Fast Lithium Diffusivity in Metastable Spinel Chloride for Rechargeable All-Solid-State Lithium-Ion Batteries. Advanced Energy and Sustainability Research **2020**, 1 (1), 2000025. https://doi.org/10.1002/aesr.202000025.

(150) Santhosha, A. L.; Medenbach, L.; Buchheim, J. R.; Adelhelm, P. The Indium–Lithium Electrode in Solid-State Lithium-Ion Batteries: Phase Formation, Redox Potentials, and Interface Stability. Batteries & Supercaps **2019**, 2 (6), 524–529. https://doi.org/10.1002/batt.201800149.

(151) Lu, Y.; Zhao, C.; Yuan, H.; Cheng, X.; Huang, J.; Zhang, Q. Critical Current Density in Solid-State Lithium Metal Batteries: Mechanism, Influences, and Strategies. Adv. Funct. Mater. **2021**, 31 (18), 2009925. https://doi.org/10.1002/adfm.202009925.

(152) Ham, S.-Y.; Yang, H.; Nunez-cuacuas, O.; Tan, D. H. S.; Chen, Y.-T.; Deysher, G.; Cronk, A.; Ridley, P.; Doux, J.-M.; Wu, E. A.; Jang, J.; Meng, Y. S. Assessing the Critical Current Density of All-Solid-State Li Metal Symmetric and Full Cells. Energy Storage Materials **2023**, 55, 455–462. https://doi.org/10.1016/j.ensm.2022.12.013.

(153) Fuchs, T.; Haslam, C. G.; Richter, F. H.; Sakamoto, J.; Janek, J. Evaluating the Use of Critical Current Density Tests of Symmetric Lithium Transference Cells with Solid Electrolytes. Advanced Energy Materials **2023**, 2302383. https://doi.org/10.1002/aenm.202302383.

(154) Wang, M. J.; Choudhury, R.; Sakamoto, J. Characterizing the Li-Solid-Electrolyte Interface Dynamics as a Function of Stack Pressure and Current Density. Joule **2019**, 3 (9), 2165–2178. https://doi.org/10.1016/j.joule.2019.06.017.

(155) Viswanathan, L.; Virkar, A. V. Wetting Characteristics of Sodium on B”-Alumina and on Nasicon. J Mater Sci **1982**, 17 (3), 753–759. https://doi.org/10.1007/BF00540372.

(156) Lee, H.; Chen, S.; Ren, X.; Martinez, A.; Shutthanandan, V.; Vijayakumar, M.; Han, K. S.; Li, Q.; Liu, J.; Xu, W.; Zhang, J.-G. Electrode Edge Effects and the Failure Mechanism of Lithium-Metal Batteries. ChemSusChem **2018**, 11 (21), 3821–3828. https://doi.org/10.1002/cssc.201801445.

(157) Sannier, L.; Bouchet, R.; Rosso, M.; Tarascon, J.-M. Evaluation of GPE Performances in Lithium Metal Battery Technology by Means of Simple Polarization Tests. Journal of Power Sources **2006**, 158 (1), 564–570. https://doi.org/10.1016/j.jpowsour.2005.09.026.

(158) Sannier, L. Mise Au Point d'un Électrolyte Gélifié Pour Accumulateurs Au Lithium Fonctionnant à Température Ambiante. These de doctorat, Amiens, 2003. https://www.theses.fr/2003AMIE0311 (accessed 2023-10-12).

(159) Otto, S.-K.; Riegger, L. M.; Fuchs, T.; Kayser, S.; Schweitzer, P.; Burkhardt, S.; Henss, A.; Janek, J. In Situ Investigation of Lithium Metal–Solid Electrolyte Anode Interfaces with ToF-SIMS. Advanced Materials Interfaces **2022**, 9 (13), 2102387. https://doi.org/10.1002/admi.202102387.

(160) Pantyukhina, M. I.; Andreev, O. L.; Martem'yanova, Z. S.; Batalov, N. N. Cation Conductivity of Li_8ZrO_6–$LiYO_2$ Solid Solutions. Inorganic Materials **2004**, 40 (4), 404–406. https://doi.org/10.1023/B:INMA.0000023965.10888.eb.

(161) Oh, J.; Choi, S. H.; Kim, J. Y.; Lee, J.; Lee, T.; Lee, N.; Lee, T.; Sohn, Y.; Chung, W. J.; Bae, K. Y.; Son, S.; Choi, J. W. Anode-Less All-Solid-State Batteries Operating at Room Temperature and Low Pressure. Advanced Energy Materials **2023**, 13 (38), 2301508. https://doi.org/10.1002/aenm.202301508.

(162) Belov, N. A.; Eskin, D. G.; Aksenov, A. A. Multicomponent Phase Diagrams: Applications for Commercial Aluminum Alloys - 1st Edition, 1st ed.; Elsevier Science, 2005.

(163) Wan, H.; Wang, Z.; Zhang, W.; He, X.; Wang, C. Interface Design for All-Solid-State Lithium Batteries. Nature **2023**, 1–6. https://doi.org/10.1038/s41586-023-06653-w.

(164) Larcher, D.; Beattie, S.; Morcrette, M.; Edström, K.; Jumas, J.-C.; Tarascon, J.-M. Recent Findings and Prospects in the Field of Pure Metals as Negative Electrodes for Li-Ion Batteries. J. Mater. Chem. **2007**, 17 (36), 3759–3772. https://doi.org/10.1039/B705421C.

(165) Okamoto, H. Supplemental Literature Review of Binary Phase Diagrams: Ag-Li, Ag-Sn, Be-Pu, C-Mn, C-Si, Ca-Li, Cd-Pu, Cr-Ti, Cr-V, Cu-Li, La-Sc, and Li-Sc. J. Phase Equilib. Diffus. **2017**, 38 (1), 70–81. https://doi.org/10.1007/s11669-016-0504-9.

(166) Sharafi, A.; Kazyak, E.; Davis, A. L.; Yu, S.; Thompson, T.; Siegel, D. J.; Dasgupta, N. P.; Sakamoto, J. Surface Chemistry Mechanism of Ultra-Low Interfacial Resistance in the Solid-State Electrolyte Li7La3Zr2O12. Chem. Mater. **2017**, 29 (18), 7961–7968. https://doi.org/10.1021/acs.chemmater.7b03002.

(167) Han, X.; Gong, Y.; Fu, K. (Kelvin); He, X.; Hitz, G. T.; Dai, J.; Pearse, A.; Liu, B.; Wang, H.; Rubloff, G.; Mo, Y.; Thangadurai, V.; Wachsman, E. D.; Hu, L. Negating Interfacial Impedance in Garnet-Based Solid-State Li Metal Batteries. Nature Mater **2017**, 16 (5), 572–579. https://doi.org/10.1038/nmat4821.

(168) Wu, C.; Emley, B.; Zhao, L.; Liang, Y.; Ai, Q.; Chen, Z.; Robles Hernández, F. C.; Wang, F.; Risal, S.; Guo, H.; Lou, J.; Yao, Y.; Fan, Z. Understanding the Chemomechanical Function of

the Silver–Carbon Interlayer in Sheet-Type All-Solid-State Lithium–Metal Batteries. Nano Lett. **2023**, 23 (10), 4415–4422. https://doi.org/10.1021/acs.nanolett.3c00720.

(169) Suzuki, N.; Yashiro, N.; Fujiki, S.; Omoda, R.; Shiratsuchi, T.; Watanabe, T.; Aihara, Y. Highly Cyclable All-Solid-State Battery with Deposition-Type Lithium Metal Anode Based on Thin Carbon Black Layer. Advanced Energy and Sustainability Research **2021**, 2 (11), 2100066. https://doi.org/10.1002/aesr.202100066.

(170) Lee, J.; Choi, S. H.; Im, G.; Lee, K.-J.; Lee, T.; Oh, J.; Lee, N.; Kim, H.; Kim, Y.; Lee, S.; Choi, J. W. Room-Temperature Anode-Less All-Solid-State Batteries via the Conversion Reaction of Metal Fluorides. Advanced Materials **2022**, 34 (40), 2203580. https://doi.org/10.1002/adma.202203580.

(171) Gao, Q.; Wu, D.; Zhu, X.; Lu, P.; Ma, T.; Yang, M.; Chen, L.; Li, H.; Wu, F. Dendrite-Free Lithium-Metal All-Solid-State Batteries by Solid-Phase Passivation. Nano Energy **2023**, 117, 108922. https://doi.org/10.1016/j.nanoen.2023.108922.

(172) Huo, H.; Chen, Y.; Li, R.; Zhao, N.; Luo, J.; Pereira Da Silva, J. G.; Mücke, R.; Kaghazchi, P.; Guo, X.; Sun, X. Design of a Mixed Conductive Garnet/Li Interface for Dendrite-Free Solid Lithium Metal Batteries. Energy Environ. Sci. **2020**, 13 (1), 127–134. https://doi.org/10.1039/C9EE01903K.

(173) Harry, K. J.; Hallinan, D. T.; Parkinson, D. Y.; MacDowell, A. A.; Balsara, N. P. Detection of Subsurface Structures underneath Dendrites Formed on Cycled Lithium Metal Electrodes. Nature Mater **2014**, 13 (1), 69–73. https://doi.org/10.1038/nmat3793.

(174) Maslyn, J. A.; Loo, W. S.; McEntush, K. D.; Oh, H. J.; Harry, K. J.; Parkinson, D. Y.; Balsara, N. P. Growth of Lithium Dendrites and Globules through a Solid Block Copolymer Electrolyte as a Function of Current Density. J. Phys. Chem. C **2018**, 122 (47), 26797–26804. https://doi.org/10.1021/acs.jpcc.8b06355.

(175) Maslyn, J. A.; Frenck, L.; Loo, W. S.; Parkinson, D. Y.; Balsara, N. P. Extended Cycling through Rigid Block Copolymer Electrolytes Enabled by Reducing Impurities in Lithium Metal Electrodes. ACS Appl. Energy Mater. **2019**, 2 (11), 8197–8206. https://doi.org/10.1021/acsaem.9b01685.

(176) Jung, Y.-C.; Hwang, C.; Kwak, M.-J.; Jeon, S.-J.; Lee, Y. J.; Kwak, W.-J.; Kim, H.; Kim, K.; Cho, W.; Yu, J.-S. On-Site Formation of Silver Decorated Carbon as Anodeless Electrode for High-Energy Density All-Solid-State Batteries. J. Mater. Chem. A **2023**. https://doi.org/10.1039/D3TA05307E.

(177) Risal, S.; Wu, C.; Wang, F.; Risal, S.; Robles Hernandez, F. C.; Zhu, W.; Yao, Y.; Fan, Z. Silver-Carbon Interlayers in Anode-Free Solid-State Lithium Metal Batteries: Current Development, Interfacial Issues, and Instability Challenges. Carbon **2023**, 213, 118225. https://doi.org/10.1016/j.carbon.2023.118225.

(178) Ye, Y.; Xie, H.; Yang, Y.; Xie, Y.; Lu, Y.; Wang, J.; Kong, X.; Jin, S.; Ji, H. Solid-Solution or Intermetallic Compounds: Phase Dependence of the Li-Alloying Reactions for Li-Metal Batteries. J. Am. Chem. Soc. **2023**, jacs.3c08711. https://doi.org/10.1021/jacs.3c08711.

(179) Molaiyan, P.; Abdollahifar, M.; Boz, B.; Beutl, A.; Krammer, M.; Zhang, N.; Tron, A.; Romio, M.; Ricci, M.; Adelung, R.; Kwade, A.; Lassi, U.; Paolella, A. Optimizing Current Collector Interfaces for Efficient "Anode-Free" Lithium Metal Batteries. Advanced Functional Materials n/a (n/a), 2311301. https://doi.org/10.1002/adfm.202311301.

(180) Luo, S.; Wang, Z.; Li, X.; Liu, X.; Wang, H.; Ma, W.; Zhang, L.; Zhu, L.; Zhang, X. Growth of Lithium-Indium Dendrites in All-Solid-State Lithium-Based Batteries with Sulfide Electrolytes. Nat Commun **2021**, 12 (1), 6968. https://doi.org/10.1038/s41467-021-27311-7.

(181) Bruce, P. G.; Saidi, M. Y. Variation of the Preexponential Factor and Activation Energy for Lithium Diffusion in Cubic Titanium Disulfide. Journal of Solid State Chemistry **1990**, 88 (2), 411–418. https://doi.org/10.1016/0022-4596(90)90236-Q.

(182) Sakuda, A.; Takeuchi, T.; Okamura, K.; Kobayashi, H.; Sakaebe, H.; Tatsumi, K.; Ogumi, Z. Rock-Salt-Type Lithium Metal Sulphides as Novel Positive-Electrode Materials. Sci Rep **2014**, 4 (1), 4883. https://doi.org/10.1038/srep04883.

(183) Flamary-Mespoulie, F. Synthèse et caractérisation de sulfures de métaux de transition comme matériaux d'électrode positive à forte capacité pour microbatteries au lithium. phdthesis, Université de Bordeaux, 2016. https://theses.hal.science/tel-01673794 (accessed 2023-10-04).

(184) Dugas, R.; Dupraz, Y.; Quemin, E.; Koç, T.; Tarascon, J.-M. Engineered Three-Electrode Cells for Improving Solid State Batteries. J. Electrochem. Soc. **2021**, 168 (9), 090508. https://doi.org/10.1149/1945-7111/ac208d.

Engineering Strategies to Improve All-Solid-State Battery Performance under Low-Pressure Conditions

Abstract: As the global shift towards renewable energy sources and electric vehicles gains momentum, lithium-ion batteries (LIBs) are seen as a building block of a decarbonised future. To meet the growing need for higher energy density and safety, all-solid state batteries (ASSBs) have emerged as a promising alternative to traditional liquid-based LIBs. Nonetheless, the implementation of ASSBs faces challenges in many aspects, notably the high operating pressure required for cycling, which prevents the use of the high capacity lithium metal anode crucial for achieving the desired energy density. Thus, this doctoral research is dedicated to addressing the challenge of operating pressure in ASSBs through two key strategies. Initially, utilising a conventional composite electrode, we capitalised on the enhanced chemical and electrochemical stability of halide-based solid electrolytes as well as their low hardness to enable low pressure cycling while accommodating high potential cathode active materials. Secondly, recognising that interfaces in composite electrodes represent a central issue in ASSBs, we utilised the concept of the solid-electrolyte-free electrode. This concept involves the development of an electrode that operates without the need for an additional ionic conductor. The outcome is an increase in energy density and a reduction in the complexity of electrode interfaces. Altogether, both of these strategies enabled cycling at pressures as low as atmospheric pressure and therefore enabled us to attempt the implementation of the lithium metal anodes.

Keywords: battery; all-solid-state; interface; low pressure.

Ingénierie pour Améliorer les Performances des Batteries Tout Solide sous Faible Pression

Résumé : Avec le développement croissant des énergies renouvelables et des véhicules électriques, les batteries lithium-ion sont considérées comme un élément clé dans un avenir décarboné. Néanmoins, pour répondre à ce besoin, des avancées majeures sont encore nécessaires en matière de densité énergétique et de sécurité. Les batteries tout-solide sont apparus comme une alternative prometteuse aux batteries traditionnelles contenant des liquides. Néanmoins, la mise en œuvre de cette technologie rencontre des défis majeur, en particulier la pression élevée nécessaire pour le fonctionnement qui empêche l'utilisation du lithium métal en tant qu'électrode négative qui est pourtant essentielle pour atteindre les hautes densités énergétiques souhaitées. Ainsi, cette thèse se concentre sur le défi associé à la pression de fonctionnement des batteries solides au travers de deux stratégies. Tout d'abord, en utilisant une électrode composite conventionnelle, nous exploitons la stabilité chimique et électrochimique accrue et la faible dureté des électrolytes solides à base d'halogénures pour faciliter le fonctionnement à basse pression tout en permettant l'utilisation des matériaux d'électrode à haut potentiel. Deuxièmement, comprenant que les interfaces dans les électrodes composites représentent un problème central, nous mettons ensuite à profit le concept d'électrode dépourvue d'électrolyte solide. Ce concept implique le développement d'une électrode qui fonctionne sans nécessiter l'ajout d'un conducteur ionique. Il en résulte une augmentation de la densité énergétique et une simplification des interfaces dans l'électrode. En somme, ces deux stratégies permettent un fonctionnement des batteries tout-solide à des pressions aussi basses que la pression atmosphérique, ouvrant ainsi la voie à la mise en œuvre de l'anode en lithium.

Mots clés : batterie ; tout-solide ; interface ; basse pression.